Étude à micro-échelle du test de pénétration du cône dans la neige

Isabel Peinke

To cite this version:

Isabel Peinke. Étude à micro-échelle du test de pénétration du cône dans la neige. Météorologie. Université Paul Sabatier - Toulouse III, 2019. Français. NNT : 2019TOU30159 . tel-02879065

HAL Id: tel-02879065
https://theses.hal.science/tel-02879065

Submitted on 23 Jun 2020

THÈSE

En vue de l'obtention du

DOCTORAT DE L'UNIVERSITÉ DE TOULOUSE

Délivré par l'Université Toulouse 3 - Paul Sabatier

Présentée et soutenue par

Isabel PEINKE

Le 28 juin 2019

Étude à micro-échelle du test de pénétration du cône dans la neige

Ecole doctorale : **SDU2E - Sciences de l'Univers, de l'Environnement et de l'Espace**

Spécialité : **Océan, Atmosphère, Climat**

Unité de recherche :
CNRM - Centre National de Recherches Météorologiques

Thèse dirigée par
Pascal HAGENMULLER et Guillaume CHAMBON

Jury
M. Henning LöWE, Rapporteur
M. Christophe MARTIN, Rapporteur
Mme Maurine MONTAGNAT RENTIER, Examinatrice
M. Jean-Pierre CHABOUREAU, Examinateur
M. Pascal HAGENMULLER, Directeur de thèse
M. Guillaume CHAMBON, Co-directeur de thèse

Acknowledgements

The manuscript is written, the thesis is defended
But one thing is needed for the work to be ended:
Think of all the people and thank them to have given me the chance
To do and finish my thesis here in France.

Le premier grand merci va a mes deux directeurs Pascal Hagenmuller et Guillaume Chambon : sans vous cette thèse n'aurait pas pu être possible, et cela ne pas uniquement d'un point administrative. Je vous remercie pour votre soutien, présence et patience pendant la thèse. Aussi merci à Samuel Morin d'avoir rendu cette thèse possible et de l'avoir mise sur de bons rails.

Je remercie également les membre du Jury de ma thèse, d'avoir accepté d'évaluer mon travail : Merci à Henning Löwe et Christophe Martin de l'avoir attentivement lu et rapporté ; merci à Maurine Montagnat Rentier et Jean-Pierre Chaboureau d'avoir accepté de l'examiner. Enfin, je souhaite remercier Frédéric Flin, Christian Geindreau et Laurent Arnaud, qui ont fait partie des comités de suivis, ils m'ont guidé et aidé à avancer ce travail.

Une thèse comme la mienne avec une partie expérimentale nécessite une équipe pour assurer les expériences. Pour cela je voudrais remercier l'équipe Microstructure qui m'a soutenu pendant les expériences de tomographie. Merci à Jacques pour tout ton aide pour les expériences : sans toi je n'aurais pas pu faire autant d'expériences, mais au moins je n'aurais pas eu froid ;) Je remercie également le laboratoire 3SR de Grenoble pour les expériences tomographie. J'ai une attention particulière pour Edward pour ses conseils sur les expériences, le traitement des images et la collaboration lors de l'utilisation de la méthode de suivi de grains.

L'équipe informatique a également été d'un grand soutien, un grand merci au Groupe ITAO d'avoir assuré un support de qualité. Delphine et Jean-Louis, j'ai également apprécié votre aide pour m'aider dans le jungle de l'administration française ;) Dominique, je te remercie d'avoir filmé ma soutenance. Je souhaite ensuite remercier tous mes collègues, ces trois ans et demi je me suis toujours sentie bien accueilli. J'ai passé des bons moments, pendant un café le matin, le repas à midi ou au yoga. Gaëlle et Rafife, d'après nos collègues, nous étions inséparables, ils étaient toujours surpris si ils on vu qu'une de nous sans les autres. Nous avons en effet passé trois superbes années ensemble et vous allez me manquer. Ni le français, ni l'anglais sont mes langues natales, je remercie alors tous ceux qui on fait partie de ma magnifique team de relecture (Ajith, Anne, Emanuel, Florence, Lionel, Neige, Solène).

On n'y croit pas toujours mais à côté de la thèse on a aussi (parfois) une vie ;) Merci à tous mes amis de me soutenir et supporter dans cet aventure. Merci à tous mes amis de m'avoir soutenu et aidé dans cette aventure. Je souhaite autant remercier les amis géographiquement proches que ceux plus éloignés pour tous ce que nous avons vécu ensemble : des repas, des sorties en montagne ou ailleurs les week-ends, des vacances, des soirées de toutes sortes, aussi la vie en colocation ou des soirée pour se faire emporter très loin avec la salsa et les rythmes latins. Merci beaucoup à toi, Ajith, d'être venu au bon moment, pour ton soutiens, ta compréhension et justement pour tout.

Und nicht zu vergessen, meine Familie: Vielen Dank an Euch, dass Ihr immer für mich da ward, an mich geglaubt habt und mich unterstützt habt. Ich bin froh Euch zu haben und zu wissen, dass Ihr da seid, was auch immer ansteht.

Abstract

Precise knowledge of the snowpack stratigraphy is crucial for different applications such as avalanche forecasting, predicting the water runoff, or estimating the Earth energy budget. The cone penetration test, which consists of recording the force required to make a cone penetrate the material of interest, is widely used to measure in situ snow profiles. The ramsonde developed in the 1930's was continuously improved into highly-resolved digital snow penetrometers. In particular, the SnowMicroPenetrometer measures the snow penetration resistance at constant speed with a vertical resolution of four microns. The force fluctuations measured at such a resolution contain information about the snow microstructure, which is essential to complete the knowledge of the mean hardness of each snow layer. Nevertheless, the link between the measured hardness profile and the snow microstructure is not yet fully understood. Indeed, existing inversion models neglect obvious interactions between the cone tip and the snow, such as the formation of a compaction zone, and have only been evaluated through empirical relations to macroscopic properties. The goal of this thesis is to investigate the interaction between the cone and the snow at a microscopic scale using X-ray tomography in order to better invert the hardness profiles into microstructural properties. In this work, we analyze cone penetration tests of a few centimeters and thus the measured profiles contain a non negligible transient part due to the progressive formation of a compaction zone. In order to explicitly account for this process in the inversion model, we successfully developed a non-homogeneous Poisson shot noise model which considers a depth dependency of the rupture occurrence rate. We used this model to characterize snow sintering with cone penetration tests under controlled cold-lab conditions. According to the model, the vertical heterogeneity of hardness profiles was due to variations of the rupture occurrence rate, while the time evolution of the macroscopic force was controlled by bond strengthening. This partition is consistent with the expected sintering processes and provides an indirect validation of the proposed model. The second part of the thesis consists of cold-lab experiments combining cone penetration tests and X-ray tomography. High resolution three dimensional images of the snow sample before and after the cone test were measured. On these images, a novel tracking algorithm was applied to determine granular displacements induced by the test. We precisely quantified the size of the compaction zone and its relation to the snow characteristics. Furthermore, we showed that the observed vertical displacements challenge the use of standard cavity expansion models as inversion models. Finally, we linked the microstructural properties obtained from tomography, such as the bond size or the number of failed bonds, to properties derived from hardness profiles. We showed that the properties estimated from cone penetration tests are proxies of the snow microstructure, but remain too conceptual to expect a straightforward relation. In the future, these studies should make it possible to derive in an objective way the stratigraphy of the snowpack from a simple and fast field measurement.

Keywords: snow, microstructure, mechanical properties, cone penetration tests, micro-tomography, SnowMicroPenetrometer

Résumé

La prévision du risque d'avalanche, les prévisions hydrologiques et l'estimation du bilan énergétique de la Terre dépendent d'une connaissance précise de la stratigraphie du manteau neigeux. Le test de pénétration du cône, qui consiste à enregistrer la force nécessaire pour faire pénétrer un cône dans le matériau d'intérêt, est largement utilisé pour mesurer des profils de neige. La sonde de battage, développée et utilisée depuis 1930, a été continuellement améliorée. Aujourd'hui, des pénétromètres numériques, tel que le SnowMicroPenetrometer, permettent de mesurer la résistance à la pénétration à vitesse constante avec une résolution verticale de quelques microns. Les fluctuations de force mesurées à cette résolution contiennent des informations sur la microstructure essentielles pour compléter la connaissance de la dureté moyenne de chaque couche de neige. Néanmoins, le lien entre le profil de dureté et la microstructure de la neige n'est pas encore entièrement compris. En effet, les modèles d'inversion existants négligent certaines des interactions entre la pointe du cône et la neige, comme la formation d'une zone de compaction, et ils n'ont été évalués que par des relations empiriques avec des propriétés macroscopiques. L'objectif de cette thèse est d'étudier l'interaction entre le cône et la neige à une échelle microscopique, à l'aide de la tomographie à rayons X, afin d'extraire, de manière plus précise, les propriétés microstructurelles de la neige à partir des mesures de résistance à la pénétration. Dans ce travail, nous analysons des tests de pénétration du cône de quelques centimètres de profondeur, qui contiennent une partie transitoire non négligeable due à la formation progressive d'une zone de compaction. Afin de prendre en compte explicitement ce processus, nous avons développé un modèle statistitique non-homogène de Poisson, qui prend en compte une dépendance à la profondeur du taux d'occurrence de rupture entre grains de neige. Nous avons utilisé ce modèle pour caractériser le frittage de la neige par des tests de pénétration du cône sous conditions contrôlées dans une chambre froide. D'après le modèle, l'hétérogénéité verticale des profils de dureté était due aux variations du taux d'occurrence de rupture, tandis que l'évolution temporelle de la force macroscopique était contrôlée par un renforcement des ponts. Cette partition est cohérente avec les processus de frittage connus et fournit une validation indirecte du modèle proposé. Une deuxième partie de la thèse a porté sur des expériences en chambre froide combinant des tests de pénétration du cône et de l'imagerie par tomographie X. Des images tri-dimensionnelles à haute résolution d'un échantillon de neige ont été prises avant et après le test du cône. Sur ces images, un nouvel algorithme de suivi de grains a été appliqué pour déterminer les déplacements granulaires induits par le test. Nous avons quantifié avec précision la taille de la zone de compaction et sa relation avec les caractéristiques de la neige. Nous avons montré que les déplacements verticaux observés compliquent l'utilisation de modèles d'expansion de cavité comme modèles d'inversion. Enfin, nous avons lié les propriétés microstructurelles obtenues par tomographie, telles que la taille ou le nombre de ruptures de ponts, à des propriétés dérivées des profils de dureté. Nous avons montré que les propriétés estimées à partir des tests de pénétration du cône sont des approximations de la microstructure de la neige, mais restent trop conceptuelles pour espérer une relation directe. A l'avenir, ces études devraient permettre de dériver, de manière objective, la stratigraphie du manteau neigeux à partir d'une mesure de terrain simple et rapide.

Mots clés: neige, microstructure, propriétés mécaniques, test de pénétration du cône, micro-tomographie, SnowMicroPenetrometer

Contents

Introduction en français

Environ 25% de la surface de la Terre est recouverte de neige, certaines régions ont un enneigement saisonnier et d'autres sont recouvertes toute l'année. L'enneigement a un impact sur la vie des habitants de ces régions. Par exemple, les Eskimos ont adapté leur vie et leur langue à la neige et ils ont pléthore de noms pour nommer les différents états de la neige [e.g. Boas, 1911, Martin, 1986]. En recherche, il existe également une classification de la neige [Fierz et al., 2009].

La neige se forme dans les nuages, là où se passe la nucléation. Ce processus peut être divisé en une nucléation homogène de gouttes d'eau surfondues [e.g. Pruppacher, 1995] et une hétérogène impliquant des particules de nucléation, comme des particules de poussière [e.g. Libbrecht, 2005]. Le cristal initial qui en résulte croîtra rapidement, en accumulant la vapeur d'eau de l'air ambiant au dépend des goutelettes d'eau surfondue avoisinantes (effet Bergeron-Findeisen, Bergeron [1935]), des cristaux plus petits et éventuellement par impact et gel à sa surface des goutelettes surfondues. Cette formation est influencée par les conditions atmosphériques. Chaque cristal lui-même est unique, et sa forme géométrique est due à la forme moléculaire de la glace dans les conditions atmosphériques terrestres (forme hexagonale).

Une fois que le cristal de glace est suffisamment grand, la gravité agit sur lui et il tombe. Pendant sa chute en dehors du nuage, il peut passer dans plusieurs masses d'air différentes. Ces masses d'air doivent être suffisamment froides pour que les cristaux ne fondent pas avant leur arrivée au sol.

Pendant le dépôt, la structure des cristaux sera également influencé par les conditions atmosphériques. En absence de vent et par des températures basses, les cristaux de neige fraîche garderont leur intégrité et leur forme géométrique régulière. En présence de vent, ces formes fragiles peuvent se briser. Dans des conditions plus chaudes, lorsque la température est légèrement positive, les cristaux peuvent être partiellement fondus et contenir de l'eau liquide. Le dépôt des cristaux de neige sur le sol va progressivement créer une couche de neige. Cette couche de neige va ensuite évoluer avec le temps et peut être recouverte par d'autres chutes de neige. Différentes métamorphoses agissent sur la neige : thermodynamique (transfert de vapeur d'eau et d'eau liquide) et mécanique.

La neige est un matériau poreux car elle contient de l'air et cette porosité élevée permet à la vapeur d'eau de diffuser dans sa matrice. Ce processus est très actif, car la température de la neige est proche du point de fusion. Sublimation de la glace, transport et dépôt de vapeur d'eau ont lieu. Ils dépendent essentiellement des différences de température dans le manteau neigeux (ce qu'on appelle le gradient de température) mais également des différences de géométrie (rayon de courbure). Selon l'intensité du gradient de température, le type de métamorphose est différent [e.g. Yosida et al., 1955, Colbeck, 1982]. En présence d'un faible gradient de température, les effets de courbures priment : les grains ont tendance à s'arrondir, grossir et les liaisons entre eux se renforcent avec le temps ; ce processus s'appelle le frittage et s'accompagne d'un gain de cohésion de la couche de neige ; les grains formés sont appelés grains fins. Un fort gradient de température favorise les flux de vapeur d'eau de la partie de la couche ayant les températures les plus élevées vers les plus basses. Il en résulte également une modification de la microstructure (grossissement des grains, apparition d'angles sur les zones de condensation) et une diminution de la cohésion ; les grains formés sont des faces planes ou des gobelets pour les très fortes valeurs de gradients [e.g. Schneebeli and Sokratov, 2004, Calonne et al., 2014].

La présence d'eau liquide arrondit les grains en augmentant leur taille ; on parle alors de grains ronds. La cohésion dépend alors de la teneur en eau liquide de la couche de neige. Une présence modérée d'eau crée des forces capillaires dans le manteau neigeux. Lorsque la teneur en eau est élevée, la cohésion de la neige diminue car l'eau liquide joue alors un rôle de lubrifiant. Si l'eau liquide regèle, ces grains ont alors une forte cohésion dite cohésion de regel.

La neige est très sensible aux contraintes mécaniques externes, comme les charges mécaniques, pour deux raisons principales : 1) le fluage de la neige peut se produire à cause des températures homologues élevées et de la nature cristalline de la glace et 2) la fragilité du matériau neige en raison de sa porosité élevée. Le vent peut agir comme une contrainte mécanique sur la neige et forme une couche cohésive. Le tassement des couches est dû à un réarrangement des grains et de la charge de la neige des couches supérieures [e.g. Chandel et al., 2007].

Un enneigement saisonnier typique consiste en différentes couches de neige ayant des propriétés différentes. Par exemple, elles diffèrent par leur densité, leur surface spécifique (SSA), la forme et la taille de leurs grains. Ces différentes propriétés géométriques et microstructurales définiront les propriétés mécaniques à l'échelle des ponts entre les grains mais aussi à l'échelle du manteau neigeux. Un exemple de ce comportement mécanique est la cohésion entre les grains. En effet, une couche qui montre une faible cohésion, une couche fragile, est l'un des principaux facteurs lors d'avalanches provoquées par les skieurs. Si ces couches fragiles sont recouvertes d'une couche compactée, avec une cohésion de frittage, un manteau à l'empilement instable se met alors en place. Lorsqu'un skieur ou un randonneur passe, la contrainte due à son poids peut atteindre la couche fragile, celle-ci s'effondre ; si l'effondrement se propage, la plaque se met alors en tension et peut finir par se rompre ; elle glisse alors vers le bas. C'est ce que l'on appelle une avalanche de plaques. D'autres avalanches peuvent se produire, comme les avalanches ponctuelles de neige fraîche ou les avalanches de neige humide. Dans les Alpes françaises, chaque année, environ 30 décès sont dus aux avalanches (source ANENA) dont la majorité sont des avalanches de plaques. Une bonne connaissance de la structure interne du manteau neigeux est primordiale, et la liaison entre les grains et leur forme à l'échelle microscopique conditionnent leur comportement macroscopique. Ainsi, dans la prochaine section, nous décrirons les mesures existantes pour décrire la stratigraphie du manteau neigeux ainsi que les modèles qui leur sont associés.

Une méthode facile et objective pour avoir une information sur la stratigraphie du manteau neigeux sont les tests de pénétration du cône (Cone Penetration Test, CPT en anglais). Une première application à la neige en a été faite dans les années 1930 avec la sonde de battage [Bader et al., 1939]. Depuis, les CPT ont été constamment améliorés, notamment par le développement de pénétromètres numériques. Bradley [1966] a développé le résistographe, qui mesure la résistance en profondeur et l'enregistre sur un papier. Plus tard, Dowd and Brown [1986] ont obtenu les premiers profils numériques à notre connaissance, en enregistrant la force de pénétration avec une résolution de 5 mm. Schneebeli and Johnson [1998] ont développé le SnowMicroPenetrometer (SMP), qui est largement utilisé aujourd'hui par la communauté de recherche sur la neige, et qui est au coeur de cette thèse. Le SMP mesure la force de pénétration à une résolution horizontale de 4 μm. En raison de sa haute résolution, on suppose que le signal est capable d'estimer les propriétés micromécaniques de la neige [Johnson and Schneebeli, 1999, p. ex.]. D'autres pénétromètres numériques existent comme le pénétromètre SABRE Mackenzie and Payten [2002] ou SP1 et SP2 [Avatech, 2014]. Il s'agit de pénétromètres qui sont poussés manuellement dans la neige. Ce type de pénétromètre a une résolution moins fine mais est néanmoins prometteur, car il comble le fossé entre les pénétromètres dédiés à la recherche comme le SMP et les instruments très simples et robuste pour une utilisation en réseau, comme la sonde de battage.

[Schweizer and Wiesinger, 2001] mentionnent que le profil de la sonde de battage classique est utile pour différencier les manteaux neigeux potentiellement stables ou instables. Cependant, Pielmeier and Schneebeli [2003] ont montré que les couches minces et fragiles ne sont pas capturées par la sonde de battage en raison de sa dureté grossière et sa faible résolution verticale. Schneebeli et al. [1999] ont souligné la haute précision avec laquelle ils ont mesuré les interfaces entre les couches de neige faible et dure. Ces résultats ont été confirmés par Kronholm et al. [2004], qui ont analysé la variabilité spatiale de la résistance du SMP par rapport à un puits à neige (sonde de battage, test rutschblock et mesures manuelles). Ils en ont conclu qu'il est possible d'identifier des couches distinctes en fonction des variations de la résistance à la pénétration.

D'autres études ont tenté de détecter et de classer les différents types de neige à partir des profils de force du SMP. Différentes études ont tenté de détecter les couches fragiles en analysant statistiquement le signal de force Pielmeier and Schweizer [2007], Lutz et al. [2007] and Herwijnen et al. [2009] ou d'indiquer la stabilité du manteau neigeux. Satyawali et al. [2009] ont développé une approche préliminaire d'une classification de neige, indépendante des observateurs, en 5 principales classes de neige. De plus, Satyawali and Schneebeli [2010] ont utilisé un semivariogramme pour l'interprétation des profils SMP et ont montré qu'il est possible d'estimer les échelles spatiales des différentes classes de neige. Des analyses similaires ont également été effectuées avec le pénétromètre SABRE ; par exemple Floyer and Jamieson [2008] et Floyer and Jamieson [2009] ont présenté une méthode pour suivre les couches fragiles dans les signaux du pénétromètre. Récemment d'ailleurs, McCallum [2014] a présenté des expériences sur l'application du CPT qui est utilisé dans les sols classiques aux sols enneigés de l'Arctique. McCallum and Wiegand [2018] ont développé un modèle simple pour estimer la résistance de la neige à partir des données de frottement du manchon de friction du CPT. Pour valider ce modèle, des données supplémentaires sont nécessaires.

Il existe plusieurs modèles statistiques pour estimer les propriétés micromécaniques à partir des profils du SMP [e.g. Johnson and Schneebeli, 1999, Marshall and Johnson, 2009, Löwe and Herwijnen, 2012]. Ils supposent tous que le profil de force macroscopique mesuré $F(z)$ est une superposition de ruptures individuelles des liaisons reliant les grains de neige. Tous ces modèles interprètent un profil SMP $F(z)$, c'est-à-dire la force de pénétration macroscopique F en fonction de la profondeur z, comme la superposition d'événements de rupture spatialement non corrélés mais identiques. Chaque événement est supposé correspondre à la rupture d'une liaison ayant un comportement de rupture élastique-fragile. Ces modèles d'inversion estiment les propriétés suivantes : flexion à la rupture δ, force de rupture de liaison f et dimension de l'élément microstructurel L. Löwe and Herwijnen [2012] à proposé un modèle statistique qui suppose ces ruptures sont aléatoirement distribué dans l'espace. Cette distribution peut être décrit pas un processus de Poisson homogène (HPP, homogeneous Poisson process en anglais). Les résultats des estimations micromécaniques de l'HPP sont utilisés dans d'autres études pour trouver les propriétés macroscopiques de la neige. Proksch et al. [2015] ont utilisé la force de pénétration médiane ($\tilde{F}$) et la dimension de l'élément microstructurel ($L = (A_c/\lambda)^{1/3}$, avec la surface de la pointe du penetromètre A_c), pour estimer des valeurs de masse volumique et de SSA. Ces formules et la formulation du module d' Young macroscopique de [Johnson and Schneebeli, 1999] sont souvent utilisées pour analyser les profils du SMP ; par exemple, les études de l'instabilité des pentes et de la propagation des fissures sont réalisées avec ces estimations [e.g. Reuter et al., 2015, Schweizer et al., 2016, Reuter et al., 2019].

Des études expérimentales ont montré qu'une zone de déformation non négligeable se forme autour de la pointe du cône en pénétrant dans la neige [LeBaron et al., 2014, Herwijnen and Miller, 2013]. Ces deux études ont modélisé la déformation autour de la pointe SMP en utilisant la vélocimétrie par image de particules (Particle Image Velocimetry, PIV en anglais). [Herwijnen, 2013] a également utilisé des images tomographiques des échantillons après le test SMP afin d'analyser la dépendance radiale de CZ à la densité de la neige. Bishop et al. [1945] a inntroduit le le « cavity expansion model » (CEM), qui retire les propriétés matérielles de l'argile et du sable à partir du CPT. Le modèle suppose que le matérielle d'intéret est un matériau continu et que les forces sont uniquement radiales. Le CEM est un modèle qui prend en compte la déformation autour du cône, alors que le HPP n'en tient pas compte. Néanmoins, l'hypothèse d'un matériau continuum est forte, car le rapport cône/grain de neige typique pour le SMP est proche de sa limite.

Une façon facile d'observer les grains de neige est d'utiliser une loupe. Certaines sont suffisamment légères et peu emcombrantes pour pouvoir être transportées sur le terrain afin d'identifier la taille et la forme des grains et les classer après Fierz et al. [2009]. Ces mesures dépendent toutefois de l'observateur. Deux observateurs donneront probablement une granulométrie différente, et même un type différent (par exemple, s'il s'agit d'une couche avec des grains fins se métamorphosant en grains à faces planes, un observateur identifiera les grains fins comme grains de neige majeurs et l'autre les cristaux facettés). À cause de cette subjectivité, malgré la valeur informative de ces informations, il est nécessaire de développer d'autres métriques de la microstructure.

Une première application de la tomographie microscopique par rayons X (μCT) sur des échantillons de neige a été faite par Brzoska et al. [1999]. Cette méthode permet d'obtenir la microstructure tridimensionnelle d'un échantillon de neige à une résolution de quelques micromètres. Habituellement, un échantillon de neige d'une telle résolution a une taille de quelques cm^3. Cette méthode est non destructive et peut donc suivre le métamorphisme de la neige in-situ [e.g. Schneebeli and Sokratov, 2004, Calonne et al., 2015]. Wang and Baker [2013] ont utilisé la μCT et des images de microscopie électronique à balayage pour observer les changements microstructurels de la neige sous compression uniaxiale. Une autre application de la μCT est la documentation de neiges naturelles recueillies sur le terrain. Comme le transport peut être critique et même détruire la structure fragile de la neige, il existe des méthodes d'imprégnation [e.g. Coleou et al., 2001, Heggli et al., 2009]. Ces méthodes sont néanmoins destructrices, car il est difficile d'éliminer complètement le matériau d'imprégnation.

Pour résumer, les tests de pénétration du cône dans la neige, dont le SMP, sont largement étudiés et des approches statistiques existent pour estimer les propriétés micromécaniques de la neige. Néanmoins, ces modèles d'inversion négligent les processus physiques autour de la pointe lors de la pénétration, comme la formation d'une zone de compaction. Pour une interprétation correcte du signal, il est crucial de savoir ce qui se déroule autour de la pointe. La μCT est un outil prometteur pour obtenir des informations sur la microstructure de la neige [e.g. Hagenmuller, 2014]. En outre, des études du champ de déformation pour des tests de pénétration du cône existent déjà pour les sols, combinant la tomographie par rayons X et la corrélation des images numériques [e.g. Paniagua et al., 2013, Silva et al., 2015].

Le but de cette thèse est de mieux comprendre les processus qui se produisent directement autour de la pointe pendant le test de pénétration à une échelle microscopique et de les inclure dans les modèles existants. C'est ainsi que nous avons centré le travail sur les questions suivantes :

Peut-on améliorer les modèles d'inversion existants afin de prendre en compte une zone de compaction ? Des études expérimentales de test de pénétration du cône dans la neige ont montré qu'une zone de compaction se forme devant et à côté de la pointe du cône pendant le processus de pénétration. Cette déformation n'est pas prise en compte dans les modèles d'inversion actuels. Ces modèles estiment les propriétés micromécaniques suivantes : force de rupture, déflexion à la rupture et taux d'occurrence de ruptures. Afin de mieux interpréter ces propriétés, il conviendrait de prendre en compte la zone de compaction.

Le SMP est-il capable de suivre l'évolution de la microstructure de la neige avec le temps ? Depuis l'élaboration du SMP, il a été largement étudié. Certaines études se sont concentrées sur l'identification des couches fragiles (i.e. les stratigraphies sujettes aux avalanches) ou même sur la classification du signal dans les principaux types de neige. Ce type d'études était basé sur l'analyse des signaux. De plus, des analyses statistiques ont été effectuées pour estimer les propriétés micromécaniques des grains de neige et de leurs liaisons. Par conséquent, le signal était censé être une superposition de ruptures élastiques-fragiles des grains de neige. A notre connaissance, il n'y a qu'une seule étude qui a essayé de suivre le métamorphisme de la neige avec le SMP. Là, le frittage a été étudié par l'évolution de la force macroscopique. Il serait donc intéressant de savoir si les estimations micromécaniques permettent de suivre l'évolution de la microstructure de la neige pour le processus de frittage, mais aussi pour le métamorphisme de gradient de la neige en conditions contrôlées.

Que se passe-t-il exactement autour de la pointe pendant le processus de pénétration ? Pour une interprétation correcte du signal, il est crucial de savoir exactement ce qui se passe autour de la pointe du cône pendant la pénétration. Jusqu'à présent, les études ont porté sur la description de la zone de compaction (PIV ou changement de densité), notamment concernant sa taille et sa forme ainsi que le déplacement des grains qui se produisent autour de la pointe. Néanmoins, il manque une information exacte sur ce qui se passe à l'échelle microscopique. Il serait intéressant de voir, par exemple, quelles sont les liaisons qui se brisent.

Comment la déformation de la neige à côté de la pointe conique est-elle liée au profil de force mesuré ? Cette question est liée à la question précédente. Si nous savons ce qui se passe exactement autour de la pointe, il sera possible d'établir un lien avec le profil de force. L'analyse micromécanique du signal de force passe par la connaissance exacte des contraintes autour de la pointe. Le signal est lié à une intensité de rupture ou à une force de rupture? Et est-ce vraiment ce que nous mesurons ?

1

Introduction

Contents

1.1 General introduction: From a snowflake to an avalanche

About 25% of the Earth's surface is covered by snow, some regions have a seasonal snowpack and some are covered the whole year. The snow cover impact the life of the people in these regions. Parts of Alaska are covered with snow the whole year and the people living there, the Inuits, have adapted their life to it. They use snow to build their houses, as a water source, and also for locomotion. For example, they use sledges to move and not wheels. Even their language adapted to this situation as linguistic studies showed [e.g. Boas, 1911, Martin, 1986]. The Inuits have three different basic word roots for snow: one for falling snow, another one for fallen snow and and the third one for snow on the ground [e.g. Boas, 1911, pp.25-26]. Based on these word roots they will further distinguish different snow types. Different words for snow on the ground Inuit are for example fresh snow, soft snow, melting snow or even a word for lower layer of sugar snow used for drinking water [Kaplan, 2003]. Life surrounded by snow also involves danger, like avalanches. Also here Inuits have a word to describe snow which is prone to avalanches. These examples show that living in snow makes the Inuits true snow observers, or even specialists of snow. Their distinction between different snow types can be set in comparison with the scientific classification of different snow grains. Fierz et al. [2009] proposed an international classification of snow, with 9 main morphological grain shape classes, which are themselves divided into sub-classes (37 in total). In general, a good knowledge of a snowpack is important for avalanche forecast, the prediction of the water runoff and estimating the Earth energy budget. More than one sixth of the world's population depends on waters resources from glaciers or seasonal snowpacks [Barnett et al., 2005]. The seasonal snowpack is a water storage, and with the knowledge of its mean density and height the snow water equivalent can be estimated. The snow, with its high albedo plays an important role on the Earth's energy budget. A high albedo means, that the main part of the incoming sun radiation is reflected, which leads to a global cooling of the atmosphere. The overall snow coverage is important for energy estimation, which can for example be measured by satellites. The next sections sum up scientifically how a snowpack is formed, beginning with the formation of the snowflakes in the cloud, going on with their deposit on the ground and ending with the formation of a snowpack, which might be avalanche prone or not.

1.1.1 Different types of snow

The origin of the snow is in the cloud, where ice nucleation takes place. This process can be divided into a homogeneous nucleation of super-cooled water drops [e.g. Pruppacher, 1995] and a heterogeneous one involving nucleation particles, like dust particles [e.g. Libbrecht, 2005]. The resulting frozen droplet will grow quickly, by accumulating further water vapour from the ambient air (Bergeron Findeisen effect, valid for a temperature range of [-5,-13°C], Bergeron [1935]) until a snow crystal is formed. This formation is influenced by the atmospheric conditions, in particular, temperature and humidity and it results in different forms, like dendrites, plates or columns (Fig. 1.1). The temperature mainly influences the growth of the snow crystals as to whether they will grow into plates or columns, while the more complex structures occur for higher supersaturations [e.g. Libbrecht, 2005]. Each crystal itself is unique, but will have a hexagonal shape, which is due to the molecular shape of a water molecule. This was already pointed out by Johannes Kepler in 1611, with the apparently first scientific description of the snow crystal symmetry [Kepler, 1966, English translation].

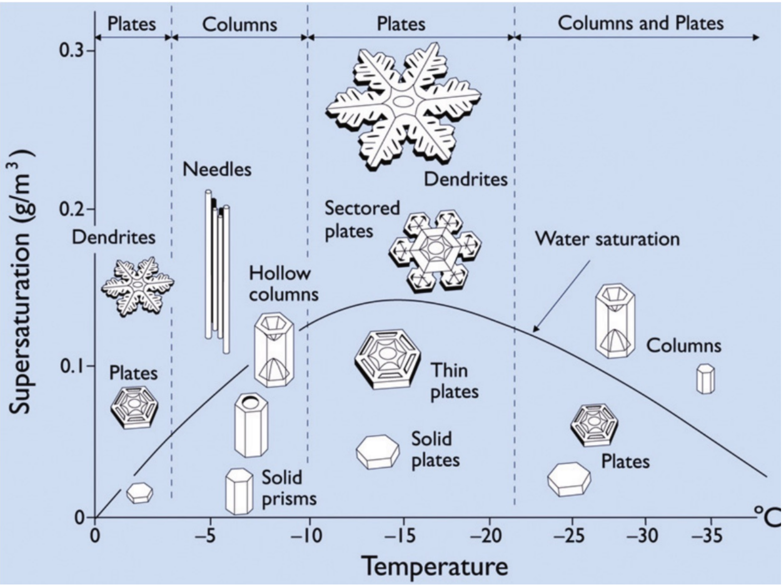

Figure 1.1: Snow crystal morphology diagram from Libbrecht [2005] showing different types of snow crystals as function of the atmospheric conditions, namely the temperature and the water vapour supersaturation.

Once the snow flake grows enough the gravity acts on it and the crystal falls down and deposits. While the snow flake is falling outside the cloud, it may pass through several different air-masses. These air-masses have to be cold enough that the snowflakes will not melt before their arrival at the ground. During the deposit, the snowflake structure will be governed by the atmospheric conditions: On nearly windless and cold conditions the snowflakes will keep their regular geometrical shape. In the presence of wind, these fragile shapes can break and the snow which is deposited is already fragmented. With warmer temperatures slightly above 0°C the snow flakes will already have a nonzero liquid water content.

The accumulation of the snowflakes on the ground will progressively create a snow layer. This snow layer will now evolve with time and may get covered further as a result of future snow events. For example, the snow grains which touch create bonds and these bonds will grow with time. This process of bond formation and growth is called sintering. In addition to this, different snow metamorphism may occur, which can be explained by these three major processes: 1) water vapour transport, 2) melting, 3) mechanical loading.

Water vapour transport: A snow layer contains mainly ice and air, where the proportion of air can be up to 90%. Thus, snow is a porous material and this high porosity is important for further evolution of the snow layer, as it enables water vapour to diffuse into it. This process is very active, as snow exists at high homologous temperatures, i.e. the temperature is close to the melting point. This allows for processes like ice sublimation, water vapour transport and deposition to take place. They are dependent on the temperature differences within the snowpack, the so called temperature gradient (∇T). Following its strength the type of metamorphism is divided into an equilibrium and a kinetic form [e.g. Yosida et al., 1955, Colbeck, 1982]. If a small temperature gradient is present, i.e. $\nabla T \leq 5$ K m^{-1} it is the equilibrium type and the grains tend to get rounded and the bond between them are thickening with time. During this process water vapour is transported from the convex to the concave forms [e.g. Flin et al., 2004, Kaempfer and Schneebeli, 2007]. The resulting grain form is called rounded grain. The kinetic metamorphism involves higher temperature gradients ($\nabla T > 5$ K m^{-1}), which occur normally close to surface. This high gradient favors water vapour fluxes from the higher temperatures to the lower ones. This leads to a change in the microstructure and the formed grains are plane facets and sharp edges [e.g. Schneebeli and Sokratov, 2004, Calonne et al., 2014]. For snow under very strong gradients ($\nabla T > 20$ K m^{-1}) for longer times (one to several weeks) depth hoar will be formed. The equilibrium metamorphism tends to stabilize the snowpack, while the kinetic one decreases the cohesion between the grains and thus decreases the stability of the snowpack.

Melting: A warm atmospheric temperature can lead to the melting of the snowpack. At this moment the snowpack contains ice and liquid water, and has a temperature of 0°C. The melting and refreezing cycles tend to round the grains and their size increases and melt forms appear. Their cohesion is dependent on the liquid water content in the snowpack. The melt forms have strong cohesion if now liquid water is present. A moderate presence of water creates capillary forces in the snowpack. However, when the water content is very high, the snow cohesion will decrease as the liquid water plays the role of a lubricant.

Mechanical loading: Snow is very sensitive to external mechanical stress, like mechanical loading for two main reasons: 1) creep deformation may occur due to high homologous temperatures and the viscoplasticity behaviour of snow, and 2) snow is fragile material due to its high porosity. Wind can act as mechanical stress on the snow. As explained earlier it can break the falling snowflakes into smaller grains, but wind can loosen and transport the snow grains (snow-drift), which could result in a change in their shape. This type of grains sinters fast and thus forms a cohesive layer. Otherwise, packing of the layers is due to a rearrangement of the grains and the weight of the overburden snow [e.g. Chandel et al., 2007].

To sum up, snow is a complex material which is formed in the clouds and once deposited on the ground changes continuously. These changes are influenced by processes like, the water vapour transport, melting processes and mechanical loading. This leads to the formation of different types of snow grains, which are classified into main snow types. Different snow events form different snow layers with different snow types and thus different mechanical properties. These properties determine the stability of the snowpack.

1.1.2 The snowpack and its stability

A typical seasonal snowpack consists of different snow layers having different properties (Fig. 1.2). For example, they differ in their density, specific surface area (SSA), grain shape and size. These different geometric and microstructural properties define the mechanical properties at the bond scale but also at the scale of the whole snowpack. One example of this mechanical behaviour is the cohesion between the grains. A layer which exhibits weak cohesion, a so-called weak layer, is one of the main trigger for avalanches. Persistent weak layers are typically made of depth hoar or faceted crystals, that means they are formed at the surface when a strong temperature gradient acts on the layer for one week of more. If these weak layers are now covered by a packed layer, also called slab-layer, with relatively strong cohesion an avalanche prone layering is formed. Such a slab-layer, is for example a layer of wind packed snow, as described in the previous section. When a skier or hiker passes over such a layer, their weight can reach the weak layer and a crack appears in the weak layer, propagates, and the slab-layer will slide downwards.

This is a so-called slab avalanche. Fig. 1.3 shows a scheme of such a snow layering with an avalanche and also a photo of such a weak layer. The danger associated with this type of avalanches is that the weak layer cannot be seen from the surface.

Figure 1.2: Photo of a snow pit. The image was taken the 25th February 2016, Col de Lautaret, French Alps.

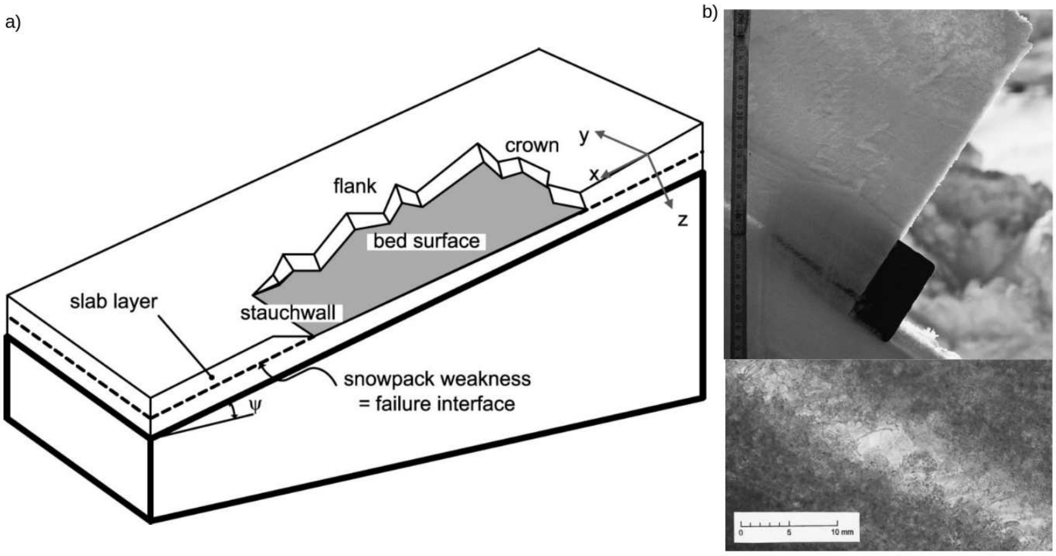

Figure 1.3: a) Scheme of a slab avalanche from Schweizer et al. [2003] and b) images of a weak layer from Jamieson and Schweizer [2000]

Other avalanches that can occur are powder snow avalanches or melt snow avalanches. If a considerable mass of fresh snow falls, it can be too heavy and if the load exceeds the capacity of the snowpack to hold the snow, a spontaneous avalanche release may happen. These are fluid-like avalanches. The melting avalanches occur most probably in spring. Due to a strong increase of the water content the snow resistance decreases and this may lead to an avalanche. This process can even be intensified if rain adds an additional load to the snowpack. The two latter avalanche types generally release spontaneously without any triggering agent. In the French Alps, each year about 30 people lose their lives due to avalanches (source ANENA). A significant number of them are due to slab avalanches.

The avalanche risk management is divided into two categories: one is the forecast of the avalanches for short-term forecast and the other one is the determination of the risk of avalanches in long term. For the second one, hazard mapping exists. These are maps, which indicate the risk of avalanches in general. This data can be of interest for industries, real estate developments, etc.

During the winter, the French weather service, Météo-France, publishes an avalanche bulletin on a daily basis. To write this bulletin, an avalanche forecaster combines information of snowpack measurements, weather conditions, results of forecasting models and certain insights that only come from experience. The snowpack forecasting model used at the French weather forecasting service is the SAFRAN-CROCUS-MEPRA model [Durand et al., 1999], which computes a stability index as a function of the past and the modeled weather conditions. The published bulletin gives information related to the avalanche danger within a scale from 1 (low) to 5 (very high) for different altitudes as well as for the different orientations of the slope. In addition to the scale, a summary is provided with the estimation of the avalanche activity, containing the frequency of the release and the size of the avalanche. It contains a more detailed description of the stability of the snowpack than the scale.

To sum up, an in-depth knowledge related to the snow structure is important for avalanche forecasting, for example. To this end, a detailed knowledge of the snow stratigraphy and the related mechanical properties is important. The following section delves into the existing measurements and models to characterize a snowpack.

1.1.3 Characterization methods for snowpacks

Detailed knowledge of snow stratigraphy is important for avalanche forecast, the prediction the water runoff and estimating the Earth energy budget.

The measurements for the snowpack are done by snow observers. The aim is to identify the different layers of the snowpack and their properties. To perform such measurements, a pit is dug and a preliminary rough identification of different layers can be done by looking at the snow pit wall. Figure 1.2 shows an example for a layered snowpack, where the layers can be clearly observed. However, normally, a more detailed analysis of the different properties is required to distinguish the different layers. One method is by touching the snow, and feeling the different layers. Once the different layers are identified, the observer will look at the grains under magnifying lenses to determine the size. An international classification [Fierz et al., 2009] exists to classify the different shapes, and the main snow types are represented by symbols. For each layer, a first symbol indicates the major type and a second one the minor grain type. Besides, the grain size is estimated as well. Figure 1.4b shows these results in the first two columns. The third column depicts the hand hardness (HH). It is a test conducted by the observer with hand to estimate the hardness of the snowpack. It is a scale from 1 to 5, one being the softest and five the hardest [de Quervain, 1950]. The last column shown in Fig. 1.4b is the humidity measurement of the layer. Humidity measurements are conducted, if the temperature of the snow layer is 0°, then liquid water may be present in the snowpack. Additional measurements which are performed on the snowpack (not shown here) are temperature and density. These measurements presented here are often observer dependent, it is for example not obvious to find the mean size of the grains and to classify them after their shape.

Another method of obtaining information related to the snowpack are by performing cone penetration tests. A cone penetration test consists of measuring the force required to penetrate the cone into the soil. In snow the swiss ramsonde penetrometer was developed in the 1930's [Bader et al., 1939]. This is an additional measurement done during a typical snowpack measurement. It consists of a hammer with a weight on top. For the measurement the observer let drop this hammer on the rod and observes the indentation height from a scale, which is engraved on the rod (Fig. 1.5a). Also higher resolution and electrical penetrometers exists. For example the SP2 (Avatech, Fig. 1.5b) is a penetrometer, which provides a digital measurement the penetration force, but is inserted by hand. And then there are digital penetrometers with constant penetration speed like the

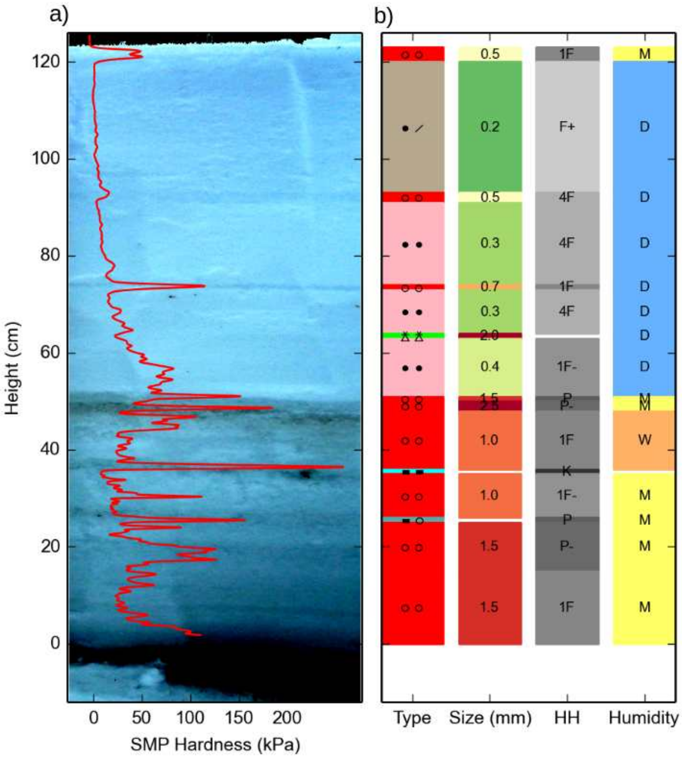

Figure 1.4: a) Image of the snow layer overlaying the smoothed force profile, b) information of the Col de Porte, Chartreuse, French Alps, 11/03/2016 Hagenmuller et al. [2018b]. The hardness profile is obtained by the SnowMicroPenetrometer (SMP) and HH is the hand hardness.

SnowMicroPenetrometer [Schneebeli and Johnson, 1998]. It is an instrument with high resolution which is nowadays used by researchers (Fig. 1.4c).

In research several other studies exist to measure the snow properties. One method is the micro-computed tomography (μCT), which results in high resolution three-dimensional images of the snow. To this end, two-dimensional radiographs covering a 360° rotation are taken, which are then reconstructed into three-dimensional grayscale images representing the attenuation coefficients of the different materials composing the samples. The resolution of such images are a couple of micro-metres, while the samples have a size of a couple of cubic centimetres. The resulting images help to obtain a detailed view of the snow microstructure and possibly the numerical computation of physical and mechanical properties of the snow sample (based on homogenization techniques). One example is the determination of the elasticity (the Young modulus) of the snow [e.g. Gerling et al., 2017]. Another example is to follow the metamorphism of snow over a couple of

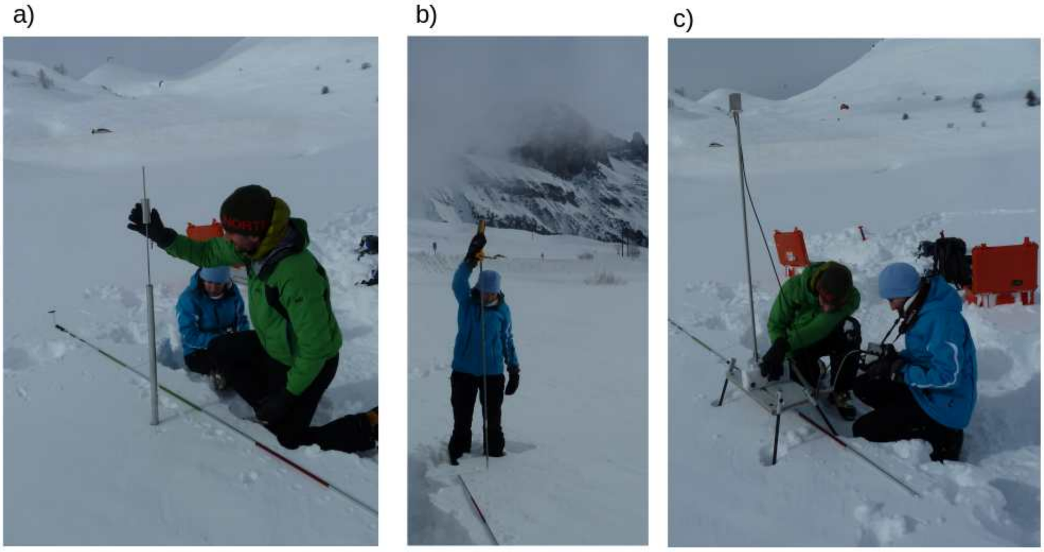

Figure 1.5: Photos of different penetration tests: a) the Ramsonde, b) the SP2 and c) the SnowMicroPenetrometer (SMP).

days to a couple of months [e.g. Schneebeli and Sokratov, 2004, Calonne et al., 2014]. The μCT cannot be conducted routinely in the field at low cost.

The SnowMicroPenetrometer (SMP) can bridge the gap between measurements of the snow microstructure and the ones conducted in the field. In general, the first ones can be only used in a cold room, wile the latter ones have less resolution and are often observer-dependent. Indeed, the SMP force measurements of such a high resolution contain data related to the snow microstructure. Another advantage of the SMP is, that it takes a couple of minutes to obtain a profile, while a complete measurement of the snowpack may take several hours. However, today, we still need to better understand the recorded force from the SMP and its link to the microstructure. In the following section a more detailed scientific approach of cone penetration tests in snow as well as existing measurements of the snow microstructure is presented.

1.2 State of the art: Snow measurements and their applications

Snow measurements are performed in the field and in the cold labs. They are helpful in measuring geometrical and mechanical properties, here we concentrate on two types of measurements used in this thesis, the cone penetration tests and the micro-computed tomography. Firstly, we present the penetration tests in general and their application to snow. Followed by a section of the measurements to visualize the snow microstructure. Finally, the link between the two methods is done by presenting the studies, that estimate the microstructure from penetration force profiles.

1.2.1 Penetration tests in snow

"Hardness is the resistance to penetration of an object into snow"[Fierz et al., 2009]. Measurements of snow hardness exist from a long time to characterize the snow. There exist different experiments to measure the hardness, like the previously explained hand-hardness measurements used by the snow observers for the avalanche prediction service. Another way to measure the hardness are the so-called push-pull gauges [Takeuchi et al., 1998], which can be explained as the digital version of the hand-hardness test. These measurements require an opened snowpack. Contrary to this, the cone penetration measurements have the advantage of measuring the profile of the snowpack without digging. Fukue [1977] showed a good correlation between the measured resistance of a penetrating blade and the unconfined compressive strength of snow.

Cone penetration tests (CPT) measure the force required to make a cone penetrate into the material of interest. In addition to the recorded forces a classical CPT in soils includes sleeve friction and pore pressure measurements [e.g. Schmertmann, 1978, Mayne, 2007]. To interpret CPT results, for example Robertson [1990] developed soil classification charts using the cone resistance and friction ratio based on empirical relations (Fig. 1.6). Other experimental studies, like Mulqueen et al. [1977] observed an increase in the limit force with increasing cohesion, which also depends on the soil and its moisture content. In addition to this experimental studies, theoretical approaches give new insights to the understanding of the recorded force. As an example, the cavity expansion model is widely applied for the interpretation of the penetration resistance. Bishop et al. [1945] developed this model to derive the material properties of clay and sand from CPT profiles. Nowadays, this model is implemented in many CPT inversion models used in studies related to soil mechanics. Two of its advantages are its easy implementation and the capability of describing elastic and plastic material deformation during CPT [e.g. Yu and Mitchell, 1998, Ruiz et al., 2016].

As mentioned earlier, the first known application of cone penetration tests to snow was done in the 1930's with the development of the Swiss ramsonde penetrometer [Bader et al., 1939]. Since then, the CPT has continuously evolved leading up to

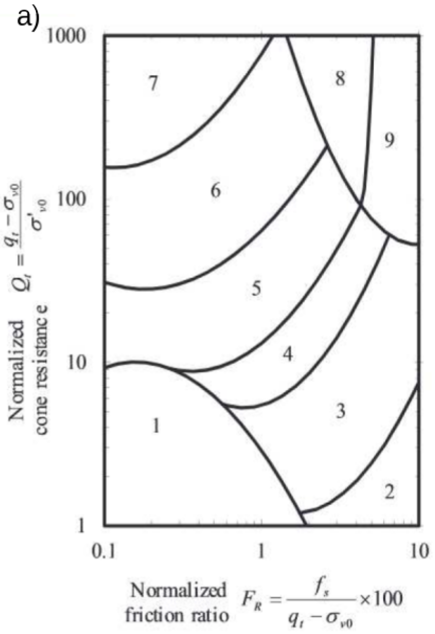

b)

Area	Soil description
1	Sensitive, fine-grained
2	Organic soils (peats)
3	Clays (clay to silty clay)
4	Silt mixtures (clayey silt to silty clay)
5	Sand mixtures (silty sand to sandy silt)
6	Sands (clean sand to silty sand)
7	Gravelly sand to sand
8	Very stiff sand to clayey sand
9	Very stiff, fine-grained

Figure 1.6: Soil classification chart for cone penetration measurements (a) and the corresponding soil classification table (b) from Wang et al. [2013] adapted from Robertson [1990].

digital CPT of today. Bradley [1966] developed the resistograph, which measured the penetration resistance with respect to the depth and records it on a paper. In later studies, [Bradley, 1968] showed a good agreement between the snow strength measured by the snow resistograph and compressive strength measured by loading to failure method. Later on, Dowd and Brown [1986], developed to the best of our knowledge, the first digital radiograph, which recorded the penetration force with a resolution of 5 mm. Brown and Birkeland [1990] further improved this radiograph, so that it was able to digitally store a large number of profiles recorded on the field, which could be quickly off-loaded onto a computer. Other penetrometers were developed, which do not measure the penetration force, like the portable capacitance snow sounding instrument [Louge et al., 1998]. This instrument records profiles of dielectric permittivity through a relatively dry snowpack. Schneebeli and Johnson [1998] developed the SnowMicroPenetrometer (SMP), which is largely used even today, and also used during this thesis. The conical tip, which measures the force, has a diameter of 5 mm and a half cone angle of 30°. It is mounted on a rod of 18 mm in diameter. The SMP measures the penetration force with a frequency of 5 kHz, and a velocity of 20 mm s^{-1} (i.e. a vertical resolution of 4 μm). Due to its high resolution, the signal is assumed to be dependent on micromechanical properties of the snow [Johnson and Schneebeli, 1999, e.g.]. Other digital penetrometer exists like the SABRE penetrometer [Mackenzie and Payten, 2002]. It is a manually operated penetrometer, which records the force with a frequency of 500 Hz. In contrast to the other penetrometer, it has a spherical tip of 12 mm diameter. It was developed for Himachal Helicopter Skiing to obtain a fast and accurate information of the snowpack for the ski runs.

Recently, the company MountainHub (before Avatech) developed manual-driven penetrometers. A first version was the SP1 and SP2 [Avatech, 2014] (Fig. 1.5b). The SP2 consists of a measuring conical tip of 5.44 mm in diameter, with a half cone angle of 30°. The penetrometer is pushed manually into the snow up to a depth of 142 cm leading to about one force measurement each millimeter. A combination of different infrared sensors, the tip force sensor and an accelerometer is used to compute the depth and hardness. Hagenmuller et al. [2018a] compared SP2 measurements to SMP profiles. They report that the SP2 displayed similar stratigraphic features to that of the SMP profiles, but were less repeatable. The SP2 showed large vertical variability, with a standard error of 7.5 cm. The Scope penetrometer is a further developed version of the SP2, which is imbedded into a ski pole (http://about.mountainhub.com/scope/). It can be directly connected to a smartphone via Bluetooth and the snow stratigraphy can be visualized directly. No scientific studies of the Scope have been reported yet in literature. Nevertheless, these type of penetrometers are promising as they bridge the gap between expensive penetrometers for research, such as the SMP, and a very simple instrument like the ramsonde.

For avalanche forecast it is crucial to estimate the snowpack stability [Schweizer et al., 2003, Gaume et al., 2014]. Cone penetration tests provide a rapid measurement of the snowpack, independent of the observers. Now, some studies shall be presented as to how CPT tests in snow were interpreted in terms of snow stability and snow type. Schweizer and Wiesinger [2001] mentioned that the ramsonde profile is useful to classify a snowpack into either being potentially stable or potentially unstable. However, Pielmeier and Schneebeli [2003] showed that thin weak layers are not recorded by the ramsonde, because of its low vertical resolution and its coarse hardness measurements. They summarize that the SMP captures stratigraphic features most effectively as compared to hand-hardness measurements and ramsonde profiles. Also Schneebeli et al. [1999] pointed out the high precision with which they measured the forces at interfaces between weak and hard snow layers. These results were confirmed by Kronholm et al. [2004], who analysed the spatial variability of the SMP resistance with respect to snow pit measurements, containing ramsonde, rutschblock test, and hand measurements. They concluded that it is possible to identify distinct layers based on the changes in penetration resistance. Birkeland et al. [2004] investigated buried surface-hoar layer with the SMP from observation of 2 measurement days which were 6 days apart. No statistically change in mean, minimum, median of the SMP force signal were noticed in these layers, but its maximum hardness, variance and coefficient of variation increased.

Further studies have tried to detect and classify the different snow layers and classes from the SMP force profiles. For example, Pielmeier and Schweizer [2007] derived a classification tree to detect a failure layer using texture index, mean structural dimension length and a computed grain dimension. They achieved a classification accuracy of 65%. Lutz et al. [2007] analysed the SMP force profiles with regard to depth hoar, by computing the coefficient of variation with a moving window statistical operations. They detected higher coefficient of variation values for depth hoar. Bellaire et al. [2009] developed a stability algorithm for SMP measurements to get an automatic detection of the layers, which is most prone to avalanches. They divided the SMP signal into stability classes (poor and fair-good) and then the microstructural parameters are analysed in a step-wise sequential manner. They obtained an accuracy of 60%. An effective and reliable, automatic identification of failure layers in a SMP profile was developed by Herwijnen et al. [2009]. Nevertheless, this methods necessity a manual picking of a reference layer from the SMP signal. Satyawali et al. [2009] developed a preliminary approach, an observer independent snow classification of the 5 major snow classes by calculating the mean penetration force over 1 mm and its coefficient of variation, which are then analysed by a flow chart. Further, Satyawali and Schneebeli [2010] used the semivariogram for the interpretation of the SMP profiles, and showed that it is possible to estimate spatial scales of different snow classes. Similar analysis were also performed with the SABRE penetrometer: e.g. Floyer and Jamieson [2008] and Floyer and Jamieson [2009] presented a method to identify weak layers in penetrometer signals. Recently, McCallum [2014] presented experiments of the application of the CPT for soils to snow in the Arctic. McCallum and Wiegand [2018] developed a simple model to estimate snow strength from CPT sleeve friction data. For a complete validation of this model, more data is required.

These results provide an overview of the existing research on the SMP, but is in by no means exhaustive. There is another method of interpreting these signals and these are by means of inversion models, which try to derive micromechanical properties from the snow. These will be presented in Sec. 1.2.3.

1.2.2 Link between cone penetration tests and snow microstructure

The previous two subsections (1.2.1 and 1.2.2) presented two different experimental methods used in this manuscript. The first one being, the cone penetration tests, which gives information of the microstructure of the snow, as it records the force with high resolution. The second one is the micro-tomography, which gives information of the microstructure of snow samples. The existing inversion models to link the CPT force profile to the snow microstructure are presented in this section.

Several statistical models exist to estimate micromechanical properties from the SMP profiles. They all assume the measured macroscopic force profile $F(z)$ to be a superposition of individual ruptures of the bonds between the snow grains. All these models interpret a SMP profile $F(z)$, i.e. the macroscopic penetration force F as a function of depth z, as the superposition of spatially uncorrelated but identical rupture events. Each event is assumed to correspond to the failure of one bond having an elastic-brittle behaviour. Indeed, Fukue [1977] showed by experiments of thin blade penetration that the brittle regime is obtained for penetration speeds above 0.6 mm s^{-1}.

Johnson and Schneebeli [1999] assumed for their model, that the recorded force is composed of friction between the penetrometer and ice, and of the elastic deflection and rupture of microstructural elements (Fig. 1.7a). These elements are supposed to have the same mean value, but can be randomly distributed in space. Further, they assume the material compaction to be negligible. Their inversion model estimates the following properties: deflection at rupture δ, bond rupture force f and microstructural element dimension L. The microstructural bond force is expressed as $f_z(z) = f/\delta \times \theta(z) \times \theta(\delta - z)$ with θ the Heaviside function. From these properties, they derived the macroscopic compaction strength (σ_{macro}) and elastic modulus (E_{macro}) as followed:

$$\sigma_{macro} = \frac{f}{L^2}\frac{\delta}{L} \quad , \quad E_{macro} = \frac{f}{\delta L}\frac{\delta}{L}$$

Marshall and Johnson [2009] extended this theory by using Monte-Carlo simulations to take into account simultaneous rupture events and inverted the signal (Fig. 1.7b,c). Löwe and Herwijnen [2012] adapted the model into the formalism of a homogeneous Poisson point process (HPP), such that individual ruptures can overlap and are randomly distributed in space and can be described by a Poisson distribution

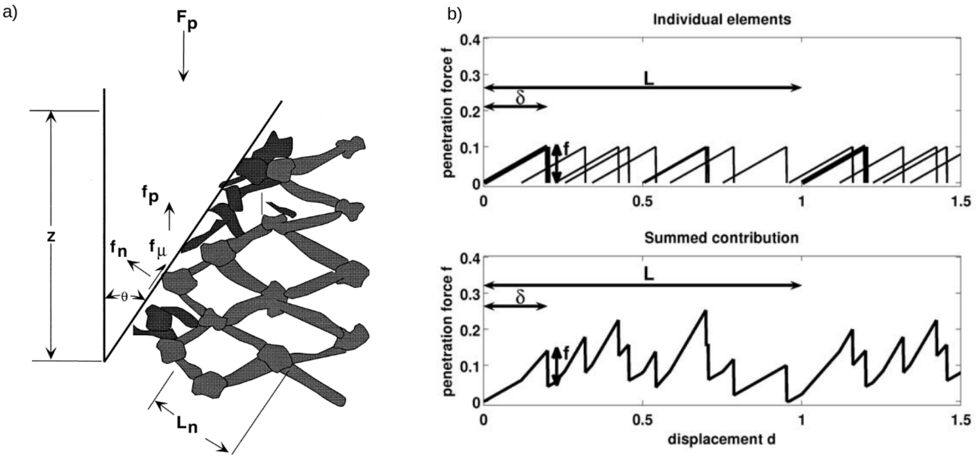

Figure 1.7: a) Schematic explication of the failure during the cone penetration [Johnson and Schneebeli, 1999], b) the individual elements of ruptures and (c) the resulting force [Marshall and Johnson, 2009].

with an intensity λ_z. The convolution of the single event function f_z and a random sampling of the number of events results in a simulated profile $F(z)$ (Fig. 1.7c). Further, Löwe and Herwijnen [2012] assumed the intensity λ_z to be constant over depth and equal to λ. Based on this, they derived analytical expressions directly linking the cumulants and correlation function of the SMP profile F to the micromechanical properties δ, f and λ. They obtained the following relations:

$$\kappa_n(z) = \frac{f^n \delta\lambda}{n+1} \quad \text{and} \quad C(z, z+r, |r| < \delta) = f^2\delta\lambda \left(\frac{1}{3} - \frac{1}{2}\frac{|r|}{\delta} + \frac{1}{6}\frac{|r|^3}{\delta^3} \right) \tag{1.1}$$

where κ_n is the cumulant of order n (e.g. κ_1 is the mean, κ_2 is the variance) and C is the two-point correlation function. The assumption of a constant intensity also implies stationarity of $F(z)$. Thus the stochastic cumulants and correlation function can be computed as "depth" cumulants and correlation function (ergodicity). Even for homogeneous snow layers, measured penetration force profiles are rarely stationary with depth [Herwijnen and Miller, 2013]. Hence, it is difficult to split a penetration profile into stationary sub-sections. Simulated HPP showed better results with larger analyzing windows [Löwe and Herwijnen, 2012]. Therefore, it is difficult to strike a balance between large windows that are stochastically representative, and small windows within which the profile can be considered stationary. In literature, typical window sizes of 1 to 5 mm are reported [e.g. Löwe and Herwijnen, 2012, Proksch et al., 2015, Ruiz et al., 2017].

The results of the micromechanical estimates from the HPP are used in further studies to find macroscopic properties of the snow. Proksch et al. [2015] used the median penetration force ($\tilde{F}$) and the microstructural element dimension, which is derived from the rupture intensity ($L = (A_c/\lambda)^{1/3}$, with A_c the cone surface of the penetrometer).

$$\rho_{SMP} = a_1 + a_2 \ln(\tilde{F}) + a3 \ln(\tilde{F})L + a_4 L$$

$$SSA_{SMP} = \frac{4(1 - \Phi_i)}{l_i}$$

with

$$\Phi_i = \rho_{SMP}/\rho_{ice} \text{ and } l_i = c_1 + c_2 L + c_3 \text{ln}(\tilde{F})$$

where $a_{1,2,3,4}$ and $c_{1,2,3}$ are coefficients obtained from regressions of their data. These equations and the one for the macroscopic elastic modulus [Johnson and Schneebeli, 1999] are often used for analyzing SMP profiles. Studies of slope instability and crack propagation are done with these estimations [e.g. Reuter et al., 2015, Schweizer et al., 2016, Reuter et al., 2019]. Recently, Kaur and Satyawali [2017] presented a new method for the estimation of the density from SMP profiles, by peak counting. Ruiz et al. [2017] compared the macroscopic elastic modulus and compaction strength obtained from the HPP to the ones obtained by a cavity expansion model (CEM). This model was introduced by Bishop et al. [1945] in order to retrieve the material properties of clay and sand from a CPT. The main assumptions of this model are: that the material of interest is a continuum material, in other words, that the ratio of cone size to grain size is sufficiently large, and further that the forces acting on the cone penetrometer are solely radial. Ruiz et al. [2017] report from their experiments, that they obtain different values for the different models. The elastic modulus derived from the micromechanical estimates of the HPP seems to be underestimate for larger densities.

Experimental studies showed, that a non-negligible deformation zone is formed around the cone tip while penetrating [LeBaron et al., 2014, Herwijnen and Miller, 2013]. These two studies examined the deformation around the SMP tip by PIV. Herwijnen [2013] also used micro-computed tomography images of the samples after the SMP test in order to analyse the compaction zone (CZ) from the computed radial ”density” field. The CEM is a model which takes into account the deformation around the cone, while this zone is limited to a layer of width delta for the HPP, thus only a very layer that is probably underestimated. Nevertheless, the assumption of a continuum material is limited, as the typical cone to snow grain ratio for the SMP ranges between 5 and 50 [Herwijnen and Miller, 2013]. As per Bolton et al.

[1993] the continuum media assumption reaches its limit for a ratio lower than 20.

In summary, cone penetration tests in snow like the SMP are largely studied and statistical approaches exist to estimate micromechanical properties of the snow. Nevertheless, these inversion models were not completely evaluated and they neglect the physical processes acting around the cone tip during penetration, like the formation of the compaction zone. For a correct interpretation of the signal it is crucial to know what happens around the tip. The μCT is a promising tool to obtain information of the snow microstructure. There exists approaches to obtain microstructural properties of the snow from tomographical images [e.g. Hagenmuller, 2014]. Besides, in soil mechanics, a combination of X-ray tomography and digital image correlation is used to study the deformation field during cone penetration tests [e.g. Paniagua et al., 2013, Silva et al., 2015].

1.2.3 Imaging of snow microstructure

The simplest method of observing the different snow grains is by using magnifying glasses. Small magnifying lenses can be taken on to the field to identify the size and shape of the grains and classify them based on Fierz et al. [2009]. These measurements are observer dependent. Two observers will probably record a different grain size, and the type for a same snow layer. For example, for a layer containing rounded grains and faceted crystals one observer may identify the rounded grains as major snow grain while the other detects the faceted crystals as predominant snow grains. Higher resolution microscopes in cold labs, with the ability to take photos provide more objective preliminary view. Lesaffre et al. [1998] developed an automated objective analysis of such snow grain digital images. Here, only individual grains are observed and hence the information concerning the bonds between the grains is missing. The bond structure plays a major role in determining the mechanical behaviour of the snow. Another method is the preparation of thin snow slices which are then observed by microscopy. A block of snow is immersed within a chemical liquid, which has a lower melting point than snow. The snow and the liquid are further cooled to obtain a solid block, which is cut into thin slices. Using polarized light the crystallographic structure of the snow grains can be made visible [e.g. Arnaud et al., 1998]. To reconstruct the three-dimensional structure of the snow, e.g. Kry [1975] used a sereological method supposing the bonds to be circular in shape. An other method is to combine the two-dimensional slices to a 3D reconstruction of the snow [e.g. Good, 1987]. This method is very time consuming. The scanning electron microscopy enables the observers to obtain information pertaining to the surface of the snow grains [e.g. Wergin et al., 1996]. Chen and Baker [2010] revealed that this method suffers from a low resolution (about 1 μm) and this low magnification limits the depth of field to which measurements can be made. Applications of this method are for example to study the bond growth during sintering [e.g. Blackford, 2007, Chen and Baker, 2010].

A first application of X-ray micro-computed tomography (μCT) to snow samples was done by Brzoska et al. [1999]. This method enables one to determine the three-dimensional microstructure of a snow sample at a resolution of some micrometers. For example, snow samples of about 1 cm^3 are used for such studies. This method is non-destructive and can thus follow snow metamorphism in-situ [e.g. Schneebeli and Sokratov, 2004, Calonne et al., 2015]. Wang and Baker [2013] used μCT and scanning electron microscopy images to observe the microstructural changes of snow under uni-axial compression. A further application of μCT is to scan the snow collected in field. Methods of impregnation exists, since the transportation of the snow sample can change or even destroy the fragile snow structure [e.g. Coleou et al., 2001, Heggli et al., 2009]. These methods are nevertheless destructive, since it is impossible to remove the impregnation material without residuals [Coleou et al., 2001] or for other methods the ice that is removed [Heggli et al., 2009]. In addition to the μCT, diffraction contrast tomography (DCT) exists to get geometrical and crystallographic structure of the snow [e.g. Roscoat et al., 2011].

1.3 Scope and structure of the thesis

1.3.1 Goals of the thesis

Cone penetration tests (CPT) are widely used for soil testing to determine their properties. They are also widely used for snow measurements to get an insight into the stratigraphy. CPT are fast measurements of several minutes and give observer independent information about the snow resistance. A deeper knowledge of the link between the recorded force and the snow microstructure would help to better interpret the force profiles conducted with the CPT and ideally evaluate the risk of an avalanche directly from a penetration test. This would help the avalanche forecasters to predict more precisely the probability of occurrence of avalanches in the bulletin for avalanche danger. One digital penetrometer widely used for snow measurements is the SnowMicroPenetrometer. Due to its high resolution, it is a promising instrument in terms of measuring the microstructure (one force measurement each four micrometers). Previous studies pointed out the need of a better understanding of the measured force signal. For instance, existing inversion models interpret the physics of the microstructure of the snow without taking into account the processes happening directly at the tip, like the build-up of a compaction zone. Besides, there is a lack of experimental studies, which evaluate the models in terms of correctness of the estimates of micromechanical properties. The aim of this thesis is to better understand the processes happening directly around the penetrating tip at a microscopic scale. Thus we have focused the work along the following questions:

Can we improve the existing inversion models in order to take into account a compaction zone? Experimental studies of cone penetration tests in snow showed that a compaction zone is forming in front of and next to the cone tip during the penetration process. This deformation is not taken into account in the current inversion models. These models estimate the following micromechanical properties: rupture force, deflection at rupture and the rupture occurrence rate. In order to better interpret these properties it would be appropriate to take into account the compaction zone.

Is the SMP able to follow the time evolution of the snow microstructure? Since the development of the SMP, it has been largely studied. Some studies focused on identifying weak layers (i.e. avalanche prone stratigraphies) or even classifying the signal into the different major snow types. This kind of studies was based on signal analysis. Further, statistical analyses were done to estimate micromechanical properties of the snow grains and their bonds. Therefore the signal was supposed to be a superposition of elastic-brittle ruptures of the snow grains. To our knowledge, there is only one study which tried to follow snow metamorphism with the SMP [Herwijnen and Miller, 2013]. There the sintering was studied by the evolution of the macroscopic force. Thus it would be interesting to know whether the micromechanical estimations are able to follow the evolution of snow microstructure for the sintering process, but also for snow metamorphism under controlled conditions.

What happens exactly around the tip during the penetration process? For a correct interpretation of the signal it is crucial to know exactly what happens around the cone tip while penetrating. Until now studies investigated the compaction zone with PIV or density change. This gives already a good information about the size and shape of the compaction zone. Also they give an idea of the displacement of the grains happening around the tip. Nevertheless, an exact information about what happens on a microscopic scale is missing. It would be interesting to see which bonds break up, for example, which could help for the interpretation of the recorded force. Indeed, several existing inversion models assume the recorded force to be the sum of uncorrelated individual ruptures of the bonds.

How is the deformation of the snow next to the cone tip linked to the measured force profile? This question is linked to the previous question. If we know what happens exactly around the tip, it will be possible to link this to the force profile. For the micromechanical analysis of the force signal it is crucial to know what happens exactly around the tip. The signal is supposed to be the sum of the individual bonds breaking during the penetration process. But is this really what we were measuring, or are other physical processes as for example friction add a non-negligible part to the recorded force ? This friction can be a friction between the cone and the snow as well as internal friction between the grains in the compaction zone.

1.3.2 Structure of the thesis

Chapter 2: This chapter describes some preliminary experiments to identify the challenges for the main experiments in this thesis. The experimental part of the thesis consists of two different sets of cone penetration test (CPT) studies: We conducted (1.) CPT measurements in snow during the first day of sintering and (2.) combined measurements of CPT and micro computed tomography (μCT). For these experiments we needed to modify the original set-up of the SMP, as its large rod (about 2 cm) would influence the measured snow. We thus extended the conical tip, which stays directly connected to the force sensor. Since our CPT configuration slightly differs from the original SMP configuration, we evaluated the possible influence of this difference on the measured penetration force. This sensitivity analysis presented here is important to extend the results obtained in this thesis to common field measurements with the SMP.

Chapter 3: Here we investigate snow sintering at microscopic and macroscopic scales with high-resolution cone penetration tests. To this end, we measured vertical profiles of the penetration force during 24h using the SnowMicroPenetrometer. The upper part of the profiles is transient due to the progressive formation of a compaction zone in front of the cone tip. To take this into account, we developed a non-homogeneous Poisson shot noise model which considers a depth dependency of the rupture occurrence rate. On statistically modeled signals we compared the non-homogeneous Poisson process with the existing homogeneous Poisson model. Applying the inversion model to our sintering data, the method shows that the vertical heterogeneity of the penetration force was essentially due to variations of the rupture rate, whereas the time evolution of the macroscopic force could be

explained mainly by a microstructural bond strengthening. The non-homogeneous Poisson point process is also used for the analysis of cone penetration tests in Chapter 4 and Chapter 6.
This work is published in Cold Region Science and Technologies as [Peinke et al., 2019]

Chapter 4: The inversion model developed in Chapter 3 is applied to further SMP measurements in field and under controlled conditions. To this end, we used the original set-up of the SMP. The first section (4.1) presents the application of the homogeneous and non-homogeneous Poisson point process to field measurements. The novelty here is that we had vertical and horizontal measurements of the snowpack. The horizontal measurements enabled us to have long quasi-stationary signals, which could be used as reference measurements for the corresponding layers. The experiments of 4.1 were done in the frame of a master thesis. The study of the second section (4.2) is the application of the inversion model to snow metamorphism. Therefore, SMP measurements during about three weeks on two snow samples were conducted. One of the sample was subjected to a temperature gradient, while the other one was kept under isothermal conditions. In the last section, the model is applied to some experiments of the sensitivity study (Chapter 2).

Chapter 5: The analysis of the combined micro-computed tomography (μCT) images and cone penetration tests are presented. The experiments consist of two high-resolution three-dimensional μCT images, one before and one after the force penetration measurement. In order to reconstruct the displacement field, we developed a morphology based tracking method. The challenge was to reconstruct large displacements, as only two μCT images exist. This method combines digital image correlation and individual grain tracking. The obtained displacement field was then compared to the cavity expansion model, which is largely used for CPT analysis in soils.
This work is submitted to Frontiers Science.

Chapter 6: This chapter combines the analysis obtained from Chapters 3 and 5. We apply the non-homogeneous Poisson process developed in Chapter 3 to the force profiles measured in the samples. These samples were images produced by the μCT. The displacement field analysis of Chapter 5 enables us to get information of the broken bonds between the grains. We are able to estimate the number of broken bonds and a mean size. In addition, we apply an existing approach to compute the minimum cut density on our images.

Chapter 7: The last chapter sums up the main results of this thesis and points out perspectives for further studies.

2

Sensitivity analysis of measurement conditions for cone penetration tests in snow

Contents

2.1 Introduction

In this thesis, we performed cone penetration tests (CPT) in snow using different testing configurations depending on specific experimental constraints:

- multiple CPT in thin snow samples (height of 5 cm, width of 30 cm) to investigate snow sintering in the first day after sieving,
- single CPT in small snow samples (height and diameter of 2 cm) whose microstructure can be clearly observed in images obtained using X-Ray tomography.

For these experiments, the SnowMicroPenetrometer (SMP) was used, but not in its original set-up. We extended the conical tip, which is directly connected to the force sensor. This modification prevents the rod of the SMP to penetrate the snow samples and destroy it completely. The snow samples were prepared by sieving natural snow in different sample holders and letting them sinter for a certain time. In the study about sintering (Chapter 3), we performed several CPT close to each other. In the study using X-ray tomography (Chapters 5 and 6), the sample holder diameter (2 cm) was close to the size of the cone tip (5 mm). Since, our CPT configuration slightly differs from the SMP configuration widely used in the snow community, we evaluated how this difference affects the measured penetration force. This sensitivity analysis presented here is important to extend the results obtained in this thesis to common field measurements with the SMP. In this section, we first describe in details the sample preparation and the different experimental set-ups. We then estimated the spatial and temporal heterogeneity of the samples prepared by sieving natural snow and the sensitivity of CPT to the cone tip set-up, the size of the sample holder or the vicinity between measurements.

2.2 Experimental procedure and penetration signal analysis

2.2.1 Sample preparation

The experiments were conducted in a cold room at -10±0.5°C. Most of the samples used for this sensitivity analysis were composed of large rounded grains (RGlr), with relatively high densities of about 500 kg m^{-3}. To obtain samples with various grain sizes, the snow was sieved with sieves of different sizes (0.8-1.6 mm, see Fig. 2.1). For one experiment, we used as well decomposing and fragmented precipitation particles (DF). A summary of the snow sample properties used in this study is presented in Tab. 2.1. The density was determined by extracting sub-samples of 50 cm^3 (or 250 cm^3 for DF) with a cutter and weighing them. The specific surface area (SSA) was measured using an optical method [DUFISSS Gallet et al., 2009]. Unfortunately, we do not have measurements of SSA for the samples snow16 and snowDF. Small differences between the samples snow8, snow10 and snow16 and the samples SSA18, SSA14 and SSA10 can be observed. It is the same snow, which experienced heating due to a breakdown of the cold room. The temperature of the snow was close to zero, which led to a slight increase in SSA.

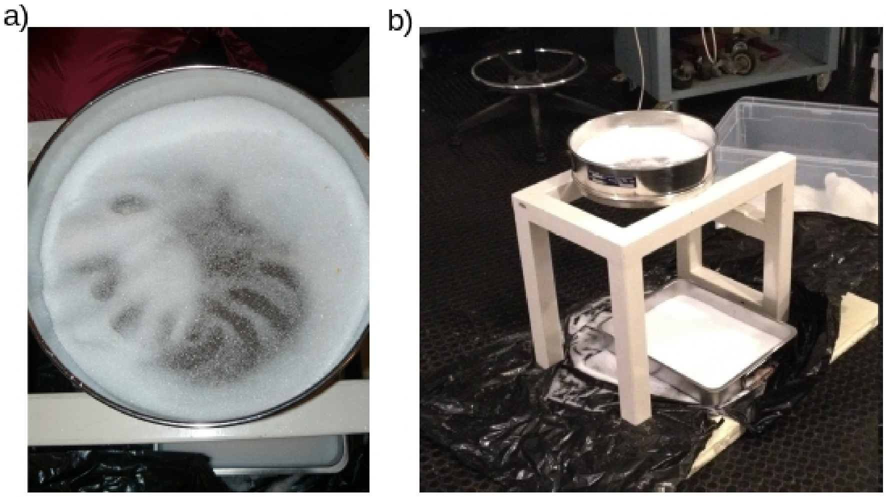

Figure 2.1: Photo of the sieving procedure. Scale: the sieve diameter is 32 cm.

Table 2.1: Mean physical properties of the snow samples used in this study. The snow type is determined according to [Fierz et al., 2009].

sample name	snow type	sieve size mm	density kg m^{-3}	SSA m^2 kg^{-1}
snow8	RGlr	0.8	500 ± 20	16.0±1.6
snow10	RGlr	1	500 ± 20	13.1±0.7
snow16	RGlr	1.6	500 ± 20	-
SSA18	RGlr	0.8	500±2	17.9±0.3
SSA14	RGlr	1.0	496±2	14.0±0.3
SSA10	RGlr	1.6	484±3	10.4±0.1
snowDF	DF	1.6	199±4	-

In general, a height of 30 to 70 mm of snow was sieved into rectangular boxes with a size of 300 x 400 mm. The sieve was installed about 45 cm above the containers

(Fig. 2.1). The sieve diameter was smaller than the sample boxes. It was thus difficult to obtain a perfectly smooth surface: differences up to about 1 cm were observed for the snow height within the sample box. Once the sieving was finished, the boxes were covered and insulated to avoid sublimation and temperature gradients in the sample.

2.2.2 Cone penetration test

The measurements were conducted with the SMP (version 4), which was mounted above the samples (Fig. 2.2). The samples were placed on a movable table, which allowed the displacement of the sample with a precision of <1 mm. The samples are allowed to rest for one to four days, up to thirty-five measurements were conducted for each box with a typical spacing of 4 cm. At least three measurements were taken for each analysis. They were spread over the box in order to take into account the heterogeneity of the sample due to different locations.

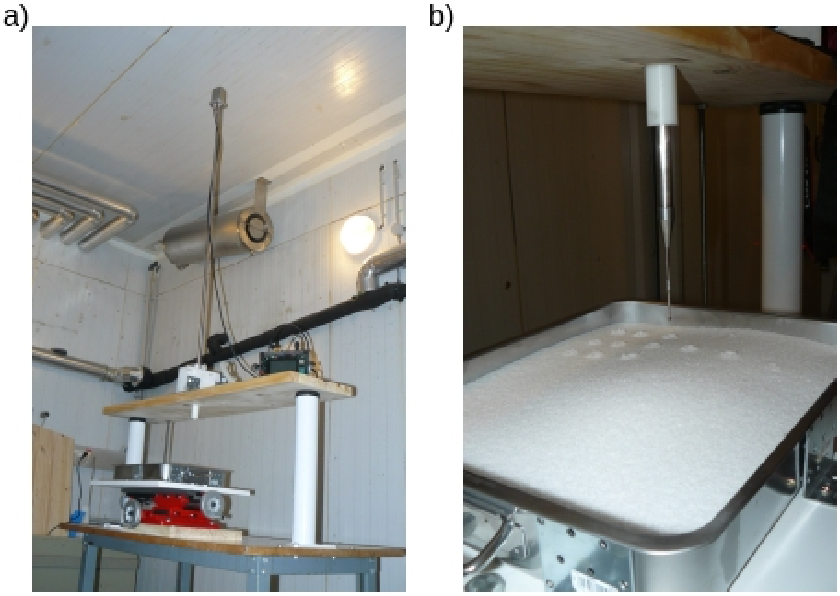

Figure 2.2: CPT test bench: movable table below a fixed SMP

The length of the tip of the SMP was modified from 40 to 70 mm(Figs. 2.3a, b). The motivation for lengthening the apex was to prevent the rod of the SMP from penetrating the snow. The rod penetration could influence the force measurement through the formation of a rod-induced compaction zone (CZ). For the study using X-ray tomography another tip was designed in order to avoid snow grains to fall in the cavity formed by the apex (Fig.2.3c). Hereafter, we will call *original SMP* the CPT with the original SMP version, μCPT the one with the lengthened SMP tip, and *tomoCPT* the one with the plain modified tip. In addition to these three set-ups, we conducted μCPT experiments with different tip diameters of 4, 5 and 8 mm. The half cone angle of the original tip (5 mm) is of 30° and for the two other tips (4 and 8 mm) is 40°.

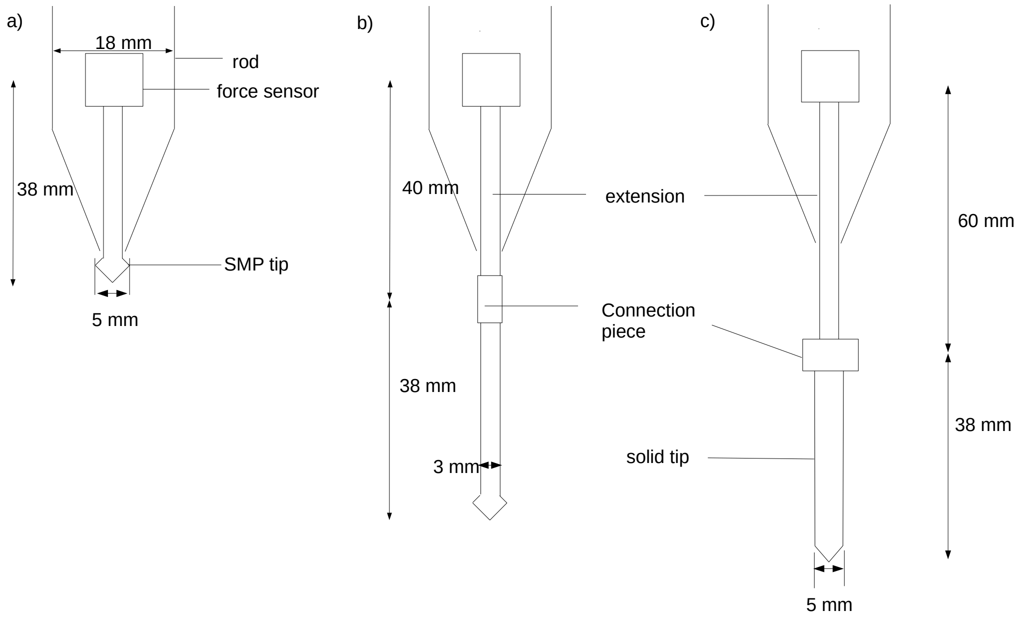

Figure 2.3: Different tip set-ups: a) the original SMP, b) the lengthened tip (μCPT and c) the plain tip used for tomography experiments (tomoCPT).

The tomographic imaging of the snow samples were conducted using a cold cell, CellDyM previously developed by Calonne et al. [2015](Fig. 2.4). To fit into this cell, the sample holder must be a cylinder with a diameter and height of 1 or 2 cm. To test the influence of the reduced size of these cylinders, we conducted CPT not directly in these sample holders, but in copper tubes, which were inserted in larger snow samples. This method had the advantage that μCPT can be performed inside and next to the tube in the same snow sample. In practice, the copper tubes were inserted into the snow directly after sieving in the snow samples (see Sec. 2.2.1). In order to assure a vertical insertion of the tubes, a small table was fixed on the box to guide the cylinder insertion (Fig. 2.5). Before the μCPT measurements, the tip was centered (Fig. 2.5, right). The minimal distance of the μCPT to the box wall was 3 cm.

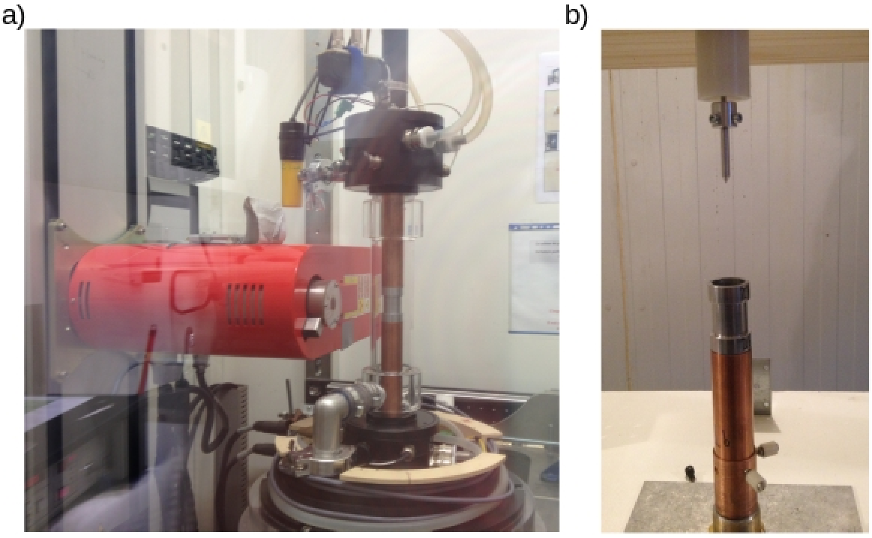

Figure 2.4: (a) Photo of the cold cell CellDyM in action in a tomograph and (b) the measurement in the sample holder designed for the cold cell.

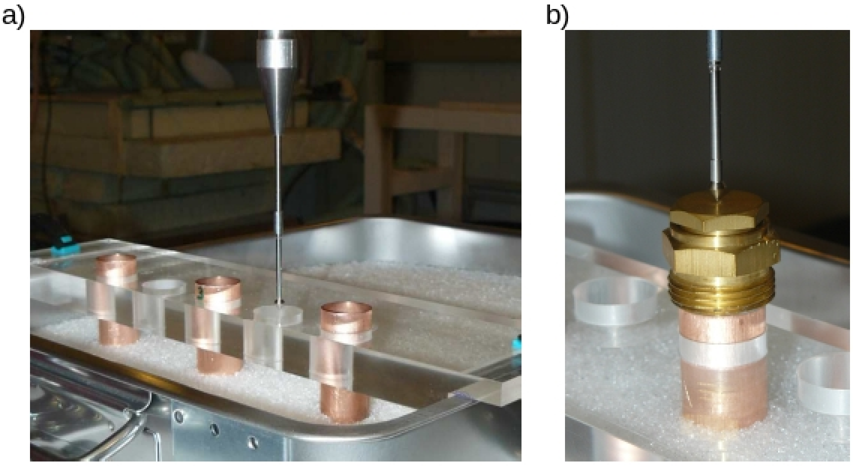

Figure 2.5: Photo of the copper tubes and centering of the μCPT tip, used to test the sensitivity of the CPT to sample holder size.

2.2.3 Force profile analysis

To evaluate the impact of different experimental conditions on the CPT, we qualitatively compared the measured force profiles and, derived and compared some key characteristics of the force signal fluctuations.

For each sensitivity test, the force profiles (sampled at one point per 4 microns penetration increase) were smoothed with a Gaussian filter with a standard deviation of 0.2 mm (50 points). Further, the average of the different force profiles measured under the same conditions but at different positions in one sample was computed. The Bold line shows this average and the shaded area displays the standard deviation of the smoothed signals (e.g. in Fig. 2.6). These plots enable visual comparison between the SMP profiles measure under different conditions.

In addition to this qualitative comparison, we compare the profiles quantitatively by computing the mean, standard deviation and correlation length of the raw force profiles. Indeed, these three quantities are the main parameters used to statistically derive proxies of the snow microstructure (see Sect. 3.2.3, [e.g. Löwe and Herwijnen, 2012]). The correlation length was computed as: $C(0)/C'(0)$, with the two point correlation function C after Löwe and Herwijnen [2012]. The standard deviation and correlation length were computed over windows of 3 mm in order to take into account the small fluctuations of the signal and not the overall fluctuations of the smoothed signal. These quantities were averaged on the profile depth, up to the depth of the shortest signal or up to 35 mm depth. The presentation of these statistics will be shown in boxplots if more than 4 profiles are available, otherwise scatterplots will be shown.

2.3 Sensitivity to sample preparation

2.3.1 Spatial variability in one sample

Creating truly homogeneous snow samples is known to be difficult [Herwijnen and Miller, 2013]. In order to quantify the heterogeneity of the samples, we compare μCPT measurements of two different samples (snow8 and snow10) which have been allowed to rest for two days after sieving (Fig 2.6a). We observe for both samples differences in penetration force of about 15 to 20% in average between the measurements at different locations in the sample box (Fig 2.6b). The relative differences are larger at the sample surface (Fig 2.6b).

Despite these differences in the profiles of one sample, the signals of the two snow samples, prepared with two different sieve sizes, are distinguishable. The smaller grains (snow8) show a higher mean force, a correlation length and a slightly higher standard deviation than the larger grains (snow10, Fig 2.6c).

In addition, to the heterogeneity of the measurements in one sample, the profiles themselves show a force increase with depth. Excluding the first 4 mm, as the tip is not fully submerged, the force continues to increase with depth. In order to exclude snow type changes with depth, optical SSA measurements were taken

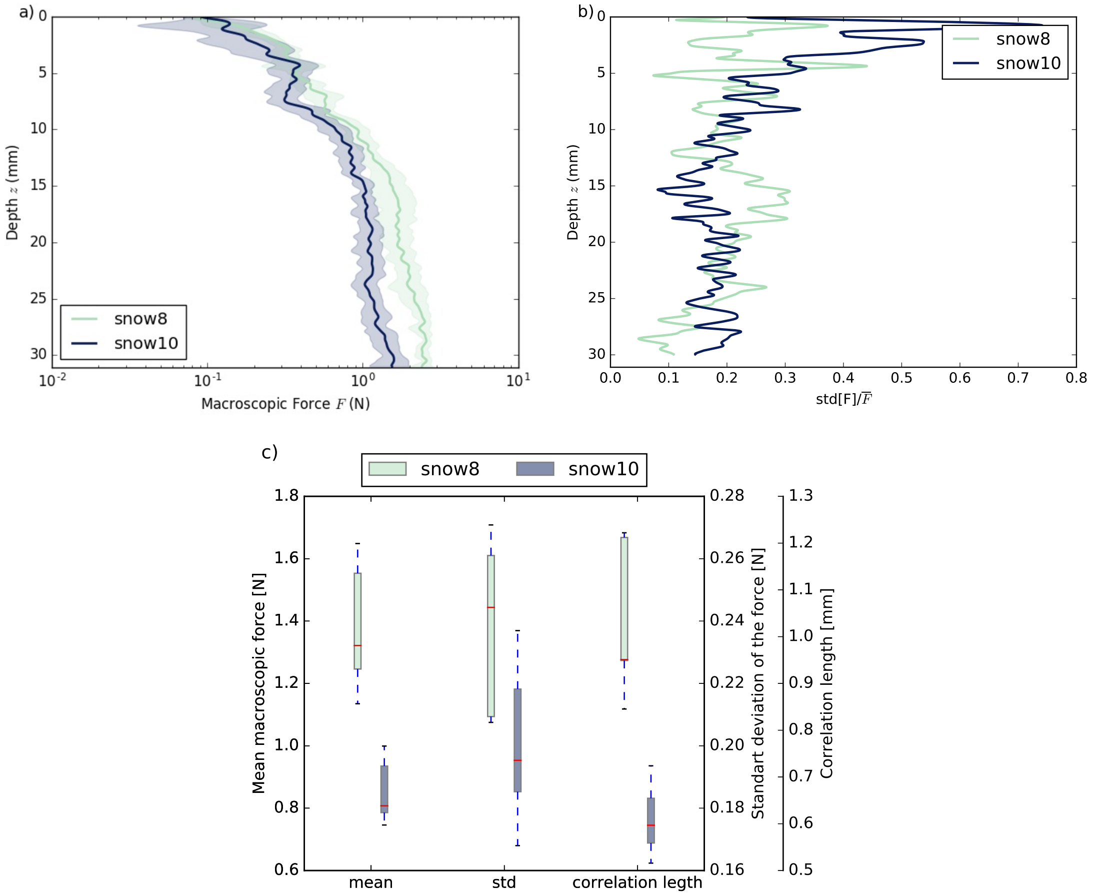

Figure 2.6: Analysis of spatial variability in two different snow samples (snow8 and snow10): a) smoothed force profiles, b) relative forces differences in one sample, c) comparison of the "statistical" descriptors of the force profiles. The measurements were taken 2 days after sieving.

at different heights [DUFISSS Gallet et al., 2009]. They showed a horizontal and vertical variability in the same order of magnitude. Typically, the standard deviations were less than 1 m^2kg^{-1}.

In summary, the relative variation of penetration force or key descriptors of the penetration profile with the CPT location in the sample generally does not exceed 20%, despite for some exceptions it reaches up to 40%. The variation of force with depth is more pronounced probably due to the build-up of the sample by successively sieving the thin snow layers and the progressive formation of a compaction zone in front of the tip. A relative difference of key signal descriptors larger than 20% can thus be attributed to a systematic difference between CPT configurations and not simply spatial variability in the prepared samples.

2.3.2 Sintering after sieving

The tomographical experiments, consisting in two μCT images and a CPT will take almost the whole day. During this time period the changes in the force signal should be negligible, thus we want to find the ideal time to wait before starting. To this end, the penetration force of a snow sample was measured directly after sieving and then one, two and three days later. An obvious increase in penetration force is observed between the measurements directly after sieving and one day later (Fig. 2.7a). For the next days only a slight increase is observed, which is less pronounced than fluctuations of the samples of one day. This can be clearly observed on the mean force over the depth (Fig. 2.7b). Additionally, the standard deviation and correlation length significantly evolve up to one day after sieving and remains stable afterwards.

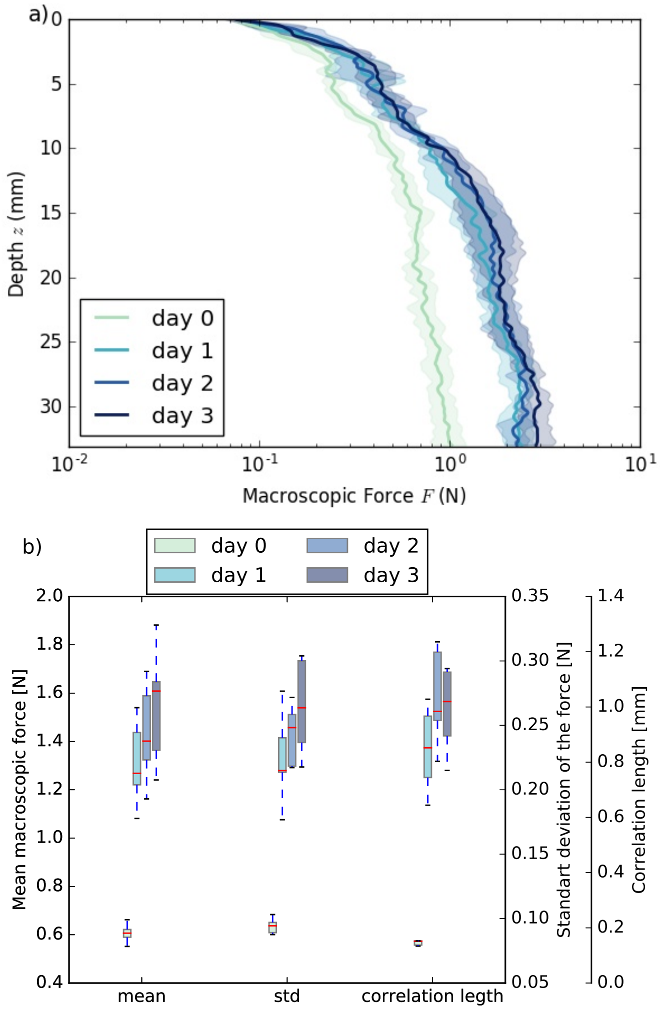

Figure 2.7: μCPT Measurements of different rest times in the snow sample snow8: a) the mean force profiles and b) the statistical computations over the height.

In summary, it appears sufficient to let the sample sinter (rest) one day after sieving to neglect any further evolution of the sample during experiments with a typical duration of one day.

2.4 Sensitivity to cone tip characteristics

The influence of the tip characteristics were evaluated on two aspects. First, the tip was modified to prevent the rod to touch the snow or to avoid any grain to fall into the cavity created by the tip penetration. The impact of these different tip geometries are estimated here. Second, the influence of the tip diameter was evaluated.

2.4.1 Tip geometry

The measurements to identify the influence of the three different cone tips (SMP, μCPT and tomoCPT, Fig. 2.3) on the force signal were conducted in snow of type RGlr and DF. In addition to the analysis of the whole profiles, only the first 4 mm of indentation were investigated. For these depths, the part of the tip in contact with the snow shows no difference in the geometry, because it corresponds approximately to height of the conical part of the tip. The standard deviation and correlation length were directly computed on the first 4 mm, instead of the usual window of 3 mm. This analysis on a limited depth enables us to see whether the tip geometry (including size and weight) influences the force sensor response (in this case the indentation of the snow sample is exactly the same for all tips).

The profiles of the different set-ups show no obvious differences for the sample of DF (Fig. 2.8a,b). Note that the sample had a height of 9 cm, thus an influence of the sample bottom is unlikely. The mean force of tomoCPT shows slightly smaller forces for shallow depths (Fig. 2.8b,d). The statistical analysis (Fig. 2.8c,d) shows very similar results for all set-ups. A slight increase in correlation length from SMP, over μCPT to tomoCPT is observed for the analysis over the whole depth. This evolution is not obvious for the first 4 mm.

For the RGlr snow, we do not have measurements of the three different set-ups on the same sample, thus we will first compare the SMP to the μCPT and then the μCPT to the tomoCPT. Higher penetration forces are observed for the SMP compared to the μCPT in the sample of RGlr (Fig. 2.9a). For shallow depths, no obvious difference between these two tips are visible (Fig. 2.9b). For the SMP measurement, the force is maximum at around 30 mm depth. Afterwards, the force decreases, which could be the result of the sample bottom being at 60 mm depth. The computation of the mean over the first 35 mm and 4 mm is in agreement with

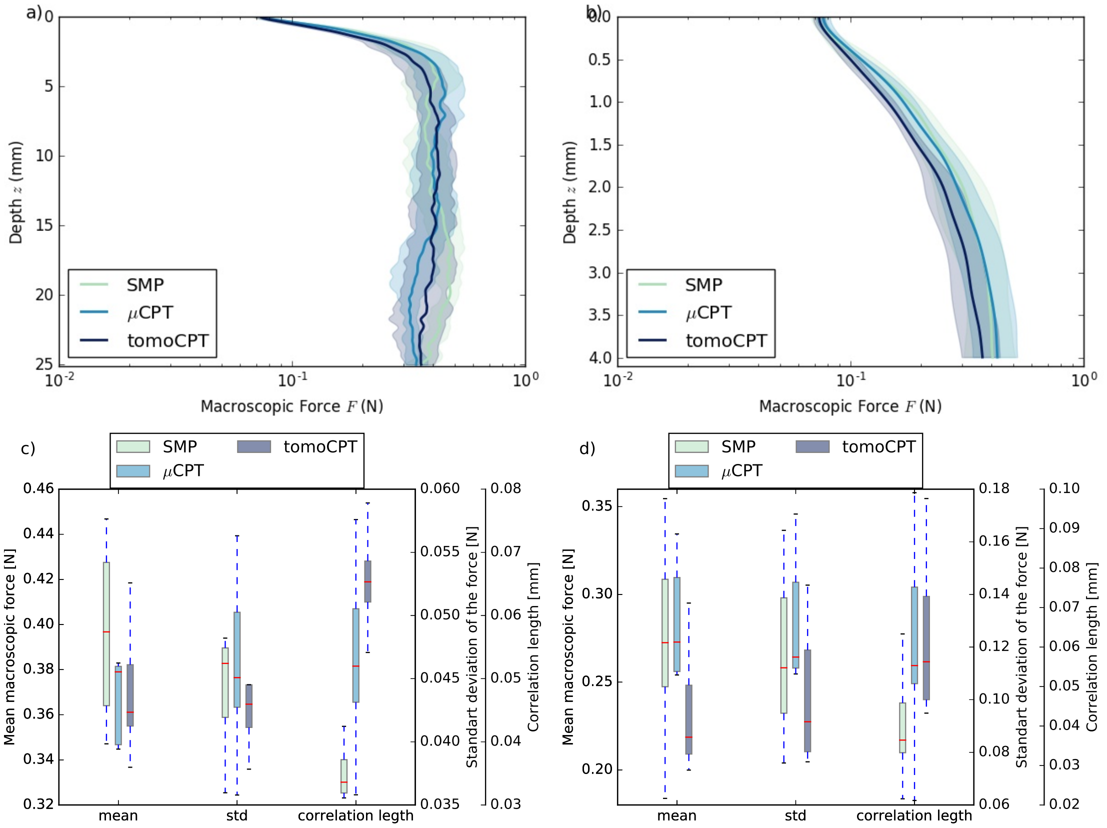

Figure 2.8: Penetration force measurements of different set-ups (SMP, μCPT and tomoCPT) conducted in the sample snowDF after one day of rest. a) and b) show the profiles, c) and d) show the computed mean force, standard deviation and correlation length. These quantities are shown on the complete profile of 24 mm (a,c) and for the first 4 mm (b,d).

the observations of the profiles (Fig. 2.9c,d). The standard deviation and correlation length of the force profiles do not show any obvious difference between the two methods. Additionally, a comparison of different extension lengths shows almost no differences in the mean force, standard deviation and correlation length (Fig. 2.9e).

The tomoCPT shows for the sample of RGlr higher mean penetration forces than the μCPT for the first 12 mm of penetration (Fig. 2.10a). This difference is almost non-existent in the first 4 mm (Fig. 2.10b). In addition, the standard deviation is higher for the tomoCPT and the correlation length is about the same for the whole profile. The differences are again less pronounced for the first 4 mm.

In summary, the modifications of the original SMP did not lead to a change in the signal acquisition (e.g. force sensor response), as the recorded signal were similar for the depths, where the geometry of the set-ups was the same (i.e. the first 4 mm). Nevertheless, the different geometry of the set-up plays a role in the force measurement and has to be taken into account for further studies.

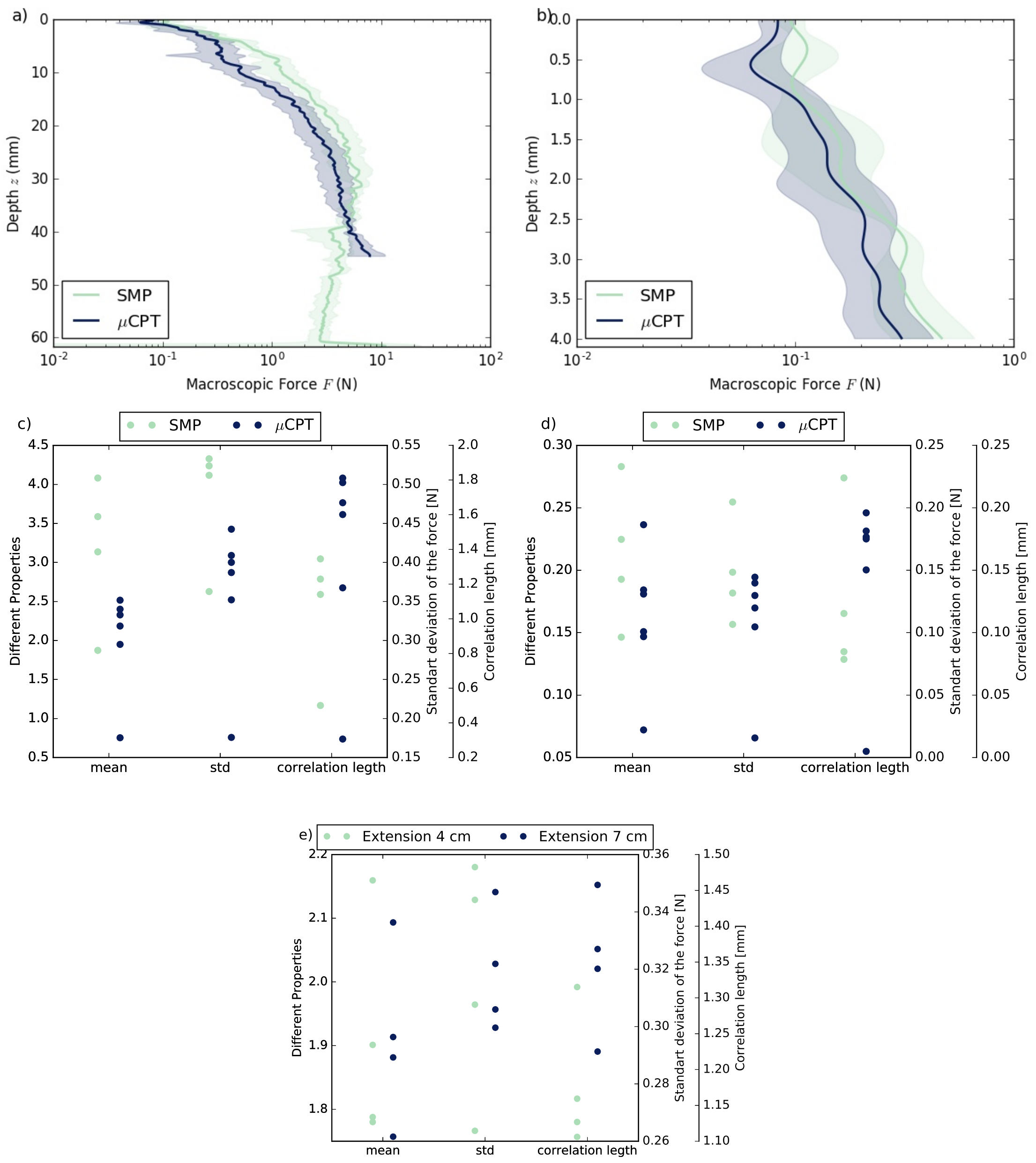

Figure 2.9: Profiles and statistics for SMP and μCPT measurements (a-d) for 35 mm (a,c) and 4 mm (b,d). And statistics for different extensions lengths e). The first experiments (a-d) were conducted in the sample snow 10 after 2 days of rest and the measurements with different extension were done 3 days after the sample preparation of snow8.

2.4.2 Sensitivity to tip diameter

μCPT tests with three different tip sizes (4, 5 and 8 mm in diameter) were conducted at a temperature -20°C. The recorded penetration force is increasing with the tip size (Fig. 2.11a). Nevertheless, the tips of 4 and 5 mm display only small differences in the measured force. The resistance (force divided by the maximum cross section

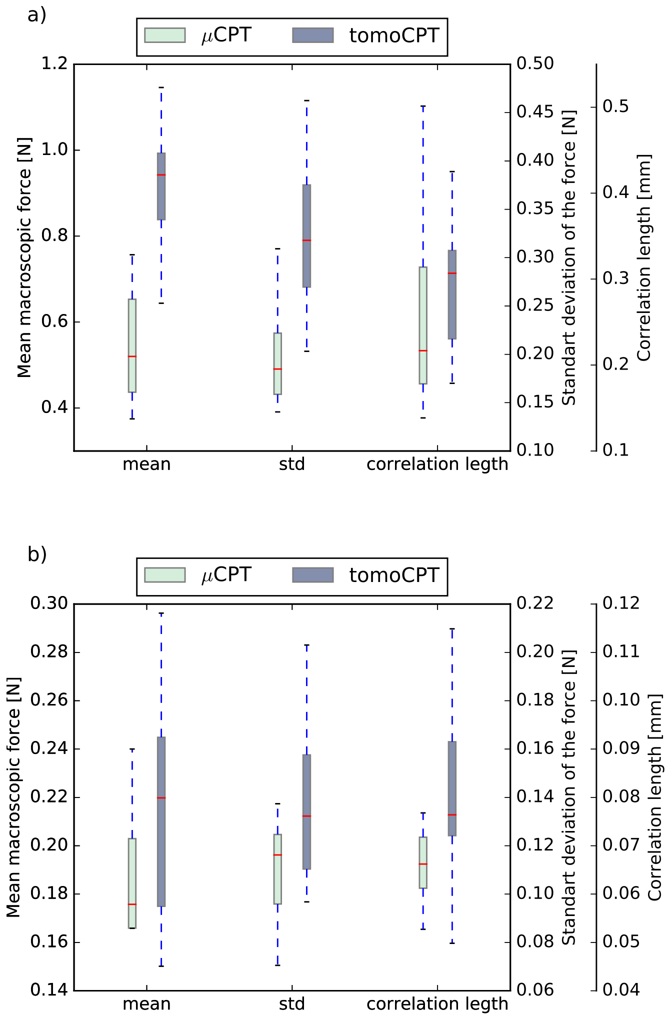

Figure 2.10: Statistical analysis of force measurement of μCPT and tomoCPT for the first 12 mm (a) and 4 mm (b). The measurements were conducted one day after the sample preparation of SSA14.

area of the tip) show a size effect for deeper depths (>10 mm), with higher resistance for a smaller tip size (Fig. 2.11b). Besides, the profile measured with the largest tip shows also the highest standard deviation and correlation length (Fig. 2.11c). Also here, no clear difference between the small and original tip size can be observed, except that the spread of the original tip is smaller.

In summary, we observe an influence of the tip size on the signal. This is not relevant for further studies of this thesis. Nevertheless, it can be an interesting information for other cone penetration tests like the SP2 or Scope, which have other tip diameters than the SMP.

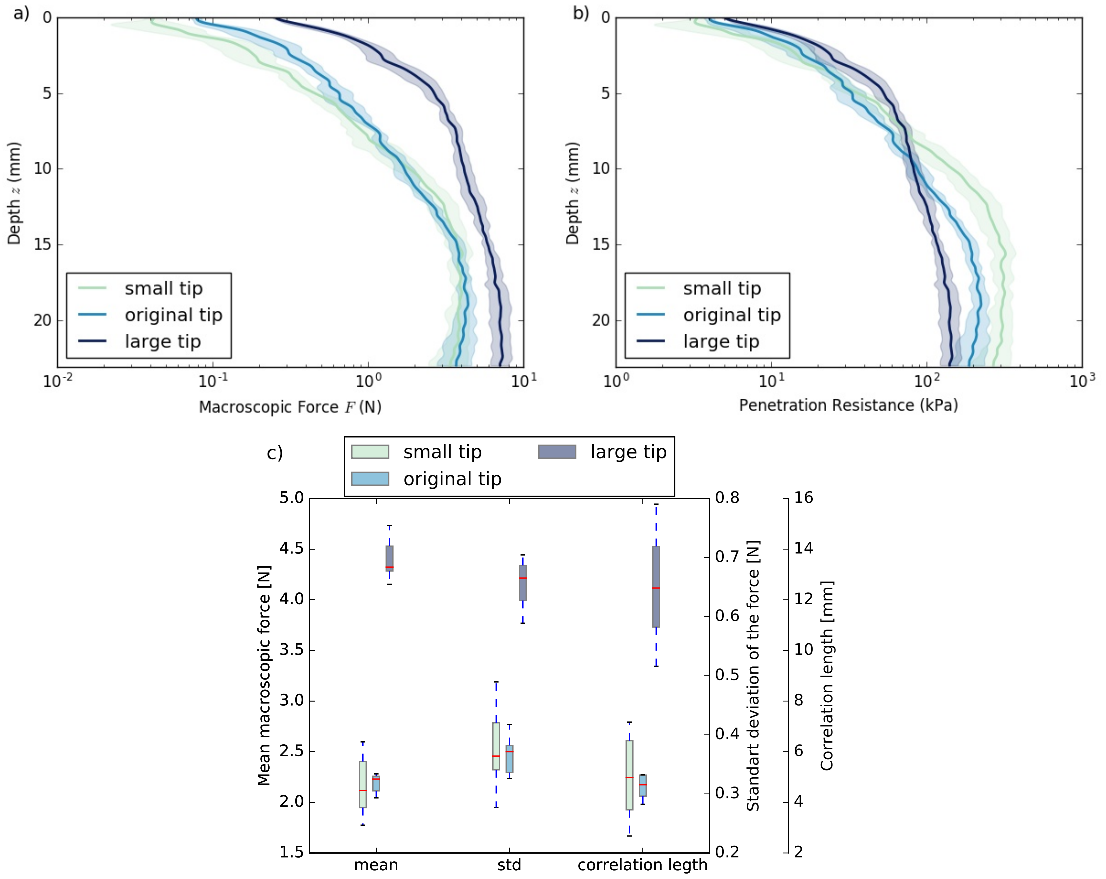

Figure 2.11: Analysis of the different tip sizes: a) average force, b) average resistance, c) the computed mean, standard deviation and correlation length over depth on the samples. The small tip has a diameter of 4 mm the original one of 5 mm and the large tip of 8 mm. The snow sample was snow8 and the rest time was 4 days at -20°.

2.5 Sensitivity to spacing between measurements and sample holder size

In this section, we will define in a first part the optimal spacing between the measurements, but also the distance to the box boundaries. In a second part, the influence of the cylinder diameter on the recorded signal will be examined.

2.5.1 Boundary and spacing effects

In order to find the ideal spacing between the μCPT we first measured 4 profiles separated by a distance of 8 cm, then we did measurements between them until we reached a distance of 1 cm between the measurements. The measured profiles show a clear interactions between CPT if spaced by only 1 cm (Fig. 2.12a). For larger spacing, no clear influence are visible. For deeper depths (>15 mm) a difference in the force measurements for all distances between the measurements can be detected, with an decrease in force due to closer measurements. The statistical analysis show a reduction of mean force, standard deviation and correlation length for closer spacing in general. The distribution of these values for a spacing of 8 cm and 4 cm are nevertheless overlapping.

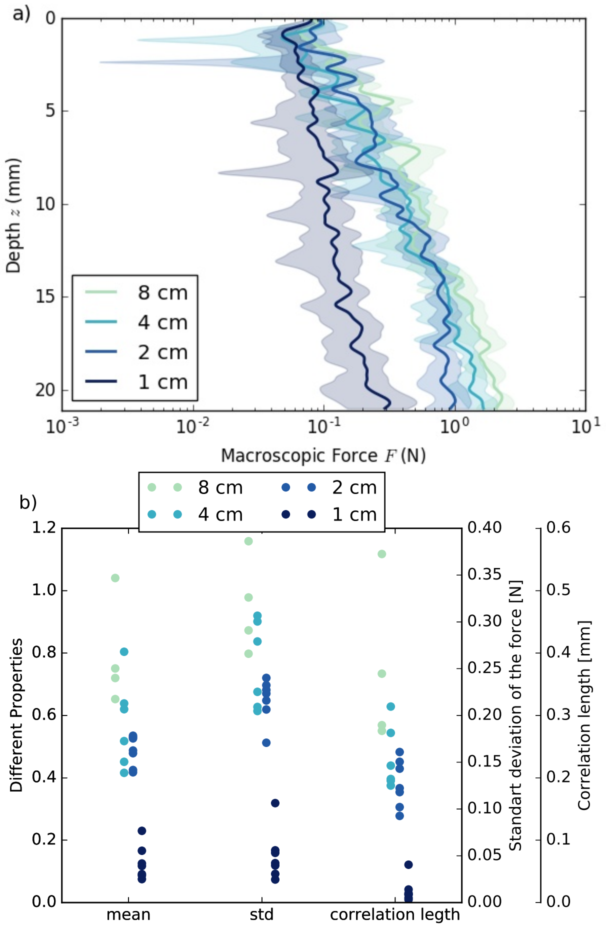

Figure 2.12: Profiles of penetration force and statistics on it for different spacing between μCPT measurements. These measurements were conducted in snow16 after two days of rest.

The force profiles which were taken with a different distances to the wall (on the same sample) are very similar for the first 18 mm (Fig. 2.13a). Below that depth, for all measurements a decrease in force is observed, which is the most pronounced for the measurements close to the wall (2 cm). No clear tendency on the mean force and its standard deviation and correlation length can be observed (Fig. 2.13b).

The influence of the box bottom on the signal was studied on μCPT profiles in two different snow samples (snow8 and SSA18, Fig. 2.14). For the snow8 no

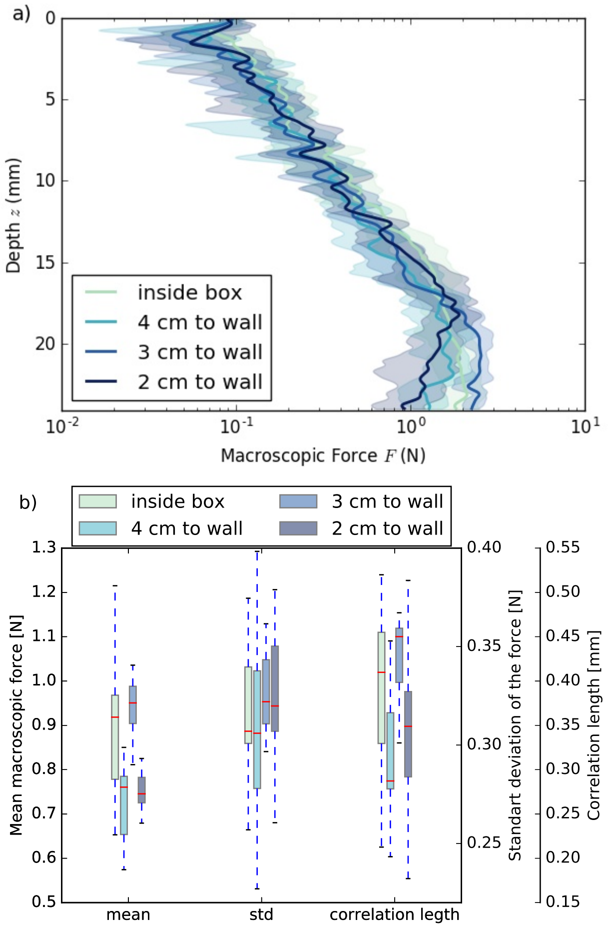

Figure 2.13: Profiles and statistics of penetration force for different distances to the box wall. These measurements were conducted in snow16 after two days of rest.

obvious influence is seen on the profiles. The bottom depth for that sample is between 30 and 40 mm (the end of the sample corresponds to the box bottom). In contrast to that, the force signal of SSA18 shows a diminution of force at a height of about 25 mm, i.e. about 10 mm above the bottom.

In summary, a minimal distance of 4 cm between the measurements themselves and the sample wall is enough to neglect an influence on the force profile due to too closed spacing. Further, the profiles show an increase in penetration force up to 1.5 cm above the sample bottom.

2.5.2 Sample diameter

The goal of this section is to evaluate whether the limited diameter of the sample holder used for X-ray tomography influences the CPT results. The force profiles (Fig. 2.15a) show a clear influence of the small cylinder (1 cm in diameter), with

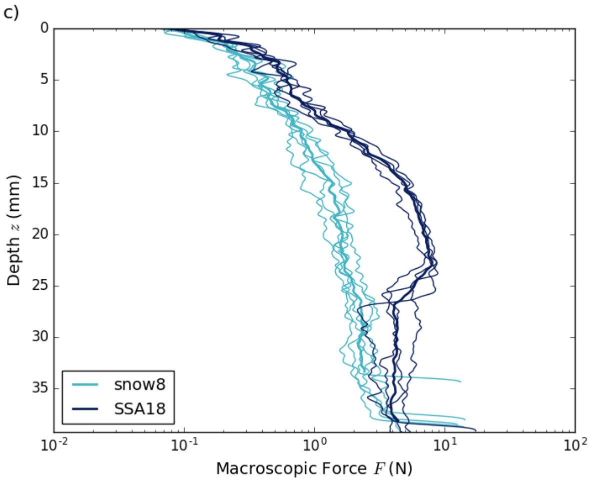

Figure 2.14: Profiles of penetration force for two different snow samples: snow8 and SSA18. These measurements were conducted one day after sieving.

weakening penetration forces over the whole depth compared to the profiles next to the cylinders. The larger cylinders (2 cm in diameter) show for the first 6 to 7 cm a similar force profile than the reference profiles. For deeper depths, the force decreases inside the cylinders, which is not observed for the profiles outside of the cylinders. The latter ones were taken with a distance of about 3 cm to the cylinder wall.

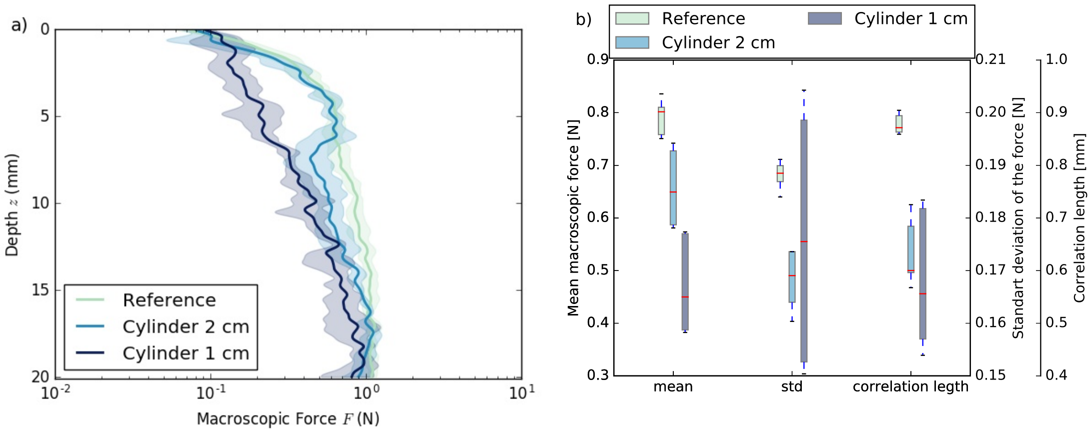

Figure 2.15: Profiles of penetration force (a) and statistics (b) inside and next to cylinders. These measurements were conducted in snow8 after two days of rest.

In general, the mean over the whole depth of 20 mm and the correlation length decrease due to the cylinders (Fig. 2.15b), while no clear trend on the standard deviation is shown. Nevertheless, the cylinders seem to influence the latter property. The differences of standard deviation and correlation length between the two cylinders are less pronounced.

In summary, a sample holder of a diameter of 1 cm shows strong influence on the measured force profile. The cylinder with diameter of 2 cm shows an influence on the force profile after about 7 mm of penetration.

2.6 Discussion and Conclusions

This chapter showed sensitivity studies to best prepare the main experiments of the thesis. The objective was to quantify the influences of the constraints of our experiments (e.g. specimen size, set-up) on the measured signal. For the measurements, we used the SMP which was adapted for our experiments.

This section pointed out the possible influence for three different set-ups of the cone penetration tip, the SMP, μCPT and tomoCPT (2.3). In general, differences between the three different set-ups are less pronounced for the first 4 mm of signal, than for deeper depths. This result indicates that the acquisition (e.g. force sensor response) of the signal is not influenced due to the modified set-up but that the interaction between the tip and the snow is different between the set-ups. The observed differences for the set-ups are much stronger for the RGlr than the DF. This could be due to the high densities of RGlr or the very brittle behaviour that the snow showed, while manipulating with it. The observed higher recorded force for the SMP, could be due to an additional compaction zone in front of the rod, which influences the snow structure before it is measured. The compaction could lead to an strengthening of the force required to penetrate the snow. The larger forces are obvious for the RGlr and only very slight for the DF. This is in accordance to literature, as the size of the compaction zone is increasing with density [Herwijnen, 2013]. Differences between μCPT and tomoCPT are only recorded for RGlr, where the forces are higher for the tomoCPT. The tip of the tomoCPT is plain and an additional force due to wall friction probably gets added. For later interpretation of the tomoCPT signal this has to be accounted for. Additionally, the size of the extension showed no significant differences for none of the computed statistics.

This sample homogeneity could be divided into a horizontal and vertical one. The horizontal heterogeneity between different signals of one sample was about 15 to 20%. Its origin seems to be due to the sample preparation method, whereas the much larger vertical heterogeneity has very likely additional origins, like the formation of a CZ. Tests of SSA and microscopic analysis of the snow shape showed similar fluctuations between the horizontal and vertical measurements.

The experiment for the different tip diameters showed higher forces for larger tips. This is expected as the larger tip has a larger surface and needs thus higher forces to penetrate a material. In contrast to this the size effect on the resistance is not obvious, as higher resistant values for smaller cone tips were observed. This is in agreement the observation of Whiteley and Dexter [1981] in soils. They observed that small CPT have to exert a greater pressure to penetrate soils than large CPT. The different cone angles can also influence the penetration resistance [e.g. Johnson, 2003, Ramamurty and Kumaran, 2004].

The spacing experiments showed already an influence for the signal with a distance of 4 cm due to the neighbouring measurements. This would mean that the radius of the CZ is larger than 2 cm, i.e. 8 times the tip size. This value is quite large, as maximal CZ sizes in snow were reported with up to 4 to 5 times the tip size for densities > 350 kgm^{-3} [Herwijnen, 2013]. Nevertheless, the influence of the neighbouring measurements was quite small and seems to increase with depth, whereas a clear modification of the signal was observed for 1 cm spacing of the measurements. The measurements to the wall showed only differences close to the bottom for a distance of 2 cm. Thus, we settled on a spacing of 4 cm between the measurement points and the box wall, which seems to have a negligible influence on the measured signal. The influence of the bottom surface on the signal was dependent on the snow. While the snow8 did not show a clear influence of the bottom, the force measured in SSA18 showed a clear diminution for distances smaller than about 1 cm to the bottom. The difference in this sample was the slight melting of the snow. The snow after melting is more influenced by the bottom. It could be due to a larger compaction zone.

Measurements in the small cylinders showed a clear influence on the signal, compared to the measurements next to the cylinder (reference profiles). Whereas, the force profiles measured in the 2 cm cylinder display clear changes to the reference profiles only after 7 mm of penetration. It could be due to the building of a CZ, which reaches the size of the cylinder after about 7 mm of penetration.

We showed that the changes after one day of rest in penetration force are negligible. Consequently, one day of rest should be enough to neglect the changes due sintering over the time of the experiment. Note that we have small sintering times, so the bonds between the grains are small, which could differ from nature.

To sum up, for the interpretation of the micro tomographical experiments we have to take into account both the influence of tomoCPT geometry as well as the influence of the sample holders. For the cylinders of 2 cm in diameter, which we use for our experiments only the first 6-7 cm can be assumed to be not influenced by the specimen size. Thus, we need to be cautious while interpreting the recorded force. Further, the tomoCPT seems to be sensitive to the shaft friction (at least for the RGlr), which is an important information for further experiments and their discussions. In addition to this, a minimal rest time of 1 day is necessary for the tomographical experiments, but a longer time would be favourable.

In general, the snow of RGlr is very particular as it shows high densities and the grains are close to spheres. The advantage of these grains is their simple structure and they will not be subjected metamorphism during the measurements. The inconvenience is that the snow seemed to have quite a large CZ. Usually, higher CZ are observed for higher snow densities [Herwijnen, 2013]. For the test of the three set-ups, we observed less impact of the set-up on the measured signal in DF than RGlr. Thus, we conjecture less influences of the different tests for other snow types than for the RGlr.

3

Investigation of snow sintering at microstructural scale from micro-penetration tests

Contents

Abstract

Snow sintering is investigated at microscopic and macroscopic scales with high-resolution cone penetration tests. In a cold room at -10°C, vertical profiles of penetration force were measured periodically during 24 hours using the SnowMicroPenetrometer in four snow samples, which differed only by their grain sizes. We estimated the evolution of snow micromechanical properties, namely the bond rupture force, the deflection at rupture and the number of ruptures per penetration increment, by applying a statistical analysis to penetration profiles. The upper part of the profiles is transient due to the progressive formation of a compaction zone in front of the cone tip. In order to explicitly account for this process in the statistical analysis, we used a non-homogeneous Poisson shot noise model which considers a depth dependency of the rupture occurrence rate. On simulated transient profiles, this analysis is shown to provide accurate estimates of the micromechanical properties. On our experimental data, the method effectively revealed that the vertical heterogeneity of penetration force was essentially due to variations of the rupture rate. Conversely, the time evolution of the macroscopic force was mainly due to microstructural bond strengthening. Both macroscopic force and bond rupture force followed a power law with an average exponent of 0.27 and 0.29, respectively. On our samples, a higher exponent for larger grains was observed on the microscopic bond force, while no trend with grain size was visible in the exponent characterizing the macroscopic force evolution.

Keywords: snow, sintering, penetration tests, mechanical properties, snow microstructure

3.1 Introduction

Snow on Earth exists at a relative high homologous temperature. Once deposited on the ground, snow thus remains very active thermodynamically and its structure changes continuously. One process of this metamorphism is sintering, i.e. the creation and growth of bonds between snow particles [Blackford, 2007]. The sintering has long been recognized to significantly affect the evolution of snow mechanical properties, generally in the form of a progressive strengthening of the material [Gubler, 1978, Reiweger et al., 2009], and manifests over a wide range of time scales: from sub-second sintering (e.g. for cornice formation [Szabo and Schneebeli, 2007]) to hourly time scales (e.g. for fracture healing [Birkeland et al., 2006]), to weekly-monthly time scales (e.g. for seasonal snowpack evolution [Colbeck, 1997]), and up to centuries (e.g. for the formation of glaciers and ice sheets, [Gow, 1975]) . Sintering thus plays an important role, for instance, in avalanche formation [Birkeland et al., 2006, McClung, 2011], in snow management practices such as grooming in ski resorts [Fauve et al., 2002], or in building an igloo.

Sintering is driven by the reduction of surface energy and, depending on environmental conditions, can involve different mechanisms: viscous flow, plastic flow, evaporation, condensation, volume diffusion, and surface diffusion [e.g. Kuczynski, 1949]. The first studies to identify the driving mechanisms of sintering were conducted in metallurgic powders [e.g. Frenkel, 1945, Kuczynski, 1949]. Kuczynski [1949] decomposed the neck growth between metallic particles into different processes and modeled the neck size evolution as a power-law:

$$\left(\frac{r_b}{r_g}\right)^n = \frac{A(T)}{r_g^{n-m}}t \tag{3.1}$$

where r_g denotes the particle radius, r_b is the neck radius, and $A(T)$ is a temperature dependent parameter. The exponents n and m depend on the active sintering process: $(n = 2,\ m = 1)$ for viscous or plastic flow, $(n = 3,\ m = 2)$ for evaporation and condensation, $(n = 5,\ m = 3)$ for volume diffusion and $(n = 7,\ m = 4)$ for surface diffusion. This formalism was then used to understand the neck growth between ice spheres [e.g. Kingery, 1960, Kuroiwa, 1961, Hobbs and Mason, 1964]. Hobbs and Mason [1964] considered that Kucynzski's model was not directly applicable to ice, particularly for vapour transport. Applied to ice, they found values of $n = 5$ and $m = 3$ in Eq. 3.1 for the sintering process corresponding to vapour transport. In their experiments on ice spheres of diameters between 50 and 700 μm and at temperatures between -3 and -20°C, they also found that the dominant mechanism for ice sintering is evaporation-condensation and that the diffusion process plays only a minor role. Maeno and Ebinuma [1983] revisited the different mechanisms contributing to ice neck growth and concluded that vapour transport from a surface source is the major mechanism in most natural and laboratory conditions, while surface diffusion dominates only for small neck radii and either high (> 0.95) or low (< 0.85) homologous temperatures. Chen and Baker [2010] showed on high resolution images that the evolution of a neck between two ice spheres is primarily due to the direction and rate of water vapour transport. In addition to grain size and temperature dependence, sintering mechanisms in snow were also shown to be controlled by contact pressure and grain shape [e.g. Mellor, 1975, Blackford, 2007].

While previous studies have provided valuable insight into the physics of snow sintering in simplified geometries, namely ice spheres, quantitative data on natural snow sintering remained rather scarce, as recalled by [McClung and Schaerer, 2006, Herwijnen and Miller, 2013]. Indeed, many studies have investigated the general evolution of the snow microstructure with time under different temperature and loading conditions [e.g. Kaempfer and Schneebeli, 2007, Wang and Baker, 2013, Schleef and Löwe, 2013, Chandel et al., 2014] but only a few ones have focused on the specific evolution of bond size without any other changes of the microstructure (e.g. grain shape evolution, settlement). Ramseier and Sander [1966] measured the influence of temperature on the strengthening of natural snow with mechanical compression tests. They observed faster strengthening in compression for higher temperature. Similarly, Matsushita et al. [2012] observed a more active sintering with higher snow temperatures and higher normal loads caused by overlying snow. Montmollin [1982] observed a regeneration of destroyed bonds under shear deformation for low deformation rates, which highlights the competition between bond re-welding by sintering and bond failure during deformation. Herwijnen and Miller [2013] used a SnowMicroPenetrometer (SMP, [Schneebeli and Johnson, 1998]) to measure sintering through the time-evolution of the penetration force in different snow types (for times up to $5-8$ hours). Podolskiy et al. [2014] developed mechanical shear tests to investigate the effect of isothermal sintering on interface strengthening at various normal pressures. These latter authors [Herwijnen and Miller, 2013, Podolskiy et al., 2014] proposed to represent the time-evolution of macroscopic force or strength as a power-law:

$$F(t) = F(t = t_0) \left(\frac{t}{t_0}\right)^{\alpha_F} \tag{3.2}$$

with F the force or strength, t the time and α_F a sintering exponent. Typical sintering exponents for seasonal snow are reported in the range between 0.07 and 0.36, as reviewed by Podolskiy et al. [2014]. In their experiments, Podolskiy et al. [2014] measured an average exponent of 0.21 ± 0.08, and observed that higher pressures applied during sintering tend to increase this exponent. Herwijnen and Miller [2013] derived a mean sintering exponent of 0.18 ± 0.05, and observed lower sintering rates for low-density snow (consisting mostly of dendritic grain morphologies) compared to higher density snow. They hypothesize that this relation is the result of two competing processes: (1) bond creation and growth and (2) bond vanishing due to the metamorphism of dendritic forms into compact rounded particles. In parallel, they simulated the microscopic bond-to-grain ratio for simplified spherical ice grains and observed a power-law growth with the same average exponent as that derived from the experiments. Based on this agreement, they suggest that the mean macroscopic penetration resistance closely relates to the microscopic bond-to-grain ratio in snow.

In spite of the advances described above, direct and concurrent measurements of sintering exponents at both microscopic and macroscopic scales in snow, are still lacking. Accordingly, the precise relation between bond growth, at the microscopic scale, and increase in mechanical strength or resistance at the macroscopic scale, largely remains to be elucidated. In this study, we use micro-cone penetration tests (μCPT) to investigate snow sintering at both macroscopic and microscopic scales. Here, the microscopic scale corresponds to the grain scale of about tenths of millimeters and the macroscopic scale corresponds to the sample scale of about a few centimeters. μCPT measurements were conducted with a modified SMP on thin snow samples during 24 hours after snow sieving in a cold room at -10°C. In parallel to the macroscopic penetration force, micromechanical properties, including the bond rupture force, are estimated through an extension of the shot noise model introduced for snow by Löwe and Herwijnen [2012]. In the first section, we present the experimental setup and models required to derive micromechanical properties from the penetration profiles. The models are first evaluated on simulated penetration profiles. The penetration profiles measured on the samples evolving with sintering are then analysed at the macroscopic and microscopic scales. Finally, the outcomes in terms of μCPT processing techniques and knowledge on snow sintering are discussed.

3.2 Material and Methods

3.2.1 Snow samples

We prepared four snow samples with a snow type characterized as large rounded grains (RGlr, Fierz et al. [2009]). The samples were prepared at a controlled temperature of -10±0.5°C by sieving about 35 mm height of snow into rectangular boxes of size 300 x 400 mm. In order to get samples with different grain sizes, the rounded grains were sieved using various sieve sizes (Tab. 3.1). Two samples with a sieve size of 0.8 mm (samples SSA18a and SSA18b) one sample with a sieve size of 1.0 mm (sample SSA14), and one sample with a sieve size of 1.6 mm (sample SSA10) were prepared. The samples showed densities of about 500 kg m^{-3}, grain sizes between 0.7 and 1.5 mm and specific surface areas (SSA) ranging between 10 and 18 m^2 kg^{-1}. Density was measured by weighing 50 cm^3 sub-samples extracted with a cutter. SSA was measured using an optical method (DUFISSS, Gallet et al. [2009]) at different heights and different horizontal locations to characterize spatial variability. The vertical variability of SSA was found of the same order as the horizontal one (typically, the standard deviations were less than 1 m^2 kg^{-1}). Grain size was estimated with microscope images (magnification by a factor of 32) of the grains.

Table 3.1: Physical properties of the snow samples used in this study.

Sample name	Snow type	Sieve size (mm)	Grain size (mm)	SSA (m^2 kg^{-1})	Density (kg m^{-3})
SSA18a	RGlr	0.8	0.7	17.9±0.3	500±2
SSA18b	RGlr	0.8	0.7	17.9±0.3	500±2
SSA14	RGlr	1.0	0.9	14.0±0.3	496±2
SSA10	RGlr	1.6	1.5	10.4±0.1	484±3

3.2.2 Micro-penetration tests in sintering snow

In the following 24 hours after the sieving, a total of 31 micro-cone penetration tests (μCPT) (4 to 5 measurements for 7 different times) were conducted in each sample. This high number of measurements enables to take into account the spatial variability of the sample due to the sieving procedure [e.g. Herwijnen and Miller, 2013]. To avoid interference in neighboring penetration tests, we kept a distance of 40 mm between the measurements. To avoid effects of the lateral walls, no measurement were performed closer than 40 mm to the walls.

The μCPTs in this study were conducted with a modified version of the SnowMicroPenetrometer (SMP version 4, [Schneebeli and Johnson, 1998]). The SMP is a high-resolution penetrometer, which consists of a conical tip with a 60° apex angle and a maximum diameter of 5 mm, driven into the snow by a motor with a constant speed of 20 mm s^{-1}. The depth and force sensors record measurement points at a sampling frequency of 5 kHz, i.e. every 4 μm penetration increment. The SMP measures the snow resisting force applied to the cone tip only and not to the rod. The modification of the SMP for this study consisted in lengthening the apex by 40 mm (Fig. 3.1). This lengthening of the apex was motivated to prevent the rod of the SMP to penetrate in the sample, and thus influence the measured force through the formation of a rod-induced compaction zone (CZ). LeBaron et al. [2014] measured the CZs around a split-axis SMP probe that has the same geometry as the SMP (tip and rod), and found significantly larger CZs than in the study of Herwijnen [2013], who analysed of the CZ around the SMP tip without the rod. Given the size of our snow samples, we wanted to avoid any potential impact of the rod, and account only for the CZ due to the tip. Note that side-by-side measurements performed with the original and modified SMP versions showed essentially identical penetration profiles, as long as the rod of the original SMP does not touch snow (3.A.1).

As a typical example, Figure 3.2 shows μCPT profiles measured after a rest time of 24 hours on sample SSA18a. Single profiles present high frequency fluctuations and

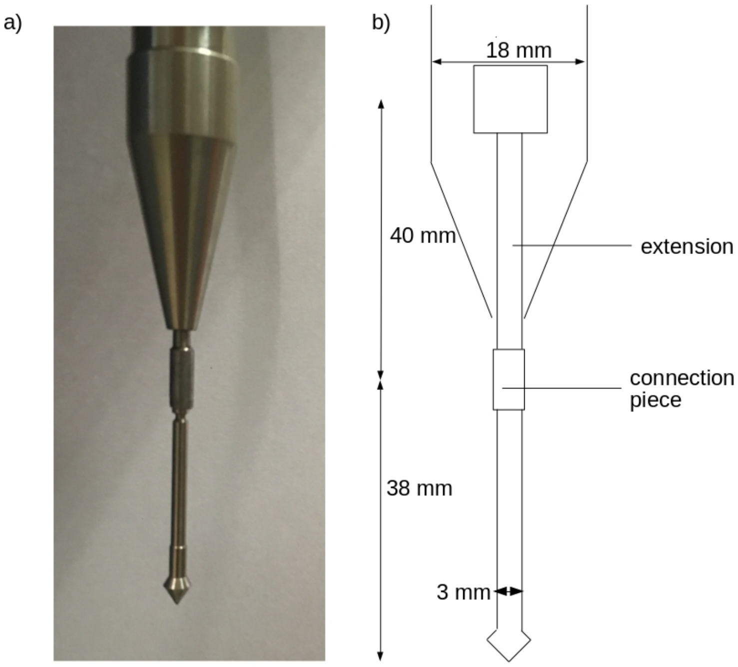

Figure 3.1: Experimental setup: (a) photo and (b) scheme of the modified tip.

large vertical variations (Fig. 3.2a). Even though the sieving procedure may induce a limited vertical heterogeneity of the snow sample [e.g. Herwijnen and Miller, 2013], vertical profiles of SSA did not reveal any significant vertical variations (standard deviations were less than 1 m^2 kg^{-1}). Based on the study of Podolskiy et al. [2014], we can also argue that pressure exerted by overburden snow is unlikely to explain this vertical heterogeneity. The overburden pressure at a depth of 35 mm was estimated about 0.2 kPa, and these authors showed no significant increase of the sintering rate for normal loads lower than 0.5 kPa.

We thus argue that the vertical heterogeneity in the μCPT profiles is mainly caused by the interaction between the snow and the μCPT tip. The increase of the penetration force up to a depth of about 5 mm is due to the progressive penetration of the conic apex into the sample. The increase of force for depths between 5 and 25 mm is then probably caused by the progressive formation of the CZ in front of the tip. According to Herwijnen [2013], the full development of the tip-induced CZ is reached after 40 mm penetration depth, and therefore probably not reached in our experiments. Finally, the decrease of force for depths larger than 25 mm is presumably due to the influence of the rigid bottom of the sample box. Penetration profiles shown by Herwijnen and Miller [2013] also exhibited a maximum force a few centimeter above the sample holder bottom. In the following

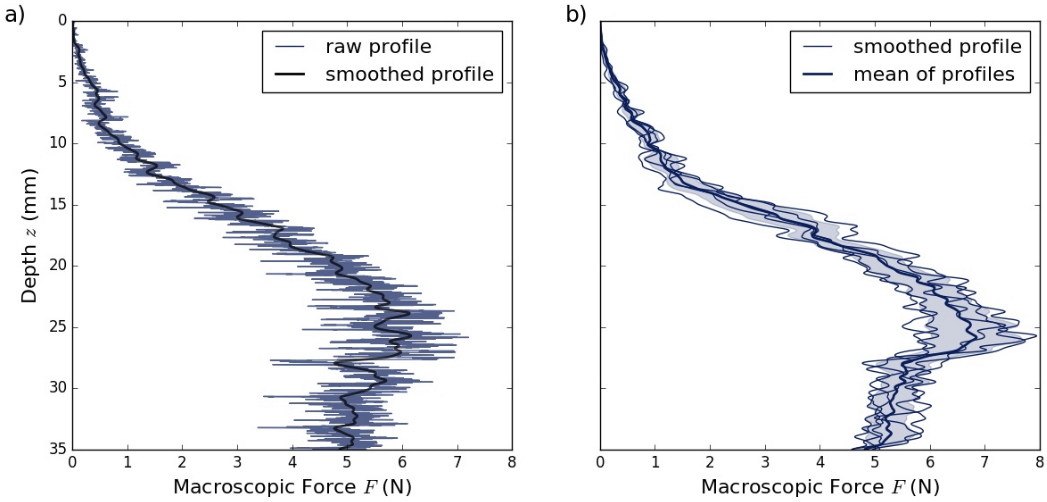

Figure 3.2: Examples of μCPT profiles measured on sample SSA18a after a rest time of 24 h: (a) one raw profile and the corresponding smoothed profile (black), (b) four smoothed μCPT profiles measured at different positions. The profiles were smoothed with a Gaussian filter with a standard deviation of 0.2 mm. The mean of the four smoothed profiles is also shown (bold line), and its standard deviation represented as the shaded area.

analyses, to avoid this artifact caused by sample bottom, we will only account for the first 25 mm of the penetration profiles.

Figure 3.2b shows four smoothed μCPT profiles measured in the same box and at the same time. Slight differences between the profiles are visible. This horizontal heterogeneity in the samples remains comprised between 10 and 15% (relative horizontal standard deviation), and is probably due to the sieving.

3.2.3 Micromechanical analysis methods

Several statistical models were proposed to interpret SMP profiles in terms of micromechanical property proxies. Johnson and Schneebeli [1999] assumed that the penetration force profile results from the superposition of spatially uncorrelated ruptures. Marshall and Johnson [2009] extended this theory by using Monte-Carlo simulations to take into account simultaneous rupture events and inverted the signal. Löwe and Herwijnen [2012] adapted the model into the formalism of a homogeneous Poisson point process (HPP), such that individual ruptures can overlap and are randomly distributed.

All these models interpret a SMP profile $F(z)$, i.e. the macroscopic penetration force F as a function of depth z, as the superposition of spatially uncorrelated rupture events (Fig. 3.3). Each single event corresponds to the rupture of one bond behaving in an elastic-brittle manner. These events are assumed to be identical, but to occur at random depths. They are described by two microstructural properties, namely the deflection length δ and the rupture force f, and express as $f_z(z) = f/\delta \times \theta(z) \times \theta(\delta - z)$ with θ the Heaviside function (Fig. 3.3 inset). The number of events occurring per penetration increment is described by a Poisson distribution with an intensity λ_z. The convolution of the single event function f_z and a random sampling of the number of events results in a simulated profile $F(z)$ (Fig. 3.3).

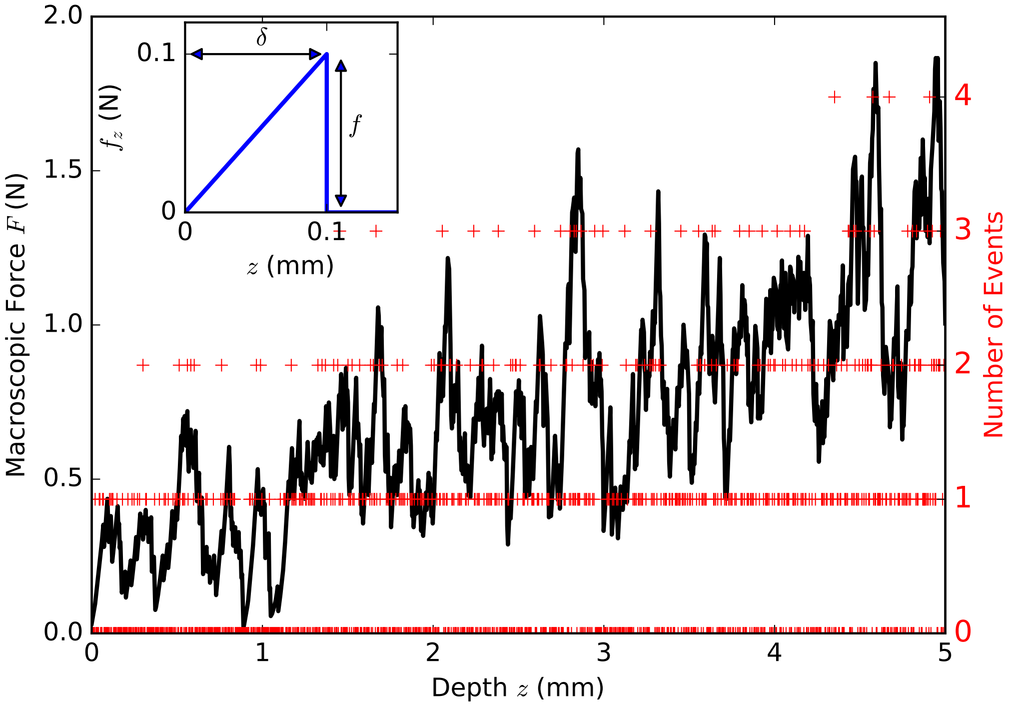

Figure 3.3: Simulated force penetration profile obtained as the superposition of uniform elastic brittle events (inset) whose number of occurrence follows a homogeneous Poisson distribution. Here, δ=0.1 mm, f=0.1 N, and λ_z is linear increasing with depth: $\lambda_z(z) = a_\lambda z + b_\lambda$ with $a_\lambda = 40$ mm^{-2} and $b_\lambda = 50$ mm^{-1}.

Homogeneous Poisson process (HPP)

Assuming that the intensity λ_z is constant over depth and equal to λ, Löwe and Herwijnen [2012] derived analytical expressions directly linking the stochastic cumulants and correlation function of the SMP profile F to the micromechanical properties δ, f and λ. In particular, they obtained the following relations:

$$\kappa_n(z) = \frac{f^n \delta \lambda}{n+1} \quad \text{and} \quad C(z, z+r, |r| < \delta) = f^2 \delta \lambda \left(\frac{1}{3} - \frac{1}{2}\frac{|r|}{\delta} + \frac{1}{6}\frac{|r|^3}{\delta^3} \right) \tag{3.3}$$

where κ_n is the cumulant of order n (e.g. κ_1 is the mean, κ_2 is the variance) and C is the two-point correlation function. This process with a constant intensity $\lambda_z(z) = \lambda$, is called henceforth homogeneous Poisson process (HPP). Note that the formalism of the Poisson processes implies constant event characteristics, i.e. δ and f are constant (or in a constant distribution). The assumption of a constant intensity also implies stationarity of $F(z)$, and thus enables to compute the stochastic cumulants and correlation function as “depth" cumulants and correlation function (ergodicity). In practice however, measured penetration profiles are rarely stationary with depth even for homogeneous snow layers [Herwijnen and Miller, 2013]. This difficulty is overcome by splitting the profile in smaller windows where the assumption of stationarity remains valid [e.g. Proksch et al., 2015]. It is observed on simulated HPPs that better results are obtained with larger windows [Löwe and Herwijnen, 2012]. Therefore, a balance between large windows that are stochastically representative, and small windows on which the profile can be considered stationary, needs to be found. Typical window sizes Δz of 1 to 5 mm are reported in the literature [e.g. Löwe and Herwijnen, 2012, Proksch et al., 2015, Ruiz et al., 2017]. Note that, in practice, the correlation function C is also generally computed on detrended profiles (i.e. the mean and linear trend are subtracted on each window) [e.g., Löwe and Herwijnen, 2012, although not shown therein].

Non-homogeneous Poisson process (NHPP)

As shown in Fig. 3.2, the penetration force measured in our experiments displays strong changes with depth. The profiles were limited to a depth of 35 mm due to the modified design of the SMP tip. As explained in Sect. 3.2.2, the snow structure exhibited a rather homogeneous vertical profile. We can thus reasonably assume that the microstructural properties δ and f are constant over the entire depth, while only the number of events, thus the intensity λ_z, varies with depth. This depth variation of λ_z can be related to the build-up of the compaction zone in front of the tip. We thus propose to analyse our measured μCPT profiles as a non-homogeneous Poisson process (NHPP), with a variable intensity λ_z, instead of a homogeneous Poisson process (HPP). Note that the NHPP equals to the HPP if λ_z is constant with depth.

We describe here the main steps of the mathematical developments. Details can be found in 3.A.2. Let us consider $F(z)$ as a NHPP characterized by an elastic brittle event f_z, whose properties f and δ are assumed to be constant with depth and a number of events in a Poisson distribution of intensity $\lambda_z(z)$. Assuming that the relative variations of $\lambda_z(z)$ over an interval of length δ are negligible, it can be shown that:

$$\kappa_n(z) = \frac{f^n \delta \lambda_z(z)}{n+1} \quad \text{and} \quad C(z, z+r, |r| < \delta) = f^2 \delta \lambda_z(z) \left(\frac{1}{3} - \frac{1}{2}\frac{|r|}{\delta} + \frac{1}{6}\frac{|r|^3}{\delta^3} \right). \tag{3.4}$$

Equation (3.4) is identical to Eq. (3.3) obtained by Löwe and Herwijnen [2012], but with $\lambda_z(z)$ instead of a constant intensity λ. However, F cannot anymore be assumed stationary, and therefore its cumulants and correlation function cannot be computed directly from a single force profile $F(z)$. We thus define $\widetilde{F}$ as:

$$\widetilde{F} = \frac{F - \kappa_1(F)}{\kappa_1(F)^{1/2}} \tag{3.5}$$

From Eq. (3.4), it can be shown that $\widetilde{F}$ is stationary and we obtain:

$$f = \frac{3}{2}\overline{\widetilde{F}^2}, \qquad \delta = -\frac{3}{2}\frac{C(0)}{C'(0)}, \qquad \lambda_z(z) = \frac{4}{3\delta}\frac{\kappa_1(F)}{\overline{\widetilde{F}^2}} \tag{3.6}$$

where $\overline{\bullet}$ denotes the mean over depth. The cumulant $\kappa_1(F)$ appearing in Eq. (3.6) is the stochastic mean of the NHPP. To compute this quantity from our data, we approximate $\kappa_1(F)$ by the "depth" mean $\overline{F}$ calculated on a running window of width Δz=3 mm and on a single profile. Since $\kappa_1(F)$ is a first order cumulant, this approximation is relatively robust, and even exact if the intensity λ_z is linear over intervals of width Δz.

3.3 Results

3.3.1 Evaluation of the μCPT analysis method

In this section, we compare the proposed NHPP analysis and the original HPP analysis both on simulated penetration profiles with known properties, and on the μCPT profiles measured in this study.

3.3.1.1 Evaluation on simulated profiles

First, we evaluated the models on profiles produced by the simulation of a non homogeneous Poisson process. A linearly evolving intensity $\lambda_z(z) = a_\lambda z + b_\lambda$ was considered. The simulated profiles have a length of 25 mm and a resolution of 4 μm, with prescribed parameters (see legend of Fig. 3.4) similar to the micromechanical properties of our samples. To analyse the influence of the different parameters (f, δ, and a_λ), we performed a sensitivity analysis by varying one parameter within a certain range while keeping the others constant. For each set of parameters, 500 independent profiles were simulated. Since the intensity $\lambda_z(z)$ varies with depth, we defined $\overline{\lambda}$ as its mean over the whole depth to provide a single scalar in the sensitivity analysis. The value $\overline{\lambda}$ was varied by varying a_λ in the range [0, 300] mm^{-2}, while b_λ was kept constant at 50 mm^{-1}. Moreover, three different analysis window sizes Δz of 1, 3 and 10 mm were tested.

Both methods provide similar estimates of the deflection at rupture δ with a root mean square error (RMSE) of 0.59 mm for the HPP and 0.54 mm for the NHPP (Figs. 3.4a,b). Note that large values of δ tend to be underestimated by the two analyses. Nonetheless, this parameter is correctly estimated if the analysis window is sufficiently large ($\Delta z = 10$ mm), especially with the NHPP.Overall, estimates of the microscopic rupture force f are more accurate with the NHPP method with a RMSE of 0.263 N for the HPP and 0.051 N for the NHPP (Figs. 3.4c,d). As expected, for profiles with an almost constant intensity (a_λ=1 mm^{-2}), the two models provide similar results: a slight underestimation of f. For profiles with a significant evolution of $\lambda_z(z)$ (a_λ=10 or 40 mm^{-2}), the HPP provides accurate estimates of f only for small window sizes, while the NHPP provides accurate estimates for all window sizes. Lastly, the NHPP produces in general a better estimation of the mean intensity $\overline{\lambda}$ (RMSE of 1305 mm^{-1}) than the HPP (RMSE of 2885 mm^{-1}) (Figs. 3.4e,f). The HPP provides correct estimates of $\overline{\lambda}$ only for large windows and very small values of a_λ, while the NHPP provides correct estimates for all tests. Note that the NHPP tends to slightly overestimate the mean intensity, especially for samples with a large δ and small window sizes.

We can thus conclude that, on non-stationary profiles with an intensity linearly increasing with depth, the NHPP analysis performs better than the HPP analysis in recovering the micromechanical properties. Larger analysis window sizes generally improve the results, especially when the deflection at rupture δ is large. As expected, on almost stationary profiles both methods show similar results.

3.3.1.2 Comparison on measured profiles

In this section, we compare the two analysis methods on real μCPT profiles. Figure 3.5 shows the micromechanical properties estimated on the μCPT profiles measured after a rest time of 24 hours as derived from the HPP and NHPP models.

As explained in Section 3.2.3, with the HPP model, δ, f and λ are assumed constant over small windows of size Δz=3 mm and were computed according to Eqs. (11) and (12) in [Löwe and Herwijnen, 2012]. With the NHPP model, δ and f are assumed constant over the whole profile, while λ_z can vary with z, and were computed according to Eq. (3.6). Therefore, the vertical resolutions of the computed micromechanical properties are, by construction, different for the two models.

The HPP analysis shows non-monotonic variations of f with depth (Fig. 3.5a). It indicates an increase of δ with depth, especially for sample SSA10 characterized by large grains (Fig. 3.5b). Lastly, an overall increase of λ with depth is observed, with a slight decrease between 10 and 15 mm depth (Fig. 3.5c). This decrease

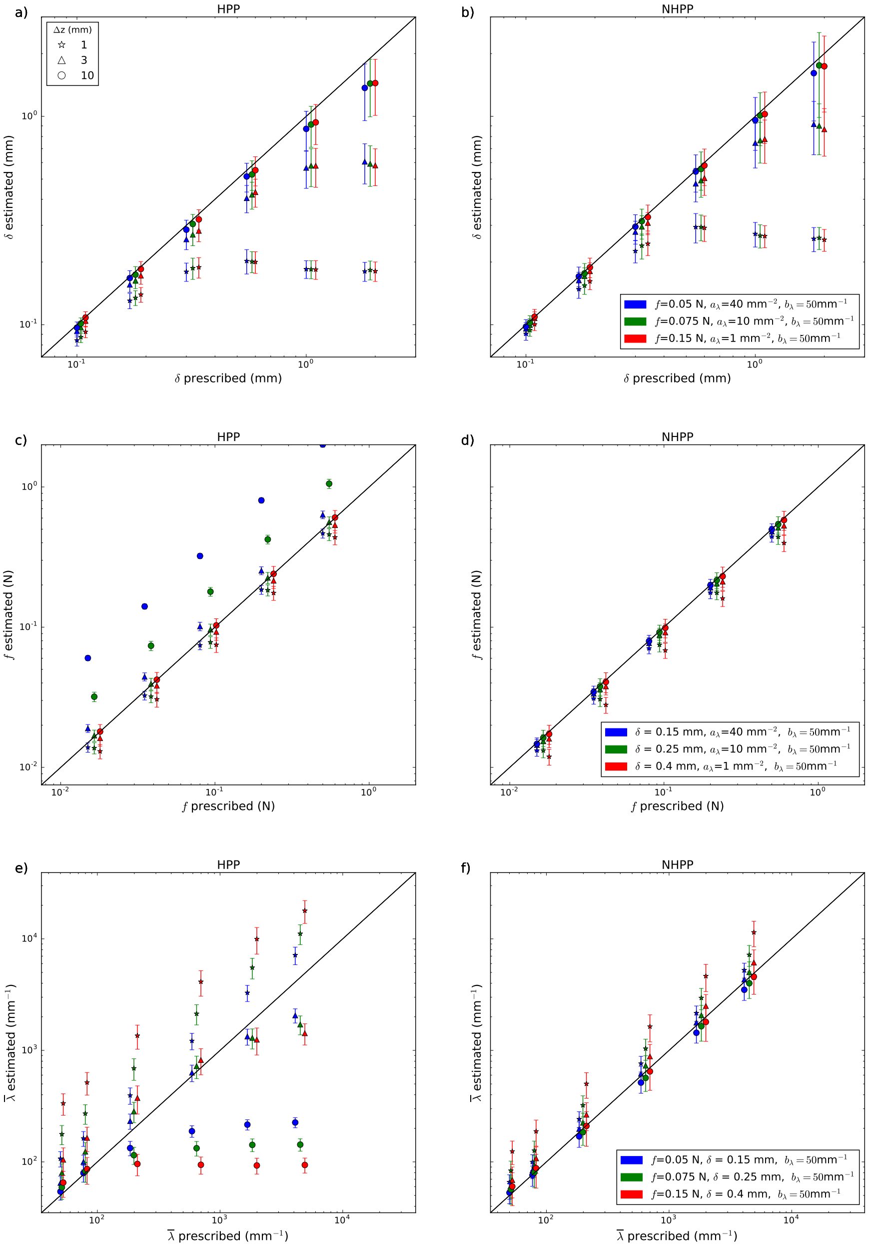

Figure 3.4: Comparison of estimated and prescribed micromechanical properties δ, f, $\bar{\lambda}$ on simulated penetration profiles. The results of the HPP analysis are shown in (a, c, e), while the results of the NHPP analysis are shown in (b, d, f). In each plot, the values of the constant micromechanical properties, chosen to be similar to those of the samples presented in this study (SSA10 in red, SSA14 in green and SSA18a,b in blue), are indicated in legend. The three different symbols denote the different window sizes Δz. Error bars correspond to the standard deviation over the 500 independent profile realizations.

might be due to the rapid increase of the macroscopic force F with z in this depth interval (Fig. 3.2), for which the HPP analysis is not well-designed. Globally, the three parameters follow the overall increasing trend with depth exhibited in the μCPT force profiles. The HPP analysis distinguishes the different samples on δ and λ, but computes a similar value of f for all samples and almost all depths.

The NHPP analysis distinguishes the different samples on all properties: the largest grains exhibit the largest values of f and δ, and the smallest values of λ. In particular, a noticeable difference between the two analyses is visible on the computed values of f (Figs. 3.5a,d): unlike the HPP analysis, the NHPP analysis shows a high dependency of f on the different samples. The values of λ_z are found to strictly increase with z, which is consistent with the progressive formation of the compaction zone around the μCPT tip (Fig. 3.5f). The differences between the two methods become smaller for depths between 20 and 25 mm.

Note that, here, no reference profile of the micromechanical properties is available to definitely evaluate the two models. However, the monotonic increase of intensity with depth, and the the increase of f with grain size, which are only visible in the NHPP estimates, seem more consistent with our knowledge of the sample properties (see Sect. 3.2.1) and of the progressive formation of the compaction zone [Herwijnen, 2013]. Indeed, Eq. (3.1) indicates a higher bond size for larger grains and thus an increase of f with grain size can be expected.

3.3.2 Evolution of the macroscopic force with time

The macroscopic force F clearly increases with time due to sintering (see Fig. 3.6 or Fig. 3.11). Moreover, the relative increase of F with time also appears to be enhanced with depth. For instance, F increases by a factor of about 1.5 over 24 hours at a depth of 5 mm, while it increases by a factor of about 3 at a depth of 20 mm.

In line with previous studies [e.g. Herwijnen and Miller, 2013, Podolskiy et al., 2014], the time evolution of the depth-averaged macroscopic force $\bar{F}$ (Fig. 3.7), was approximated by fitting power laws of the form:

$$\overline{F}(t) = F_{1h} \left(\frac{t}{t_{1h}} \right)^{\alpha_F}, \tag{3.7}$$

with $t_{1h} = 1$ hour and F_{1h} is the mean macroscopic force value after 1 hour of sintering. $\bar{F}(t)$ is computed as the mean between 0 and 25 mm depth, to exclude any potential influence of the bottom of the box (see Sect. 3.2.1). The start time $t = 0$ is defined as the middle of the sieving procedure, which took between 5 and 10 minutes. Hence, the error on sintering time is estimated to be half of the sieving time. The fit was performed with an orthogonal distance linear regression (ODR) on the logarithm of the data using scipy python package [Boggs and Rogers, 1990].

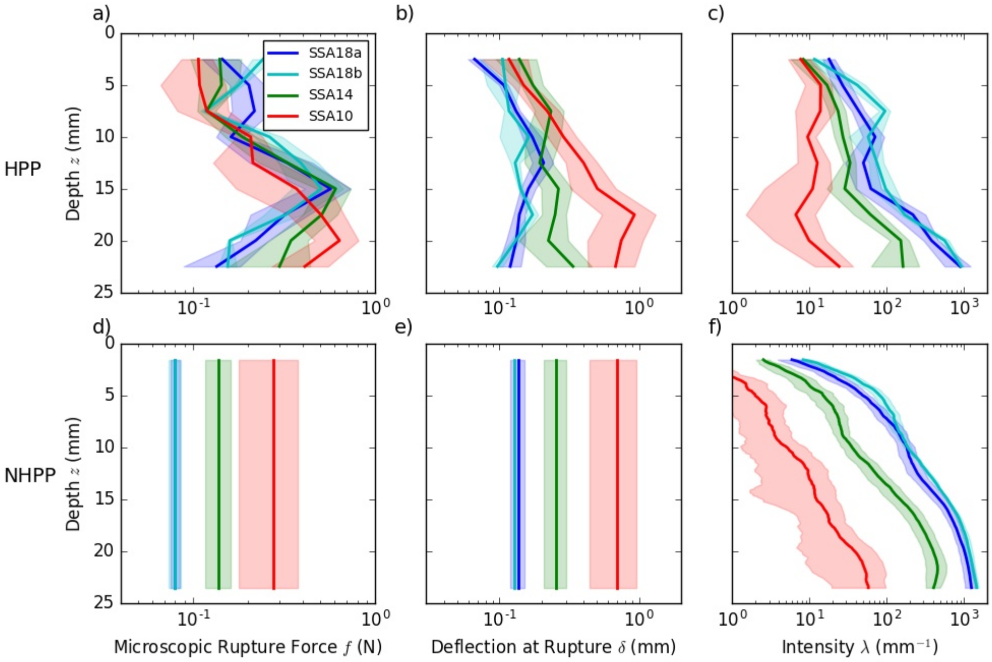

Figure 3.5: Estimated micromechanical properties derived from the μCPT profiles measured on the samples after a rest time of 24 hours: (a, c) microscopic rupture force f, (b, d) deflection at rupture δ, and (e, f) intensity λ_z, as computed by the HPP (a, b, c) and NHPP (d, e, f) models. The shaded area around the curves represents the standard deviation of the values obtained for the different profiles measured at one sampling time.

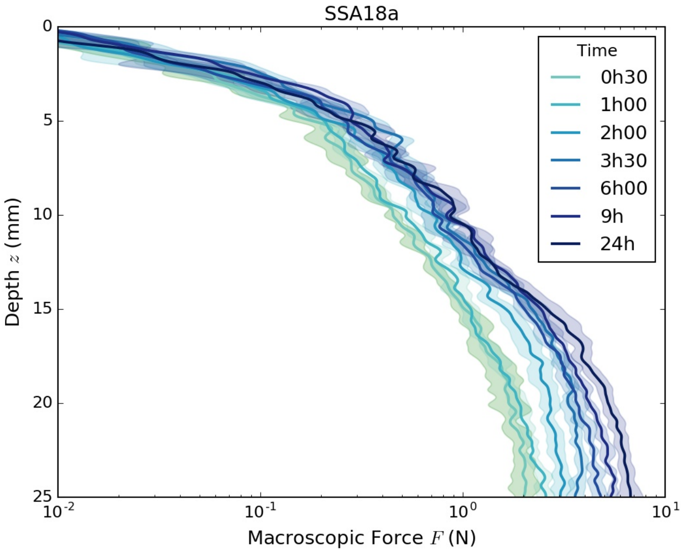

Figure 3.6: Vertical profile of the macroscopic force F for different sintering times, measured on sample SSA18a.

The function finds the maximum likelihood and gives the estimated properties with their standard error, i.e. the error at one sigma interval. We accounted for the time error in the ODR fit and used all the 4 to 5 profiles measured at any given time. We chose a Pearson p-value of 1% to analyse the significance of the fit.

Figure 3.7 shows that the mean macroscopic force exhibits a clear power law trend. Only little deviations from the power law are observed, and the confidence intervals on the fitted parameters are rather small. The pre-factor F_{1h} ranges between 0.36 N and 1.22 N depending on the considered sample, and increases with specific surface area. Note that the values of F_{1h} for samples SSA18a and SSA18b, which are composed of similar grains, are very close but do not exactly coincide (see indicated errors). The exponent α_F is about 0.3 for all samples. Hence, it appears that the initial value of the macroscopic force F_{1h} depends on sample properties, while the power law exponent α_F is independent of the sample.

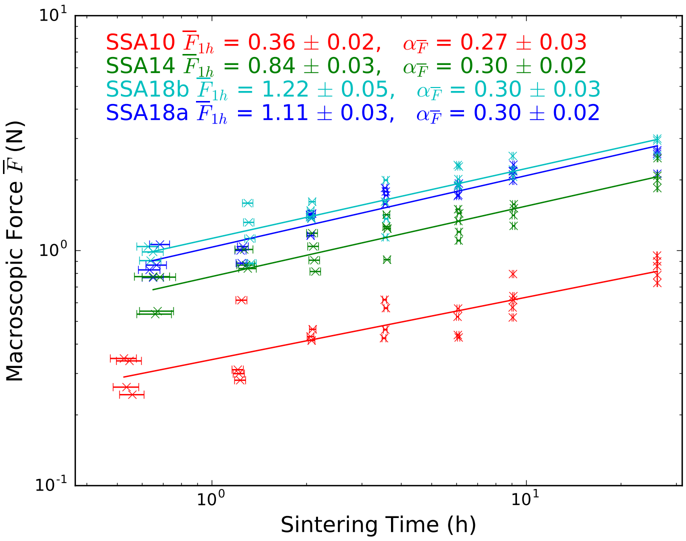

Figure 3.7: Evolution of the depth-averaged macroscopic force $\bar{F}$ with time for the different snow samples. The power law fits are shown by the solid lines, and the corresponding parameters are indicated in legend. The horizontal error bars represent the time error (around 10 minutes) due to non-instantaneous sample preparation.

3.3.3 Evolution of the micromechanical properties with time

Figure 3.8 shows the evolution with time, for sample SSA18a, of the micromechanical properties estimated by the NHPP analysis. Similar plots for the other samples are visible in 3.A.3, Figs. 3.12, 3.13, 3.14. The deflection δ and intensity λ_z do not show

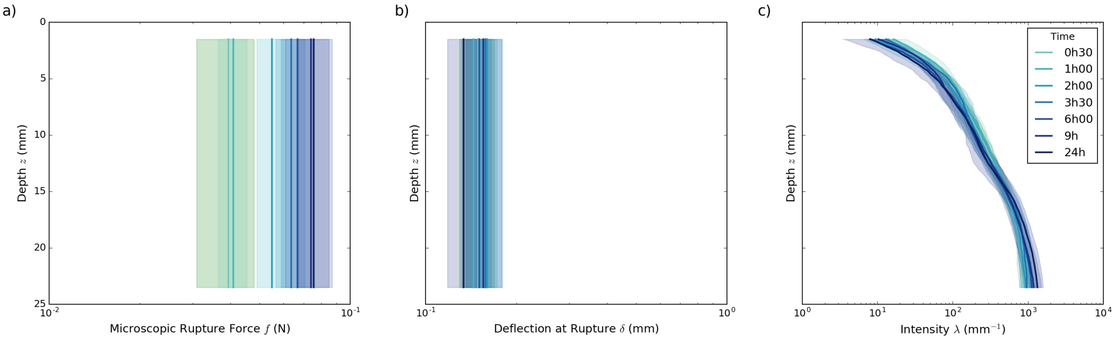

Figure 3.8: Vertical profiles of the micromechanical properties estimated by the NHPP model on sample SSA18a for different sintering times. The shaded area around the curves represents the standard deviation obtained for the different profiles at one sampling time.

obvious changes with time (Figs. 3.8b, c). On the contrary, for the microscopic rupture force f, a clear increase with time is observed (Fig. 3.8a). Hence, according to the NHPP analysis, the evolution of the macroscopic force F (Fig. 3.6) with time is mainly due to the evolution of the microscopic rupture force, whereas its evolution with depth is explained by the vertical profile of the intensity. We recall that the NHPP model assumes that the microscopic rupture force is constant over depth, but not that intensity is constant over time.

As in Sect. 3.3.2, the time evolution of the micromechanical properties was approximated by fitting a power law : $X(t) = X_{1h}\,(t/t_{1h})^{\alpha_X}$, were X is either f, δ or $\overline{\lambda}$ (Figure 3.9). Again, a Pearson p-value of 1 % is used to assess the significance of the fits. The lines in Fig. 3.9 are dotted if the fit is not significant. Note that we consider here the averaged intensity over depth. Figures 3.9b,c confirm that the deflection and average intensity do not significantly change with time. The initial values of δ and $\overline{\lambda}$ are however dependent on sample properties. On the contrary, the microscopic rupture force f exhibits a clear power law trend. Again, only little deviations from the power law are observed, and the confidence intervals on the fit parameters are rather small. The pre-factor f_{1h} ranges from 0.05 N to 0.09 N and decreases when specific surface area increases. The value of f_{1h} for samples SSA18a and SSA18b, which were composed of similar snow grains, are very close. The exponent α_f ranges from 0.18 to 0.34, and appears to decrease with increasing specific surface area (or decreasing grain size). Hence, both the initial value and power law exponent of the microscopic rupture force are dependent on grain size.

3.4 Discussion

Due to a limited sample height of 35 mm, the presented μCPT profiles exhibit a non-stationary regime due to the progressive build-up of a compaction zone in front

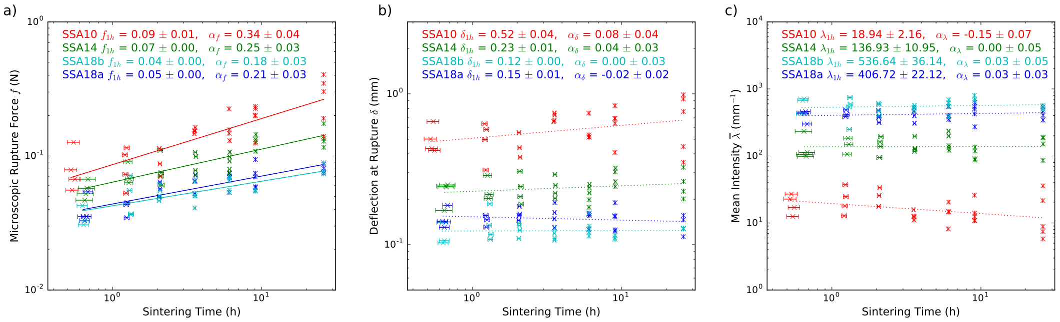

Figure 3.9: Time evolution of the micromechanical properties estimated by the NHPP model. The significant (resp. non-significant) power law fits are represented by the solid (resp. dotted) lines, with corresponding parameter indicated in legend. The horizontal error bars represent the time error (around 10 minutes) due to non instantaneous sample preparation.

of the cone tip. To properly account for this feature and to estimate micromechanical properties from the μCPT profiles, we proposed a non-homogeneous Poisson shot noise model (NHPP). This approach follows up on the ideas of Löwe and Herwijnen [2012], who described the fluctuating penetration force as a homogeneous Poisson shot noise process (HPP) with a single event described as an elastic-brittle rupture. We showed, under the assumption that the relative variations of intensity over an interval of size δ are small, that the analytical expressions for the cumulants and the correlation of the macroscopic force given by Löwe and Herwijnen [2012] (Eq. 6 and 10 there) can be extended to a non homogeneous process, i.e. with an intensity λ_z varying with depth. This extension amounts to separate two spatial scales: the scale of the bond rupture characterized by δ and f, and the scale of the compaction zone that governs the evolution of λ_z. Using simulated force profiles with a linear evolving intensity (and properties close to those of the snow samples used in this study), we showed that the NHPP model was able to retrieve accurate micromechanical properties (Fig. 3.4). In particular, on simulated profiles characterized by large variations of λ_z with depth, which mimic our measurements, the NHPP was more accurate than the HPP whose underlying assumptions are violated. On this type of profile, no window size, small enough to satisfy the assumption of constant parameters and large enough compared to the event spatial extent δ, can be found to correctly apply the HPP. The NHPP development was thus required to provide a robust estimates of the micromechanical parameters from the presented measurements. The main approximation of the NHPP model is the calculation of the first cumulant $\kappa_1(F)$. We approximate $\kappa_1(F)$ by its running mean over a window size of Δ_z=3 mm. Therefore, we assumed that the profile can be approximated by a linear evolution over such window sizes. A window of 3 mm was chosen as the best compromise between a sufficiently large window to get a better estimation of the parameter, and a sufficiently small window to assume the signal to evolve linearly over it. Comparing the HPP and NHPP on measured profiles showed clear differences between the estimated parameters by the two models (Fig. 3.5). Nevertheless, these differences become less pronounced for depths larger than 20 mm. In particular, the models estimate similar values of δ. The two models predict a similar evolution of f and λ with SSA but the estimated values are different for these depths. Thus, it would be interesting to compare the NHPP and HPP on thicker snow-samples, where the CZ can fully develop. In such a case, the NHPP and HPP would probably lead to similar estimates. Indeed, the NHPP is a generalization of the HPP, as it also includes zero-slope evolution of the intensity with depth. On a profile with no significant evolution of lambda, the NHPP would not provide any advantage over the standard HPP method but would perform as well as this method. Besides, it would be interesting to apply the NHPP on a whole profile of a snowpack with different snow layers. In particular, it may be still possible that a new compaction zone develops at each transition between a soft layer and a harder one, and not only at the snowpack surface.

We measured numerous μCPT profiles in quasi-homogeneous snow samples created in the laboratory and let to sinter during 24 hours at -10°C. The NHPP model was applied to these measurements. The derived micromechanical properties consistently distinguished the four snow samples prepared with different sieve sizes and varying mainly by grain size (or SSA) and slightly by density. The largest values of microscopic rupture force f and deflection δ, and lowest values of intensity λ_z, were obtained for the largest grains and slightly lower densities than average (Fig. 3.5). Furthermore, only the microscopic rupture force was found to evolve significantly with time, while the parameters λ_z and δ remained essentially constant with time (Fig. 3.8). These results can be interpreted as a progressive growth of the bonds without any other structural changes in the snow.

The microstructural analysis thus exhibits a partition between the variations with depth (borne only by the intensity) and with time (borne only by the microscopic rupture force) of the macroscopic force profile. This observation is consistent with our expectation that the evolution over one day of the snow microstructure, excepted bond growth, would remain limited for samples composed of large rounded grains with a density around 500 kg m^{-3} and a SSA between 10 and 18 m^2 kg^{-1}. Hence, μCPT profiles with an appropriate statistical analysis indeed appear to provide relevant proxies of bond evolution during sintering. This point corroborates the finding of Herwijnen and Miller [2013] who suggested that the SMP profile relates to bond scale processes, based on an agreement between the SMP mean force evolution and a physical bond-to-grain evolution model.

In previous studies, snow sintering was investigated at different scales, from the bond scale by recording the evolution of the bond size [e.g. Kuroiwa, 1961, Hobbs and Mason, 1964, Chen and Baker, 2010] to the snowpack scale by recording the evolution of macroscopic mechanical properties such as shear or compression strength [e.g. Ramseier and Sander, 1966, Montmollin, 1982]. With the μCPT and the NHPP analysis, we were able to characterize the sintering process at two scales, through simultaneous records of the macroscopic penetration force F (Fig. 3.7) and of the microscopic rupture force f (Fig. 3.9a), a direct proxy for the bond size. Both F and f were shown to obey power laws with time, with similar exponents, namely $\alpha_F \approx 0.29$ (Fig. 3.7) and $\alpha_f \approx 0.27$ (Fig. 3.9a) (average values). Hence, the time-evolution of the macroscopic force F appears closely related to the evolution of the microscopic force f. Recall also that the intensity profile λ_z remains essentially constant over time, meaning that the progressive build-up of the tip-induced compaction zone is unaffected by sintering, at least in the considered dataset.

The obtained values of α_F are in agreement with previous studies at the macroscopic scale: Herwijnen [2013] observed exponents between 0.2 and 0.3 for rounded grains with densities between about 350 to 400 kg m^{-3}. To compare the values of α_f to sintering exponents involved in the evolution of bond size (a geometrical property), we can assume that f is proportional to $\sigma_{ice} \times r_b^2$ with σ_{ice} the strength of ice and r_b the bond radius. This assumption yields the relation $\alpha_f = 2\ \alpha_{rb}$ between the sintering exponents of f and bond radius r_b. According to Hobbs and Mason [1964], the evolution of the bond-to-grain ratio for ice can be theoretically described by Eq.3.1 with $n = 5$ and $m = 3$, which yields $\alpha_{rb} = 1/5$. From experimental data, Hobbs and Mason [1964] estimated sintering exponents of bond size between 0.16 and 0.24 at a temperature of -10°C. Kingery [1960] measured exponents between 0.15 and 0.18 at temperatures of about -9.5°C and Kuroiwa [1961] got an exponent of 0.2 at the same temperature. The sintering exponents of microscopic rupture force that we measured (between 0.18 and 0.34) are effectively higher than the ones theoretically obtained for bond size, but not by a factor of 2. Note, however, that all these studies considered ice spheres, while we worked with irregular grain shapes. Besides, Kuroiwa [1961] and Hobbs and Mason [1964] worked with much smaller ice spheres than ours, only Kingery [1960] used ice spheres with a diameter between 0.6 and 1 mm. Moreover, deviations to the relation $\alpha_f = 2\ \alpha_{rb}$ can be expected if the stress distribution in a bond between grains is not homogeneous. The measured values of α_F do not change with SSA in the range between 10 and 18 $m^2\ kg^{-1}$ and densities between 480 and 500 kg m^{-3}. In contrast, the values of α_f were found to slightly increases with grain size, as observed by Hobbs and Mason [1964]. Lastly, it is also noteworthy that a different behaviour with grain size was observed for the two pre-factors F_{1h} and f_{1h}: F_{1h} decreases, while f_{1h} increases, with increasing grain size. The behaviour of f_{1h} is consistent with classical sintering models predicting that bond radius should increase with grain size according to $r_b \propto r_g^{m/n}$ (see Eq. 3.1) [Kuczynski, 1949].

3.5 Conclusions

We investigated snow sintering at -10°C by measuring numerous μCPT profiles conducted with a modified version of the SMP on samples characterized by different grain sizes during 24 hours. To analyse the fluctuating macroscopic force in terms of micromechanical properties, we extended the work of Löwe and Herwijnen [2012] based on an homogeneous Poisson shot noise model. To this end, we also considered the penetration force as the result of the contribution of independent elastic-brittle failure events, but we relaxed the assumption that the number of failure occurrences per penetration increment, i.e. the intensity, is constant over a certain analysis window. This non-homogeneous Poisson shot noise model is able to characterize the snow micromechanical properties of a homogeneous snow layer even if the cone penetration test is in a transient state, due to the progressive formation of a compaction zone in front of the cone tip. On simulated profiles with prescribed spatial variations of the intensity, the model provided accurate estimates of the micromechanical properties. On the measured μCPT profiles, the model decomposed the evolution of the macroscopic force with depth and time as a constant vertical intensity profile and a time evolution of the microscopic rupture force. This partition is consistent with the absence of evolution of the grain themselves (e.g. shape) in the tested samples and bond growth with sintering. The power law exponents for the macroscopic and microscopic rupture forces ($\alpha_F \approx 0.29$ and $\alpha_f \approx 0.27$, respectively) were very close and in line with previous studies. In addition, the analysis of α_f revealed a higher sintering rate for the largest grains and the pre-factor f_{1h} of the power law was shown to increase with grain size, which is in line with the theory of bond growth. However, the limited number (four) of tested samples did not enable us to provide quantitative relations between grain size and sintering rate. Our analysis nevertheless showed that micro-cone penetration tests, combined with an appropriate analysis method enables a fast and simple characterization of the snow structure. It would be thus possible to investigate the snow evolution with metamorphism on snow samples spanning a wider range of microstructural patterns.

The HPP and NHPP models could be evaluated with micro-tomographical measurements, as mentioned by Löwe and Herwijnen [2012]. Indeed, micro-tomography can be used to provide direct estimates of microstructural properties derived from μCPT. In particular, the contact force f could be related to the bond size derived from tomographic data using the concept of the minimum cut surface [Hagenmuller et al., 2014 b]. We are currently working on combined μCPT and micro tomographical measurements. This data includes high-resolution measurements of the snow microstructure before and after a μCPT. It could provide a direct evaluation of the HPP and NHPP models and could give new insights on the deformation mechanisms occurring at the cone tip.

3.A Appendix

3.A.1 Evaluation of modified SMP

In this appendix, we compare the measured force signal of the original SMP and the modified version used in our study. For simplicity, we denote the measured profiles as followed: μCPT profiles are measured with the modified SMP and SMP profiles are measured with the original setup. Fig. 3.10 shows two couples of SMP and μCPT profiles, which were measured within a distance of about 5 cm in one snow sample. The snow sample was made of large rounded grains, with a density of about 480±20 kg m^{-3} and a SSA of 14.38±0.9 m^{2} kg^{-1}. The maximal depth of the SMP profiles is the height of the snow sample. Small differences in the sample height are due to the sieving procedure. Comparing the first 35 mm of the profiles, we notice a higher force for the SMP profiles, than for the μCPT profiles. A clear difference between the profiles can be observed for depth larger than about 5 mm of penetration, where the rod touches in the snow. Above, no obvious difference is visible.

A more quantitative analysis was done by computing the mean and standard deviation on the first 5 and 25 mm of the profile. At a depth of about 5 mm, the SMP rod reaches the snow surface and its CZ could influence the measured signal. To get an information of the fluctuations of the force profile, we computed the mean of the macroscopic force, its standard deviation, and its correlation length ($C(0)/C'(0)$, with the two point correlation function C, [Löwe and Herwijnen, 2012]) over the two depth intervals. The results of these computations are shown in Tab. 3.2. For the computed properties over the first 5 mm, we observe a good agreement between the SMP and μCPT profiles. In contrast to this, the analysis over 25 mm depth

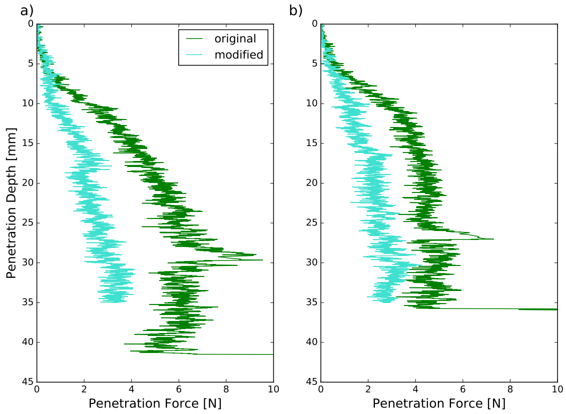

Figure 3.10: Penetration profiles measured with the original setup (SMP) and the modified setup (μCPT). The comparison was repeated for two couples of profiles (a and b). In one couple, the profiles were measured close to each other.

Table 3.2: Statistical calculations on the profiles of the SMP and μCPT measurements. The calculations were done over two different windows, the first 5 and the first 25 mm of the profile.

window	mean				standard deviation				C(0)/C'(0)			
(mm)	SMP		μCPT		SMP		μCPT		SMP		μCPT	
5	0.13	0.22	0.17	0.16	0.13	0.18	0.17	0.15	0.067	0.078	0.077	0.094
25	2.94	2.82	1.37	1.38	2.14	1.71	0.88	0.89	0.15	0.38	0.10	0.11

shows obvious differences between both measuring methods. Here, a clear influence due to the indentation of the SMP rod is observed. These results show that the extension seems to have no influence on the force sensor, as there were no remarkable differences in the signals for the depths where the rod did not touch the snow. In contrast, large differences in the measured profile were observed when the rod indented the snow, which might be enhanced by the limited depth of our samples.

3.A.2 Mathematical developments

In this appendix, we prove Eq. 3.4 and explain why $\widetilde{F}$ can be considered as stationary.

The general equation for the cumulant κ_n of order n of a signal, which can be described by a non-homogeneous shot noise process, is given by Campbell's theorem [e.g. Papoulis, 1991]:

$$\kappa_n(z) = \int_{-\infty}^{\infty} \lambda_z(\tau) f_z^n(z-\tau) d\tau \tag{3.8}$$

Furthermore, the auto-correlation C of the signal is given by [e.g. Papoulis, 1991]:

$$C(z, z+u) = \int_{-\infty}^{\infty} \lambda_z(\tau) f_z(z-\tau) f_z(z+u-\tau) d\tau \tag{3.9}$$

We now express $\lambda_z(z)$ a polynomial function $\sum_{m=0}^{M} a_m z^m$. Inserting the expression $f_z(z) = f/\delta \times \theta(z) \times \theta(\delta - z)$, where θ is the Heaviside function, into Eqs. 3.8 and 3.9, we obtain

$$\kappa_n(z) = f^n \delta \sum_{l=0}^{M} \left[\frac{\delta^l (-1)^l}{(l+n+1) l!} \frac{d^l}{dz^l} \left(\sum_{m=0}^{M} a_m z^m \right) \right], n = 1, 2 \tag{3.10}$$

$$C(z, z+u) = \frac{f^2}{\delta^2} \sum_{l=0}^{M} \left[(-1)^l \left(\frac{u(\delta - u)^{l+2}}{(l+2) l!} + \frac{(\delta - u)^{l+3}}{(l+3) l!} \right) \frac{d^l}{dz^l} \left(\sum_{m=0}^{M} a_m z^m \right) \right] \tag{3.11}$$

If the variations of the intensity over an interval of the size of δ are small compared to the mean intensity, all the terms with $l \geq 1$ in the above summation can be neglected. Equation 3.11 then simplifies to:

$$\kappa_n(z) = \frac{f^n \delta \lambda_z(z)}{n+1} \quad \text{and} \quad C(z, z+r, |r| < \delta) = f^2 \delta \lambda_z(z) \left(\frac{1}{3} - \frac{1}{2} \frac{|r|}{\delta} + \frac{1}{6} \frac{|r|^3}{\delta^3} \right). \tag{3.12}$$

Computing the cumulants and the correlation function of $\widetilde{F} = (F - \kappa_1(F))/\kappa_1(F)^{1/2}$ with Eq. 3.12, it appears that they are independent of z, which indicates that $\widetilde{F}$ is stationary.

3.A.3 Time evolution of the macroscopic and microscopic property profiles

This appendix provides the equivalents of Figs. 3.6 and 3.8 (corresponding to sample SSA18a above) for samples SSA18b, SSA14 and SSA10.

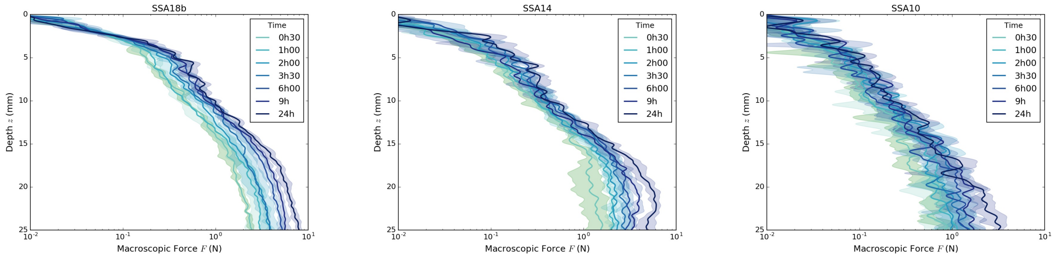

Figure 3.11: Evolution of the vertical profiles of the macroscopic force with time, measured on the samples SSA18b, SSA14 and SSA10.

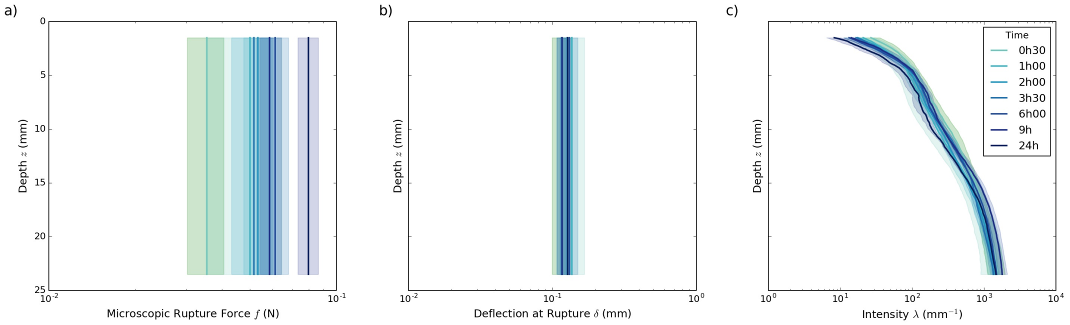

Figure 3.12: Time evolution of the profiles of the micromechanical properties estimated by the NHPP model on sample SSA18b. The shaded area around the curves represents the standard deviation obtained for the different profiles at one sampling time.

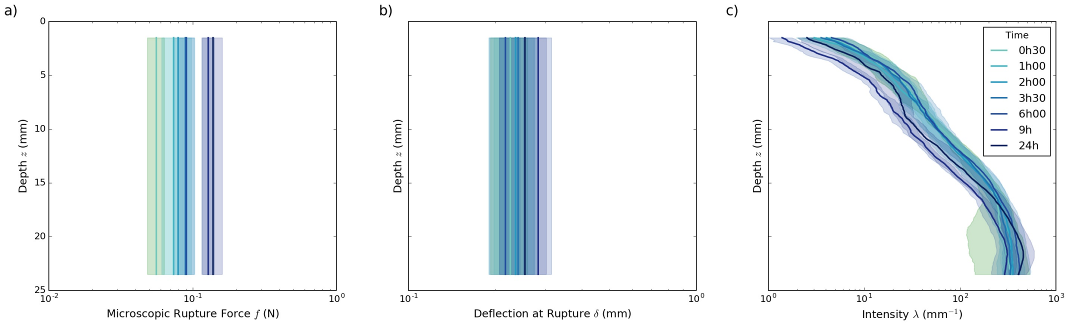

Figure 3.13: Time evolution of the profiles of the micromechanical properties estimated by the NHPP model on sample SSA14. The shaded area around the curves represents the standard deviation obtained for the different profiles at one sampling time.

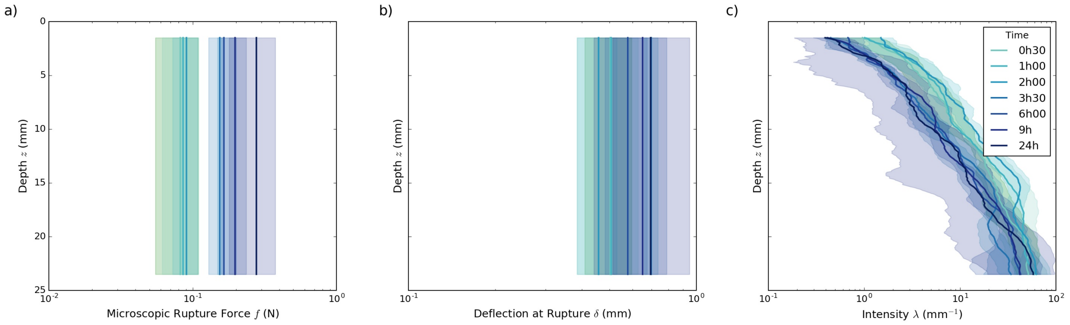

Figure 3.14: Time evolution of the profiles of the micromechanical properties estimated by the NHPP model on sample SSA10. The shaded area around the curves represents the standard deviation obtained for the different profiles at one sampling time.

4

Microstructural analyses of penetration tests for different applications

Contents

The previous chapter presented the NHPP (Non Homogeneous Poisson Process) model as an extension to the HPP (Homogeneous Poisson Process) model. This method was applied on a rather limited number of samples in order to study the sintering at microstructural scale. In this chapter, we will apply the NHPP to a larger range of measurement types. We used the NHPP model to analyse profiles measured in the field and during cold lab experiments on snow metamorphism. An additional section shows the application of the NHPP model to some experiments presented in Chapter 2.

4.1 Field measurements

The application of the NHPP to field measurements was done by comparing the HPP and the NHPP on two different snow profiles and analysing the differences and the similarities between the two methods. In addition to the traditional vertical profiles, horizontal profiles were measured in different homogeneous snow layers. A comparison of the estimated properties of the horizontal measurement and the ones from the corresponding layer of the vertical profile are presented.

4.1.1 Experiments and analysis

The experiments were conducted on the 25th of February (day 1) and the 17th of March 2016 (day 2) at Col du Lautaret, in the French Alps. For each day, measurements of SSA, density and SMP were performed in and next to a snow pit. SSA was measured with DUFISSS [Gallet et al., 2009] at a vertical resolution of about 5 to 10 cm with about 3 measurements at each height. The density measurements were conducted with a snow cutter of a volume of 250 cm^3 and a height of 2 cm. The resolution of the density profile was one to two centimetres. Several SMP measurements were taken for each pit but we will only present one example of these profiles. In addition to the SMP profiles, horizontal penetration tests were taken at different depths. To this end, the SMP was put on a table in front of the snow pit wall to assure a horizontal penetration (Fig. 4.1). The distance of the horizontal profiles to the SMP measurements were up to 30 cm. Due to the spatial variability of the snowpack, it is possible that the layers are not exactly corresponding in height [Kronholm et al., 2004].

The analysis of the hardness profiles was done with the NHPP and the HPP models [Löwe and Herwijnen, 2012]. We recall shortly the formulas here for the NHPP and describe then how they were applied to the measurements:

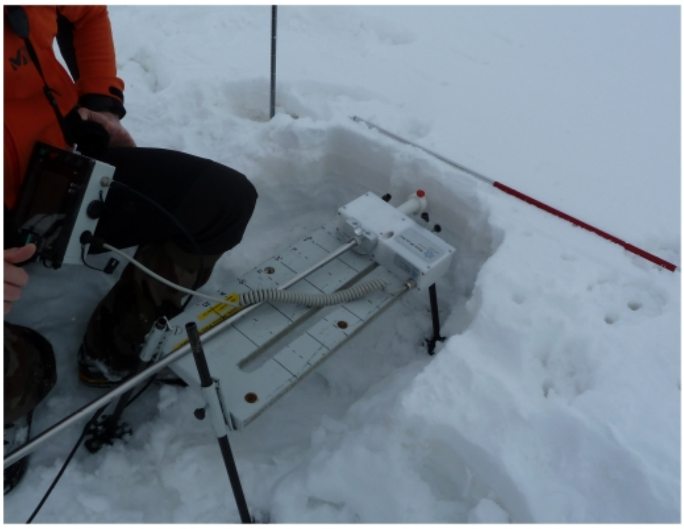

Figure 4.1: Photo of the measurement procedure used to record horizontal hardness profiles with the SMP.

We define a stationary force $\widetilde{F}$ as:

$$\widetilde{F} = \frac{F - \kappa_1(F)}{\kappa_1(F)^{1/2}} \tag{4.1}$$

This leads to the following equations for the micromechanical parameters:

$$f = \frac{3}{2}\overline{\widetilde{F}^2}, \qquad \delta = -\frac{3}{2}\frac{C(0)}{C'(0)}, \qquad \lambda_z(z) = \frac{4}{3\delta}\frac{\kappa_1(F)}{\overline{\widetilde{F}^2}} \tag{4.2}$$

where $\overline{\bullet}$ denotes the mean over depth, which was applied on a window of height w. The cumulant $\kappa_1(F)$ is the mean, which we approximate by the "depth" mean $\overline{F}$ calculated on a running window of width Δz. The HPP assumes all three micromechanical properties to be constant over the analysis window w and thus the signal is assumed to be stationary ($F = \widetilde{F}$). Equations 4.2 will be computed on a window w, while $\widetilde{F}$ is replaced by F and the cumulant is a simple mean over the depth of the window ($\kappa_1(F) = \overline{F}$).

For the micromechanical analysis of the profiles, we choose a window size (w) of 3 and 5 mm for the HPP. For the NHPP w equals to 5 and 10 mm, with a corresponding Δz of 3 and 5 mm, respectively. For the HPP, a larger window than 5 mm is not adapted, as it assumes a quasi-stationary signal. For the NHPP the assumption is that the properties of δ and f are constant over the window w, thus the analysis at a boundary of two different layers could be distorted for the larger windows. The values of w for the horizontal measurements were of 10 and 30 mm, as the signal is close to a stationary signal in one single layer. Here, the Δz for the NHPP was set to 5 mm for the smaller window size and 10 mm for the larger one.

4.1.2 Stratigraphy of the snowpack

Figure 4.2 shows the penetration profiles, the measured SSA and density values and the snow types. The two measured snowpacks show in majority melt forms and rounded grains. The profile of day 1 (Fig. 4.2a, b) can be divided in more and smaller snow layers, than the profile of day 2 (Fig. 4.2c,d). This can also be seen in the signal of the SMP, which shows more changes for day 1. Overall the SMP signal shows similar layers than the stratigraphy measured by hand. The layer interfaces are not always at the exact same depth due to the different spatial location of the measurements. Besides, the different layers are also distinguished by different values of SSA and density.

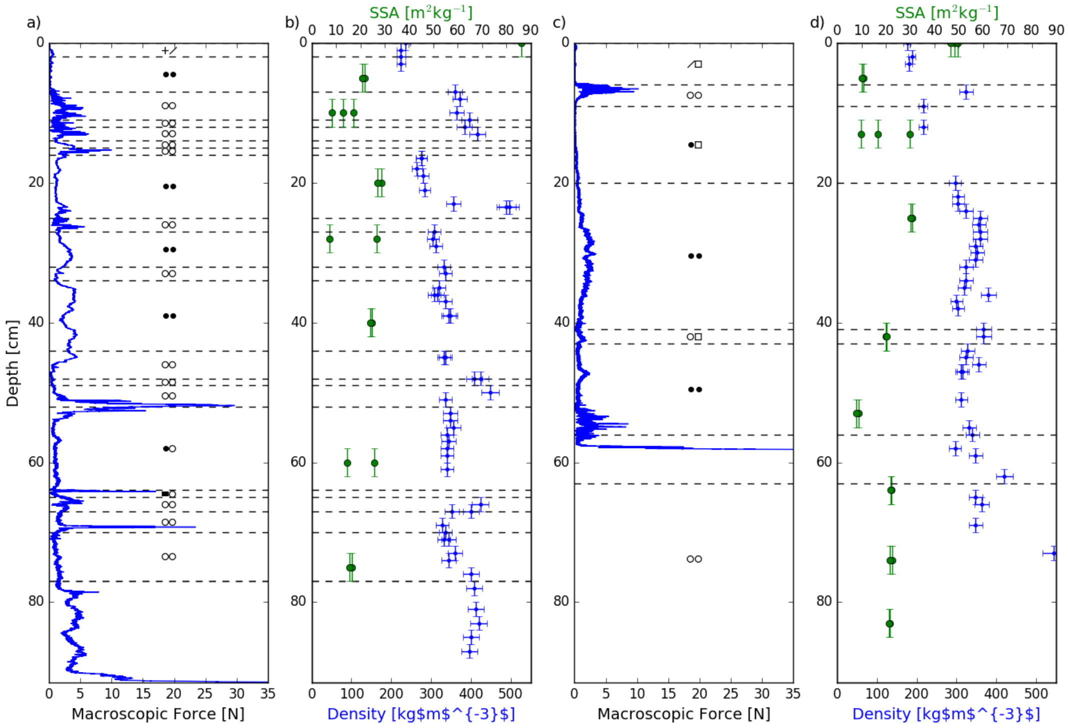

Figure 4.2: Stratigraphy measurements: (a,c) the SMP profile and the snow layers and types (observed by eye); (b,d) SSA and density measurements. The measurements were taken at two different days: 25/02/2016 (a,b) and 17/03/2016 (c,d) at Col de Lautaret in the French Alps. The symbols of the snow types are after Fierz et al. [2009].

Figures 4.3 and 4.4 display the estimated micromechanical parameters by the HPP and the NHPP for the two SMP profiles presented in Fig. 4.2. The estimated micromechanical properties, show as the profiles of SMP or by hand, much more layers and thus more changes in the properties for day 1. For larger layers (e.g. day one between approximately 50-65 cm or day 2: 10-20 cm) the micromechanical properties show only slight variations compared to the changes at layer interfaces: Within a layer the estimates show a factor up to 10 of two adjacent estimates, whereas at interfaces one or more micromechanical properties show changes in the values of 2 to 4 orders of magnitude. Nevertheless fluctuations and differences between the different methods are observed. For day 1 between about 11-16 cm we have detected 4 layers by hand and the SMP signal shows large fluctuations at these depths. The layers are almost as large as the analysis windows, thus it is hard to identify these layers on the profiles of the micromechanical properties. Contrary to this, clear interfaces like the one at about 6 cm at day 2 are represented in the micromechanical properties.

Comparing the NHPP and the HPP, we observe several differences: in general, the HPP seems to show more fluctuations than the NHPP, even in layers which are detected by hand to be homogeneous. For example at day 2 in layer between 20 and 40 cm the HPP shows up to a factor 3 between two neighboring estimated of δ and even a factor of 10 for f. Whereas the NHPP shows a maximal factor of 2 for both estimates. Apart from some exceptions, the differences between the two estimates with different window sizes are smaller with the NHPP than with the HPP. This indicates that the different window sizes seem to have a larger influence on the estimated parameters for the HPP than for the NHPP.

In order to better compare the different methods and window sizes, a zoom on a layer with its transition is done for each day (Figs. 4.5,4.6). At day 1 at 34 cm the increase of the force at the layer interface is represented with an increase in intensity for the NHPP, while the other two micromechanical properties (δ and f) show no obvious change (Fig. 4.5). The HPP displays at that depth an increase in the microscopic rupture force and a decrease in the intensity. After this transition of about 2 cm, the two methods show less differences in the estimated micromechanical properties. The increase in λ could be an indication for a built-up of a new CZ in the next layer. However, it may be possible that there are just more grains in that layer. The fluctuations within a layer, are mostly represented by a changing intensity for the NHPP. For the HPP, these force fluctuations are represented in all micromechanical properties. We observe smaller intensities for the larger windows in both cases, whereas the estimates of δ and f are increasing with window size. We cannot say at this stage which of the methods is better, as we have no clear reference of the properties in this layer.

The zoom between 4 and 22 cm on the profile of day 2 shows two complete layers with the beginning of their adjacent layers (Fig. 4.6). The first layer is positioned approximately between 6 and 8 cm and presents a higher macroscopic

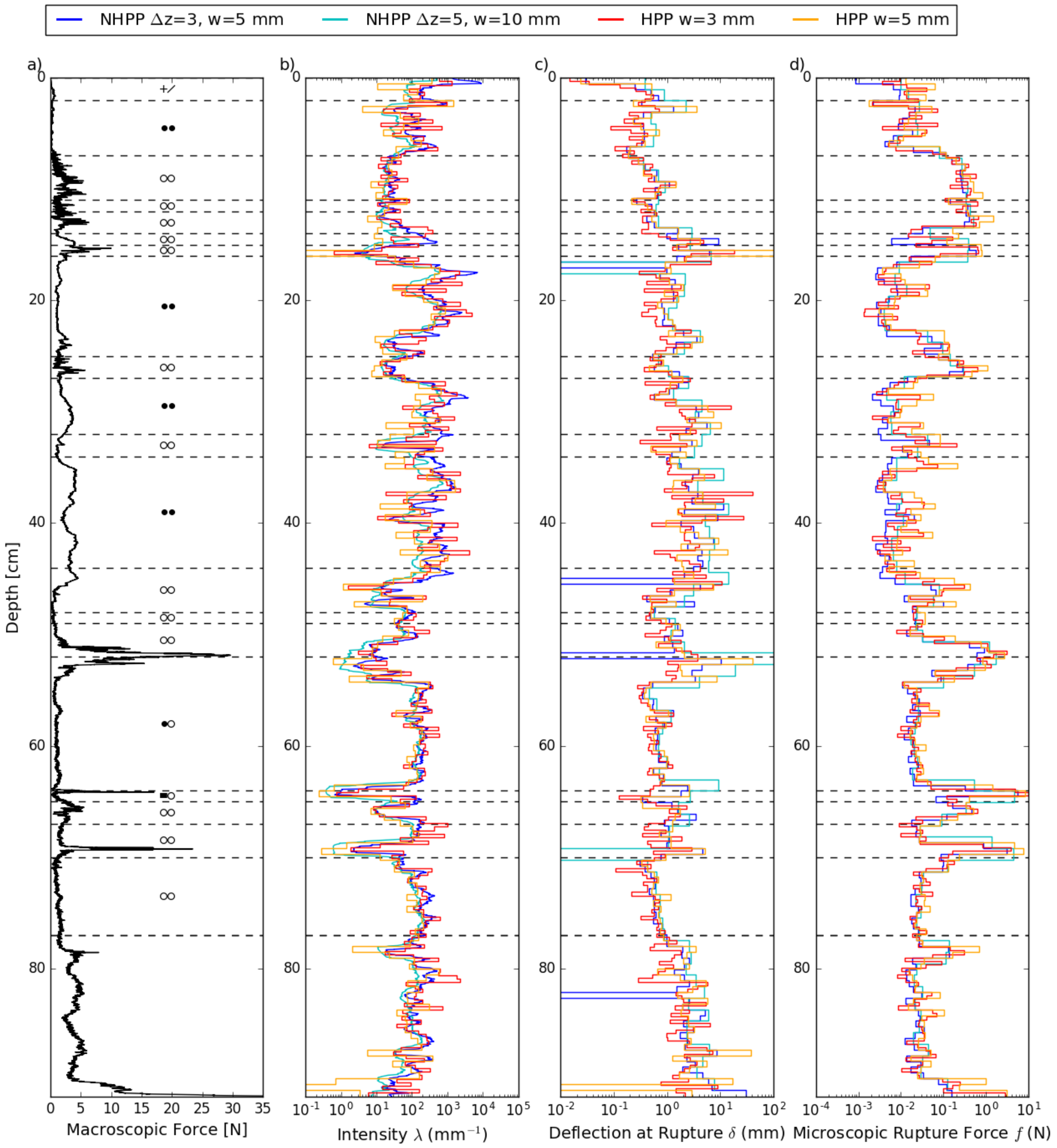

Figure 4.3: Micro-analysis of the SMP measurement at day 1: a) macroscopic force, b)-d) micromechanical properties estimated by the HPP and the NHPP for two different window sizes.

force with higher fluctuation compared to the neighbouring layers. The increase of the force at 6 cm is represented by a decrease in the rupture intensity and an increase in the two other micromechanical properties. We observe an earlier transition (i.e. decrease in λ and increase in δ and f) for the larger window of NHPP. The transition to the next layer (between 8 and 9 cm depth) is detected later for this window size. Inside this layer (between 6 and 8 cm, approximately) the values of the three values are estimated similar for the two window sizes of the NHPP. This is in general also the case for the HPP, although there are some

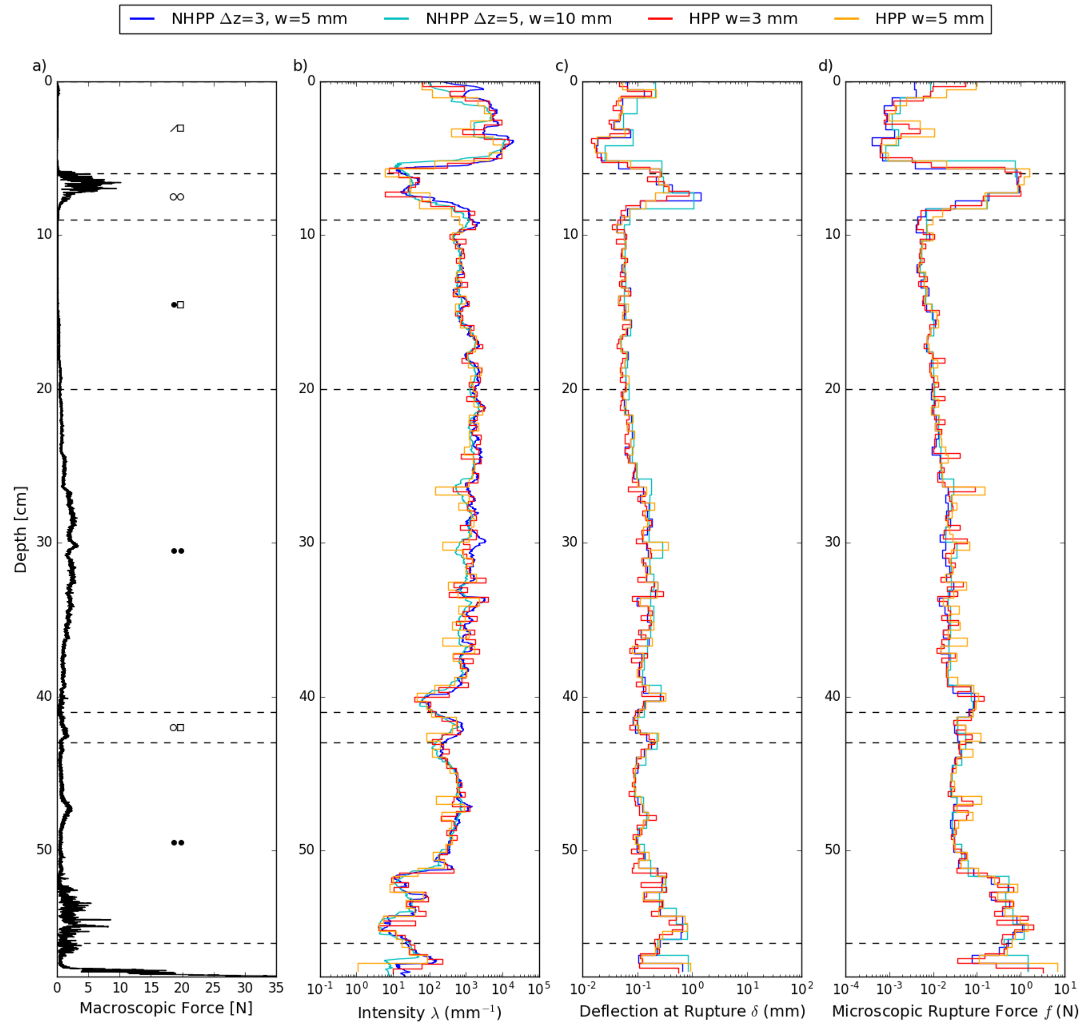

Figure 4.4: Micro-analysis of the SMP measurement at day 2: a) macroscopic force, b)-d) micromechanical properties estimated by the HPP and the NHPP for two different window sizes.

differences, for instance the intensity around 7 cm displays a factor of ten between the window of 3 and 5 mm. The second layer of this zoom (9-20 cm) shows a weak penetration force, which is enhancing slightly after 15 cm depth. All three micromechanical properties are virtually constant up to 15 cm and then the rupture intensity is slightly increasing on average. In this layer, the different methods (HPP and NHPP) and window sizes, do not show obvious differences. The interface to the next layer is an example where no clear transition is observed.

These analyses of the SMP profiles showed differences in the different methods (HPP and NHPP), but also for the different window sizes for the same method. The NHPP seems to predict estimates which are more constant within a layer, but

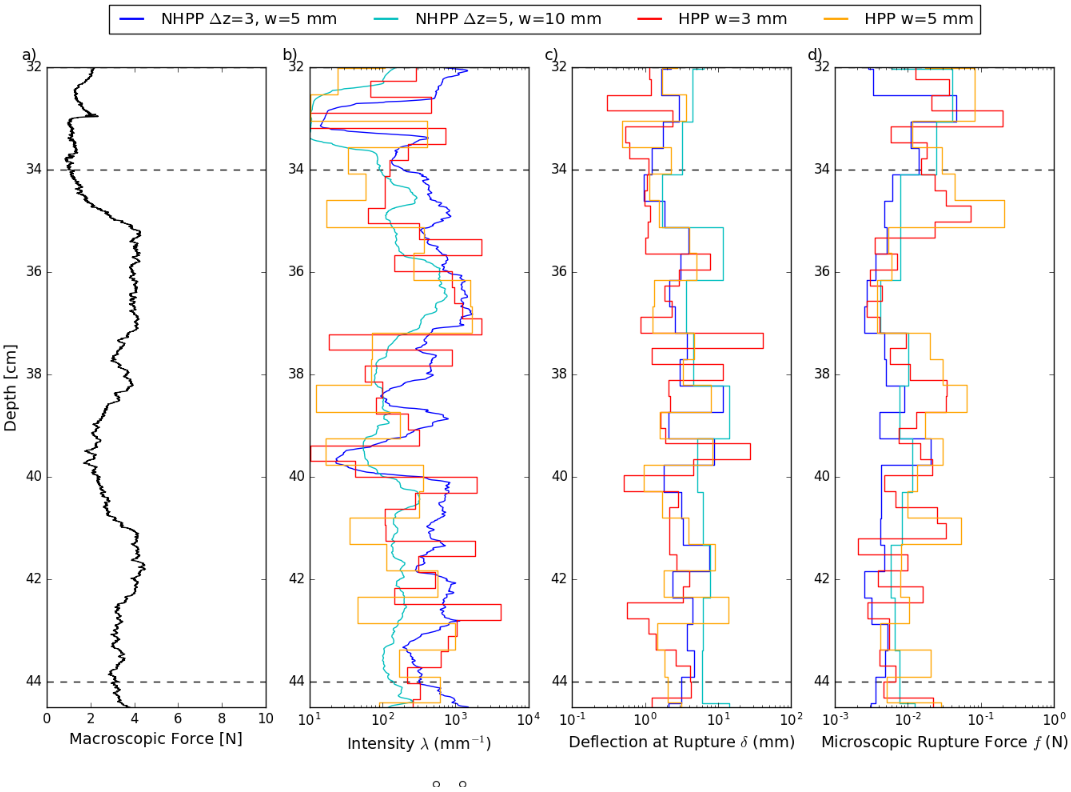

Figure 4.5: Micro-analysis of one layer of the SMP measurement at day 1: a) macroscopic force, b)-d) micromechanical properties estimated with the HPP and the NHPP for two different window sizes.

still strong differences between the two different window sizes are observed. The transitions between different layers are represented in changes of the estimates, but this is limited for small layers of about 1 cm. This analysis gives no information on the correctness of the values. Further analyses are required to evaluate the estimates properly. This is a quite challenging task, as no field measurements of the micromechanical properties exist to compare them directly.

4.1.3 Horizontal SMP measurements of selected snow layers

In this section we will present the horizontal SMP measurements, which we took at different heights of the snow pit. These horizontal measurements have the advantage, that they are in one layer and they should thus show a close to stationary signal. Nevertheless, some signals display not a stationary force over the whole penetration (e.g. Fig. 4.7).

For the close to stationary parts of measurement 243 and 218, the HPP and the NHPP estimated similar micromechanical properties (Fig. 4.7c-h). The strongest

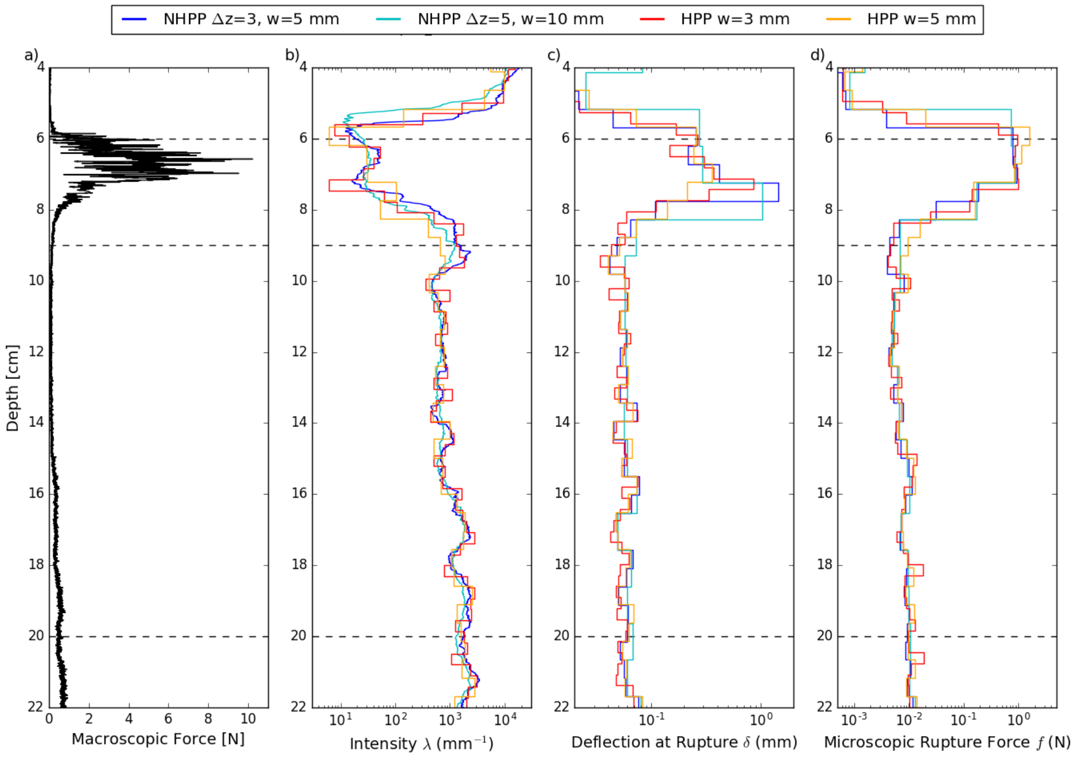

Figure 4.6: Micro-analysis of one layer of the SMP measurement at day 2: a) macroscopic force, b)-d) micromechanical properties estimated with the HPP and the NHPP for two different window sizes.

differences are observed for the intensity, as it is assumed to be constant in each window for the HPP and linear for the NHPP. The larger window of 30 mm shows very similar values for the two methods, which are almost constant for the stationary part of the signal. The advantages of the large windows are, that statistically the estimations are better. Indeed, Löwe and Herwijnen [2012] showed that small windows will lead to underestimation of f and δ and an overestimation of λ (also see Chapter 3). This statistical effect can be neglected for large windows as we chose here. So the measurements of the horizontal signal, can be chosen as reference for evaluate the vertical profiles. The interpretation still has to be done carefully: it only means that for these estimates no statistical bias exists.

4.1.4 Comparison of vertical and horizontal profiles

In order to evaluate the vertical SMP profiles, we compare them to the horizontal profiles. In practice, the reference value of one measurement is the mean of the estimated value over penetration distance and over the two methods. We decided to take the horizontal ones as reference, as the statistical bias of the window size

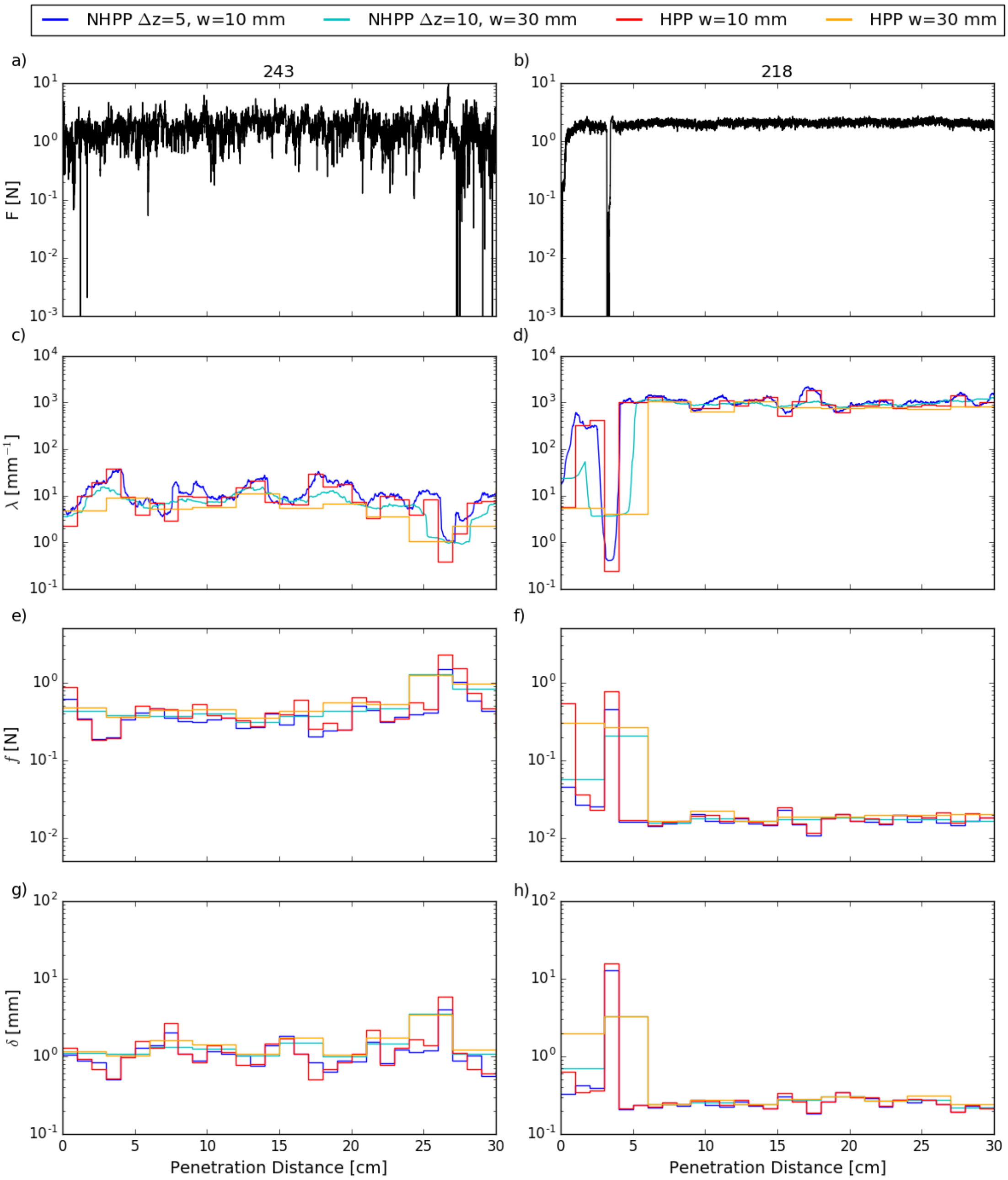

Figure 4.7: Micro-analysis of two examples of horizontal profiles: (a,b) macroscopic force, c)-h) micromechanical properties estimated with the HPP and the NHPP for two different window sizes.

should be negligible (as explained in the previous section). Here, only the sections of stationary signals of the horizontal measurements are taken into account. Then, we estimate the micromechanical properties on the corresponding layer in the profile. To this end, the HPP and the NHPP were applied on a layer of 5 cm height with its center at the height of the horizontal measurement. The height of 5 cm was taken in order to have a large enough signal to apply the HPP and

NHPP analyses and a short enough window to be sure to stay inside the layer. We assume that the estimates of the horizontal signal are the best values we could get, and thus take them as reference to compare them to the estimated values on the profile of the corresponding depth.

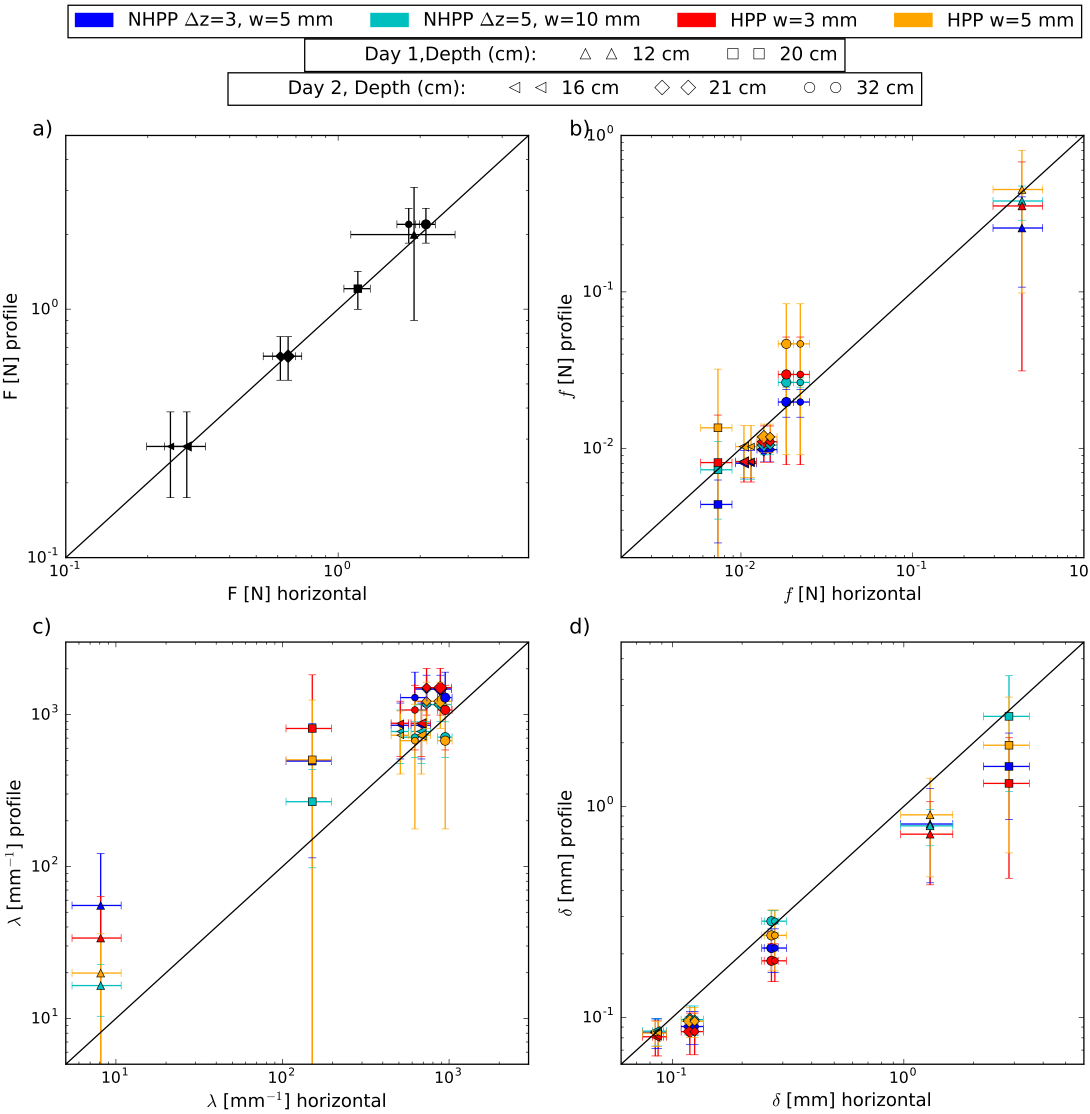

Figure 4.8: Comparison of the force and NHPP estimates of selected layers of the profiles to horizontal measurements of the corresponding layer: a) the force measurements, b) the microscopic rupture force, c) the mean rupture intensity, d) the deflection at rupture. Two measurements exists for each height for day two and are represented by different marker sizes.

The compared force of the horizontal and vertical profiles for the same layers are in good agreement (Fig. 4.8,a), thus we can assume that it is actually the same layer.

The estimates for the HPP show better results for micromechanical force f for the smaller analysis window for the layers at day 1 at 20cm and day 2 at

32 cm, whereas for the other layers the estimates of the larger windows are closer to the reference estimates (Fig. 4.8,b). The NHPP displays better estimates for f for the larger window for both layers of day 1, whereas the estimations of the two window sizes are similar on day 2. For the micromechanical force, the large window of NHPP shows the overall best estimations. This is also the case for the estimation of the rupture intensity λ (Fig. 4.8,c). The larger window sizes of HPP (or NHPP) in general predict λ better than the smaller ones. Usually, λ is overestimated, which corresponds to the observed overestimation for small window sizes on statistical signals [Löwe and Herwijnen, 2012]. The deflection at rupture δ shows an overall underestimation, which can also be linked to the statistical bias (Fig. 4.8d). In general, the larger windows show better estimates for both methods. Besides, the NHPP outperforms the HPP for the layer day 1 at 20 cm, whereas the HPP shows better estimates for the layer day 1, 12 cm. For the other layers, both methods provide similar estimates.

In almost all cases, the NHPP shows closer estimates to the reference values than the HPP. Except for some cases, the larger window of the HPP shows better results. Thus, it is difficult to define an ideal window size for the HPP, to have the best estimates for all three properties. Besides, the NHPP 10 mm shows the closest values to the reference for all three parameters. This good agreement can be interpreted as the absence of an influence of the window size on the statistical analysis. Nevertheless, 10 mm is quite large, as some layers have this size, so if the borders of the layers are not the ones of the window, the difference could not be seen.

4.1.5 Conclusion

In this section, we applied the HPP and the NHPP to SMP field measurements. In general, the NHPP showed less fluctuations of the estimated micromechanical properties within one layer. In addition to the classical SMP profiles, we collected horizontal SMP measurements for several layers. The latter ones had the advantage of having a relatively long quasi stationary signal. Thus, we can choose large analysis windows and consequently the statistical estimations would be better. Comparing these results to the micromechanical estimates directly on the profile showed best results for the estimation with NHPP with Δz=5 mm and w=10 mm. However, the micromechanical rupture force and deflection at rupture are supposed to be constant over the depth of w, so small layers may be overlooked, which is also the case for large w for the HPP. Larger windows may also result in slightly different localization of the transition between two layers. Thus, it would be interesting to perform analyses layer after layer, or chose the windows in a way that the window limits are identical to the limit of the layers.

4.2 Snow metamorphism

This section presents a characterization of snow metamorphism through cone penetration tests. To this end, SMP measurements were conducted during about three weeks on two snow samples. One sample evolved under isothermal conditions, while another one evolved under a temperature gradient. This work was conducted in collaboration with B. Poirier during his bachelor internship (18/01/2018 - 18/05/2018, école technologie supérieure, Montréal, Québec) at CEN, which P. Hagenmuller and I supervised.

4.2.1 Experiments and analysis

4.2.1.1 Experimental Set-up and Preparation

The experiments were conducted under controlled conditions in a cold room. The ambient temperature was set to -4°C with a relative humidity of about 50%. During 18 days, we observed the evolution of snow properties under isothermal and temperature gradient conditions. The temperature gradient was produced by two copper plates (Fig. 4.9, left, [Calonne et al., 2014]). The lower plate was set to -1°C and the upper one to -7°C, yielding a gradient of about 27 K m^{-1}. This is considered as a strong temperature gradient. The isothermal set-up consisted of a large box of polystyrene (Fig. 4.9, right). The dimensions of the two set-ups were about 50 x 100 cm with a height of about 20 cm. Further on, the two samples are denoted TGM for the temperature gradient set-up and ISO for the isothermal set-up. The two set-ups were equipped with PT-100 temperature sensors located on their inner surface on the bottom and top of the experiment to monitor temperature trend throughout the experiment (see in 4.A.1, Fig. 4.18).

The snow used for our experiments was composed of precipitation particles and decomposing and fragmented precipitation particles [PP/DF, Fierz et al., 2009]. It was collected one week before the measurement at the Col d'Ornon (1367 m) in the French Alps at -4°C in windless and cloudy conditions and then stored at -20°C. The density during sample collection was about 100 kgm^{-3}. For the experiments, a snow height of about 22 cm was sieved directly into the containers of the TGM and ISO set-ups. It was done at a temperature of -10°C with a sieve size of 4x6 mm. Afterwards, the temperature was slowly increased to -4°C.

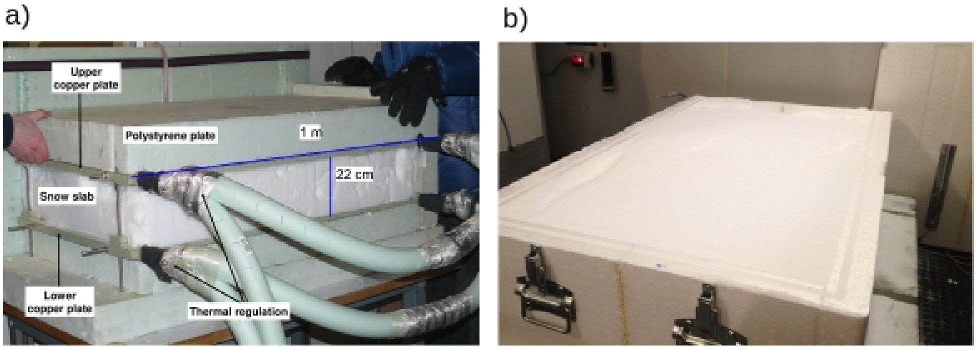

Figure 4.9: Photo of the experimental setup: a) Temperature gradient (TGM) sample Calonne et al. [2015], b) the isothermal (ISO) sample.

4.2.1.2 Measurements

During the whole period, measurements of SMP, specific surface area (SSA) and density were conducted. SSA measurements were conducted with DUFISSS [optical method, Gallet et al., 2009] and density measurements with a rectangular snow cutter with a volume of 250 cm^3 and a height of 2 cm. A complete measurement consisted in three SMP tests, three SSA and four density measurements (see Fig. 4.10). The SSA and density were measured at different heights. A minimal distance of 8 cm was chosen between the SMP measurements. Additionally, microscopy images of the snow grains were taken to follow the shape of the grains.

Directly after sieving, first SMP tests were conducted. After a rest time of 40 hours the first complete measurement was taken and continued on a daily rhythm (on week days). The rest time of 40 hours was chosen to decrease effects of sintering, which are the strongest into the first 10 hours after sieving, approximately [Herwijnen and Miller, 2013, Peinke et al., 2019]. This time was also necessary to attain a stable temperature in the ISO set-up.

4.2.1.3 Microstuctural analysis

The SMP profiles were analysed with the NHPP (Eqs. 4.2). To this end, we approximate $\kappa_1(F)$ by the "depth" mean calculated on a running window of width Δz=3 mm. The depth mean $\overline{\tilde{F}}$ was applied on the profile height divided by height. This was done in order to have always the same number of layers, as a packing of the snow layer was observed. This led to eight values of the deflection at rupture δ and individual rupture force f. The λ was a continuous estimation with

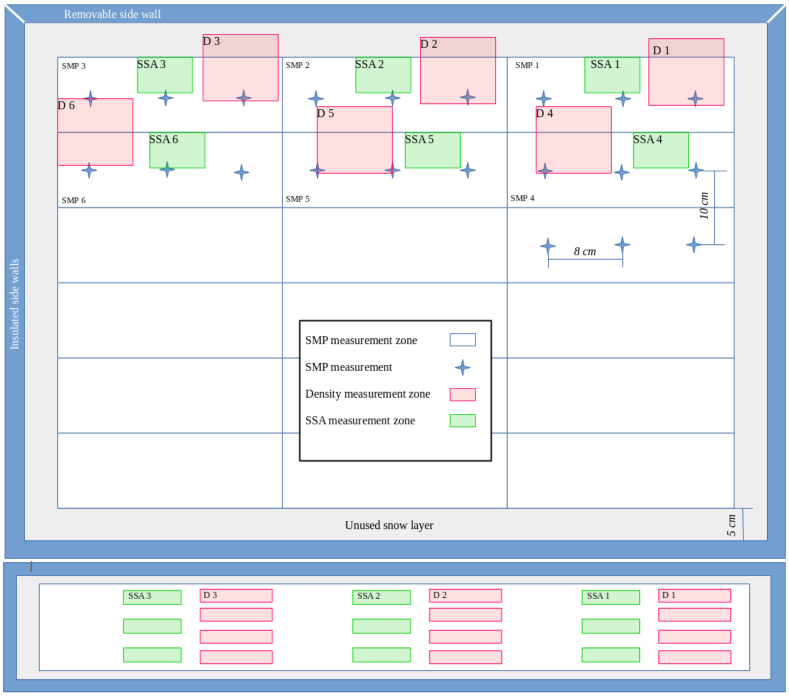

Figure 4.10: Scheme of the locations of the measurements: The upper one shows a view from the top and the lower one a front view of the horizontal measurements.

height. For visualization, we took means of the micromechanical properties for the different measurements at each time and over two layers. Thus, we will present measurements for 4 different heights for each day.

4.2.2 Time evolution of density and SSA

The density for both experiments is increasing with time, while the SSA is decreasing (see Fig. 4.11). Besides, we observe higher densities at the bottom, with a smaller stratification for isothermal conditions. The ISO sample does not show a meaningful SSA evolution along depth. This is similar for the TGM at the beginning of the measurements, but after about 14 days it displays higher SSA values close to the surface. In general, the ISO and TGM display similar SSA values at the beginning, but the TGM decreases faster.

4.2.3 Evolution of the penetration force

The force averaged over the profiles increases with time under isothermal conditions (Fig. 4.12a,c). This force increasing is less pronounced close to the surface than in deeper depths. In contrast to this, the measured force in the TGM shows no obvious change during the first four days, which is followed by a drop in penetration force between day 4 and 7 (Fig. 4.12b,d). Afterwards, we observe a

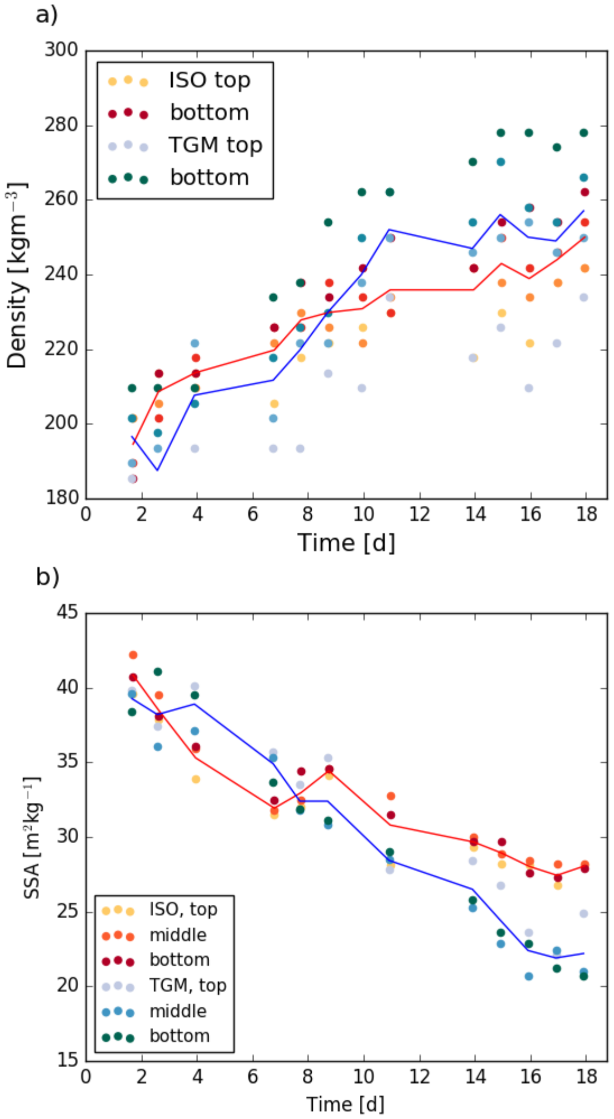

Figure 4.11: Time evolution of the density (a) and the Specific Surface Area (SSA, b). Under isothermal conditions (red to orange) and under temperature gradient (blue/green). The dots represents the measurements at different depths and the curves show the mean evolution of the properties over depth for the ISO (red) and TGM sample (blue).

slight increasing during five days and then the force is almost constant (day 14 to 18). For the two different conditions, we observe an increasing force with depth. This difference is slightly increasing with time and shows a similar magnitude for the two conditions. Besides, the two set-ups provide a decrease in profile height with time reflecting the observed densification.

4.2.4 Microstructural analysis (NHPP)

The time evolution of the estimated micromechanical properties are displayed in Fig. 4.13. The microscopic force f increases with time for the two set-ups

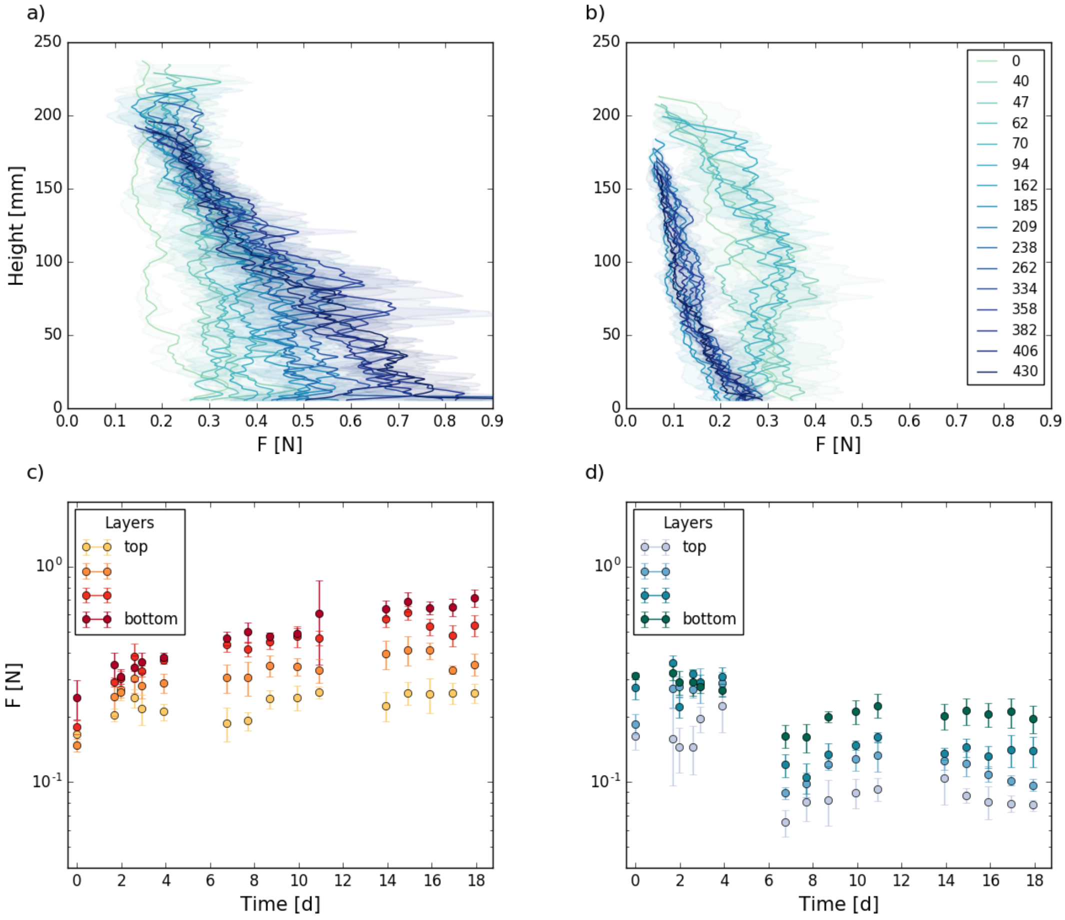

Figure 4.12: Measured force profiles (a,b) and time evolution of the depth-averaged force (c,d). Left are the results of the ISO sample and right the TGM sample. The legend shows the time in hours.

(Fig. 4.13 a, b). This increase is slightly higher under isothermal conditions. Additionally both set-ups exhibit higher values of f in deeper layers. While the deflection at rupture shows no obvious trend for the ISO sample, it shows an increase with time for the TGM (Fig. 4.13 c, d). The evolution with depth is not obvious, but a tendency of higher δ in deeper depths is observed, especially after some days of experiments. The rupture intensity λ is decreasing for both samples with time (Fig. 4.13 e, f). For the TGM this decrease is stronger and continuous with time. After about eight days, the intensity shows higher values close to the surface. The decrease for the ISO sample consists in a drop of the intensity between the first two measurements, followed by a slight decrease. The intensity show no clear tendency with depth.

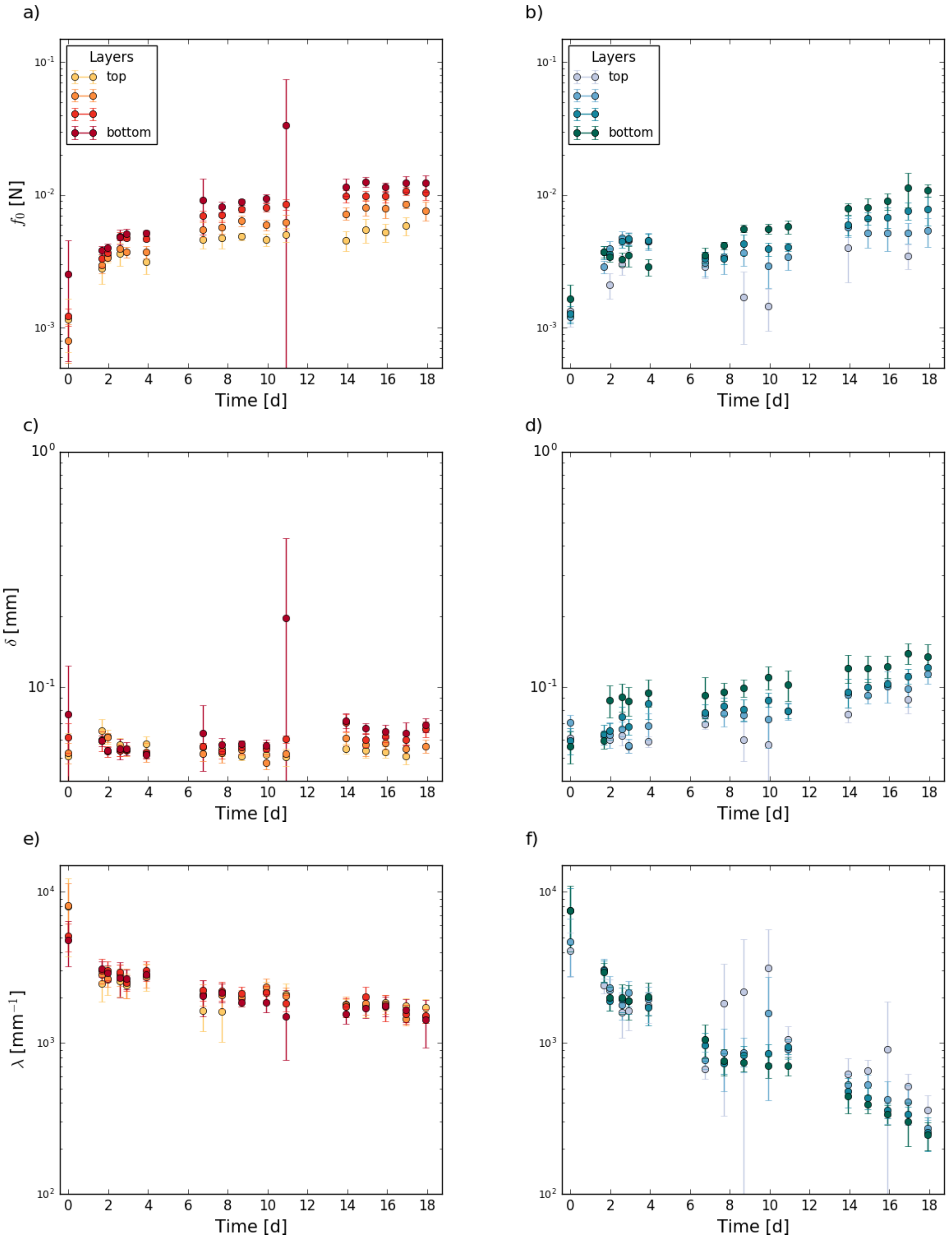

Figure 4.13: Time evolution of the micromechanical properties: a,b) micromechanical rupture force f, c,d)deflection at rupture δ; e,f) mean rupture intensity (λ). Left are the results of the ISO sample and right the TGM sample.

4.2.5 Discussion and conclusion

The time evolution of density and SSA is in agreement with literature [e.g. Taillandier et al., 2007, Calonne et al., 2014]. The stratification of the density is likely due to the overburden snow [e.g. Chandel et al., 2007]. Let us recall here that the interest of this study is to investigate the evolution of the micromechanical properties, which were estimated by the NHPP. To this end, we assume that the estimated micromechanical properties are proxies of the physical property, e.g. an increase in f is interpreted as a strengthening of the bonds.

The results of the microscopic analysis of the ISO sample show that the macroscopic force evolution with time and with depth are governed by the corresponding changes in the microscopic force. For both the macro- and the microscopic forces, an increase with time and depth are observed. The other two micromechanical parameters (λ, δ) do not display such clear links to the macroscopic force. The rupture intensity even shows a decrease with time. These results let us conjecture that the main change is a strengthening of the bonds with time, which is enhanced at deeper depths. This could be due to an additional force due to the overburden weight of the snow. Indeed, it is known that pressure between grains can accelerate various sintering mechanisms [e.g. Flin and Brzoska, 2008].

The TGM sample displays obvious changes for all three micromechanical parameters with time. Thus, the macroscopic force is not governed by only one micromechanical property unlike in the ISO sample. The force signal underwent a drop between day 4 and 7, followed by a slight increase. In the micromechanical properties this drop is not very clearly pronounced. The microscopic force and the deflection at rupture stay almost constant between these two measurements. Only the intensity displays an obvious decrease. At day 7 the first faceted snow grains were observed in the microscopy images. Later on (after day 7) the macroscopic force is slowly increasing with time. This increase can also be observed in the microscopic force and the deflection at rupture, while the intensity is still decreasing. From these results, we conjecture that the faceting of the grains leads to a diminution of the number of bonds while the bonds themselves are not weakening. A higher deflection at rupture could be due to a growth of the snow grains.

This behaviour of the micromechanical properties give a new insight to the evolution of the bond properties with time. In general a bond strengthening is observed for isothermal and temperature gradient conditions. The temperature gradient seems to lead to a vanishing of bonds. Nevertheless, this interpretation of the results has to be treated with caution, as the NHPP is not completely validated yet and only provides proxies of the bond physical properties. A verification of these results by comparing them to micro tomographical imaging would be interesting.

4.3 Application to sensitivity analysis

In this section, the goal is to estimate the influence of the cylinders, the different cone tips and cone tip size on the NHPP estimates. To this end, we apply the NHPP to some of the experiments studied in Chapter 2, where we already studied the signals of these experiments. One scope of this section is to point out these changes in order to be aware of these influences for later analyses of the signals.

4.3.1 Experiments

The experiments, presented here, were the same as the ones for the sensitivity analyses of chapter 2. A detailed description of the experimental set-up and the snow properties is shown in Sec. 2.2. Let us recall that we did measurements with three different set-ups: SMP, μCPT and tomoCPT, which were conducted in DF snow and an additional comparison of SMP and μCPT were done in a sample of RGlr. The μCPT with the different tip sizes and the cylinders were done in an RGlr sample.

The different measurements were analysed with the NHPP (Eqs 4.2). To this end, we approximate $\kappa_1(F)$ by the "depth" mean calculated on a running window of width Δz=3 mm. The depth mean $\overline{\widetilde{F}}$ was applied on the indicated height.

4.3.2 Results and discussion

The micromechanical properties of the conducted measurements in DF were analysed on a depth of 24 mm and on a zoom on the first 4 mm (Fig. 4.14). Let us recall that there is no geometrical difference in the three set-ups for the first 4 mm. The intensity is the highest for the tomoCPT for both depths, but this difference is less pronounced for the first 4 mm (Fig. 4.14a). The SMP and μCPT show no obvious differences for the estimated rupture intensity. The microscopic rupture force shows no obvious differences between the three set-ups for both analysed lengths (Fig. 4.14,b). The largest differences are in the predicted δ, which is the highest for the SMP, than μCPT and tomoCPT (Fig. 4.14,c), this differences are also strong for the first 4 mm.

The comparison of the estimated micromechanical parameters for the μCPT and SMP measurements in RGlr (Fig. 4.15) shows similar differences for the estimates than in DF. Despite some exceptions the NHPP predicts similar micromechanical properties for the first 4mm of the SMP and μCPT measurements. Only, the estimated δ of the μCPT differs to the other tests.

The NHPP was applied on the first 24 mm of the μCPT with different tip sizes (Fig. 4.16). The analysis shows a slight increase in intensity between the 4 and

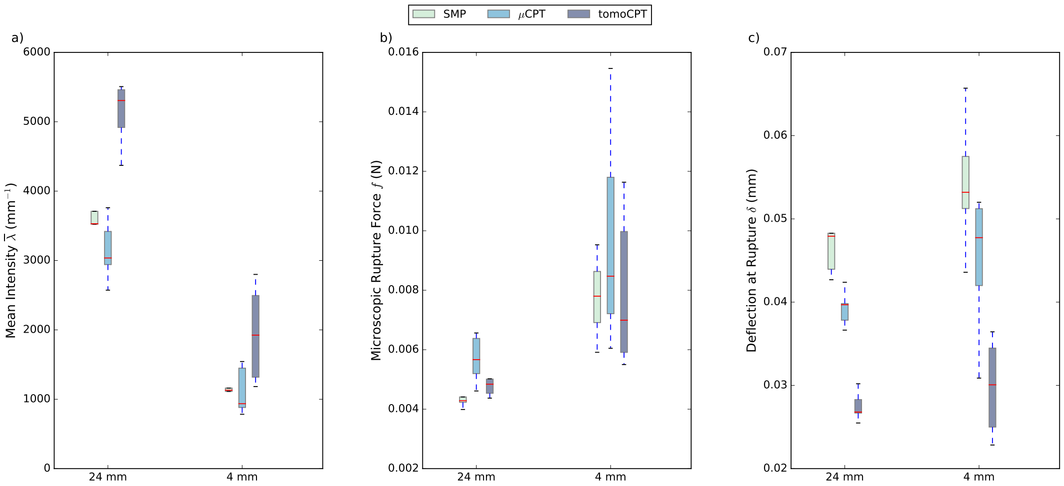

Figure 4.14: Micromechanical properties of different set-ups (SMP, μCPT and tomoCPT), estimated with the NHPP: a) the intensity, b) the microscopic force and c) the deflection at rupture. The penetration force measurements were conducted in the sample snowDF after one day of rest.

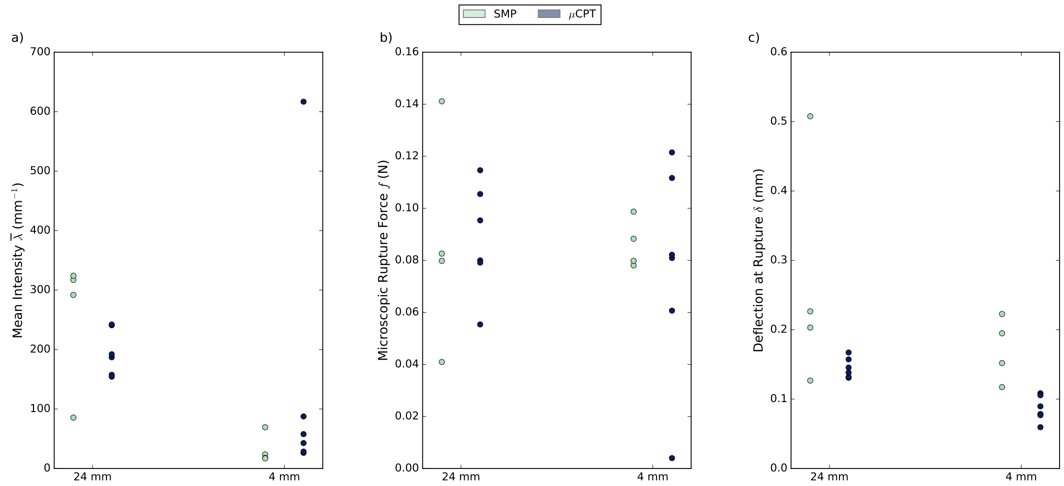

Figure 4.15: Micromechanical properties of different set-ups (SMP and μCPT), estimated with the NHPP: a) the intensity, b) the microscopic force and c) the deflection at rupture. The penetration force measurements were conducted in the sample snow10 after 2 days of rest.

5 mm tips but no obvious change between the 5 and 8 mm tips. Besides, the tip size seems to influence more the properties f and δ than λ, but shows no clear size effect, as the smallest values are predicted for the original tip. These results are not straightforward, as we could conjecture that a larger cone should only lead to a higher intensity, e.g. more broken bonds per penetration step. For a correct prediction of the NHPP, the size of the cone tip should not change the rupture

properties f and δ. The differences of the small and large tips compared to the original tip could be due to the different half cone angles (40° and not 30°), but even the two cone tips with the same cone angle show a change in f and δ.

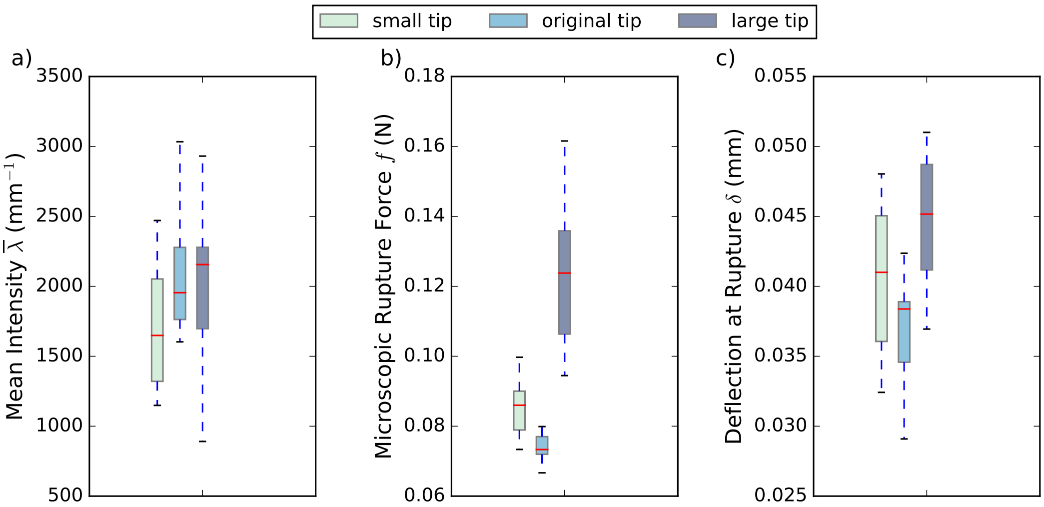

Figure 4.16: The micromechanical properties obtained with the NHPP for three different tip sizes with diameters of 4, 5, and 8 mm: a) the intensity, b) the microscopic force and c) the deflection at rupture. The NHPP was applied on the first 24 mm of the measurements, conducted in sample snow8 after a rest time of 4 days at -20°.

The presence of the cylinders leads to a decrease in the estimated intensity (Fig. 4.17), which is stronger for the smaller cylinder. The other two properties are clearly influenced by the small cylinder, but not by the large one. A slight increase in δ is observed for the measurements in the large cylinder, compared to the reference measurements. This may be explained by a limited horizontal expansion of the CZ in the cylinder, and thus less bonds that break. Another possible source of the differences in the estimated parameters can be due to the insertion of the cylinders, as we have no proof if and how this changes the snow structure.

4.3.3 Conclusions

This section showed that the different set-ups, tip sizes, and cylinders showed influences on the micromechanical properties estimated by the NHPP. For the microscopic rupture force, no notable differences for the SMP and the μCPT are observed, while the mean intensity is slightly changing as well as the deflection at rupture. Assuming the values of the NHPP as correct estimate for the micromechnical properties, the rod of the SMP seems to influence the deflection at rupture and their occurence rate, but not their rupture force. A larger tip diameter impacted

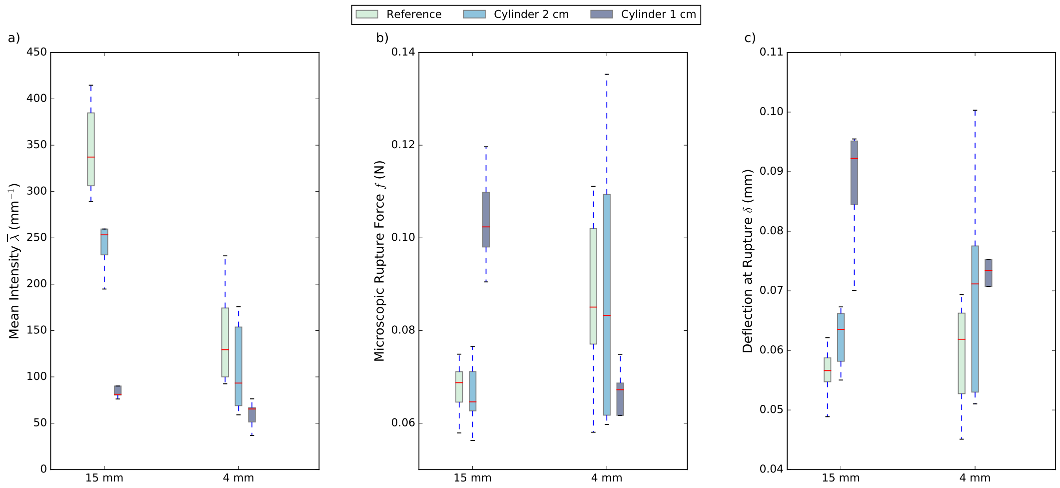

Figure 4.17: The micromechanical properties obtained with the NHPP in cylinders of 1 and 2 cm in diameter and close to the cylinders: a) the intensity, b) the microscopic force and c) the deflection at rupture. The measurements were conducted in sample snow8 after two days of rest.

all three micromechanical properties, with no clear size effect. In theory we would expect, that only the mean rupture intensity increases with diameter size, which is not the case. This does not necessarily mean that the NHPP is not correct. The force signal could be changed due to the different tips. Maybe the large tip is too large to detect all the ruptures. The larger cylinder of 2 cm influenced especially the mean intensity, while the small cylinder influenced all three estimates. It is not obvious to find the source of these changes. Nevertheless, this study gives us indications for the interpretation, especially for the cylinders. It can be interesting for the later analysis of the microtomographical measurements.

4.A Appendix

4.A.1 Snow metamorphism

Here we will give the temperature during the experiments as additional data (Fig. 4.18). In both set-ups we measured the temperatures at the tip and the bottom of the boxes (TG up iso up and TG down, iso down). The fluctuations in the upper temperatures are due to the removing of the lids in order to conduct the measurements. About at day 12 the cold chamber had a problem and the ambient temperature increased, but we can see that this had only a small influence on the temperature in the isothermal set-up and almost no influence for the TGM.

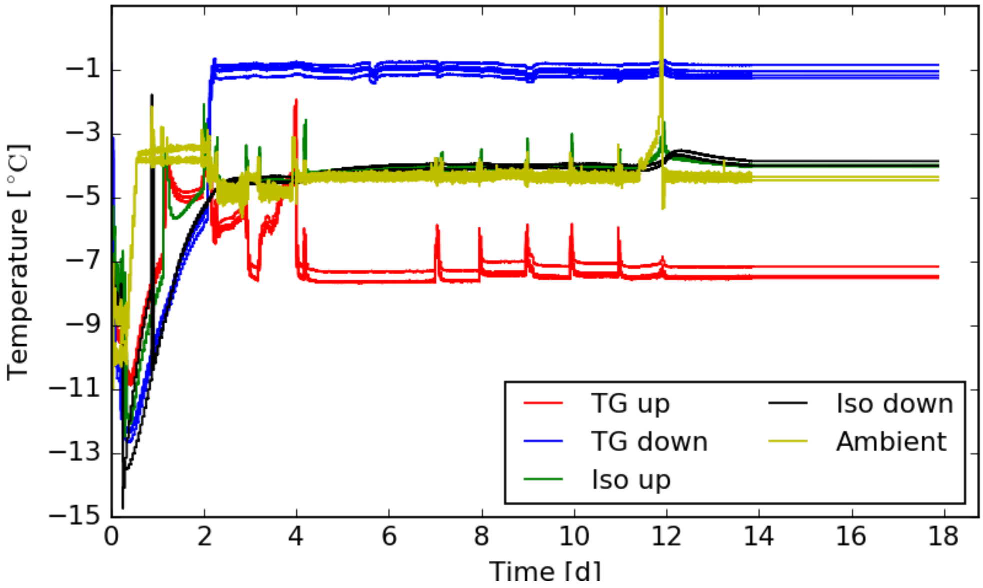

Figure 4.18: Temperature measurements during the experiments of snow metamorphism. These measurements were done at the bottom and top of the temperature gradient (TG) and of the isothermal sample (iso). Also measurements of the ambient temperature are shown.

5

Experimental study of cone penetration in snow using X-ray tomography

Contents

Abstract

The cone penetration test is widely used to determine the mechanical properties of snow and to delineate snow stratigraphy. Precise knowledge of the snow stratigraphy is essential for many applications such as avalanche forecasting or estimating the snowpack energy budget. The cone penetration test remains one of the only objective methods to measure snow stratigraphy and is becoming more sophisticated with the development of high-resolution digital penetrometers such as the SnowMicroPenetrometer. An accurate interpretation of the measured hardness profiles requires to understand the interaction between the cone tip and the snow material. In this study, we measured the displacement induced by the penetration of a conic tip with a radius of 2.5 mm in eight different snow samples using X-ray tomography. The experiments were conducted at a temperature of -10°C. To recover the full three-dimensional displacements between the tomographic images measured before and after the test, we specifically designed a tracking algorithm which exploits the unique shape of each snow grain. The measured displacements are shown to be oriented downwards below the tip apex, upwards close to the snow surface, and nearly only radially in between. We observed and quantified the development of a compaction around and below the tip. Surprisingly, we also observed dilation of the snow material close to the snow and tip surfaces in very high-density samples. The radial extent of the compaction zone ranged between 1.6 and 2.3 times the tip radius. The observed deformation field was compared to existing models of cone penetration, which gives new insights on their limitations.

Keywords: snow, cone penetration test, CPT, DIC, grain tracking, X-Ray tomography

5.1 Introduction

The cone penetration test (CPT) is widely used to determine the geotechnical engineering properties of soils and to delineate soil stratigraphy. This test consists in driving an instrumented tube with a conic tip into the ground and recording the forces required for penetration. In general, the recorded forces can include cone penetration resistance, sleeve friction and pore pressure [e.g. Schmertmann, 1978, Mayne, 2007]. Many investigations aimed to establish a frame to interpret CPT results. Most of them are based on empirical relations [Mayne, 2007]. For instance, Robertson [2009] developed soil classification charts using the cone resistance and friction ratio based on empirical relations. Theoretical approaches have also been proposed and provided a useful framework of understanding. In particular, Bishop et al. [1945] introduced the cavity expansion model (CEM) to retrieve the material properties of clay and sand from a CPT. Many of the current CPT inversion models in soil mechanics derive from this initial model, due to its ease of implementation and capability of describing elastic and plastic material deformation during CPT [e.g. Yu and Mitchell, 1998, Ruiz et al., 2016]. However, M. Baligh [1986] showed that the CEM does not correctly account for the strain paths followed by soil elements, which could lead to inconsistencies in the subsequent test interpretation. Many studies have thus investigated the strain and stress paths at specific locations in a soil around a penetrating tip [e.g. White and Bolton, 2004]. More recently, a full three-dimensional analysis of the deformation field was proposed by Paniagua et al. [2013] using X-ray tomography and digital image correlation.

The CPT was first used for snow with the ramsonde in the 1930's [Bader et al., 1939]. The ramsonde is a very simple and robust probe driven into the snow by mechanical hammer blows on its top. It is commonly used, e.g., by the observers of avalanche warning services to record snow hardness profiles. Ramsonde profiles provide an overall indication of snowpack structure, which can be used, for instance, to classify the snowpack as either potentially stable or potentially unstable with respect to avalanche release [Schweizer and Wiesinger, 2001]. More recently, several digital snow penetrometers have been developed to overcome the limited resolution of the ramsonde, e.g. the SnowMicroPenetrometer [SMP, Schneebeli and Johnson, 1998], the SABRE penetrometer [Mackenzie and Payten, 2002], or the SP2 [Avatech, see Hagenmuller et al., 2018a]. In addition, digital penetrometers initially designed for soils were also directly used to characterize the snowpack stratigraphy in Antarctica [McCallum, 2014]. These instruments accurately determine the penetration resistance of very fine layers and are able to capture numerous stratigraphic features of the snow cover [e.g. Pielmeier and Schneebeli, 2003]. They can generally detect the presence of a weak layer of snow below a cohesive slab, which is an avalanche prone configuration [Hagenmuller et al., 2018a]. Reuter et al. [2015] derived promising quantitative indicators of snowpack stability directly from a SMP profile. Proksch et al. [2015] estimated the main snow structural parameters, namely density, correlation length, and specific surface area (SSA), solely from SMP profiles.

Snow differs from typical soils in two main aspects. Firstly, compared to soils, snow is a very fragile and porous material with a void ratio up to 90%. Thanks to the resulting low resistance, the cone penetration tests in snow can be performed at a constant speed (driven by a light-weight motor) with a small conic tip. Typically, the size of CPT tip radius in snow is of a few millimeters, and the typical snow grain size is about 0.1 to 1 mm. The penetration resistance is measured at high resolution in terms of force (around 0.01 N for the SMP) and vertical position (around 4 μm for the SMP) [Hagenmuller and Pilloix, 2016]. The high-frequency fluctuations of penetration force with depth contain valuable information about snow microstructure, as they are directly linked to failure at bond scale [e.g. Löwe and Herwijnen, 2012]. Secondly, snow exists on Earth at a high homologous temperature. Its mechanical behavior is therefore highly rate-dependent because of very rapid sintering processes and ice viscosity [e.g. Blackford, 2007, Peinke et al., 2019], in contrast to typical soils. In general, CPTs in snow are conducted with a penetration speed of a few centimeters per second. At this speed, snow mechanical behavior can be assumed to be brittle and quasi-static [Narita, 1984, Floyer and Jamieson, 2010].

Several specific models were proposed to interpret CPTs in snow [e.g. Johnson and Schneebeli, 1999, Marshall and Johnson, 2009]. Löwe and Herwijnen [2012] used the framework of Homogeneous Poisson Processes (HPP) to relate the measured force signal to the mechanical properties of individual bonds between snow grains. In particular, they assumed that the overall penetration force results from the superposition of spatially uncorrelated ruptures. These ruptures are supposed to be elastic brittle and to occur at the contact with the cone tip. This approach was generalized to the case of spatially inhomogeneous rupture intensities by Peinke et al. [2019]. Ruiz et al. [2017] applied the cavity expansion model (CEM) to analyse CPT in snow and to derive the elastic modulus and yield strength of the material.

These two classes of models are based on very different approaches. On the one hand, the CEM considers snow as a continuum material and describes the cone penetration by the formation of a cavity, with elastic and plastic zones surrounding the cavity. Further, only radial forces acting on the cone tip are considered. The typical cone-to-grain ratio for the SMP in snow is in the range 5-50 [Herwijnen and Miller, 2013], while after Bolton et al. [1993], the continuum media assumption reaches its limit for a ratio lower than 20. On the other hand, the HPP model aims to identify the contribution of individual bond ruptures occurring directly next to the tip. This model accounts for the discrete nature of bond failures. However, experimental studies showed the formation of a significant compaction zone (CZ) around the cone tip [e.g. Herwijnen, 2013, LeBaron et al., 2014], which challenges the assumptions of the HPP model. In particular, the effective radius of the cone tip is increased by the CZ, and the rupture events may be spatially correlated. Knowledge of the strain paths around the penetrating tip are thus essential to interpret the measured force profiles.

Different studies aimed at investigating the displacement of snow grains induced by a CPT. Herwijnen [2013] used Particle Image Velocimetry (PIV) to quantify the displacement around the tip. With a digital video camera, they recorded images of the front face of a snow box via a viewing window through which the progression of the SMP tip could be observed. They also acquired micro-tomographic images of snow samples after the SMP tests to measure the radial density field from mean pixel intensity. They observed a CZ with a radius equal to twice the cone radius, on average. The CZ radius was shown to increase with snow density. Further, they observed the formation of a quasi-stationary CZ after about 40 mm of penetration. LeBaron et al. [2014] also used PIV on two-dimensional images of a split-axis snow micro-penetrometer along a viewing window. They observed a CZ width of about three times the tip width. The radial cross-section area of the CZ was estimated to be about 10 times larger than that of the SMP tip. Assuming axial symmetry, the CZ volume was estimated to be about 1 cm^3, with nearly 50% of the CZ volume ahead of the tip. Floyer and Jamieson [2006, 2010] measured the extension of compaction and deformation zone with PIV on a rounded-tip penetrometer. They showed that the spike occurring in the force signal corresponds to the development of the compaction zone below the penetrometer tip.

The goal of this study is to quantify the three-dimensional deformation field in snow around the CPT tip, which is critical to interpret the recorded force signals. To this end, we combined micro-tomography and CPT, and developed a novel tracking method based on digital image correlation and matching of grain characteristics. The displacements at grain scale can then be recovered, from which the deformation around the tip is evaluated. The method was applied to samples spanning different snow types, thereby providing new insights and valuable information to assess the consistency of existing models.

5.2 Methods

5.2.1 Experiments

We conducted cone penetration tests (CPT) in eight samples of different snow types, and measured the induced deformation through micro-tomography (μCT).

Table 5.1: Overview of the eight snow sample properties. Snow types are classified according to Fierz et al. [2009]. Sample density and specific surface area (SSA) were derived from the μCT images.

Sample name	Snow type	Sieve size (mm)	Density (kg m^{-3})	SSA (m^2 kg^{-1})
RG1	Rounded Grains	1.6	289	23.0
RG2	Rounded Grains	1.6	304	23.7
RGlr1	Large Rounded Grains	1	530	10.1
RGlr2	Large Rounded Grains	1	544	10.3
RGlr3	Large Rounded Grains	1	557	9.86
DH1	Depth Hoar	1.6	345	16.9
DH2	Depth Hoar	1.6	364	15.9
PP1	Precipitation Particles	1.6	91.3	53.5

5.2.1.1 Sample Preparation

The snow samples were prepared by sieving natural snow into sample holders dedicated to tomography and letting them rest by, at least, 24 hours before conducting the measurements. The preparation of the samples and the experiments were performed in a regulated cold room at a constant temperature of -10°C. The samples covered a variety of seasonal snow types, namely rounded grains (RG, RGlr), depth hoar (DH) and precipitation particles (PP), with bulk densities between 90 and 560 kg m^{-3} and specific surface areas between 10 and 54 m^2 kg^{-1} (Tab. 5.1). The sample holders were aluminium cylinders, which have the advantage of high thermal conductivity and relatively low X-ray absorption. Their size was limited to 2 cm height and 2 cm diameter, in order to enable μCT imaging with a pixel size small enough to resolve snow microstructure.

5.2.1.2 Micro-tomography (μCT)

Two tomographic images of each sample were acquired: one before (pre-CPT image) and one after (post-CPT image) the cone penetration test. The samples were scanned at a pixel size of 15 μm pix^{-1} with an X-ray tomograph (RX Solutions). The X-ray tube was powered by a voltage of 80 kV and a current of 100 μA. Each scan consisted of 1440 radiographs covering a 360° rotation. In order to maintain a constant and uniform temperature of -10°C, a cryogenic cell (CellDyM) was used [Calonne et al., 2015].

The sets of radiographs were reconstructed into three-dimensional grayscale images representing the attenuation coefficients of the different materials composing the samples. Marks on the sample holder permitted us to register the pre- and post-CPT images, and correct unavoidable shifts due to movements of the tomograph elements with a sub-voxel accuracy. The aluminium sample holder was then masked in the images, and the ice was segmented from the air using the energy-based segmentation developed by Hagenmuller et al. [2013]. Density was computed on the binary images by voxel counting. Surface areas were computed on the segmented images by Crofton approach, which showed good accuracy on anisotropic structures [Hagenmuller et al., 2016]. The ratio between the area of the air/ice interface and the mass of ice defines the specific surface area (SSA).

5.2.1.3 Cone Penetration Tests (CPT)

The cone penetration tests were conducted by inserting a cylinder of radius $R = 2.5$ mm with a conic tip of 60° apex angle, into the snow samples (Figs. 5.1a, b). This cylinder with a conic tip was mounted on the SnowMicroPenetrometer [SMP version 4, Schneebeli and Johnson, 1998] to control the vertical displacement and measure the penetration force. The SMP force sensor (Kistler 9207) measures forces in the range of [0, 40] N with a resolution of 0.01 N. The samples were placed on a micrometric positioning plate, which allowed us to perfectly center the tip in the snow sample (Fig. 5.1c). After the acquisition of the first μCT image of the sample, the cone was inserted vertically at a constant speed of 20 mm s^{-1}. The penetrometer was not removed from the sample directly after the test, to let the loosened snow grains sinter. This waiting time avoided any grain to fall into the cavity created by the cone removal. In our tests, the cone tip reached an average depth of 10 to 15 mm, corresponding to an approximate distance of 5 to 10 mm to the sample bottom.

5.2.2 Displacement Analysis

Snow mechanical behavior is highly rate-dependent, in particular due to very active sintering between grains. Hence, incremental CPTs followed by μCT, as conducted in sand [e.g. Paniagua et al., 2013], are not adapted to snow. The advantage of incremental CPTs is to have small grain displacements between two successive μCT scans [e.g. Andò et al., 2012]. Here, we measured only the initial, intact snow microstructure and its final state after CPT. Characterizing the large grain displacements between these two images is a notoriously challenging task. However, at the considered penetration rate, snow behaves as a brittle material [e.g. Narita, 1984, Floyer and Jamieson, 2010] and can reasonably be considered as a granular assembly, i.e. we can assume that each grain moves as a solid body [Johnson and Hopkins, 2005, Hagenmuller et al., 2015]. This feature was exploited to retrieve the displacement fields by combining: (1) tracking of individual grains [ID-track, Andò

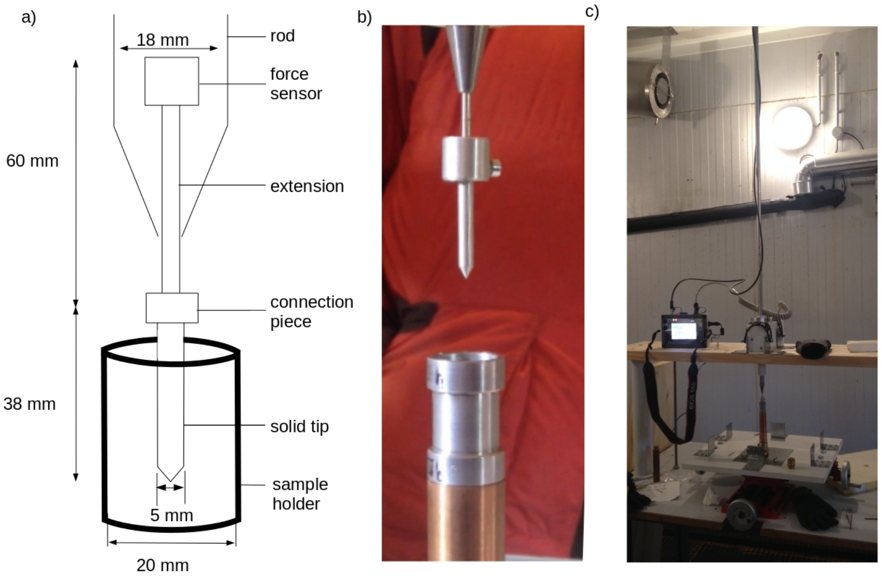

Figure 5.1: Set-up of cone penetration tests: a) scheme of the cone tip, b) photo of the cone tip, and c) photo of the whole experimental setup with the positioning plate.

et al., 2012] based on their geometrical properties to obtain an initial displacement guess, and (2) digital image correlation (DIC) to refine this guess and achieve high accuracy and resolution [Hall et al., 2010].

5.2.2.1 Grain Segmentation

In order to track individual grains between the pre- and post-CPT images, a first identification of snow grains in the binary images of ice and air is required. Individual grains were segmented by applying a curvature-based algorithm developed by Hagenmuller et al. [2014]. This algorithm detects preferential zones of mechanical weakness based on two geometrical criteria: negative minimal principal curvature and low contiguity between the grains. A threshold of $\kappa_t = 1.0$ on normalized curvature was used, as suggested by Hagenmuller et al. [2014]. A contiguity parameter of $c_t = 0.1$ was chosen, to limit the number of grains by detecting only the thinnest bonds (see details in Hagenmuller et al. [2014]).

5.2.2.2 ID-Track

The ID-Track follows the approach of Andò et al. [2012]. The main idea is to pair grains in the pre- and post-CPT images which have similar geometrical properties and whose derived displacement is consistent. To this end, we considered three criteria on grain geometry: (i) similar grain volume (relative difference less than

50%), (ii) similar grain elongation (relative difference less than 50%), and (iii) large overlap (grains overlapping by at least 70%) between the grains aligned along their principle axis. In addition, we considered two criteria on the resulting displacement between the paired grains: (i) small distance between the grain centers of mass in the two images (<20 voxels), and (ii) a globally outward displacement vector with respect to the cone center (i.e. the grain moves away from the cone). For each grain in the pre-CPT image, several grains of the post-CPT image may satisfy these five criteria. To select the best candidate out of this grain set, digital image correlation is used (see Sect. 5.2.2.3).

5.2.2.3 Digital Image Correlation (DIC)

The DIC method follows the approach of Hall et al. [2010]. The main idea is to perform digital image correlation between the pre- and post-CPT grayscale images on numerous analysis windows corresponding to each individual grain of the initial image. Figure 5.2 shows the main steps of the three-dimensional DIC method in a simplified two-dimensional scheme for one grain. First, an analysis window surrounding the grain of interest is defined (Fig. 5.2a). The window corresponds to the grain volume dilated in the air by three voxels. Then, a standard image registration is performed to find the transformation that best matches the pre- and post-CPT images masked on the analysis windows (Fig. 5.2e). The quality of this match is quantified by the cross-correlation between the transformed pre-CPT image and the post-CPT image. The possible transformations were limited to solid displacements (6 degrees of freedom: 3 translations, 3 rotations). If the final value of the registration metric exceeded $CC_{max} = 0.75$, the registration was considered successful, i.e. the grain in the pre-CPT image is correctly detected in the post-CPT image. Python package SimpleITK [Yaniv et al., 2018] was used to perform this image registration.

The example presented in Fig. 5.2 shows a grain with a small displacement between the pre- and post-CPT images. In case of larger displacements, the registration optimizer does not necessarily find the optimum of the registration metric in the complex domain of solid transformations. In that case, the displacements estimated by the ID-track method were used to seed the DIC algorithm (see Sect. 5.2.2.4).

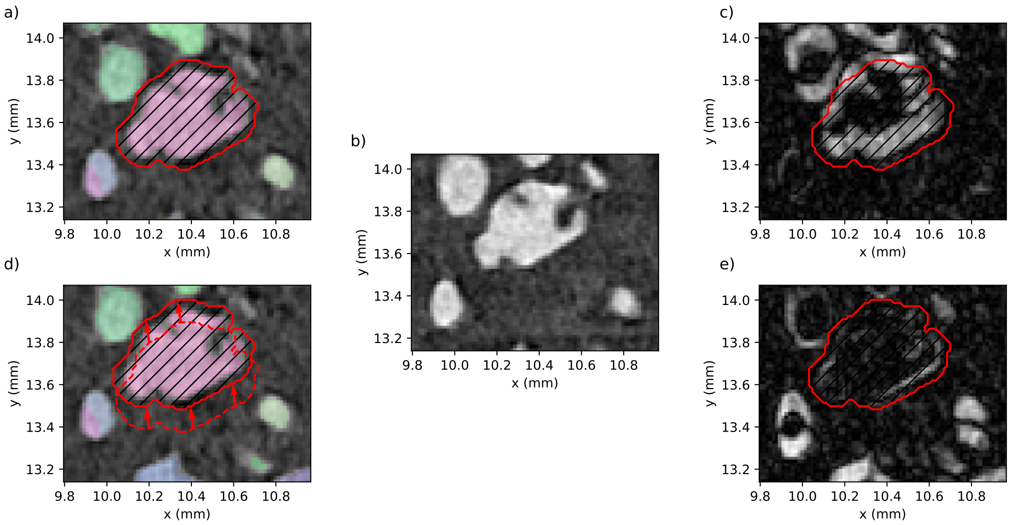

Figure 5.2: Digital image correlation technique: a) selection of one grain in the pre-CPT image and associated analysis window (dashed area) b) post-CPT image, c) grayscale difference of the pre- and post-CPT images with the analysis windows, d) displaced pre-CPT image with the displaced (red, solid line) and initial analysis windows (red, dashed line), e) grayscale difference of the displaced pre-CPT and post-CPT images.

5.2.2.4 Application to experiments

To optimize computing costs, ID-track and DIC were combined as follows. First DIC was performed with a null displacement as seed. This first pass detects most of the small displacements under 10 voxels magnitude (corresponding to about 80% of the total grains). The successfully matched grains in the pre- and the post-CPT images are then masked before applying the ID-track, which significantly reduces the computing cost. ID-track is then used with relatively restrictive criteria to detect potential pairs of grains and the associated displacement seeds. Finally, DIC is applied with these seeds to find the best image of the moved grains, and refine the displacement seeds to sub-voxel accuracy. If the best DIC result (quantified by the coefficient of correlation between the grayscale images) exceeds the threshold of $CC_{max} = 0.75$, the grain is assumed to be successfully matched. In addition, a last method was applied to the remaining unmatched grains. We used the idea that a grain most likely moves like its neighbours, and seeded DIC for these remaining grains with the displacements of the seven closest grains whose displacements were already detected.

5.2.3 Theoretical Displacement Field Analysis

In this section, we present two existing, mechanically-based, interpretation models for CPT: the first is based on the angle of compaction around a penetrating cone, and the second is based on the cavity expansion model.

5.2.3.1 Angle of Compaction

Johnson [2003] defines the angle of compaction as the angle of the compaction zone (CZ) relative to the cone surface. The model assumes that grains inside the CZ have the same size and microstructural properties as outside the CZ. It is also assumed that grain bonds can only fail at the interface between the CZ and intact snow. Before failure is reached, the snow grains deform elastically in a direction normal to the penetrometer surface. After failure, the grains compact until they lock up, also in normal direction. Johnson [2003] showed that the angle of compaction γ depends on the half cone angle θ of the penetrometer tip, the initial density ρ_0 and the density ρ in the CZ as follows:

$$\gamma = \tan^{-1}\left[\tan\theta\left(\frac{1}{\sqrt{\beta}} - 1\right)\right] \tag{5.1}$$

where β is defined as a volumetric strain, i.e. $\beta = (1 - \rho_0/\rho)$

Equation (5.1) is easily applicable to our measurements, as density is directly measured on the tomographic images. The value of ρ_0 and ρ were computed in the area close to the cone tip, namely for radial positions in the range $[1, 1.5]R$ (with R the cone radius, see Fig. 5.3), on the pre- and post-CPT images, respectively.

5.2.3.2 Cavity Expansion Model

Bishop et al. [1945] first pointed out the possibility to compute an approximate value for the load required to force a cone deep into an elasto-plastic continuum material. We consider here a cylindrical (given the shape of the tip) cavity expansion model (CEM) in an infinite medium, with a zero initial cavity radius. Snow is described as a cohesive-frictional material with a non-associated Mohr-Coulomb model. The analytical approximate solution of the cavity expansion problem proposed by Yu and Carter [2002] is used.

Mohr-Coulomb model for snow involves the following material parameters: Young's modulus E, Poisson ratio ν, angle of friction ϕ, angle of dilation ψ, and cohesion C. Typical values for these parameters were chosen according to Mellor [1975] (Tab. 5.2). The boundary conditions far from the cavity are characterized by a hydro-static pressure p_0, that was here set to 0. Similarly to Ruiz et al. [2017], an interfacial friction coefficient $\mu = 0.5$ between the tip and the snow was considered.

CEM distinguishes three zones: the cavity (position of the penetrating cone), a surrounding plastic zone, and an outer elastic zone (Fig. 5.3). Yu and Carter

[2002] showed that the radial and orthoradial normal stress components σ_r and $\sigma_\perp$ in the elastic region can be obtained from the equilibrium equation and elastic stress-strain relations as follows:

$$\sigma_r = -p_0 - Br^{-2}$$

$$\sigma_\perp = -p_0 + \frac{B}{2}r^{-2}$$

where r is the radial coordinate (Fig. 5.3) and B is a constant of integration [see Eq. (54) in Yu and Carter, 2002]. In the plastic region, Yu and Carter [2002] found that the stress components satisfying the equilibrium equation and the yield condition are:

$$\sigma_r = \frac{Y}{a-1} + Ar^{-\frac{a-1}{a}}$$

$$\sigma_\perp = \frac{Y}{a-1} + \frac{A}{a}r^{-\frac{a-1}{a}}$$

where $Y = \frac{2C\cos\phi}{1-\sin\phi}$ is the yield stress, $a = \frac{1+\sin\phi}{1-\sin\phi}$, and A is a constant of integration [see Eq. (53) in Yu and Carter, 2002]. The resulting penetration force F_p acting on the cone is computed similarly to Ruiz et al. [2017]. The radial force acting on the conical tip is given by:

$$F_r = 2\pi\text{cot}(\theta)\int_0^R \sigma_r(r)rdr$$

where R is the maximal cone radius. The resulting axial force required for cone penetration is, in the frictionless case:

$$F_z = F_r\tan(\theta)$$

By adding frictional effects, the resulting total penetration force is:

$$F_p = F_z(1+\mu\text{cot}(\theta)) \tag{5.2}$$

The model prescribes a purely radial displacement field. The displacement in the elastic zone is given by:

$$u = \delta r\left(\frac{c}{r}\right)^2$$

with δ and c depending on the material parameters [see Eqs. (40) and (55) in Yu and Carter, 2002]. The displacement in the plastic zone depends on the plastic flow rule. With a non-associated Mohr-Coulomb flow rule, the explicit expression of the radial displacement is complex. Displacement in this zone was computed

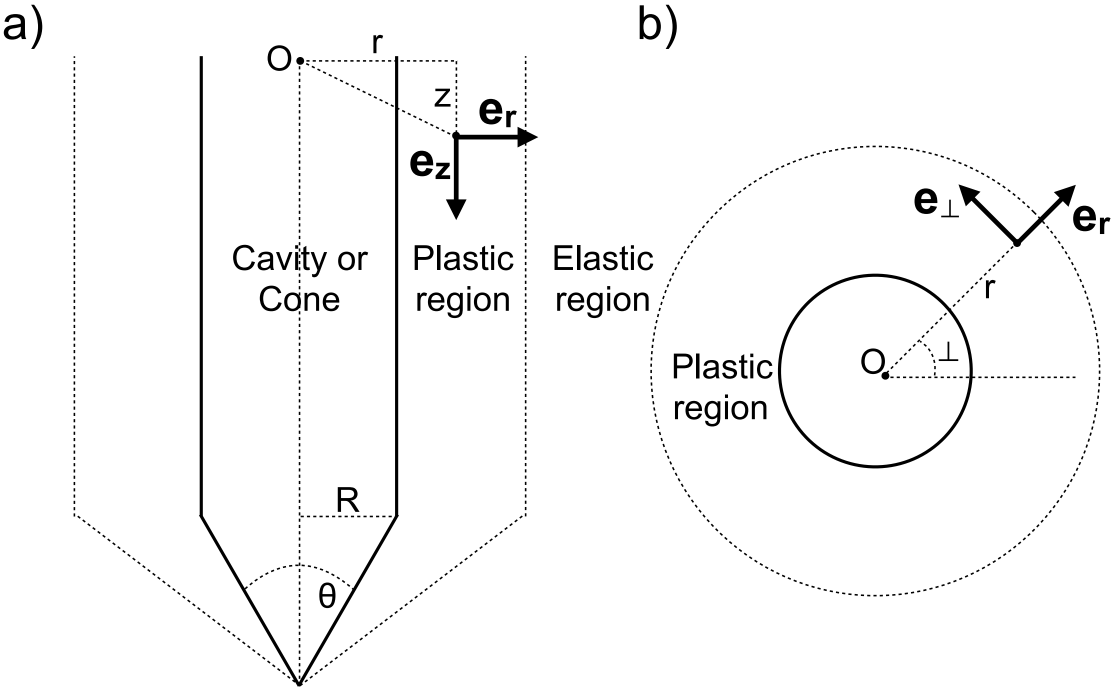

Figure 5.3: Different regions and coordinate system used in the CEM: a) vertical view and b) horizontal view.

Table 5.2: Material parameters describing snow as a Mohr-Coulomb material, and results of sensitivity analysis on force and displacement computed by the CEM.

Property	Symbol	chosen value	range	displacement change	force change
Young's modulus (Pa)	E	10^8	[10^5, 10^{10}]	22%	152%
Poisson ratio	ν	0.2	[0.1, 0.4]	0.2%	3%
Angle of friction (°)	ϕ	20	[10, 30]	0.03%	44%
Angle of dilation (°)	ψ	-30	[-20, -40]	125%	91%
Cohesion (Pa)	C	1000 Pa	[10^2, 10^4]	0.6%	192%

by numerically integrating the radial velocity V (radial displacement derived with respect to cavity radius expansion), whose analytical expression is:

$$V = \gamma \left(\frac{c}{r}\right)^{-\frac{1}{a}} + [2\delta - \gamma] \left(\frac{c}{r}\right)^{\frac{k}{\beta}}$$

where β and γ are constants defined in Eqs. (39) and (74) in Yu and Carter [2002].

Figure 5.4 shows the displacement field computed for the parameter values indicated in Tab. 5.2, as well as the corresponding density changes and force profile. Density changes were estimated from the volumetric strain under the assumption of small strains. Most of the displacement and density changes takes place in a region of about $1.5R$ (Fig. 5.4 a,b). The force profile shows a parabolic increase

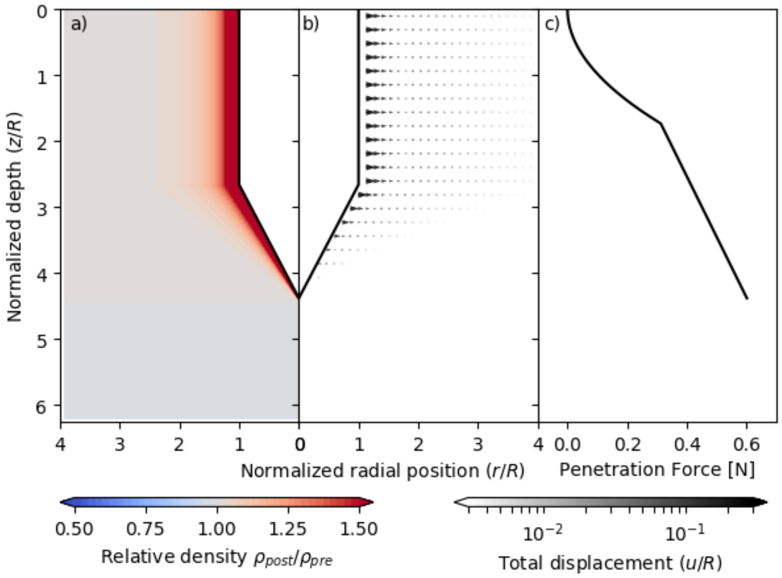

Figure 5.4: CEM prediction according to analytical solution of Yu and Carter [2002]: a) relative density change, b) displacement field normalised by tip radius R, and c) penetration force profile. The relative density change is defined as the ratio between the density ρ_{post} after the CPT and the density ρ_{pre} before the CPT.

with depth until the conical part of the tip has completely penetrated the snow material, followed by a linear increase with depth due to friction (Fig. 5.4 c).

We evaluated the sensitivity of the computed displacements and forces on the material parameters (Tab. 5.2). To this end, each parameter was varied in a realistic range (see column “range” in Tab. 5.2), while the other parameters were kept constant (see column “chosen value” in Tab. 5.2). The impact of the parameter values was evaluated on the radial force at the interface between the plastic and the cavity regions, and on the mean displacement for radial positions in the range $[1, 4]R$. In both cases, Tab. 5.2 reports relative differences with respect to values obtained with the "chosen value" of the parameter. Results show that the displacement field is almost only controlled by the angle of dilation ψ. In contrast, the force mainly depends on the cohesion C, Young’s modulus E, and angle of dilation ψ.

5.3 Results

In this section, we first evaluate the performance of the tracking algorithm on the experimental data. The CPT-induced displacement field and compaction zone are then analysed. Finally, the measured displacement and force are compared to the predictions of the mechanical models presented in section 5.2.3.

5.3.1 Tracking of snow grains

Figure 5.5 displays the grains in the pre-CPT image and the displacements induced by cone penetration for sample RG1. Similar figures for other samples can be found in Fig. S2 in the supplementary material. We observe significant displacements in a region of about twice the cone radius. In general, movements are directed outwards and downwards, but also upwards close to snow surface. Note that displacements are here plotted as straight lines between the initial and final positions, which might not correspond to the exact grain trajectory, especially for large displacements.

The tracking algorithm fails to recover the displacement of all grains (see white grains in Fig. 5.5). Nevertheless, as shown in Tab. 5.3, 90% of the grains, at least, were successfully tracked. Most of grains did hardly move, and were thus easy to track. However, in the zone of radius $2R$ where the largest displacements are observed, about 40 to 80% of the grains were still successfully tracked. If we only consider the grains initially located in the cavity, i.e. the zone occupied by the cone tip after the CPT, about 10% to 50% of the grains were successfully tracked.

The percentage of tracked grains depends on snow type. The algorithm detects the largest percentage of grains in samples composed of large rounded grains (RGlr), followed by depth hoar (DH) and rounded grains (RG). The lowest percentage of detection is obtained for samples composed of precipitation particles (PP). The grains composing the RGlr and DH samples are large and exhibit relatively unique shapes (see Fig. A1 in supplementary material), which makes the ID-track particularly efficient. Additionally, the tracking method also relies on the consistency of the grain segmentation. Grains can be efficiently tracked only if they are segmented in the same way in pre- and post-CPT image, without over- or under-segmentation. On RGlr or DH snow types, individual grains can generally be unambiguously identified, whereas the definition of grains in the PP type strongly depends on the chosen segmentation thresholds and can be affected by potential noise at the ice-air interface [Hagenmuller et al., 2014].

Accuracy of the computed displacement field was evaluated through two different approaches. Let us first recall that a grain is considered as successfully tracked when a correlation coefficient larger than $CC_{max} = 0.75$ is obtained between the pre- and post-CPT images (see Sect. 5.2.2.3 and 5.2.2.4). While this threshold indicates that the associated grains are similar, it does not guarantee that the association is physically correct. Hence, we checked visually the computed displacements on some selected grains, which appeared to be correct according to the displacements of the neighbouring grains (Fig. 5.5). More quantitatively, the obtained displacements were used to compute the volumetric strain ϵ_v. Combined to the initial snow density

Table 5.3: Number of grains tracked in the different snow samples

		percentage of tracked grains in a zone corresponding to:		
Snow	total number of grains	the whole sample	twice the tip radius	the cavity
RG 1	68 880	92%	50%	17%
RG 2	90 316	90%	39%	13%
RGlr 1	16 314	97%	77%	51%
RGlr 2	17 846	92%	54%	41%
RGlr 3	18 026	93%	51%	13%
DH 1	27 738	90%	39%	13%
DH 2	27 263	95%	68%	42%
PP	34 901	90%	39%	11%

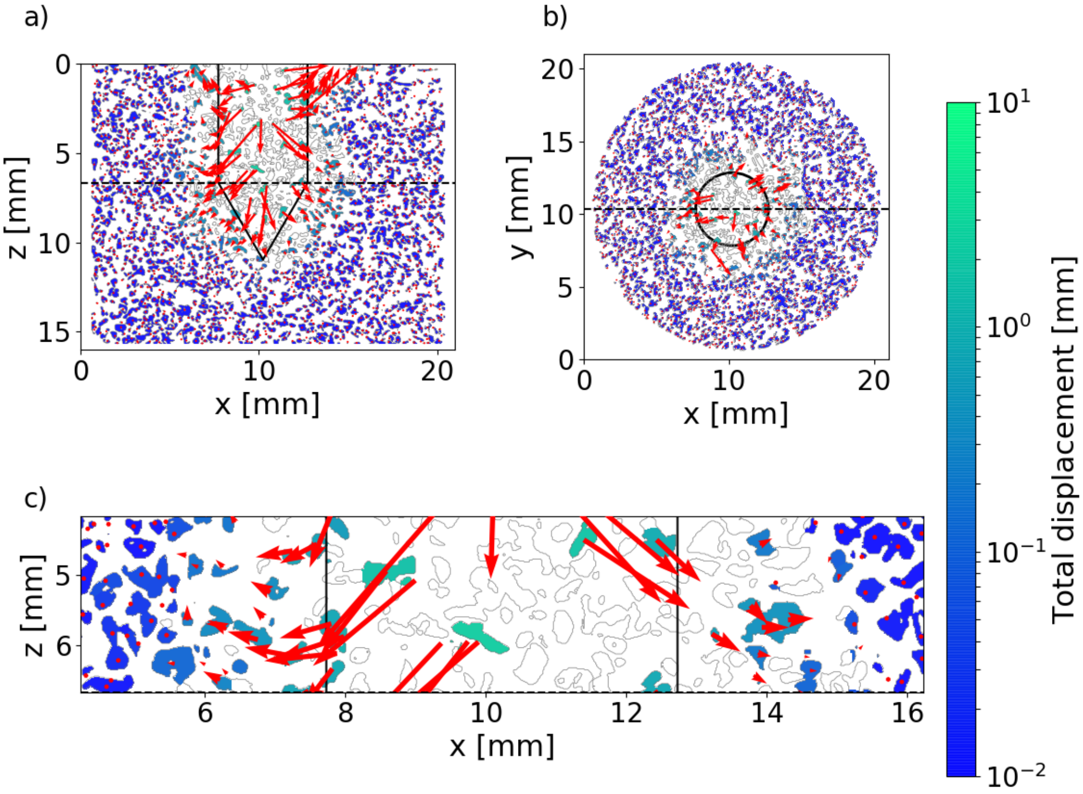

Figure 5.5: Tracked displacement field for sample RG1 shown on a) a vertical slice, b) a horizontal slice and c) a zoom on the vertical slice. The dotted line in the vertical slice shows the position of the horizontal slice and vice versa. The contours of the grains in the pre-CPT image are shown in gray. Colors indicate the absolute displacement, and arrows show displacement components in the slice plane.

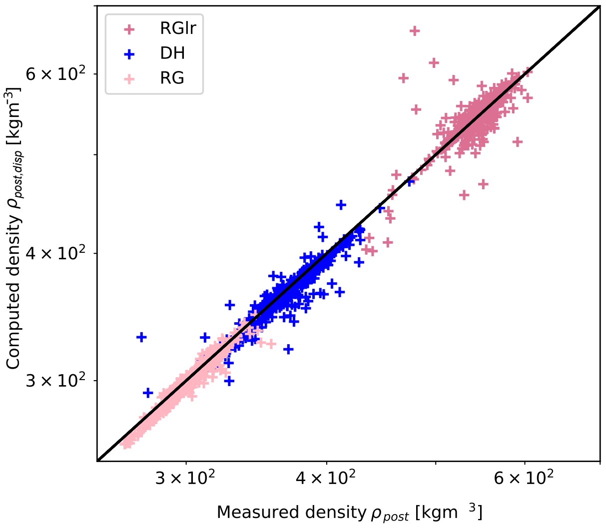

Figure 5.6: Comparison between the post-CPT density computed from the displacement field $\rho_{post,disp}$ and the post-CPT density directly measured on the tomographic image ρ_{post} for the seven snow samples of type RG, RGlr and DH. Snow type is distinguished by point color. Computed density is considered as representative, and shown on the figure, only if more than 30% of the grains are successfully tracked in the considered sub-volume.

measured in the pre-CPT image ρ_{pre}, snow density after the test was then derived according to: $\rho_{post,disp} = (1+\epsilon_v)\rho_{pre}$. This value can then be compared to the density directly measured on the post-CPT image ρ_{post}. This calculation thus provides a quantitative evaluation of the tracking method accuracy. In details, volumetric strain was computed only in regions with small displacements (radial and vertical displacements smaller than 30 voxels), so that the assumption of infinitesimal strain remains valid, and the displacements were assumed to be invariant with rotation around the cone axis. Density values $\rho_{post,disp}$ derived from the displacement field, and density values ρ_{post} computed directly from the post-CPT image, were averaged on all angles, a radius grid of step $dr \approx 30$ voxels, and a height grid of step $dz = 40$ voxels. As shown in Figure 5.6, values of $\rho_{post,displ}$ and ρ_{post} generally follow the 1:1 line, which indicates the consistency of the computed displacement field. Small deviations may originate from segmentation errors of the ice, which can cause variations of the density of up to 5% according to Hagenmuller et al. [2014 b]. Some outliers can be observed, especially for DH and RGlr snow types, which exhibit the lowest relative compaction.

5.3.2 Analysis of the deformation around the cone

5.3.2.1 Deformation and compaction zones

Figure 5.7 shows density changes and displacement fields for samples RG1 and DH2 (corresponding plots for the other samples are visible in Fig. S2 in the supplementary material). As previously (Sect. 5.3.1), density and displacement were averaged on all angles, a radius grid of step $dr \approx 30$ voxels and height grid of step $dz \approx 40$ voxels. Both radial and vertical displacements are observed. Vertical displacements are oriented upwards close to the surface, and tend to be downwards close to the tip apex. Upward movements close to snow surface tend to be more pronounced for snow types RGlr and DH, whereas downward movements close to the apex are more pronounced for snow type RG. The displacement field generally varies with both r and z, precluding the existence of solid blocks of compacted snow moving downwards or radially with the tip. The deformed zone rather progressively forms and evolves with cone penetration. Cone penetration is associated to compaction next to the tip in moderately dense samples (samples RG1, RG2, PP), but to dilation in denser samples (samples RGlr1, RGlr2, RGlr3, DH1, DH2).

We define the deformation zone (DZ) as the zone where displacement magnitude is larger than 30 μm, and the compaction zone (CZ) as the zone where absolute relative density change is larger than 5%, i.e. $0.95 < \rho_{post}/\rho_{pre} < 1.05$ (Fig. 5.7). The radial and vertical extents of these two zones depend on the considered sample. Table 5.4 summarizes the average values obtained for all samples. For sample PP1, we did not track enough grains to derive the DZ. Sample RGlr2 showed an upward movement in the whole cylinder, probably due to the DZ reaching sample bottom. In this case, no relevant DZ can be determined. In general, the radial extent of the DZ varies between $1.8 - 2.7R$, with the highest values for snow type DH, followed by RGlr and RG (Tab. 5.4). The radial size of DZ and CZ are similar for RG samples, while the CZ is slightly smaller than the DZ for RGlr and DH samples. Lastly, RG and PP samples show CZ of similar radial extents (about $2R$). The vertical extents of the CZ and DZ are similar, and smaller or equal than $1R$, for all samples.

5.3.2.2 Radial profiles

Radial profiles of displacement and density changes were calculated by averaging measured values over the cylindrical part of the penetrometer, i.e. just above the transition between the conic tip and the cylinder, and up to a height equal to tip radius (Figs. 5.8, 5.9). As shown in Figure 5.8, a fast decay of the vertical and radial displacements with the radial position is observed for the different samples.

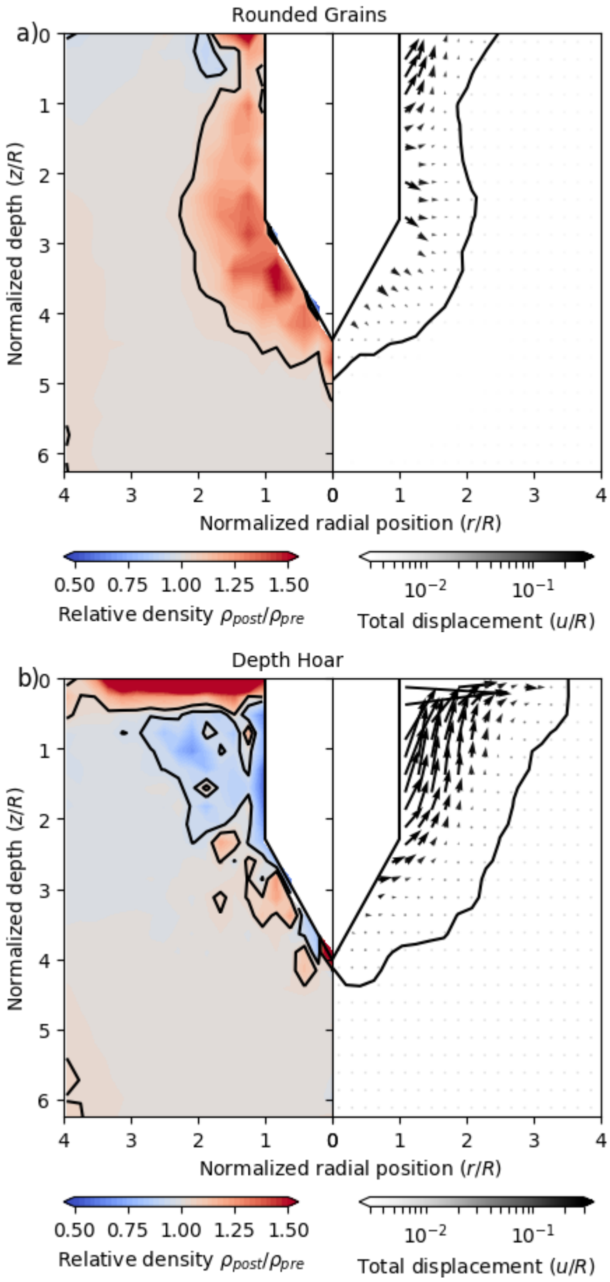

Figure 5.7: Averaged density change (left side) and displacement field normalised by tip radius R (right side) around cone tip for two snow types: a) RG (sample RG1), b) DH (sample DH2). Contours show the compaction and deformation zones around the tip. Displacements are plotted only if more than 30% of the grains in the corresponding sub-volume are successfully tracked.

Table 5.4: Size of the compaction (CZ), deformation zones (DZ) normalized by tip radius R and compaction angle according to the model of Johnson [2003], for all samples. The radial extents (CZ_r, DZ_r) are defined as averages computed from the tip base (transition between cone and cylinder) up to about 2.5 mm beneath snow surface. The vertical extents (CZ_z, DZ_z) are the distances between the tip and the deepest point in the CZ or DZ. The total penetration depth of the CPT is also indicated.

Sample	RG1	RG2	RGlr1	RGlr2	RGlr3	DH1	DH2	PP
penetration depth	4.38	4.80	4.12	5.49	3.48	4.42	4.01	5.35
CZ_z	0.90	0.84	0.23	> 0.75	0.9	1.0	0.44	0.51
CZ_r	1.81	1.95	1.69	1.64	1.72	1.89	2.28	1.99
std CZ_r	0.21	0.08	0.09	0.23	0.15	0.1	0.2	0.05
DZ_z	0.62	0.77	0.34	> 0.98	0.93	0.99	0.44	-
DZ_r	1.86	1.95	1.96	-	2.22	2.38	2.70	-
std DZ_r	0.09	0.10	0.01	-	0.07	0.03	0.15	-
compaction angle (°)	27	30	57	56	59	35	44	20

Accordingly, the definition of the DZ (see above) is not very sensitive to the chosen displacement threshold. The vertical displacements are the smallest for RG samples, and the largest for RGlr and DH samples. They are positive (downwards) for RG samples and negative (upwards) for the other snow types. Radial displacements are of the same magnitude for all snow types.

Density change profiles (Fig. 5.9) clearly show that compaction or dilation is located in a zone whose radius is about $2.5R$. As expected, largest density changes are observed close to the cone tip. Clear compaction is observed for snow types RG and PP, with maximal compaction values between 1.4 and 1.5. In addition, the strongest relative compaction is observed for the less dense samples (PP). For samples with larger initial densities (DH and RGlr), dilation next to the tip is observed. However, DH samples, which are less dense than RGlr samples, show less dilation and even slight compaction in one case. RGlr samples show maximal dilation values (0.6).

5.3.3 Comparison between measurements and models

5.3.3.1 Compaction angle model

Table 5.4 presents the theoretical compaction angle computed from Eq. (5.1) on all samples. We recall that the compaction angle model also provides the radial

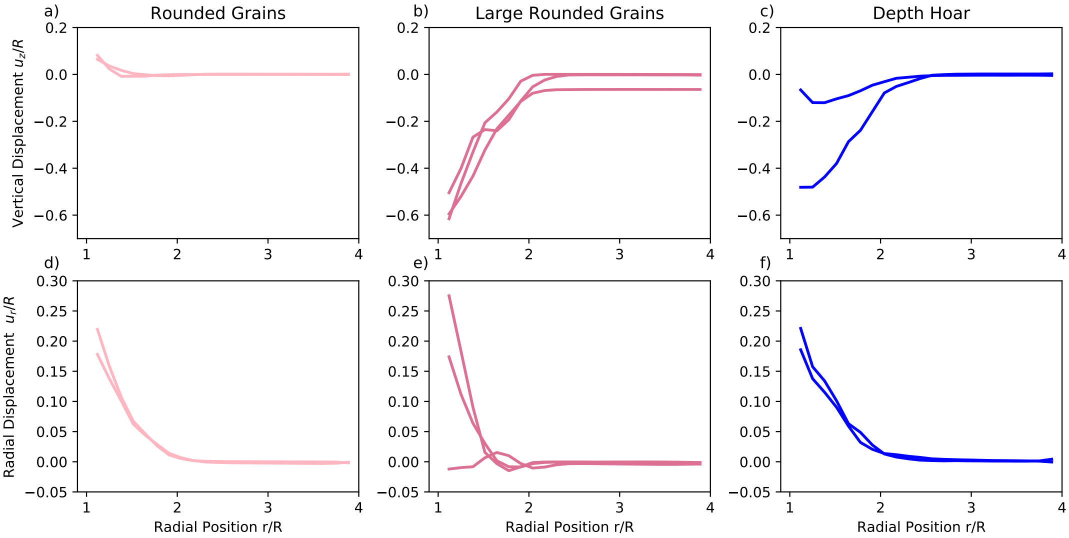

Figure 5.8: Radial profiles of vertical (a, b, c) and radial displacement (e, f, g) normalised by tip radius R for RG (a, d), RGlr (b, e) and DH (c, f) snow types. In all plots, the different profiles correspond to the different samples for each snow type.

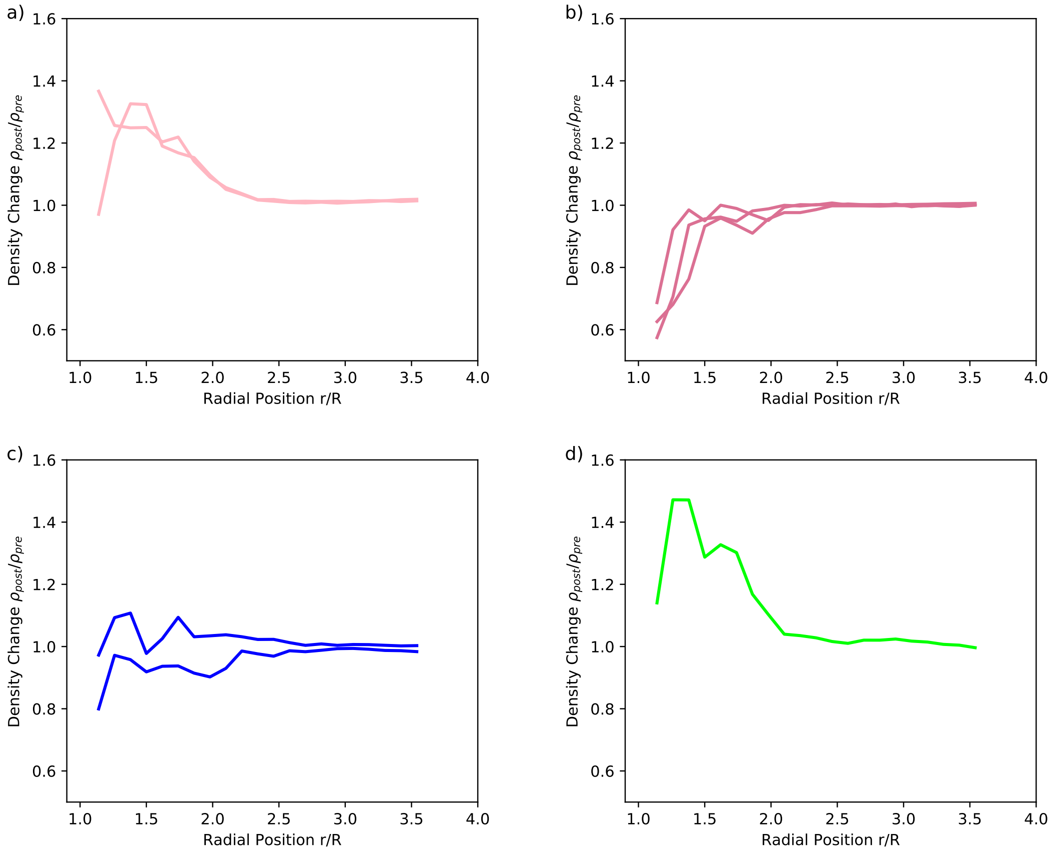

Figure 5.9: Radial profiles of density changes for RG (a), RGlr (b), DH (c), and PP (d) snow types. In all plots, the different profiles correspond to the different samples for each snow type.

extent of the compaction zone as the transition between the theoretically uniform compacted snow and the intact snow. The derived radial extent is smaller than the size of the sample (less $4R$) for only four samples. The smallest radial extent ($2.1R$) is obtained for PP, followed by RG ($2.8R$) and DH ($4.0R$). The extent of the CZ derived from the model is in agreement with the measured values for sample PP (see Tab. 5.4), but is over-estimated for the other snow types. Indeed, Johnson [2003]'s compaction model assumes an abrupt transition between intact snow and snow compacted to its critical density, which is not observed in our experiments (Fig. 5.9). The samples either exhibit dilation next to the tip, or progressive compaction from the intact snow to the interface of the cone.

5.3.3.2 Cavity expansion model

Figure 5.10 compares the measured radial displacement profiles and the displacements predicted by the CEM. We recall that the model predicts null vertical displacements, while all tested samples (besides PP, for which we were not able to retrieve a displacement field) display a vertical displacement component (Figs. 5.8a, b, c). The radial displacements (Figs. 5.10d ,e ,f) for the RG and DH snow types show relatively good agreement with the model. Best agreement was obtained for $\psi = -30^o$, with values of $R^2 > 0.9$. However, no value of the dilation angle ψ enabled to fit the model over the whole range of r values. For radial positions in $[1, 1.5]R$, the best fit is obtained with $\psi \in [-25, -30]^\circ$, but the faster displacement decay for larger r is better captured with $\psi = -35^\circ$. For RGlr snow type, radial displacements decay to zero much faster than the model regardless of the considered value of ψ, and for one sample (RGlr3) there is almost no radial displacement observed.

Figure 5.11 compares the force measured during the CPT to CEM predictions.All material properties of the model, except for cohesion, were chosen according to typical snow properties (Tab. 5.1). Cohesion C was varied between 500 and 1500 Pa. The general shape (parabolic) of the force profile appears to be well reproduced by the model. Obviously the CEM, which is based on the assumption of a continuum material, fails to reproduce the discrete nature of bond failures resulting in force fluctuations with depth. The recorded force profiles for the RG, RGlr and DH snow samples agree with theoretical estimates obtained for cohesion values in the range [250, 1500] Pa, while the force recorded for the PP sample appears to correspond to a lower cohesion.

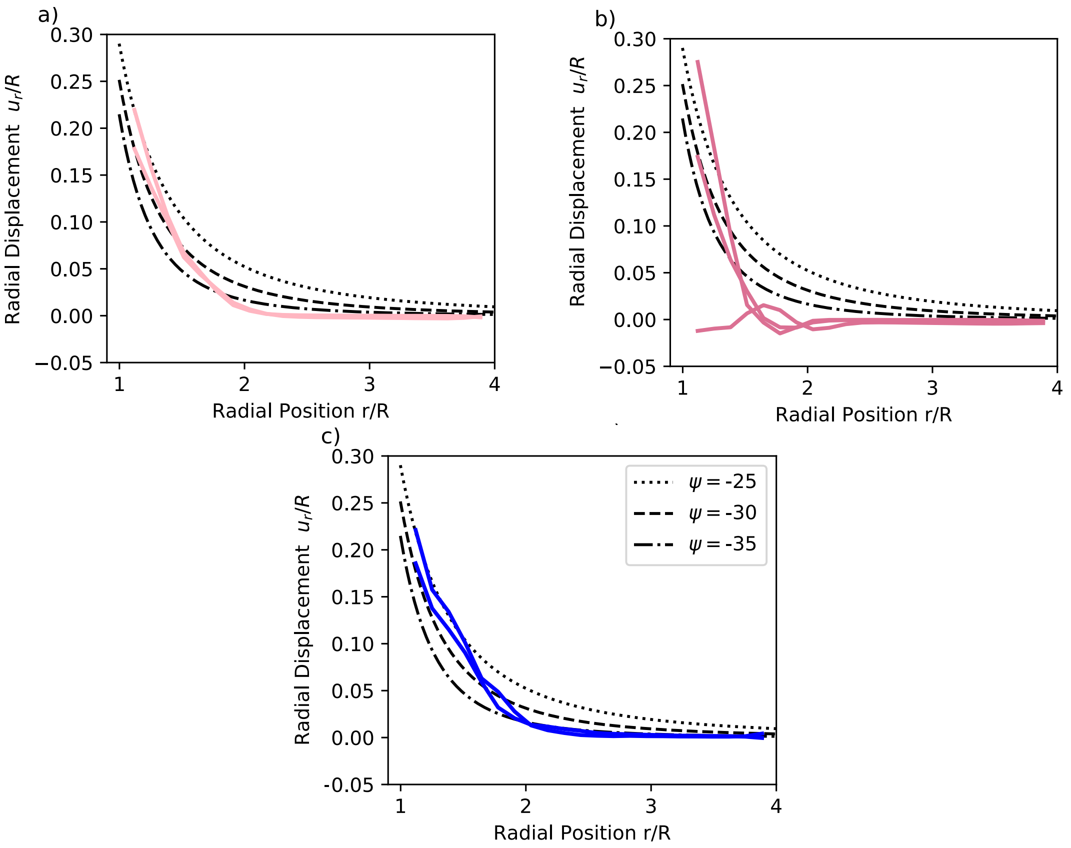

Figure 5.10: Comparison between measured radial displacement profiles and predictions of cavity expansion model for different snow types: a) RG, b) RGlr, c) DH. Predicted profiles are shown for three different dilation angles ψ, which is the only material parameter that significantly affects the computed displacements (Tab. 5.2).

5.4 Discussion

5.4.1 High-resolution three-dimensional measurements of snow deformation

A novel method for three-dimensional tracking of individual grains around a CPT in granular materials was presented. It was applied to μCT images of eight snow samples, covering four different snow types. For each sample, two images were measured, one before and one after the CPT. The main challenge consisted in identifying the large displacements. Indeed, the highly rate-dependent mechanical behavior of snow did not allow us to conduct incremental CPT. However, compared to previous experimental studies of CPT in sand or soils [e.g. Paniagua et al., 2013, Silva et al., 2015], the relatively unique shape of each snow grain renders tracking applicable on such large displacements.

Our study provides the first observation of the full 3D displacement field at grain scale during a CPT in snow. Some grains could not be successfully tracked

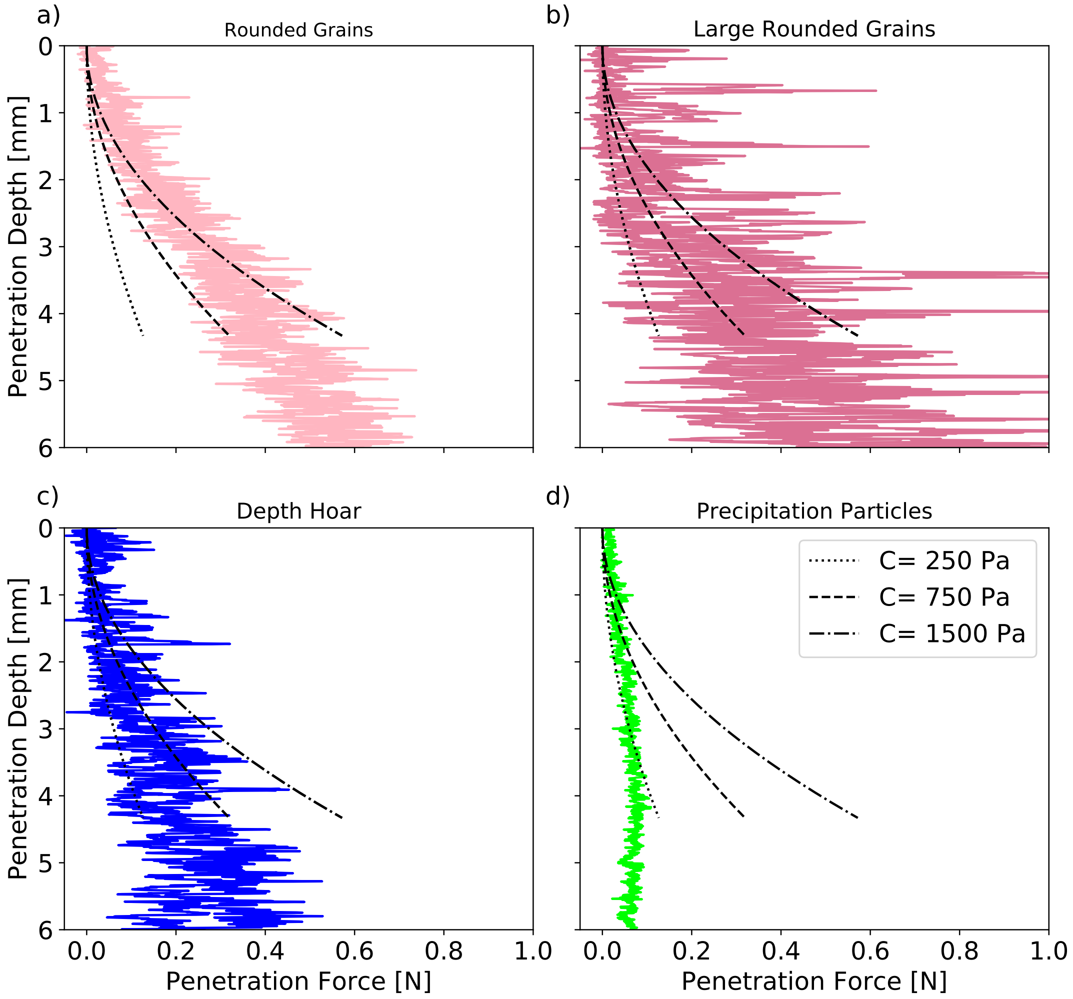

Figure 5.11: Measured and computed CPT force profiles for the different snow types: a) RG, b) RGlr, c) DH, d) PP. Computed profiles are obtained from Eq. (5.2) with different values of cohesion C.

between the pre- and post-CPT images (Fig. 5.5). However, assuming invariance of the displacement with rotation around the cone axis, we were able to reconstruct the displacement field everywhere outside the cavity (Fig. 5.7). While direct validation of the tracking algorithm is out of reach, due to the absence of reference, the chosen methodology (high threshold on correlation coefficient to consider a successful tracking) and indirect validation on the density field (Fig. 5.6) provide good confidence in the obtained results.

The use of X-Ray tomography at a resolution of 15 μm inherently limited the size of the snow samples. The samples were cylinders of diameter and height of 20 mm ($4R$), confined in aluminum holders. Cone penetration reached an average depth of 10 mm, corresponding to an approximate distance of 7 mm ($\approx 2.5R$) to sample bottom. Herwijnen [2013] showed that a steady-state penetration behavior is reached on average after 40 mm of penetration depth in homogeneous snow samples. In this study, we clearly observed different displacements close to snow surface, in comparison to larger depths (Figs. 5.7 and Fig. S2 in the supplementary material). However, on samples composed of rounded grains or precipitation particles (Fig. 5.9 and Tab. 5.4), we did not observe any evidence of an increase or decrease of compaction zone radius with depth below the snow surface (depth $>$ 1 mm).

For low-density snow, the confinement of the samples is expected to have little influence on the measured displacements and forces. Some tested samples (RGlr1, 2 and 3) do however exhibit a high initial density, up to about 560 kg m^{-3}. In this case, the confinement may affect the CPT, in comparison to a test performed in a infinite medium. This impact was obvious on sample RGlr2, for which the largest penetration depth was reached and an overall upward movement of the sample was observed. Nevertheless, it has to be recalled that previous studies [e.g. Herwijnen, 2013, LeBaron et al., 2014], principally based on 2D imaging of snow samples through a viewing window, may also inevitably be affected by some border effects. In addition to sample confinement, the removal of the cone before the second tomographic scan may also affect the observed displacement field. Even if the cone was removed after about 2 hours of sintering to solidify the cavity, we could observe that some grains were eroded from the sample and deposited on the top surface because of residual friction with the cone, particularly on samples characterized by a high initial density (Figs. 5.7 and Fig. S2 in the supplementary material).

5.4.2 Analysis of CPT deformation in snow

Snow deformation around the cone was analysed using the displacements retrieved by the tracking algorithm and the density evolution directly computed from the tomographic images. These two techniques are complementary. Tracking provides the full 3D, vectorial displacement field at grain scale, but fails to identify all the grains, especially when displacements are large. Density evolution can be directly computed on the whole volume and is more robust, but it is a scalar value and its resolution is limited to several grains.

In general, downwards movements were observed at tip apex, and upwards movements close to sample surface (e.g. Fig. 5.7). In the literature, similar displacement patterns are reported for granular soils and clays [e.g. Arshad et al., 2014, Ni et al., 2010]. Similar displacement patterns were also observed by Jiang et al. [2006] on numerical experiments with a discrete element model. Our experiments showed a dependence of the displacement pattern with snow type. In particular, the vertical displacement component was the smallest for RG samples, and the strongest upward movements were observed for DH and RGlr samples (Figs. 5.8). These two latter snow types are characterized by the largest initial densities, which may be the origin of the upward movement. This interpretation is in agreement with the observed density fields, which show almost no compaction for these samples. Hence the grains, instead of being compacted, are pushed upwards to let the cone penetrate.

Deformation and compaction zones DZ and CZ were defined on the base of thresholds on displacement magnitude and absolute density change. Unlike Floyer [2008], however, we did not observe significant differences between the two zones, i.e. grain displacements were systematically associated to density changes (compaction or dilation). Specifically, we did not observe any solid bulb of snow grains moving with the tip. Instead, the compaction zone appears to continuously reform with depth. The radius of the CZ obtained from our experiments appears to be smaller than values found in previous studies (Tab. 5.4). LeBaron et al. [2014] reported CZ radius of about $3R$. Herwijnen [2013] measured an average ratio of 2 between CZ radius and tip radius, with values up to 4.7 for dense snow (390 kg m^{-3}). Floyer [2008] obtained a radial CZ extent of about $2R$. Here, we observed values in the range $[1.6, 2.3]R$ for the CZ radius (see Tab. 5.4), which might be due to a not fully developed CZ. Indeed, Herwijnen [2013] (Fig. 11 therein) showed a slight increase of CZ radius with depth: from $1.5R$ for a penetration depth of 15 mm to $2R$ for a depth of 40 mm.

5.4.3 Applicability of CPT interpretation models

We used our experimental data to evaluate the displacement field predicted by the compaction angle model of Johnson [2003] and the cavity expansion model [Yu and Carter, 2002, Ruiz et al., 2017]. The compaction angle model assumes that the compacted material around the cone tip reaches a uniform critical density. We showed that this assumption is not valid for snow (e.g. Fig. 5.7), and leads to wrong predictions of compaction zone size (Tab. 5.4).

The cavity expansion model relies on the assumption of a continuum material. Bolton et al. [1993] showed that the continuum assumption reaches its limit when the ratio of cone penetrometer size to grain size is lower than 20. In our case, this corresponds to a mean grain radius larger than 0.125 mm. Samples of DH and RGlr are clearly above this limit, which may explain deviations from the model. A relatively good agreement was nevertheless observed between the measured and predicted radial displacement profiles for samples of DH. The RG samples are characterized by much smaller grains, and the assumption of a continuum medium is more justified in this case. Accordingly, a good agreement was observed with the model in terms of radial and vertical (null) displacements. For both DH and RG snow types, the best fit was obtained for a dilation angle of -30°. The modeled force reproduced relatively well the parabolic shape of the measured profiles. The values of cohesion (about 1000 Pa, see Fig. 5.11), required to model the force, are in agreement with literature [Chandel et al., 2014, Reiweger et al., 2015]. In our samples, the lowest cohesion is obtained for the PP sample, followed by DH, while the largest values were reported for RG and RGlr samples (see Fig. 5.11).

5.5 Conclusion

A reliable interpretation of CPT force profiles requires a correct estimation of the displacement around the cone tip. We measured this displacement on snow with X-ray tomography, and proposed a novel method for recovering large displacements between two μCT scans. The method was applied to our data consisting of pre- and post-CPT tomographic images for eight snow samples. Most of the grains were successfully tracked between the two images. Measured displacements were oriented downwards at tip apex, upwards close to sample surface, and nearly radially in between. Displacements were shown to be sensitive to the initial sample density. In particular, upward movements were particularly pronounced for high density samples. CPT generally caused snow compaction around the tip but, surprisingly, dilation was also observed for the highest density (> 350 kg m^{-3}) samples. Nevertheless, sample confinement and shallow penetration depths might affect this behavior. The radial extent of the compaction zone (CZ) ranged between $[1.6, 2.3]R$, while the vertical extent of the CZ below the tip ranged between $[0.2, 1.0]R$. We did not observe a clear variation of the size of the compaction zone with density.

Our results show that the size of the compaction zone cannot be accurately estimated by the simple model of Johnson [2003] for snow, as density progressively increases from intact snow to the snow in contact with cone tip. The cavity expansion model (CEM) captures this progressive compaction. Moreover, force profiles predicted by the CEM for relevant material properties are in good agreement with measured profiles. Clearly, however, the CEM fails to reproduce force fluctuations due to the discrete nature of bond failures, and is unable to capture the vertical movement of snow particles during CPT.

Our results also provide an indirect evaluation of Poisson shot noise models [Löwe and Herwijnen, 2012, Peinke et al., 2019] for CPT. These models assume the force to

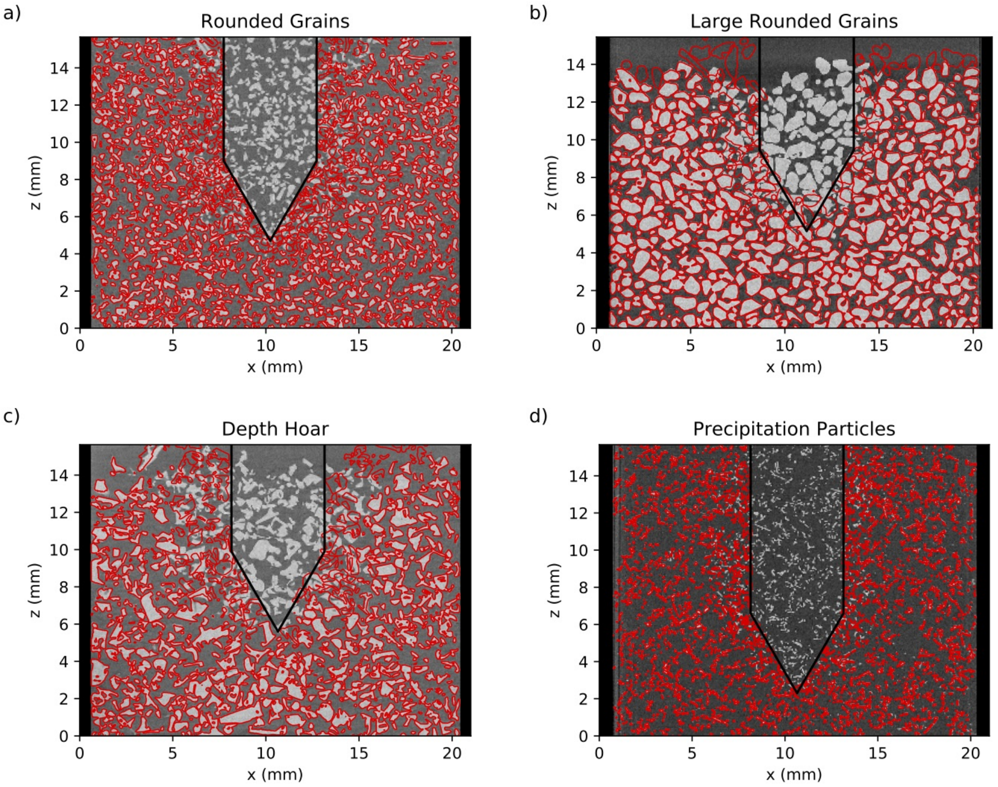

Figure 5.12: Pre- post- CPT images of different samples: a) RG 1, b) RGlr 1 c) DH 2 d) PP. The pre-image is shown in gray scale. The ice contour in the post-image is shown red.

be the sum of independent elastic brittle failures, and that grains do not contribute to the overall force once their bonds are broken, thus effectively disregarding the existence of the CZ. Consistently with Herwijnen [2013] and LeBaron et al. [2014], our measurements show that the CZ is not negligible and may play an important role for the force interpretation, even in very low density samples (PP).

5.A Appendix

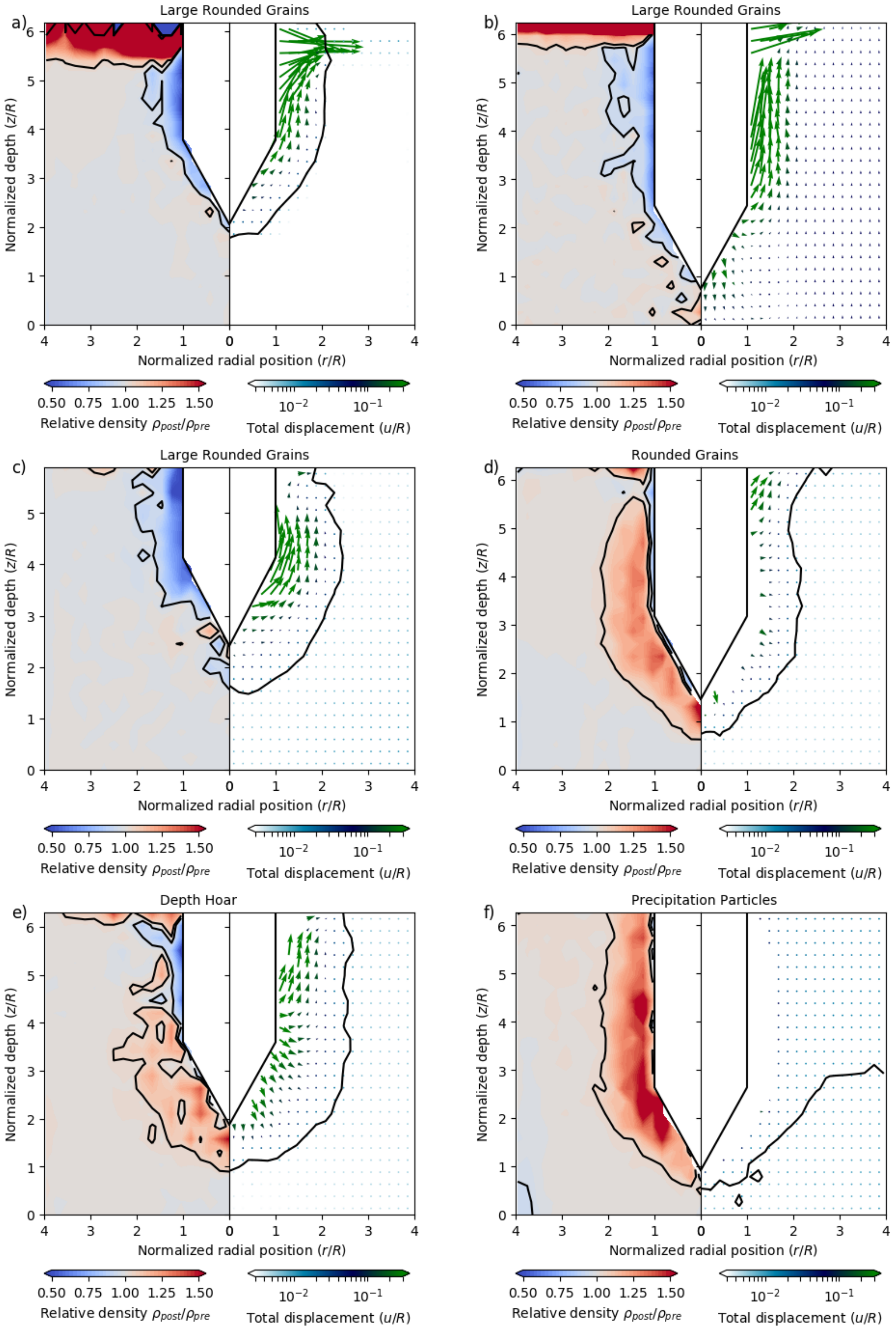

Figure 5.13: Measured and averaged density change (left side) and displacement field (right side) around a CPT for the following snow types: a) RGlr1 , b) RGlr2, c) RGlr3, d) RG2, e) DH1, f) PP1. The contours show the compaction zone and deformation zone around the tip. Fig. 5.6) and the displacements were accounted for if more than 30% of the grains is the corresponding volume are found

6

Evaluation of snow structural proxies derived from cone penetration tests with X-ray tomography

Contents

6.1 Introduction

In this thesis, we developed a statistical model to derive micro-mechanical proxies from cone penetration tests (CPTs, sew Chap. 3). Further, we performed CPTs combined with micro-tomographical (μCT) imaging (Chap. 5). The developed algorithms and obtained data will be analysed by power-law correlations in this chapter: the micro-mechanical estimates derived from CPTs will be compared with microstructural parameters directly derived from μCT images. For this purpose, we use the non-homogeneous Poisson process (NHPP) model to derive proxies of bond occurrence density, bond strength and structural elongation from penetration force profile (Chap. 3). We recall that this model is particularly suited to analyse shallow depth CPTs as the ones measured during the tomographical experiment, presented in Chapter 5. On large homogeneous snow samples, the NHPP performs similarly to the homogeneous Poisson process (HPP) model, developed by Löwe and Herwijnen [2012]. Further, the NHPP can take into account the transient building of a compaction zone in front of a penetrometer tip, as observed in the small samples dedicated to tomographical scans (Chap. 5). The tomographical images before and after the CPT were analysed by a morphology based tracking method presented in Chapter 5. This method allowed us to reconstruct a large part of the grain displacements. These displacements were used to compute the number and size of the bonds that broke during the CPT can be computed. These quantities are directly related to the micro-mechanical proxies derived with the statistical analysis. In addition, the average size of the bonds in the whole sample were estimated using the concept of the minimum cut density [Hagenmuller et al., 2014 b].

A second part of this chapter consists in the analysis of the correlation between the identified micromechanical proxies and the macroscopic properties of the snow. Proksch et al. [2015] proposed a model to compute the density and specific surface area (SSA) from the recorded force of the CPT and the results of the HPP. This motivated us to study the correlation between the micromechanical properties, obtained with NHPP, and the density and SSA, measured from the μCT images.

In summary, we want to evaluate the NHPP method: we compare the micromechanical properties obtained with NHPP to the ones obtained from the tracking method and to the ones obtained from the minimum cut density. In addition, the micromechanical snow properties, obtained from NHPP, are compared to macroscopic snow properties.

Table 6.1: Overview of snow sample properties. The sample names are composed of the snow type and a number. Snow types are classified according to Fierz et al. [2009]. The density and specific surface area (SSA) were derived from the μCT images.

Sample name	μCT images (number)	Sintering time (days)	Sieve size (mm)	Density (kg m^{-3})	SSA (m^2 kg^{-1})
RG1	2	4	1.6	289	23.0
RG2	2	5	1.6	304	23.7
RG3	1	5	1.6	317	21.0
RGlr1	2	5	1	530	10.1
RGlr2	2	4	1	544	10.3
RGlr3	2	6	1	557	9.86
RGlr4	1	4	1	510	10.3
RGlr5	3	4	1	533	10.1
RGlr6	1	5	1	519	10.2
DH1	2	4	1.6	345	16.9
DH2	2	1	1.6	364	15.9
DH3	1	2	1.6	358	17.0
PP1	2	2	1.6	91.3	53.5
PP2	1	5	1.6	131	41.9

6.2 Experiments

This chapter is based on the same experiments as Chapter 5, but with a larger amount of samples. To prepare the 14 samples, snow of four different snow types was sieved directly into the cylindrical sample holders (2 cm in both, diameter and height, see Fig. 6.1). The samples had densities between 90 and 560 kg m^{-3} and specific surface areas (SSA) between 10 and 50 m^2 kg^{-1} (Tab. 6.1). Their names are composed by the shortcut of the grain classification, according to Fierz et al. [2009], and a number. Further information of the sieve size, the number of successfully effected μCT images, and the sintering time are given in Tab. 6.1.

The μCT scan was done at ambient temperature, while we used the CellDyM [Calonne et al., 2015] to maintain the temperature of the sample at -10°C. The CPT test was done in a cold room. A short transport was necessary from the cold room to the μCT. A complete measurement consisted in a cone penetration test (CPT) and two microtomographical (μCT) images, one before and one after the CPT. The sample RGlr5 was scanned three times, the first two scans were measured with a time difference of about one day, the third one was done after transporting the sample without conducting a CPT. The scans of this sample were motivated to study the possible changes on the snow structure due to time and transportation of the sample.

The CPT measurements were conducted with a solid tip, consisting of a cylinder of 5 mm in diameter, which had a conical tip with a half cone angle of 30° (Fig. 6.1).

The cone was inserted in the center of the sample, vertically at a constant speed of 20 mm s^{-1}. For that, we mounted the tip on the SnowMicroPenetrometer [SMP version 4, Schneebeli and Johnson, 1998] to measure the penetration force with depth (see Fig. 6.1). After inserting the cone into the snow, it was not removed directly to let the loosened snow grains sinter. A rest time of about one hour hindered grains to fall into the cavity which was created by removing the cone. The penetration depths of the CPTs were between 8 and 18 mm. For some samples, the snow stuck on the cone tip and was lifted with the homing tip. Thus, for three samples (RG3, DH3 and PP2) only one scan exists. For the samples RGlr4 to 6, we detached the tip from the SMP and let it in the sample during the μCT imaging. On the μCT image after penetration, we observed that the tip has moved during transport. Thus these images were not useful for the tracking method (see Sec. 6.3.2).

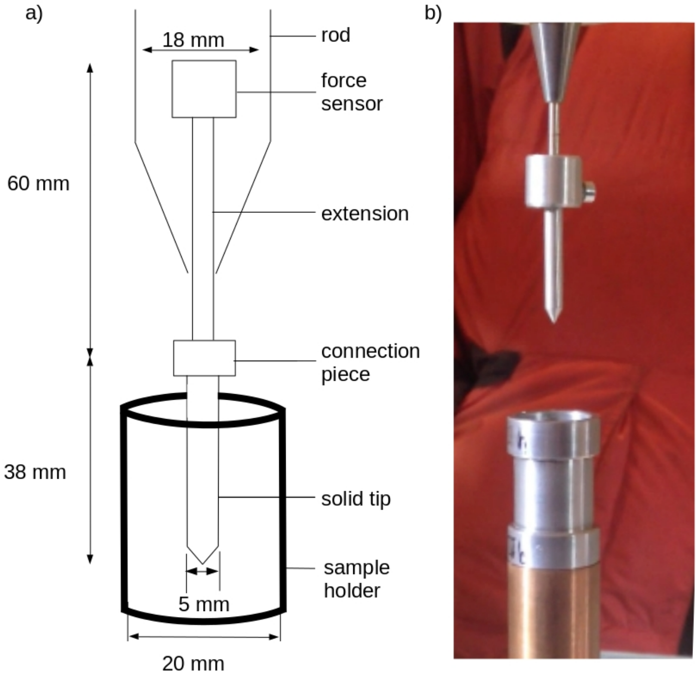

Figure 6.1: The experimental set-up: a) a scheme and b) a picture. Same figure as in chapter 5, Fig. 5.1

6.3 Methods

In this section we will recall the different methods we applied to analyse the μCT and the CPT data and we will present how we compared the different results.

6.3.1 Micromechanical analysis of the penetration force

One method to analyse high resolution penetration force profiles are statistical models, like the homogeneous poisson process (HPP) and its extension to the non-homogeneous model (NHPP), which were explained in Chapter 3. We will recall here the main assumptions of these models and how we applied them to our profiles. These inversion models assume that the recorded force is a superposition of spatially uncorrelated ruptures accordingly to a Poisson point process. Each rupture event corresponds to an elastic brittle failure of a bond (Fig. 6.2, inset). Over an analysis window, these events are assumed to be identical, but can occur at random depths. They are described by the following two microstructural properties: the deflection length δ and the rupture force f. The difference of the two methods HPP and NHPP, is that the HPP assumes a constant rupture occurrence rate λ, while the NHPP considers this rate to be dependent on depth, thus called λ_z.

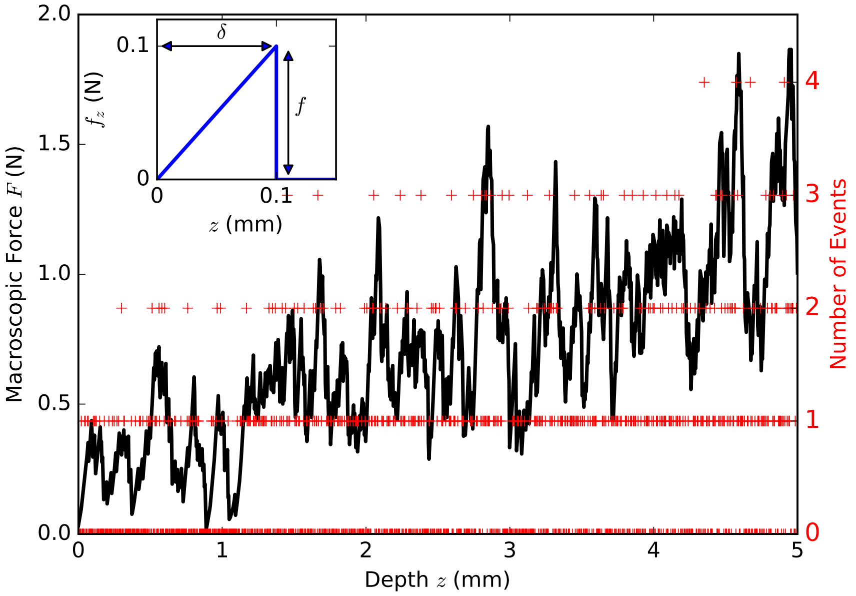

Figure 6.2: Simulated force penetration profile obtained as the superposition of uniform elastic brittle events (inset) whose number of occurrence follows a homogeneous Poisson distribution. Here, δ=0.1 mm, f=0.1 N, and λ_z is linearly increasing with depth: $\lambda_z(z) = a_\lambda z + b_\lambda$ with $a_\lambda = 40$ mm^{-2} and $b_\lambda = 50$ mm^{-1}. Source Figure: Peinke et al. [2019]

For our signals, we used for both methods an analyzing window of 3 mm. We chose this size, as the profiles are transitory and thus to have a compromise between a large enough window to get statistical correct values and a small enough window to assume stationary behaviour for the HPP and linear behaviour with depth for the NHPP. To compute the total number of broken bonds (N_{HPP} or N_{NHPP}), we multiplied the mean occurrence rate by the total depth of the force profile.

6.3.2 Grain tracking

In Chapter 5 we developed a morphological based grain tracking method to reconstruct the displacements of the grains caused by the CPT. This method requires the three-dimensional images of the initial and final state of the snow samples, as well as a grain segmentation. Thus, the tracking can only be applied on the samples containing a complete set of measurements (pre and post μCT image and CPT). An example of the resulting displacement field and the relative density change is shown in Fig. 6.3.

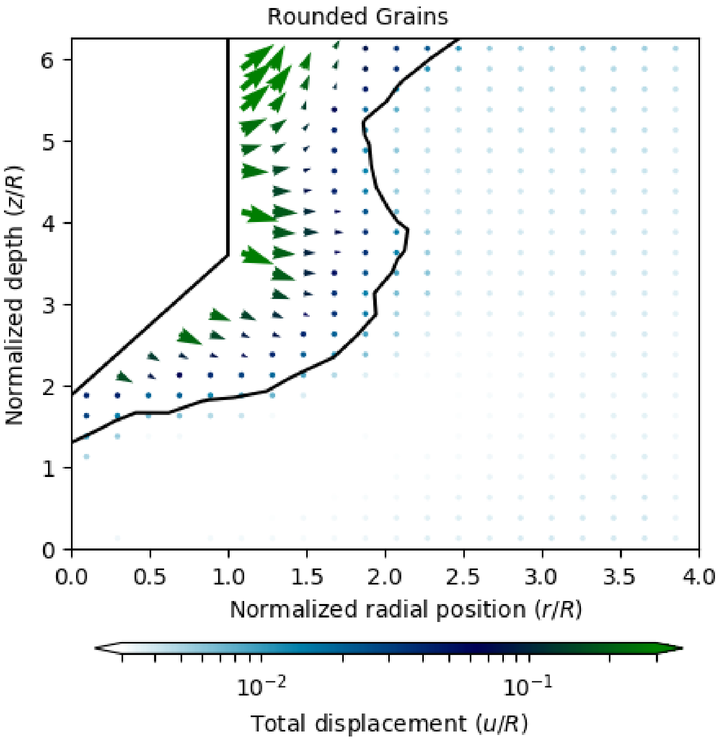

Figure 6.3: Example resulting from the displacement field for the snow sample RG1. The displacement field and deformation zone (contours) are computed with the tracking method presented in Chapter 5.

One inconvenience of the method is that it depends on an appropriate segmentation. We observed over-segmentation in our grains, i.e. not all the grains break up. It is not straightforward to identify all broken bonds. Bonds of the non-tracked grains can also break up. Nevertheless, the tracking method enabled us to obtain for the successfully tracked grains information about which bonds broke up and which stayed intact. Further, we could compute the surface of these bonds.

Here, the idea is to use the information of the broken bonds from the grain tracking results to estimate the mean size of the broken bonds and their total number. To this end, we assume that the number of tracked grains is high enough to be representative for the whole sample. Further we assume that non-tracked grains have large displacements. This assumption is reasonable, as we showed that almost all small displacements were found in Chapter 5. We will extrapolate the information of the tracked grains with large displacements to the lost grains.

In practice, we compute the adjacency matrix of the pre- and post-images. This matrix gives us information which grains are in contact and what size these contacts have. We define the size of the contact by the contact surface of two grains. From this matrix, we choose only the successfully tracked grains with larger displacements than 30 μm (2 voxels). A check with a higher threshold of 5 voxels lead to a difference in the broken bond number of less than 2 % for all samples (except 7 % for sample RGlr3). In a further step it was checked if the existing bond in the pre-image still exists in the post-image. If this is not the case, we know that the bond broke up. For the existing bonds, we introduce another check, in order to be sure that the bond did not break up due to the CPT and sintered afterwards. To this end, we compute the distance between the center of mass of the grains. For changes in distance higher than 4 voxels (two times the threshold for large displacements) the bond is detected as possibly broken. If then the bond size reduces more than 50% it is detected as broken. This check was added, as for some cases a different segmentation in both images leads to a change in the distance of the center of masses. We chose 50% as it was approximately the average of size change between the intact bonds in the pre-and post-image. The ratio of the broken bonds, obtained by this method, is multiplied by the total number of grains ($N_{tracking}$) with large displacements (i.e. the sum of the lost grains and the tracked grains with a displacement $> 30\ \mu$m). The bond size ($S_{tracking}$) is obtained by computing the mean surface of the detected broken bonds. The distribution of the bond size is not symmetric, much more smaller bonds exist than larger ones (Fig. 6.4).

This method is slightly dependent on the grain segmentation, as the broken contacts could be different from the detected contacts. Nevertheless, this difference is supposed to be small, as both grains are detected by the grain tracking method and thus are similar in shape.

6.3.3 Minimum cut density

The tracking method gave a first estimation of the bond number and bond size. Nevertheless, this method is dependent on the grain segmentation and how the interfaces between the grains are detected. The identification of the different grains of snow is not as obvious as for sand, for example. Hagenmuller et al. [2014 b]

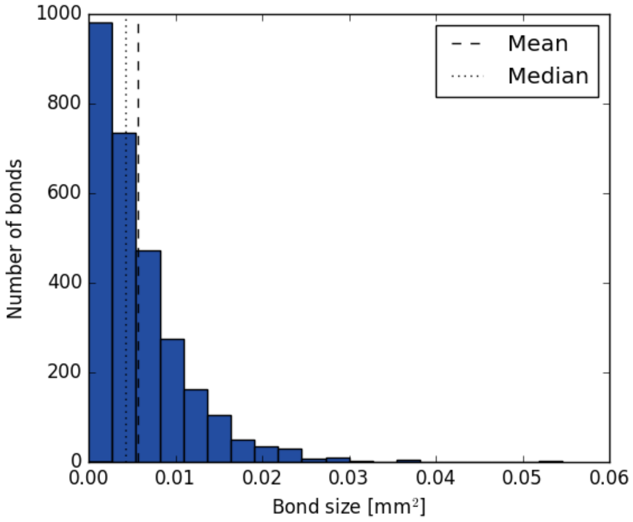

Figure 6.4: Distribution of the bond sizes obtained from the tracking method. The bond size correspond to the contact surface between two grains.

developed an algorithm that computes the minimal connection surface on three-dimensional microtomographical images of snow. This algorithm quantifies the mean characteristics of the intact bonds independently on their deformation (e.g. by penetration or traction). In our case this means, that we get information of the mean properties of the snow, and not the ones, which were activated by the CPT as with the previous methods. This section sums up the different properties obtained with this method and how the algorithm was applied to our samples.

The algorithm searches the minimum surface to separate the 3D image into 2 parts and is equal to the area of all the surfaces which disconnect the two parts (Fig. 6.5). The identified surface, called minimum cut surface, contains thus only a small fraction of the bonds. These bonds are expected to be most significant for traction experiments, as they are the first bonds which will break. For the penetration of a cone, which includes compaction, we can also expect larger bonds to break, as we expect the bonds under the tip to break. Hagenmuller et al. [2014 b] defined the minimal cut density as $\rho_{mc} = \rho_{ice} S/l^2$, with ρ_{ice} the density of ice, S the minimum cut surface computed in one direction (x,y or z) and l the side length of the cubic sample.

The minimum cut surface was computed on a sub-volume of 600x600x600 voxels of the initial μCT image with a reduced resolution having a voxel size of 30 μm. We computed the minimal cut density as well as the mean size of the areas which disconnect the two parts of the 3D images (black surfaces in Fig. 6.5). The obtained mean is called from now on mean bond size (S_{MinCut}). An example of the

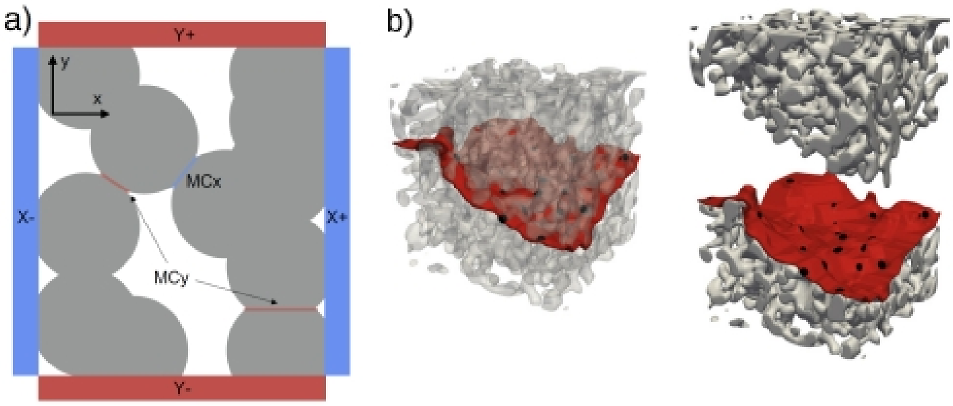

Figure 6.5: a) The minimum cut surface (MC): in blue the minimum cut surface between the faces X-/X+ and in red the minimum cut surface between faces Y-/Y+. b) the vertical minimal cut on an example of a 3D sample of RG. In black the disjoint small surfaces, which union will form the minimum cut surface. In red the surface connects these small surfaces. Hagenmuller et al. [2014 b]

obtained bond size distribution of sample RG1 (Fig. 6.6) shows a not symmetric distribution. We observe a lot of small bonds, corresponding to a bond size of 1 pixel (30x30 μm^2), but also some relatively large bonds. Thus the mean of the bond sizes is much higher than the median value.

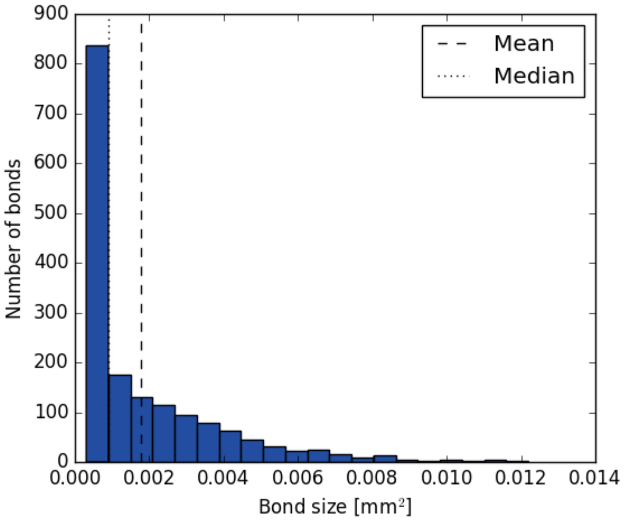

Figure 6.6: Distribution of the bond size of sample RG1.

6.3.4 Correlation analysis

We presented three different methods to obtain microstructural properties of the snow samples. Two methods based on the μCT images, while the third method is based on the recorded penetration force. To quantify the accuracy of the micromechanical properties, obtained by the inversion model, we correlate them to the corresponding properties, obtained from the μCT images. The correlation analysis was done on the logarithmic data using the package linregress of scipy. This package provides directly the R^2 and the p-value of the significance of the fit. It is a two-sided p-value for a hypothesis test. The null hypothesis is that the slope is zero and the statistical test uses the Wald Test with t-distribution. All correlations, which were shown in the results were within the 0.1% confident interval.

The estimated number of broken bonds ($N_{HPP,NHPP}$) can be directly compared to the broken bonds estimated from the tracking method ($N_{Tracking}$). Whereas, the micromechanical rupture force (f) cannot be directly measured from the μCT images. Nevertheless, the individual rupture force is reasonably supposed to correlate with the bond surface S. The force required to break the bond is assumed to fulfill the following condition: $f \leq \sigma_{ice}S$, σ_{ice} the strength of ice.

In the second part of the correlation analysis, we will compare the macroscopic properties, as density and SSA, obtained from the μCT images. To this end, we use the three micromechanical properties (f, δ, and λ), as they are obtained from the HPP and the NHPP. The depth dependent rupture occurrence rate λ_z was averaged over depth. With this correlation analysis we want to see which properties are the best for estimations of the density and SSA, like obtained by Proksch et al. [2015].

6.4 Results

The results will be divided into two parts, the first one is a direct evaluation of the estimates obtained by the micromechanical analysis of the force profiles. The second part presents the relations between micro- and macroscopic parameters.

6.4.1 Evaluation of micromechanical properties obtained from the force profiles

At first, the number of rupture obtained from the HPP and the NHPP is compared to the number of broken bonds estimated by the tracking method (Fig. 6.7). The correlation between the properties in a log scale is rather poor ($R^2 = 0.6$). The power law has a exponent of 3.3. For the snow samples of rounded grains more ruptures were predicted by the NHPP and HPP than detected by the tracking method. In opposite to this, the two models seem to underestimate the ruptures of RGlr and DH. No obvious difference between the HPP and the NHPP are shown; the HPP shows a slightly smaller exponent.

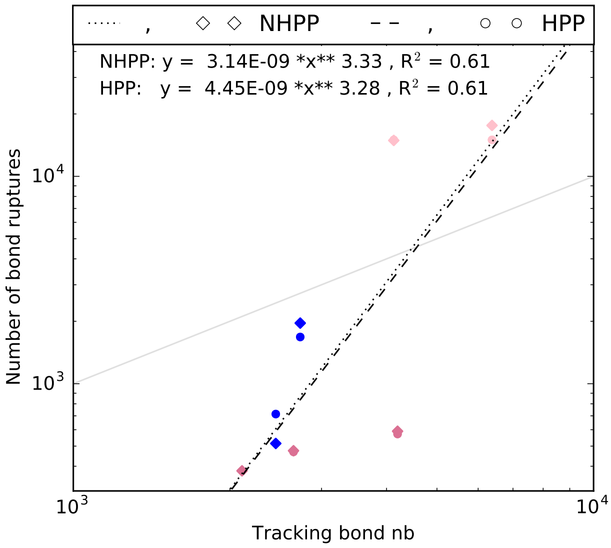

Figure 6.7: Comparison between the number of ruptures obtained from the HPP and the NHPP to the Number of detected bonds by the tracking method. The power law fit is represented by the dotted lines, and the light grey represents the 1:1 line. The colors correspond to the different snow types, classified according to Fierz et al. [2009].

The comparison of the micromechanical force with the bond surface, obtained by the minimum cut density (MinCut bond size, Fig. 6.8,a) has to take into account the fact that the MinCut bond sizes are the smallest bonds [Hagenmuller et al., 2014 b]. The HPP and the NHPP shows an almost quadratic relation between the two sizes. The correlation of HPP to the bond size is with $R^2 = 0.81$ better than the one of the NHPP ($R^2 = 0.67$).

Comparing the obtained rupture forces with the mean bond size obtained from the tracking shows quite different results for the exponents of the power law for the HPP and the NHPP (Tracking bond size, Fig. 6.8,b). The estimated rupture force shows a better correlation for the NHPP with the bond size than for the HPP. Both methods estimate a power law with an exponent >1, while the exponent is 2.2 for the HPP, so smaller than 3.4 for the NHPP.

6.4.2 Correlations between microstructural estimates and macroscopic properties

Mean and median penetration forces increase with density (see Fig. 6.9a). The exponent of the power law fit is close to one (especially for the median force), but

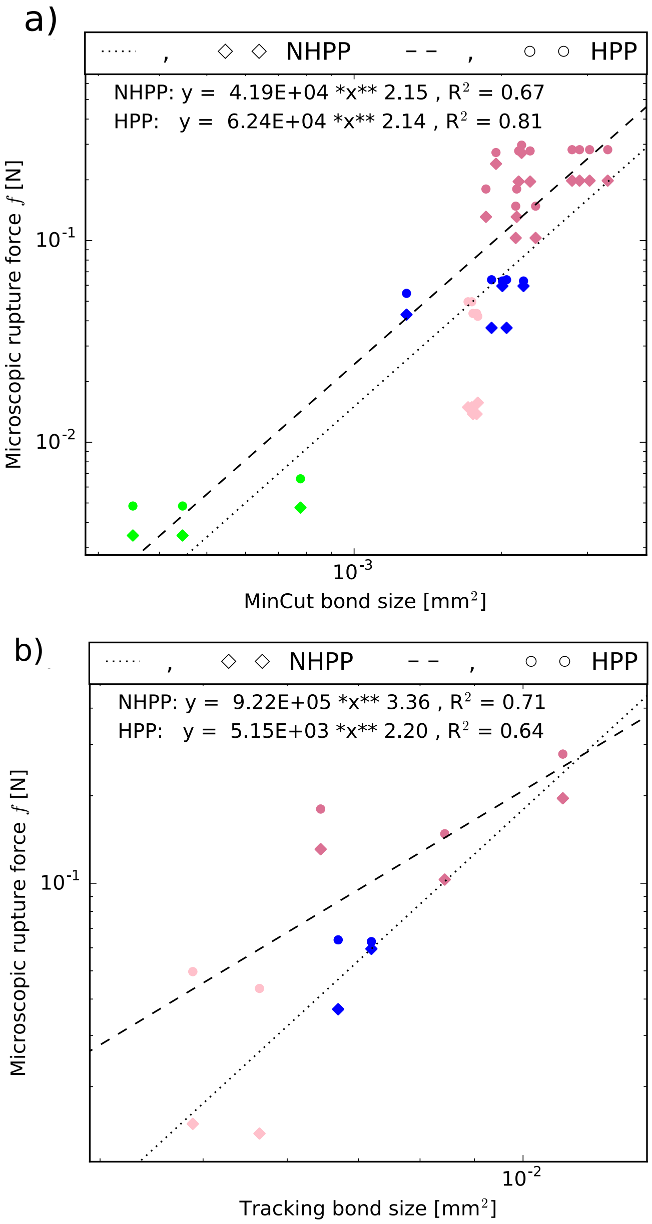

Figure 6.8: Comparison between the microscopic rupture force obtained from the HPP and the NHPP to the MinCut bond size (a) and to the tracking bond size (b). The power law fit is represented by the dotted lines. The colors correspond to the different snow types, classified according to Fierz et al. [2009].

the correlations are not very strong ($R^2 = 0.51$ for the median force and 0.67 for the mean force). In addition to this general relation, the measured forces show a dependency on the snow type, for example the snow types of RG and RGlr display similar mean penetration forces but different densities. The SSA shows even poorer correlations with the macroscopic force, and we observe a similar dependence on the grain type, which cannot be taken into account in this analysis (Fig. 6.9b).

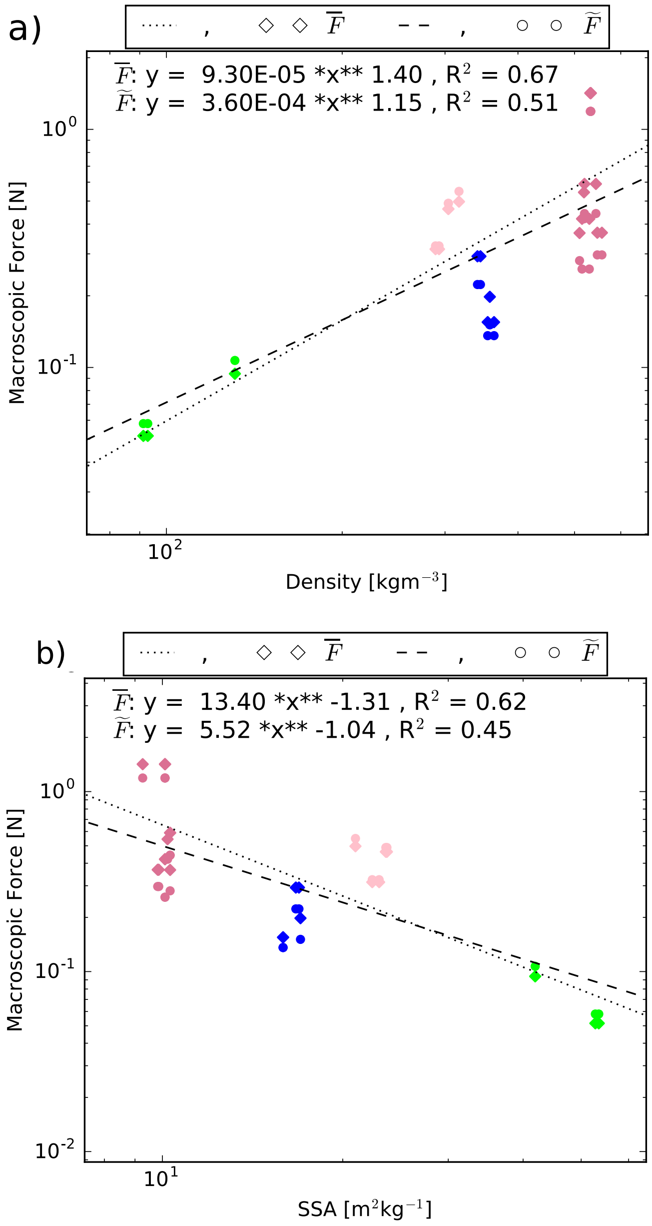

Figure 6.9: Comparison of the mean and median penetration forces ($\overline{F}$ and $\tilde{F}$) with density (a) and SSA (b). The power law fit is represented by the dotted lines. The colors correspond to the different snow types, classified according to Fierz et al. [2009].

The rupture intensity shows better correlations with the SSA than with the density (Fig. 6.10). For both correlation analysis, the HPP shows slightly better correlations and slightly higher exponents. In general, a decrease of rupture intensity with density is observed, while it is increasing with SSA. The samples of RG show the largest outliers from the fitted curve.

Further, we compared the other two micromechanical properties (δ, f) to the density and SSA (Figs. 6.11, 6.12). All the four fits show high correlations of

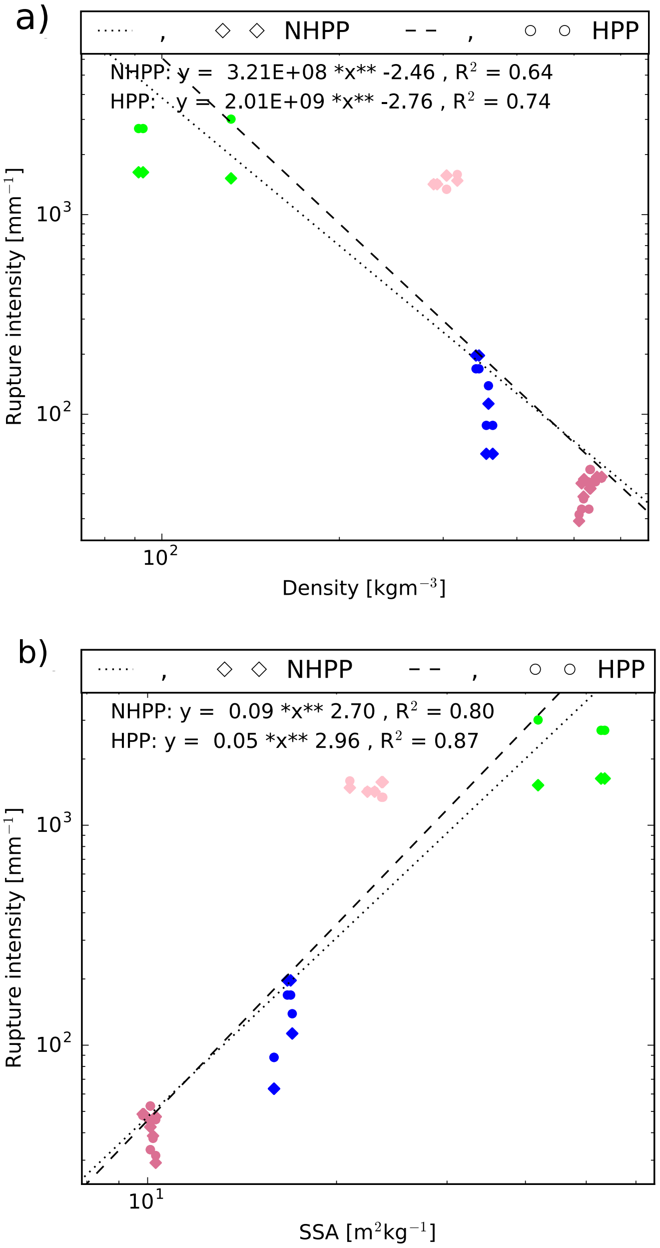

Figure 6.10: Comparison between rupture occurence rate obtained from the HPP and the NHPP to density (a) and SSA (b). The power law fit is represented by the dotted lines. The colors correspond to the different snow types, classified according to Fierz et al. [2009].

$R^2 > 0.8$. Again, the snow samples of RG deviate the strongest from the fit, but this discrepancy is less pronounced than for the intensity. The HPP and the NHPP show obvious differences in the estimation of the microscopic rupture force for the RG samples. For the other samples, the fits show much less scattered values. The correlations of the micromechanical properties with the SSA are better than the ones with the density, as already observed for the rupture intensity. The correlation coefficients (R^2) with SSA are above 0.9. A higher SSA corresponds to a smaller optical radius of the grains. We thus observe higher microscopic rupture forces and higher deflection at ruptures for the larger optical radii.

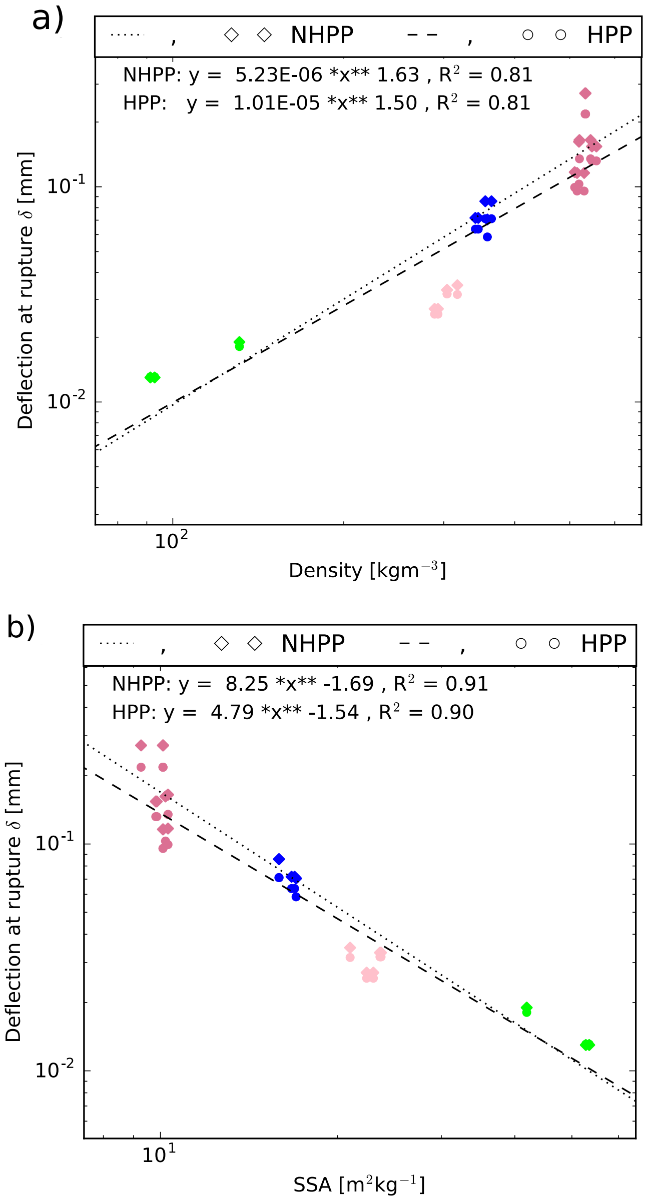

Figure 6.11: Comparison between the deflection at rupture obtained from HPP and NHPP to density (a) and SSA (b). The power law fit is represented by the dotted lines. The colors correspond to the different snow types, classified according to Fierz et al. [2009].

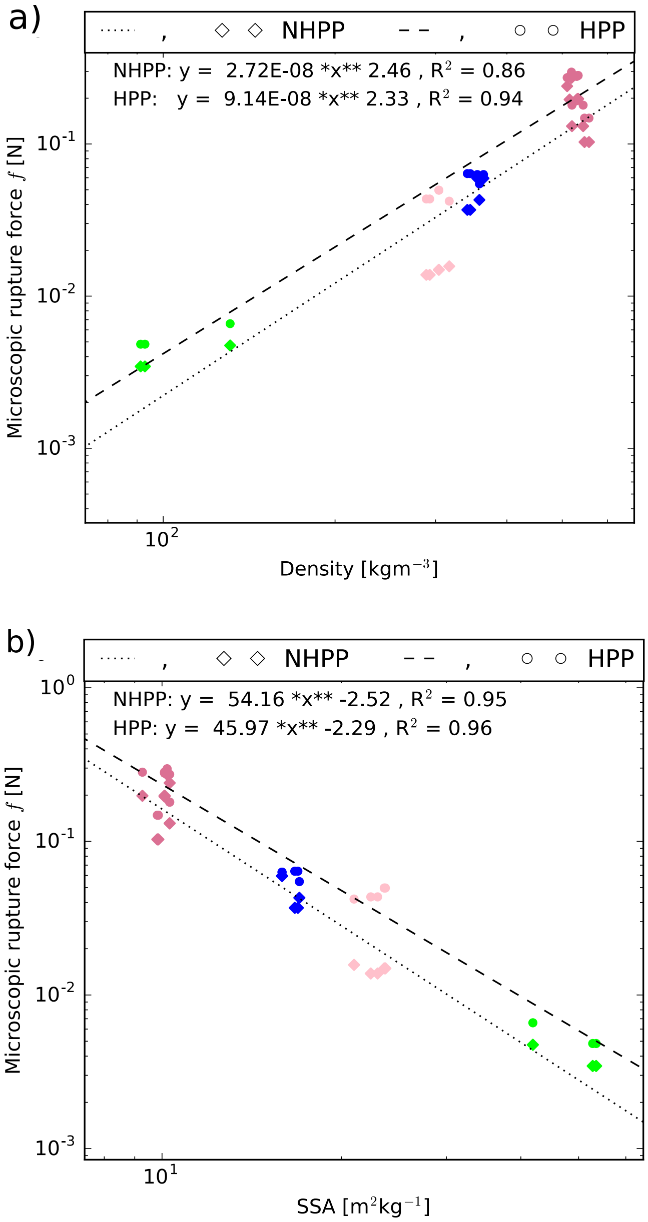

Figure 6.12: Comparison between the microscopic rupture force obtained from HPP and NHPP to density (a) and SSA (b). The power law fit is represented by the dotted lines. The colors correspond to the different snow types, classified according to Fierz et al. [2009].

6.5 Discussion and conclusion

A direct comparison of the micromechanical estimates from the NHPP and the HPP with the measured properties from the μCT images showed that the relation between them is not straightforward. For example, the power law regression between the number of broken bonds obtained by the HPP/NHPP and by the tracking method resulted in an exponent of 3.3. The HPP and the NHPP seem to underestimate the snow types with a smaller total number of bonds (like the RGlr and DH), while they overestimate the values for the RG sample with respect to the estimated number of broken bonds by the tracking method. The latter one is also only an estimation, as we did not track all the grains. Nevertheless, this method seems to be quite robust as the change of a threshold of large displacements from 2 to 5 voxels changed the total number of detected bond ruptures only by several per cents. Further, the power law regression between the microscopic rupture force $f_{HPP,NHPP}$ and the bond size (e.g. the contact surface between two grains) showed exponents of values between 2.1 and 3. The measured bond sizes are only estimations and dependent on the accuracy of the segmentation. We took the MinCut bond size and the tracking bond size as reference values, but this do not signify that these values contain no errors. For example, the actually broken bonds may not exactly correspond to the bond detected by the segmentation of the grains. Further, the distribution of the broken bond sizes is not symmetric. The bond sizes of the tracking neglected a lot grains with large displacements, as they were not found by the method. Larger displacements may lead to larger bonds, which broke up. The MinCut bond size, gives an general information of the weakest bonds in the snow sample, which are not necessarily the ones which break during the CPT. However, these possible errors do not explain such a large difference from the expected correlations. It let us suppose that the HPP/NHPP do not exactly represent the micromechanical values. A very strong assumption of the HPP and the NHPP is that the occurring ruptures are behaving in a perfectly elastic brittle behaviour and that they are independent. As the snow is a fragile material it is very likely that one rupture causes further ruptures. Further, the ruptures occurring due to the cone penetration may not have a perfect elastic brittle behaviour. It is very likely that internal friction took place in the CZ. Also friction between the tip shaft and the snow could have modified the estimates. This friction may be represented in the recorded penetration force. Further, all the occurring ruptures were assumed to be identical, which is clearly not the case. The bond size distribution showed us, that a large range of broken bond sizes exist (Fig. 6.4). Nevertheless, qualitatively the properties are behaving like expected. We have a positive correlation between them, which can be interpreted that there is a relation between the properties obtained from the different methods.

The second part of this chapter consisted in a power regression analysis between the micromechanical properties, obtained from the HPP/NHPP, and the macroscopic properties of the snow, obtained from the μCPT samples, namely the density and SSA. Proksch et al. [2015] proposed a model to estimate the density and the

SSA from the SMP. To this end, they used the median penetration force and the element size L which is directly related to the rupture intensity by the equation $L = (A_c/\lambda)^{1/3}$. A_c is the area of the cone tip of the penetrometer. They calibrated the coefficients of the model by combining SMP data with 3-D microstructural data from μCT. The computation of the element size L has in our point of view a weakness: it neglects the compaction zone as the intensity is divided by the surface of the cone tip. The element size is dependent on the compaction zone size and it is thus not pure material parameter, so it is maybe not the best parameter to rely on. Further, Reuter et al. [2019] mentioned that other microstructural parameters than the element size could be useful to improve the parametrization of snow density. They took the example of sintering, where the bond size increases with time and thus also the recorded macroscopic force, while the density stays almost constant [e.g. Herwijnen and Miller, 2013]. With our analysis we showed a better correlation for f and δ with density and SSA, than the correlation of the macroscopic force and the rupture intensity (and thus also the element size) with the density and SSA. We had 14 different snow samples with 24 μCT images. This sample set limited us to establish new correlations, but gave already enough information to conjecture that f and δ should be integrated in the estimation of SSA and density.

Our samples have small sintering times of a couple of days, thus the bonds are relatively small and similar in size. In a natural snowpack, the bonds between the grains have sintered longer and are thus supposed to be larger. Consequently, it may be interesting to conduct further studies with snow from the field. The advantage of such a micromechanical analysis with the SMP is that we are no longer limited to estimations of density and SSA, but can get precise knowledge of the snow mechanics. It is out of the scope of this thesis, but for fracture mechanisms it could be interesting to go further analyze the data in order to estimate more appropriate micromechanical properties of the snow.

7

Conclusion and perspectives

Contents

7.1 Conclusion

The general objective of this thesis was to investigate the cone penetration tests (CPT) in snow at microstructural scale and its ability to provide proxies of the snow microstructure. Existing inversion models do not take into account the processes happening around the cone tip during penetration. Indeed, it is known that a compaction zone exists. A single model takes this into account, the cavity expansion model, but for that model we have to assume a continuum medium. This assumption is only valid for small grain sizes and reaches its limits with our ratio of the SMP cone size and the snow grains. Further, no validation of these inversion models exists. To this end, we conducted experimental work: series of CPT measurements in snow evolving under controlled conditions and an experiment combining micro-tomographical imaging and CPT. On the modeling side, we proposed a new statistical analysis to interpret the force profile in terms of microstructural proxies of the snow. Besides, a new tracking method was developed to get the displacement field around the cone.

Operating with small penetration depths and thus transitory penetration force profiles, we had to adapt existing inversion models to interpret the force signal in terms of microstructural parameters. Therefore, we further developed the existing homogeneous Poisson model [Löwe and Herwijnen, 2012] to a non-homogeneous Poisson process [Peinke et al., 2019] (HPP and NHPP, respectively). The rupture occurrence rate is assumed to be depth dependent, while the deflection at rupture and the micromechanical rupture force are assumed to be constant over a certain analysis window. On simulated transient signals, the NHPP provided more accurate estimates of the microstructural parameters than the HPP. Indeed, for the HPP, it is difficult to find an analysis window large enough to be statistically representative and small enough that the assumption of a stationary signal is not broken.

We investigated sintering by measuring numerous CPT profiles conducted with a modified version of the SMP on snow samples characterized by different grain sizes during 24 hours. The application of the NHPP to these experiments revealed that the vertical heterogeneity of penetration force was essentially explained by variations of the rupture occurrence rate. Meanwhile, the time evolution of the macroscopic force was mainly due to an increase in the bond rupture force, i.e. due to microstructural bond strengthening. These two forces followed a power law with an average exponent of 0.27 and 0.29, respectively. These exponents are in agreement with sintering exponents in literature Herwijnen and Miller [e.g. 2013], Podolskiy et al. [e.g. 2014]. Already, Herwijnen and Miller [2013] conjectured that the main part of the increase in the measured force is due to bond growth. This result relied on the comparison of the sintering exponents obtained by experimental macroscopic force evolution and by modeled sintering at bond scale. We were able to show that NHPP is able to follow the sintering at microscopic scale and thus that the micromechanical properties can be interpreted physically. The samples used for our experiments were large rounded grains, which had forms close to spheres, thus we were sure that only sintering took place and no change in the grain shape. Nevertheless, the sample set with three different snow types was rather limited.

Further experiments consisted in monitoring snow metamorphism based on SMP measurements. To this end, we measured on a daily rhythm, during 3 weeks, the evolution of a snow sample obeying a temperature gradient, while a second sample was kept under isothermal conditions. The application of the inversion model to these experiments gave new insights into the micromechanical interpretation of the macroscopic force evolution. For isothermal conditions, an overall increase of the macroscopic force with time and depth was observed, which can be explained by bond strengthening (sintering). The increase of penetration force and bond strengthening with depth is probably due to the overburden weight of the snow, which causes an additional pressure on the grains and accelerates various sintering mechanisms [e.g. Flin et al., 2004]. The rupture occurrence rate and the deflection at rupture did not contribute to the macroscopic force increase, as the occurrence rate decreased slightly with time, while the deflection at rupture showed no obvious time evolution. The force measurement for the sample evolving under a temperature gradient, showed first a slight increase, followed by a drop in force and then increased slightly again. We observed by microscopy the first faceted snow grains appearing around the time where the force drop is observed, which might be its origin. It was not obvious to find a micromechanical property governing that process. The bond rupture force and the deflection at rupture showed a general increase with time. Conversely, the rupture occurrence rate showed a decrease with time. These results suggest that the small cohesion of faceted snow and depth hoar is due to the small amount of bonds even though these bonds can be strong. It would be interesting to verify this conjecture with data collected by microtomography, like from Calonne et al. [2015], Hagenmuller et al. [submitted].

Another study of this thesis consisted in applying the HPP and NHPP to SMP field measurements of two days and comparing the results of the two methods. In addition to the SMP profiles, for each day we took a detailed profile of density and SSA as the standard stratigraphy measurements. Further, we collected horizontal SMP measurements for several layers in order to have relatively long quasi stationary signals of a layer. In general, within a detected layer the NHPP showed less fluctuation of the estimated micromechanical properties than the HPP. Both methods detected the interfaces well, but the values differed sometimes. As no reference values exist, we used the horizontal measurements as reference. On these horizontal measurements, we could choose larger analysis windows and thus the resulting statistical estimates were better and similar for both methods. We can now compare the obtained values from the vertical profiles to the horizontal ones to find the best analysis window for the snowpack profiles. The NHPP with $\Delta z = 5$ mm and $w = 10$ mm showed the best results. For this window of 10 mm, the micromechanical rupture force and deflection at rupture are supposed to be constant over the depth, so small layers may be overlooked, which also happens when using the HPP with large windows. Larger windows can also lead to slightly different interpretations of the transition between two layers. Thus, it would be interesting to first divide the profile into the corresponding layers and then apply the inversion model to it.

These first results of the application of the HPP and NHPP to different studies showed that we can follow snow metamorphism at microscopic scale with high-resolution micro-cone penetration tests. The physical interpretation of these micromechanical properties are in agreement with literature [e.g. Blackford, 2007, Calonne et al., 2014]. The correctness of the values requires further studies.

Another part of this thesis was carrying out and analysing combined micro-tomographical and cone penetration measurements. As snow is a very active material due to its high homologous temperatures, it is not possible to do incremental penetration tests. Thus we measured high resolution three-dimensional images of the snow microstructure before and after the CPT. The challenge was to correctly reconstruct the displacement field based on the 3D images. Therefore, we developed a morphology based grain tracking algorithm. Most of the grains were successfully tracked between the two images. A downwards directed movement at the tip apex and an upwards movement close to the surface were observed, while between them the displacements were nearly only radial. The upwards movement was most pronounced for the samples with high densities (depth hoar and large rounded grains). For these samples, a dilation was observed whereas the samples of rounded grains and precipitation particles showed clear compaction. Further, no clear increase of the size of the compaction zone with density was observed. We compared our results to the cavity expansion model and found rather good coherence for the force measurements and for the mean radial displacement field, especially for the snow samples of rounded grains. Nevertheless, the density change obtained from the model was different from the measurements. Further, the observed vertical movement was not reproduced by the model. As it is a continuum model, it fails to reproduce the discrete nature of bond failure. In our cases the cone diameter to mean grain size ratio is close to the limit for assuming a continuum medium, which might explain deviations from the model.

Finally, we compared the micromechanical properties obtained by the inversion model with the microstructural properties obtained from the micro-tomographical images and the particle tracking. The particle tracking enables us to estimate a mean size of the broken bonds and their number. We had to assume that the successfully tracked grains are representative of all the grains in the sample. In addition to the tracking method, we applied the minimum cut density algorithm, developed by Hagenmuller et al. [2014 b]. This gave us the mean bond size of the smallest bonds and a minimum cut density. A correlation analysis showed no linear correlation between the computed total rupture occurrence by the inversion model and the estimated number of broken bonds from the tracking method. A power law regression estimated an exponent about 3 between the two properties, with a rather poor correlation $R^2 = 0.6$. We assumed that the microstructural rupture force is correlated to the bond size (i.e., to the mean surface of the bonds). We obtain correlations between $0.6 < R^2 \leq 0.8$ with exponents between 2 and 3. We thus assumed that the properties obtained by the inversion model do not represent exactly the corresponding micromechanical properties of the snow. Possible reasons for this can be found in the assumptions of the models, like the elastic brittle behaviour of the failures or the fact that the ruptures are supposed to occur independently. The friction between the cone tip and the grains is not taken into account in the model. It is very likely that internal friction happens in the compaction zone, which is also neglected. Further analysis of the correlation between the micromechanical and macroscopic properties showed that the micromechanical ones give better proxies than the macroscopic force. The best correlations were obtained for the microstructural rupture force to the SSA and to the density ($R^2 > 0.85$), even though the deflection at rupture showed good correlations to these two properties ($R^2 > 0.8$). In summary, this analysis showed that the estimated micromechanical properties are not representing directly the microstructure of the snow, but are better linked to macroscopic properties (as SSA and density) than the mean macroscopic force.

7.2 Perspectives

The work of the thesis is finished, but not the work of the subject. I present here some perspectives and ideas of what could be done next and for what this work can be used.

General perspectives:
The performances of the experiments were influenced by various limitations: for example the available snow, the set-ups (e.g. the CellDym or the SMP) or the time (e.g. 2 weeks of μCT experiments). Thus, I list here some ideas how the experiments could be improved and what we can learn for further experiments.
The sintering study was conducted on small layers with transitory profiles. We lengthened the tip so that the rod of the SMP did not touch the snow. We did the experiments only for 35 mm as then the connection piece touched the snow. A thinner connection piece, with the larger lengthening of 7 mm, could give longer profiles where the quasi stationary regime is obtained [Herwijnen, 2013]. Further, if the snow layer were larger, the effects of the bottom could be neglected. Besides, it would be interesting to have more samples, covering different seasonal snow types. We used only large rounded grains, which had the advantage that changes due to snow metamorphism could be neglected.
In our measurements series that aimed at monitoring snow metamorphism, we unfortunately missed the interesting period and had no measurements between day 4 and 7, when the drop in the macroscopic penetration force was observed. As mentioned earlier, it would be interesting to complete this analysis with μCT experiments, like from Calonne et al. [2015], Hagenmuller et al. [submitted]. Estimations of the size and number of bonds in a snow microstructure could be approached by the Minimal cut density approach from Hagenmuller et al. [2014 b]. Then, this could be compared to the behaviour we observed with the SMP and the inversion model.
Concerning field measurements, we used only one vertical profile to compare with the horizontal one, so it might be interesting to use more profiles for statistical analysis.
The combined experiments of μCT and CPT would have been much easier if the tomograph was in the cold room. This would not require the use of the CellDym and thus larger sample holder could be used. A taller snow sample would reduce the effects of the bottom and would allow deeper penetration depths. Furthermore, a longer tip would give a longer force measurement, which may then reach stationarity.

In addition, larger samples in diameter would assure that the force signal is not disturbed by side effects. As indicated in Chapter 2 and 4, we observed that the cylinders of 2 cm do slightly change the recorded force. Another important point is the friction of the tip: its cylindrical shape was important to avoid that the grains fell into the hole formed after penetration, but added friction to the measurement. Maybe the shaft of the tip could be a little smaller than the maximal tip as reported in literature [e.g. Bishop et al., 1945]. The correlation studies of chapter 6 gave us first results on the quality of the micromechanical estimates, but they could be improved with more samples to be statistically representative.
All the experiments conducted in my thesis were done with samples that had relatively short sintering times of a couple of days, so that a rather small growth of bonds occurred. Thus, the samples used only represent a subset of rounded grains that can be found in a natural snowpack. Several of these experiments, especially the ones of the μCT, would be interesting to perform with snow samples collected in the field.

Improvement of existing laws to estimate snow properties from the micro cone penetration tests:
Proksch et al. [2015] estimated snow properties, like the density and the SSA, from micromechanical analyses of the SMP signal. Therefore, they use the element size (defined as the mean size between two rupture events) and the median force. The computation of the element size does not take into account the compaction zone, which is formed in front of the cone during penetration. Both our experiments and Herwijnen [2013] shows that the presence of the compaction zone is not negligible. We showed quite a good correlation between the deflection at rupture and the SSA. It would be interesting to test if this relation gives better results. In addition to that, Reuter et al. [2019] mentioned that these two properties (element size and median force) cannot correctly characterize snow evolution during sintering (macroscopic force is increasing, but not the density). Our correlation results showed that the deflection at rupture as well as the microscopic bond strength are better correlated to the SSA and density than the macroscopic force and the rupture occurrence rate. We thus conclude that it would be interesting to work also with these properties to analyse the signal.

Discrete element model of the penetration test:
In granular soils several studies of discrete element models (DEM) exist to model the cone penetration test [e.g. Jiang et al., 2006, Butlanska et al., 2009]. DEM

models also exist for snow, like the one developed by Hagenmuller et al. [2015] and further developed by Mede et al. [2018a]. This model takes μCT images as input to reproduce the snow microstructure. Further, the model enables the simulation of large-strain response of snow samples and was used to model for example failure mechanism [Mede et al., 2018b]. The μCT images obtained in this thesis could be used as input to this model. Then the penetration of a cone could be modeled. The results of the model on the penetration force and on the deformation field could then be compared with the measurements. This could once help to evaluate the model and bridge the gap of the missing incremental data. The model, developed by Hagenmuller et al. [2015] was not yet evaluated by experiments, which is essential to give it credit. The incremental data could be studied to trace the exact displacement of the grains, and not only assume that the displacement is the direct trace between the initial and final position of the grain, like we did. It may also explain the origin of the force, for example how much internal friction exists. This would help to improve the existing inversion models and maybe find other inversion models based on the physics happening during penetration. Once the model is evaluated and validated, further tests for larger samples, different snow types could be done. It would also be interesting to study the geometry of the cone tip. Maybe another shape would give better results, or smaller compaction zones for example.

Link to other penetrometer in snow:
A better understanding of the processes happening next to the tip during penetration, as well as the link to the recorded force, could help to evaluate other existing snow penetrometers. Besides, it can help for the development of future penetrometers. Further studies of the cavity expansion model would be beneficial to get macroscopic properties of the snow, therefore larger penetrometers with smaller resolution would be sufficient. A recently developed penetrometer, the Scope from Mountainhub, has a lower resolution than the SMP but it is cheaper and smaller. It is integrated into a ski pole. Unfortunately, no study exists about the quality of this instrument. The idea of such a penetrometer, which can be used by skiers, for example, could provide a large area-covering information of the snowpack. This one would help the avalanche forecasters to improve their prediction of the avalanche risk evolution.

Conclusion et perspectives en français

Conclusions

L'objectif général de cette thèse était d'étudier les tests de pénétration du cône (CPT, cone penetration test en anglais) dans la neige à l'échelle de la microstructure ainsi que la capacité de dériver des paramètres microstructuraux de la neige à partir de ces tests. La plupart des modèles d'inversion existants ne prennent pas en compte les processus se déroulant localement autour de la pointe du cône lors de la pénétration, notamment l'effet de compaction de la neige. Un unique modèle prend cet effet en compte, le « cavity expansion model », mais nécessite de faire l'hypothèse d'un milieu continu. Cette hypothèse n'est valide que pour de petites tailles de grains et atteint sa limite avec le rapport entre les tailles du cône SMP et des grains de neige que nous avons ici. De plus, aucune validation de ces modèles d'inversion n'existe. Pour cela, nous avons mené un travail expérimental : une série de mesures de CPT dans différentes couches de neige évoluant sous conditions contrôlées et une expérience combinant imagerie par micro-tomographie et CPT. En ce qui concerne la modélisation, nous avons proposé une nouvelle analyse statistique permettant d'interpréter le profil de force obtenu lors d'un CPT en termes d'estimateurs de la microstructure de la neige. En outre, une nouvelle méthode de suivi a été développée pour obtenir le champ de déplacement autour du cône.

Les CPT étant réalisés sur des couches de neige de faibles profondeurs et obtenant donc des profils de force de pénétration transitoires, nous avons dû adapter les modèles d'inversion existants permettant d'interpréter le signal de force en termes de paramètres microstructuraux. Par conséquent, nous avons modifié un modèle existant [Löwe and Herwijnen, 2012] basé sur un processus de Poisson homogène (HPP, homogeneous Poisson process en anglais) afin de décrire un processus de Poisson non homogène (NHPP, non-homogeneous Poisson process en anglais). Le taux d'occurrence des ruptures est supposée dépendant de la profondeur, tandis que la déflexion à la rupture et la force de rupture micro-mécanique sont supposées constantes dans une certaine fenêtre d'analyse. Sur des signaux transitoires simulés, le NHPP a permis d'obtenir de meilleures estimations des paramètres de la microstructure que le HPP. En effet, pour le HPP, il est difficile de trouver une fenêtre d'analyse à la fois suffisamment grande pour être statistiquement représentative et suffisamment petite pour que l'hypothèse d'un signal stationnaire reste valide.

Nous avons étudié le phénomène de frittage en réalisant une série de profils de CPT avec une version modifiée du SMP pendant 24 heures sur des échantillons de neige de différentes tailles de grains. L'utilisation du modèle NHPP sur ces expériences a révélé que l'hétérogénéité verticale du signal de force de pénétration s'expliquait essentiellement par des variations du taux d'occurrence des ruptures. Dans le même temps, l'évolution temporelle de la force macroscopique était principalement due à une augmentation de la force de rupture des liaisons de glace entre grains, qui traduit une consolidation microstructurelle de ces liaisons. Ces deux forces suivaient une loi de puissance avec un exposant respectif de 0,27 et 0,29 en moyenne. Ces exposants sont en accord avec les exposants de frittage présentés dans la littérature. Herwijnen and Miller [2013] ont supposé que l'essentiel de l'augmentation de la force mesurée était dû à la croissance des liaisons entre grains. Ils se sont basés sur la comparaison d'une valeur expérimentale de l'exposant de la loi de puissance décrivant l'évolution de la force macroscopique à une valeur d'exposant obtenue à partir d'un modèle de frittage à l'échelle des ponts de glace. Nous avons pu montrer que le modèle NHPP était capable de reproduire le frittage à l'échelle microscopique et donc que les propriétés micro-mécaniques pouvaient être interprétées de manière physique. Les échantillons utilisés pour nos expériences étaient de la neige de type grains fins présentant des grains assez larges et de forme proche de sphères, où seul le frittage avait lieu (grossissement des liaisons de glace) mais la forme générale des grains ne changeait pas. Néanmoins, la série d'échantillons composée de trois types de neige différents était plutôt limitée.

D'autres expériences ont consisté à suivre les métamorphoses de la neige par des mesures SMP. Pour cela, nous avons mesuré quotidiennement l'évolution d'un échantillon de neige soumis à un gradient de température pendant 3 semaines, tandis qu'un deuxième échantillon était conservé dans des conditions d'isothermie. L'utilisation du modèle d'inversion sur ces expériences a permis d'interpréter l'évolution temporelle de la force macroscopique en termes micro-mécaniques. Pour les échantillons soumis à des conditions d'isothermie, une augmentation générale de la force macroscopique avec le temps et avec la profondeur a été observée, ce qui peut s'expliquer par la consolidation des liaisons de glace entre grains au cours du temps (frittage). L'augmentation de la force de pénétration et le renforcement des liaisons de glace avec la profondeur sont probablement dus au poids des couches supérieures de neige qui engendre une pression supplémentaire sur les couches sous-jacentes, ce qui amplifie divers mécanismes de frittage [e.g. Flin et al., 2004]. Le taux d'occurrence des ruptures et la déflexion à la rupture n'ont pas contribué à l'augmentation de la force macroscopique, car le taux d'occurrence a légèrement diminué au cours du temps tandis que la déflexion à la rupture ne présentait pas d'évolution évidente. Pour les échantillons soumis à un gradient de température, les mesures de force ont montré premièrement une légère augmentation, suivie d'une baisse, puis à nouveau une légère augmentation. Nous avons observé au microscope que l'apparition de grains de neige facettés coïncide à peu près avec le moment où une diminution de la force a été observée, ce qui pourrait en être l'origine. Nous n'avons pas pu mettre en évidence les propriétés micro-mécaniques qui régissaient ce processus. La force de rupture des liaisons de glace et la déflexion à la rupture ont augmenté de manière générale avec le temps. A l'inverse, le taux d'occurrence des ruptures a diminué avec le temps. Ces résultats suggèrent que la faible cohésion de la neige à faces planes et du givre de profondeur est due à la faible quantité de liaisons de glace entre grains, même si ces quelques liaisons peuvent être massives. Il serait intéressant de vérifier cette hypothèse avec les données obtenues par micro-tomographie, comme l'ont fait Calonne et al. [2015], Hagenmuller et al. [submitted]. L'estimation de la taille et du nombre de liaisons dans une microstructure de neige pourrait être effectuée en se basant sur la méthode de coupe de densité minimale de Hagenmuller et al. [2014 b].

Une autre étude de cette thèse a comparé les résultats des modèles HPP et NHPP avec les données issues de 2 jours de mesures SMP de terrain. En plus des profils SMP, nous avons établi chaque jour un profil détaillé de la densité et de la SSA, mesures stratigraphiques standards. Nous avons également réalisé des mesures de SMP horizontales pour plusieurs couches afin d'obtenir des signaux quasi-stationnaires relativement longs au sein d'une même couche. En général, le modèle NHPP présentait moins de fluctuation des propriétés micro-mécaniques estimées au sein d'une couche que le modèle HPP. Les deux méthodes détectaient correctement les interfaces entre couches, mais parfois leurs positions différaient. En l'absence de valeurs de référence, nous avons utilisé les mesures horizontales. À partir de ces mesures horizontales, nous avons pu choisir des fenêtres d'analyse plus grandes et ainsi obtenir de meilleures estimations statistiques qui étaient également similaires pour les deux méthodes. Nous avons ensuite pu comparer les valeurs obtenues à partir des profils verticaux à celles obtenues à partir des profils horizontaux afin de trouver la fenêtre d'analyse optimale pour les profils de manteau neigeux. Le NHPP a montré les meilleurs résultats avec $\Delta z = 5$ mm et $w = 10$ mm. Pour cette fenêtre de 10 mm, la force de rupture micro-mécanique et la déflexion à la rupture sont supposées être constantes sur la profondeur, de sorte que les couches fines peuvent être négligées, ce qui est également valable pour les grandes fenêtres du modèle HPP. Des fenêtres plus grandes peuvent également conduire à des interprétations légèrement différentes de la transition entre deux couches. Ainsi, il serait intéressant de commencer par diviser le profil en couches et ensuite d'appliquer le modèle d'inversion.

Ces premiers résultats de l'application des modèles PPH et NHPP à différentes études ont montré que nous pouvons suivre les métamorphoses de la neige à l'échelle microscopique avec des tests de micro-pénétration du cône à haute résolution. Les interprétations physiques des propriétés micro-mécaniques sont en accord avec la littérature. Néanmoins, d'autres études sont nécessaires pour évaluer plus amplement les valeurs obtenues.

Une autre partie de la thèse portait sur la réalisation et l'analyse de mesures combinées de micro-tomographie et de pénétration du cône. La neige étant un matériau pouvant évoluer rapidement en raison de ses températures homologues élevées, il n'est pas possible de faire des tests de pénétration incrémentaux. Ainsi, nous avons imagé en 3D et à haute résolution la microstructure des échantillons de neige avant et après le CPT. Le défi consistait à reconstruire correctement le champ de déplacement de la microstructure en se basant sur les images 3D. Par conséquent, nous avons développé un algorithme de suivi des grains de glace basé sur leurs morphologies. La plupart des grains ont été suivis avec succès entre deux images. Un déplacement vers le bas a été observé au sommet de la pointe, tandis qu'un mouvement vers le haut a été observé près de la surface. Entre ces deux zones, les déplacements étaient presque uniquement radiaux. Le mouvement ascendant était plus prononcé pour les échantillons de masse volumique élevée (givre de profondeur et gros grains fins), où une dilatation a été observée. A l'inverse, les échantillons de grains fins et de neige fraîche montraient une densification significative. En outre, aucune augmentation nette de la taille de la zone de densification avec la masse volumique n'a été observée. Nous avons comparé nos résultats au « cavity expansion model » et avons trouvé une bonne concordance pour le champ de déplacement radial moyen, en particulier pour les échantillons de neige de grains fins et pour les mesures de force. Néanmoins, le changement de masse volumique obtenu à partir du modèle était différent des mesures. De plus, le mouvement vertical observé n'a pas été reproduit par le modèle. Comme il s'agit d'un modèle supposant un milieu continu, il ne représente pas la nature discrète de la rupture d'une liaison de glace.

Enfin, nous avons comparé les propriétés micro-mécaniques obtenues avec le modèle d'inversion à celles obtenues à partir des images micro-tomographiques et du suivi de particules. Le suivi de particules nous a permis d'estimer la taille moyenne des liaisons rompues ainsi que leur nombre. Nous avons supposé que les grains suivis avec succès étaient représentatifs de l'ensemble des grains de l'échantillon. En plus de la méthode de suivi de grains, nous avons appliqué l'algorithme de densité de coupe minimale, développé par Hagenmuller et al. [2014 b] afin d'obtenir la taille moyenne minimale des liaisons de glace à couper pour séparer l'échantillon en deux ainsi que la densité de coupe minimale. Une analyse de corrélation a montré qu'il n'existe pas de corrélation linéaire entre l'occurrence de rupture totale calculée par le modèle d'inversion et le nombre de liaisons de glace rompues estimé à l'aide de la méthode de suivi de grains. Une relation de loi de puissance entre les deux propriétés a été testée, aboutissant à un exposant d'environ 3 et une corrélation plutôt faible de $R^2 = 0.6$. Nous avons supposé que la force de rupture microstructurelle était corrélée à la taille des liaisons (c'est-à-dire à la surface moyenne des liaisons) et avons obtenu des corrélations entre $0.6 < R^2 \leq 0.8$ et des exposants entre 2 et 3. Nous supposons donc que les propriétés obtenues par le modèle d'inversion ne représentent pas fidèlement les propriétés micro-mécaniques correspondantes de la neige. Des causes peuvent être trouvées dans les hypothèses des modèles, par exemple considérer un comportement élastique fragile des ruptures ou que les ruptures se produisent indépendamment. D'autre part, le frottement entre la pointe du cône et les grains n'est pas pris en compte dans le modèle. Il est aussi très probable que des frottements internes se produisent dans la zone de densification, également négligés. Une analyse plus poussée de la corrélation entre les propriétés micro-mécaniques et les propriétés macroscopiques a montré que les propriétés micro-mécaniques permettaient d'obtenir de meilleurs estimateurs que la force macroscopique. Les meilleures corrélations ont été obtenues pour la force de rupture microstructurelle par rapport à la SSA ou à la densité ($R^2 > 0.85$), mais la déflexion à la rupture a également montré de bonnes corrélations avec ces deux propriétés ($R^2 > 0.8$). En résumé, cette analyse a montré que les propriétés micro-mécaniques estimées ne permettent pas une représentation directe de la microstructure de la neige, mais sont davantage liées aux propriétés macroscopiques (comme la SSA et la masse volumique) que la force macroscopique moyenne.

Perspectives

Mon travail de thèse est terminé, mais pas le travail sur le sujet. Je présente ici quelques perspectives et idées de ce qu'il me semblerait intéressant de faire dans le futur et en quoi le travail présenté pourrait être utilisé.

Perspectives générales :

Les performances des expériences ont été influencées par diverses limitations comme la quantité et le type de neige disponibles, la configuration des instruments expérimentaux et de mesure (par exemple la CellDym ou le SMP) ou le temps (par exemple créneau de 2 semaines d'expériences de tomographie). Je vais donc énumérer ici quelques idées d'amélioration des expériences.

L'étude de frittage a été réalisée sur des couches fines à l'aide de profils CPT transitoires. Nous avons rallongé la pointe du SMP de manière à ce qu'elle seule touche la neige et non la tige du SMP. Les mesures n'étaient par ailleurs réalisées que sur 35 mm de profondeur, profondeur à partir de laquelle la tige du SMP touchait la neige. Une tige plus fine avec le rallongement de la pointe le plus important de 7 mm pourrait donner des profils plus longs, pour lesquels le régime quasi stationnaire est obtenu [Herwijnen, 2013]. D'autre part, la réalisation d'expériences avec une couche de neige plus épaisse permettrait de négliger les effets de bord (fond de la couche). Il serait également intéressant de disposer de plus d'échantillons couvrant différents types de neige saisonnières. Nous avons utilisé en effet uniquement de la neige de type grains fins de large taille ayant l'avantage d'évoluer très lentement au cours du temps dans les conditions de nos expériences, ce qui nous a permis de négliger ces modifications.

Dans les mesures de suivi des métamorphoses de la neige, la période intéressante est malheureusement manquante puisque aucune mesure n'a été réalisée entre le 4^e et 7^e jours, quand la chute de la force macroscopique de pénétration a été observée. Comme mentionné précédemment, il serait intéressant de compléter cette analyse par des expériences de tomographie, comme celles de Calonne et al. [2015], Hagenmuller et al. [submitted]. En utilisant la méthode de la densité de coupe minimale de Hagenmuller et al. [2014 b], la taille et le nombre de liaisons de glace dans une microstructure de neige pourraient être estimés à partir des images 3D. Cela pourrait ensuite être comparé au comportement observé avec les mesures SMP et le modèle d'inversion.

En ce qui concerne les mesures sur le terrain, nous n'avons utilisé qu'un seul profil vertical pour comparer aux profils horizontaux et il serait intéressant de faire l'analyse statistique avec plus de profils.
Les expériences combinées de tomographie et de TCP auraient été plus faciles à mettre en œuvre en utilisant un tomographe de chambre froide. Ainsi, nous n'aurions pas eu besoin d'utiliser la cellule de froid CellDym et de nous restreindre fortement sur la taille des échantillons de neige. Une hauteur de neige plus importante réduirait les effets du fond et permettrait une mesure de pénétration plus longue. De plus, des échantillons de diamètre plus grand garantiraient que le signal de force ne soit pas perturbé par des effets de bord. Comme indiqué aux chapitres 2 et 4, nous avons observé que des cylindres de 2 cm modifient légèrement la force enregistrée. Un autre point important est le frottement de la pointe du pénétromètre. La forme cylindrique de la pointe était importante pour éviter que les grains ne tombent dans le trou formé après la pénétration, mais augmentait le frottement lors de la mesure. Pour diminuer ce dernier, peut-être que le manche de la pointe pourrait être légèrement plus petit que la pointe maximale, comme indiqué dans la littérature [e.g. Bishop et al., 1945]. Les études de corrélation du chapitre 6 nous ont d'abord fourni des informations sur la qualité des estimations micro-mécaniques, mais pourraient être améliorées en utilisant davantage d'échantillons pour augmenter la représentation statistique.
Toutes les expériences menées dans ma thèse ont été effectuées avec des échantillons qui ont fritté durant des temps relativement courts (quelques jours), ce qui implique que les liaisons entre les grains ont peu grossi. Les échantillons utilisés ne représentent donc qu'une partie des grains fins rencontrés dans les manteaux neigeux naturels. Plusieurs de ces expériences, en particulier la tomographie, seraient intéressantes à réaliser avec de la neige naturelle collectée sur le terrain.

Amélioration des lois existantes pour estimer les propriétés de la neige à partir des tests de micro pénétration du cône :

Proksch et al. [2015] ont estimé les propriétés de la neige, telles que la masse volumique et la SSA, à partir d'analyses micromécaniques du signal SMP. Ils se basent sur la taille d'un élément (définie comme la taille moyenne entre deux événements de rupture) et la force médiane. Cependant, le calcul de la taille d'un élément ne prend pas en compte la zone de densification qui se forme devant le cône lors de la pénétration. Nos expériences ainsi que Herwijnen [2013] ont montré que la présence de la zone de densification n'était pas négligeable. Nous avons montré une assez bonne corrélation entre la déflexion à la rupture et la SSA. Il serait intéressant de vérifier si l'utilisation de cette relation permet d'obtenir de meilleures estimations. De plus, Reuter et al. [2019] ont mentionné que ces deux propriétés (taille d'un élément et force médiane) ne peuvent pas caractériser correctement l'évolution de la neige lors du frittage (la force macroscopique augmente, mais pas la masse volumique). Nos résultats montrent que la déflexion à la rupture et la force de liaison microscopique sont bien mieux corrélées à la SSA et la masse volumique que la force macroscopique et le taux d'occurrence des ruptures. Nous concluons donc qu'il serait intéressant de travailler également avec ces propriétés pour analyser le signal SMP.

Modèle d'éléments discrets du test de pénétration :
Il existe des modèles d'éléments discrets (DEM, discret element model en anglais) pour modéliser la microstructure de la neige et son comportement mécanique. Par exemple, le modèle développé par Mede et al. [2018a] utilise des images de tomographie en entrée pour reproduire la microstructure de la neige. Les images μCT, obtenues dans cette thèse, pourraient être utilisées comme entrée pour ce modèle et la pénétration d'un cône pourrait ensuite être modélisée. Les résultats du modèle, la force de pénétration et le champ de déformation pourraient ensuite être comparés aux mesures. Cela pourrait aider à évaluer le modèle mais également à combler le manque de données incrémentales. Le modèle, développé par Hagenmuller et al. [2015] n'a pas encore été évalué par des expériences, ce qui est essentiel pour le valider. Les données incrémentales pourraient être étudiées pour suivre le déplacement exact des grains, afin de ne pas avoir à interpoler le déplacement entre la position initiale et finale des grains comme nous l'avons fait. Cela pourrait aussi expliquer l'origine de la force et l'importance des frictions internes, par exemple. Cela aiderait à améliorer les modèles d'inversion existants et permettrait peut-être de développer d'autres modèles d'inversion basés sur la physique en oeuvre lors de la pénétration. Une fois le modèle évalué et validé, des tests supplémentaires pour des échantillons plus grands et de différents types de neige pourraient être effectués. Il serait également intéressant d'étudier la géométrie de la pointe du cône. Peut-être qu'une autre forme donnerait de meilleurs résultats, ou des zones de densification plus petites par exemple.

Bibliography

E. Andò, S. A. Hall, G. Viggiani, J. Desrues, and P. Bésuelle. Grain-scale experimental investigation of localised deformation in sand: a discrete particle tracking approach. *Acta Geotech.*, 7(1):1–13, Mar 2012. ISSN 1861-1133. doi: 10.1007/s11440-011-0151-6.

L. Arnaud, V. Lipenkov, J.-M. Barnola, M. Gay, and P. Duval. Modelling of the densification of polar firn: characterization of the snow–firn transition. *Annals of Glaciology*, 26:39–44, 1998. doi: 10.1017/s026030550001452x.

M. Arshad, F. Tehrani, M. Prezzi, and R. Salgado. Experimental study of cone penetration in silica sand using digital image correlation. *Géotechnique*, 64(7): 551–569, 2014. doi: 10.1680/geot.13.P.179.

Avatech. *SP1 Owner's Manual*, 2014. URL `http://s3.amazonaws.com/sp1manual/AvatechSP1UserManualEnglish1114.pdf`.

H. Bader, R. Haefeli, E. Bucher, J. Neher, O. Eckel, and C. Thams. Der Schnee und seine Metamorphose. Beiträge zur Geologie der Schweiz. Schweizerische Schnee- und Lawinenforschungskommission (Snow and its metamorphism). *SIPRE Trans.*, 14:1954, 1939.

T. P. Barnett, J. C. Adam, and D. P. Lettenmaier. Potential impacts of a warming climate on water availability in snow-dominated regions. *Nature*, 438:303–309, 2005. doi: 10.1038/nature04141.

S. Bellaire, C. Pielmeier, M. Schneebeli, and J. Schweizer. Stability algorithm for snow micro-penetrometer measurements. *J. Glaciol.*, 55(193):805–813, 2009. doi: 10.3189/002214309790152582.

T. Bergeron. On the physics of cloud and precipitation. *5th Assembly of the U.G.G.I. Paul Dupont, Paris*, pages 156–178, 1935.

K. Birkeland, K. Kronholm, M. Schneebeli, and C. Pielmeier. Changes in the shear strength and micro-penetration hardness of a buried surface-hoar layer. *Ann. Glaciol*, 38:223–228, 2004. doi: 10.3189/172756404781815167.

K. Birkeland, K. Kronholm, S. Logan, and J. Schweizer. Field measurements of sintering after fracture of snowpack weak layers. *Geophys. Res. Lett.*, 33(L03501), 2006. doi: 10.1029/2005gl025104.

R. F. Bishop, R. Hill, and N. F Mott. The theory of indentation hardness tests. *Proceedings of the Physical Society*, 57(321), 1945. doi: 10.1088/0959-5309/57/3/301.

J. Blackford. Sintering and microstructure of ice: a review. *J. Phys. D: Appl. Phys.*, 40:R355–R385, 2007. doi: 10.1088/0022-3727/40/21/r02.

F. Boas. *Handbook of American Indian Languages.* Number n° 1 in Bulletin (Smithsonian Institution. Bureau of American Ethnology). U.S. Government Printing Office, 1911.

P. T. Boggs and J. E. Rogers. Orthogonal distance regression. In C. Mathematics, editor, *Statistical analysis of measurement error models and applications: proceedings of the AMS-IMS-SIAM joint summer research conference held June 10-16, 1989*, number 112, page 186, 1990. doi: 10.1090/conm/112/1087109.

M. D. Bolton, M. W. Gui, and R. Phillips. Review of miniature soil probes for model tests. In *Proceedings of the 11th Southeast Asian Geotechnical Conference*, pages 85–90, 1993.

C. C. Bradley. The snow resistograph and slab avalanche investigations. *International Association of Scientific Hydrology Publication*, 36, 1966.

C. C. Bradley. Instruments and methods: The resistograph and the compressive strength of snow. *J. Glaciol.*, 7(51):499–506, 1968. doi: 10.3189/S0022143000020682.

R. Brown and K. Birkeland. A comparison of the digital resistograph with the ram penetrometer. In *Proceedings International Snow Science Workshop, Bigfork, MT, USA*, pages 19–30. Citeseer, 1990.

J.-B. Brzoska, C. Coléou, B. Lesaffre, S. Borel, O. Brissaud, W. Ludwig, E. Boller, and J. Baruchel. 3D visualization of snow samples by microtomography at low temperature. *ESRF Newsletter*, 32:22–23, 1999.

J. Butlanska, M. Arroyo, and A. Gens. Homogeneity and symmetry in DEM models of cone penetration. *Powders and Grains*, 1145:425–428, 2009. doi: 10.1063/1.3179952.

N. Calonne, F. Flin, C. Geindreau, B. Lesaffre, and S. Rolland du Roscoat. Study of a temperature gradient metamorphism of snow from 3-d images: time evolution of microstructures, physical properties and their associated anisotropy. *The Cryosphere*, 8(6):2255–2274, 2014. doi: 10.5194/tc-8-2255-2014.

N. Calonne, F. Flin, B. Lesaffre, A. Dufour, J. Roulle, P. Puglièse, A. Philip, F. Lahoucine, C. Geindreau, J.-M. Panel, S. Rolland du Roscoat, and P. Charrier. CellDyM: A room temperature operating cryogenic cell for the dynamic monitoring of snow metamorphism by time-lapse X-ray microtomography. *Geophys. Res. Lett.*, 42(10):3911–3918, 2015. doi: 10.1002/2015gl063541.

C. Chandel, P. Srivastava, and A. Upadhyay. Estimation of rheological properties of snow subjected to creep. *Defence Science Journal*, 57(4):393–401, Jul. 2007. doi: 10.14429/dsj.57.1786.

C. Chandel, P. K. Srivastava, and P. Mahajan. Micromechanical analysis of deformation of snow using X-ray tomography. *Cold Reg. Sci. Technol.*, 101:14 – 23, 2014. ISSN 0165-232X. doi: https://doi.org/10.1016/j.coldregions.2014.01.005.

S. Chen and I. Baker. Structural evolution during ice-sphere sintering. *Hydrol. Processes*, 24(14):2034–2040, 2010. doi: 10.1002/hyp.7787.

S. C. Colbeck. An overview of seasonal snow metamorphism. *Rev. Geophys.*, 20(1): 45–61, 1982. doi: 10.1029/rg020i001p00045.

S. C. Colbeck. A review of sintering in seasonal snow. *CRREL Report, US Army Corps of Engineers, Cold Regions Research & Engineering Laboratory*, pages 97–10, 1997. doi: 10.21236/ada335556.

C. Coleou, B. Lesaffre, J.-B. Brzoska, W. Ludwig, and E. Boller. Three-dimensional snow images by x-ray microtomography. *Ann Glaciol*, 32:75–81, 2001. doi: 10.3189/172756401781819418.

M. de Quervain. Die Festigkeitseigenschaften der Schneedecke und ihre Messung. *Geofisica pura e applicata*, 18(1):179–191, Dec 1950. ISSN 1420-9136. doi: 10.1007/BF02000325.

T. Dowd and R. L. Brown. A new instrument for determining strength profiles in snow cover. *Journal of Glaciology*, 32(111):299–301, 1986. doi: 10.3189/S0022143000015628.

Y. Durand, G. Giraud, E. Brun, L. Mérindol, and E. Martin. A computer-based system simulating snowpack structures as a tool for regional avalanche forecasting. *J. Glaciol.*, 45:469–484, 1999. doi: 10.3189/s0022143000001337.

M. Fauve, H. Rhyner, and M. Schneebeli. *Préparation et entretien des pistes. Manuel pour le praticien.* Davos, Institut fédérale pour l'étude de la neige et des avalanches, 2002.

C. Fierz, R. L. Armstrong, Y. Durand, P. Etchevers, E. Greene, D. M. McClung, K. Nishimura, P. K. Satyawali, and S. A. Sokratov. The international classification for seasonal snow on the ground. *Tech. Doc. Hydrol., 83, UNESCO, Paris*, 2009.

F. Flin and J.-B. Brzoska. The temperature-gradient metamorphism of snow: vapour diffusion model and application to tomographic images. *Annals of Glaciology*, 49: 17–21, 2008. doi: 10.3189/172756408787814834.

F. Flin, J.-B. Brzoska, B. Lesaffre, C. Coléou, and R. A. Pieritz. Three-dimensional geometric measurements of snow microstructural evolution under isothermal conditions. *Ann. Glaciol.*, 38:39–44, 2004. doi: 10.3189/172756404781814942.

J. Floyer. *Layer detection and snowpack stratigraphy characterisation from digital penetrometer signals.* PhD thesis, University of Calgary, 2008.

J. Floyer and B. Jamieson. Predicting the fracture character of weak layers from snowpack penetrometer signals. *Cold Reg. Sci. Technol.*, 59(2-3):185–192, 2009. doi: 10.1016/j.coldregions.2009.06.008.

J. Floyer and J. Jamieson. Avalanche weak layer tracing and detection in snow penetrometer profiles. In *Proceedings of the 4th Canadian Conference on Geohazards, Quebec City, QC*, pages 161–168. Citeseer, 2008.

J. Floyer and J. Jamieson. Rate-effect experiments on round-tipped penetrometer insertion into uniform snow. *J. Glaciol.*, 56(198):664–672, 2010. doi: 10.3189/002214310793146322.

J. A. Floyer and J. B. Jamieson. Empirical analysis of snow deformation below penetrometer tips. In *Proceedings of the International Snow Workshop*, pages 555–561, Telluride, Colorado, 2006.

J. Frenkel. Viscous flow of crystalline bodies under the action of surface tension. *Journal of Physics U.S.S.R.*, 9(5):385–431, 1945.

M. Fukue. *Mechanical performance of snow under loading.* PhD thesis, McGill University, 1977.

J.-C. Gallet, F. Domine, C. S. Zender, and G. Picard. Measurement of the specific surface area of snow using infrared reflectance in an integrating sphere at 1310 and 1550 nm. *The Cryosphere*, 3:167–182, 2009. doi: 10.5194/tc-3-167-2009.

J. Gaume, J. Schweizer, A. van Herwijnen, G. Chambon, B. Reuter, N. Eckert, and M. Naaim. Evaluation of slope stability with respect to snowpack spatial variability. *Journal of Geophysical Research: Earth Surface*, 119(9):1783–1799, 2014. doi: 10.1002/2014jf003193.

B. Gerling, H. Löwe, and A. Van Herwijnen. Measuring the elastic modulus of snow. *Geophys. Res. Lett.*, 44(21):11–088, 2017. doi: 10.1002/2017gl075110.

W. Good. Thin sections, serial cuts and 3-D analysis of snow. *IAHS Publ*, 162: 35–48, 1987.

A. Gow. Time - temperature dependence of sintering in perennial isothermal snowpacks. *Snow Mechanics*, 114:25–41, 1975.

H. Gubler. Determination of the mean number of bonds per snow grain and of the dependence of the tensile strength of snow on stereological parameters. *J. Glaciol.*, 20:329–341, 1978. doi: 10.3189/s0022143000013885.

P. Hagenmuller. *Modélisation du comportement mécanique de la neige à partir d'images microtomographiques.* PhD thesis, Université de Grenoble, 2014.

P. Hagenmuller and T. Pilloix. A new method for comparing and matching snow profiles, application for profiles measured by penetrometers. *Front. Earth Sci.*, 4: 52, 2016. ISSN 2296-6463. doi: 10.3389/feart.2016.00052.

P. Hagenmuller, G. Chambon, B. Lesaffre, F. Flin, and M. Naaim. Energy-based binary segmentation of snow microtomographic images. *J. Glaciol.*, 59:859–873, 05 2013. doi: 10.3189/2013JoG13J035.

P. Hagenmuller, G. Chambon, F. Flin, S. Morin, and M. Naaim. Snow as a granular material: assessment of a new grain segmentation algorithm. *Granular Matter*, 16(4):421–432, Aug 2014. ISSN 1434-7636. doi: 10.1007/s10035-014-0503-7.

P. Hagenmuller, N. Calonne, G. Chambon, F. Flin, C. Geindreau, and M. Naaim. Characterization of the snow microstructural bonding system through the minimum cut density. *Cold Reg. Sci. Technol.*, 108:72 – 79, 2014 b. ISSN 0165-232X. doi: https://doi.org/10.1016/j.coldregions.2014.09.002.

P. Hagenmuller, G. Chambon, and M. Naaim. Microstructure-based modeling of snow mechanics: a discrete element approach. *The Cryosphere*, 9:1969–1982, 2015. doi: 10.5194/tc-9-1969-2015.

P. Hagenmuller, M. Matzl, G. Chambon, and M. Schneebeli. Sensitivity of snow density and specific surface area measured by microtomography to different image processing algorithms. *The Cryosphere*, 10(3):1039–1054, 2016. doi: 10.5194/tc-10-1039-2016.

P. Hagenmuller, A. van Herwijnen, C. Pielmeier, and H.-P. Marshall. Evaluation of the snow penetrometer avatech SP2. *Cold Reg. Sci. Technol.*, 149:83 – 94, 2018a. ISSN 0165-232X. doi: 10.1016/j.coldregions.2018.02.006.

P. Hagenmuller, L. Viallon, C. Bouchayer, M. Teich, M. Lafaysse, and V. Vionnet. A new metric between vertical snow profiles using dynamic time warping. In *EGU General Assembly*, 2018b.

P. Hagenmuller, F. Flin, M. Dumont, F. Tuzet, I. Peinke, P. Lapalus, A. Dufour, J. Roulle, L.Pezard, D. Voisin, E. Ando, S. R. du Roscoat, and P. Charriernd. Motion of dust particles in dry snow under temperature gradient metamorphism. *The Cryosphere*, submitted.

S. Hall, M. Bornert, J. Desrues, Y. Pannier, N. Lenoir, G. Viggiani, and P. Bésuelle. Discrete and continuum analysis of localised deformation in sand using X-ray CT and volumetric digital image correlation. *Géotechnique*, 60, 01 2010. doi: 10.1680/geot.2010.60.5.315.

M. Heggli, E. Frei, and M. Schneebeli. Snow replica method for three-dimensional x-ray microtomographic imaging. *J. Glaciol.*, 55(192):631–639, 2009. doi: 10.3189/002214309789470932.

A. Herwijnen and D. A. Miller. Experimental and numerical investigation of the sintering rate of snow. *J. Glaciol.*, 59(213):1–6, 2013. doi: 10.3189/2013jog12j094.

A. V. Herwijnen. Experimental analysis of snow micropenetrometer (SMP) cone penetration in homogeneous snow layers. *Can. Geotech. J.*, 50:1044–1054, 2013. doi: 10.1139/cgj-2012-0336.

A. V. Herwijnen, S. Bellaire, and J. Schweizer. Comparison of micro-structural snowpack parameters derived from penetration resistance measurements with fracture character observations from compression tests. *Cold Reg. Sci. Technol.*, 59:193–201, 2009. doi: 10.1016/j.coldregions.2009.06.006.

P. V. Hobbs and B. J. Mason. The sintering and adhesion of ice. *Philos. Mag.*, 9 (98):181–197, 1964. doi: 10.1080/14786436408229184.

J. B. Jamieson and J. Schweizer. Texture and strength changes of buried surface-hoar layers with implications for dry snow-slab avalanche release. *Journal of Glaciology*, 46(152):151–160, 2000. doi: 10.3189/172756500781833278.

M. Jiang, H.-S. Yu, and D. Harris. Discrete element modelling of deep penetration in granular soils. *Int. J. Numer. Anal. Meth. Geomech.*, 30:335–361, 2006. doi: 10.1002/nag.473.

J. Johnson. A statistical micromechanical theory of cone penetration in granular materials. *ERDC/CRREL. Technical Report 03-3.*, 51(174):1–12, 2003.

J. Johnson and M. Hopkins. Identifying microstructural deformation mechanisms in snow using discrete-element modeling. *J. Glaciol.*, 51, 2005. doi: 10.3189/172756505781829188.

J. Johnson and M. Schneebeli. Characterizing the microstructural and micromechanical properties of snow. *Cold Reg. Sci. Technol.*, 30:91–100, 1999. doi: 10.1016/s0165-232x(99)00013-0.

T. Kaempfer and M. Schneebeli. Observation of isothermal metamorphism of new snow and interpretation as a sintering process. *Journal of Geophysical Research (Atmospheres)*, 112, 12 2007. doi: 10.1029/2007JD009047.

L. Kaplan. Inuit snow terms: How many and what does it mean? In *Building Capacity in Arctic Societies: Dynamics and shifting perspectives. 2nd IPSSAS Seminar*, Iqaluit, Nunavut, Canada, May 26 - June 6, 2003. Montréal: Université Laval.

S. Kaur and P. Satyawali. Estimation of snow density from SnowMicroPen measurements. *Cold Reg. Sci. Technol.*, 134:1 – 10, 2017. ISSN 0165-232X. doi: 10.1016/j.coldregions.2016.11.001.

J. Kepler. *The Six-Cornered Snowflake.* Oxford: Clarendon P., 1966.

W. D. Kingery. Regelation, surface diffusion, and ice sintering. *J. Appl. Phys.*, 31: 833–838, 1960. doi: 10.1007/978-94-009-0741-6_31.

K. Kronholm, M. Schneebeli, and J. Schweizer. Spatial variability of micropenetration resistance in snow layers on a small slope. *Ann. Glaciol*, 38:202–208, 2004. doi: 10.3189/172756404781815257.

P. R. Kry. Quantitative stereological analysis of grain bonds in snow. *J. Glaciol.*, 14(72):467–477, 1975. doi: 10.3189/S0022143000021973.

G. C. Kuczynski. Self-diffusion in sintering of metallic particles. *Transactions of AIME*, 185:169–178, 1949. doi: 10.1007/bf03398090.

D. Kuroiwa. A study of ice sintering. *Tellus*, 13, 1961. doi: 10.1111/j.2153-3490.1961.tb00082.x.

A. LeBaron, D. Miller, and A. van Herwijnen. Measurements of the deformation zone around a split-axis snow micropenetrometer tip. *Cold Reg. Sci. Technol.*, 97: 90 – 96, 2014. ISSN 0165-232X. doi: 10.1016/j.coldregions.2013.10.008.

B. Lesaffre, E. Pougatch, and E. Martin. Objective determination of snow-grain characteristics from images. *Ann. Glaciol.*, 26:112–118, 01 1998. doi: 10.1017/S026030550001466X.

K. Libbrecht. The physics of snow crystals. *Rep. Prog. Phys.*, 68, 04 2005. doi: 10.1088/0034-4885/68/4/R03.

M. Y. Louge, R. L. Foster, N. Jensen, and R. Patterson. A portable capacitance snow sounding instrument. *Cold Regions Science and Technology*, 28(2):73–81, 1998. ISSN 0165-232X. doi: https://doi.org/10.1016/S0165-232X(98)00015-9.

H. Löwe and A. Herwijnen. A Poisson shot noise model for micro-penetration of snow. *Cold Reg. Sci. Technol.*, 70:62–70, 2012. doi: 10.1016/j.coldregions.2011.09.001.

E. Lutz, K. W. Birkeland, K. Kronholm, K. Hansen, and R. Aspinall. Surface hoar characteristics derived from a snow micropenetrometer using moving window statistical operations. *Cold Reg. Sci. Technol.*, 47:118–133, 2007. doi: 10.1016/j.coldregions.2006.08.021.

M. M. Baligh. Undrained deep penetration, i: shear stresses. *Geotechnique*, 36: 471–485, 01 1986. doi: 10.1680/geot.1986.36.4.471.

R. Mackenzie and W. Payten. A portable, variable-speed, penetrometer for snow pit evaluation. In *Proceedings of the International Snow Workshop*, pages 294–300, 2002.

N. Maeno and T. Ebinuma. Pressure sintering of ice and its implication to the densification of snow at polar glaciers and ice sheets. *J. Phys. Chem.*, 87:4103–4110, 1983. doi: 10.1021/j100244a023.

H.-P. Marshall and J. Johnson. Accurate inversion of high-resolution snow penetrometer signals for microstructural and micromechanical properties. *J. Geophys. Res.*, 114:F04016, 2009. doi: 10.1029/2009jf001269.

L. Martin. "eskimo words for snow": A case study in the genesis and decay of an anthropological example. *American Anthropologist*, 88(2):418–423, 1986. doi: 10.1525/aa.1986.88.2.02a00080.

H. Matsushita, M. Matsuzawa, and O. Abe. The influences of temperature and normal load on the shear strength of snow consisting of precipitation particles. *Ann. Glaciol*, 53(61):31–38, 2012. doi: 10.3189/2012aog61a022.

P. Mayne. In-situ test calibrations for evaluating soil parameters. *Characterisation and Engineering Properties of Natural Soils*, 3:1601–1652, 01 2007. doi: 10.1201/NOE0415426916.ch2.

A. McCallum. A brief introduction to cone penetration testing (CPT) in frozen geomaterials. *Ann. Glaciol.*, 55(68):7–14, 2014. doi: 10.3189/2014AoG68A005.

A. B. McCallum and A. Wiegand. Simple method for estimating snow strength using cpt sleeve friction data. *J. Cold Reg. Eng.*, 32(4), 2018. doi: 10.1061/(asce)cr.1943-5495.0000170.

D. M. McClung. The critical size of macroscopic imperfections in dry snow slab avalanche initiation. *J. Geophys. Res*, 116:F03003, 2011. doi: 10.1029/2010jf001866.

D. M. McClung and P. Schaerer. *The Avalanche Handbook*. Mountaineers, Seattle, Wash, 3rd edition, 2006.

T. Mede, G. Chambon, P. Hagenmuller, and F. Nicot. A medial axis based method for irregular grain shape representation in dem simulations. *Granular Matter*, 20(1):16, 2018a. doi: 10.1007/s10035-017-0785-7.

T. Mede, G. Chambon, P. Hagenmuller, and F. Nicot. Snow failure modes under mixed loading. *Geophys. Res. Lett.*, 45(24):13–351, 2018b. doi: 10.1029/2018gl080637.

M. Mellor. A review of basic snow mechanics. *IAHS Publication*, 114:251–291, 1975.

V. d. Montmollin. Shear test on snow explained by fast metamorphism. *J. Glaciol.*, 28(98):187–198, 1982. doi: 10.1017/s0022143000011898.

J. Mulqueen, J. V. Stafford, and D. W. Tanner. Evaluation of penetrometers for measureing soil strength. *J. Terramech.*, 14(3):137–151, 1977. doi: 10.1016/0022-4898(77)90012-x.

H. Narita. An experimental study on tensile fracture of snow. *Contributions from the Institute of Low Temperature Science*, A32:1–37, 1984.

Q. Ni, C. Hird, and I. Guymer. Physical modelling of pile penetration in clay using transparent soil and particle image velocimetry. *Geotechnique*, 60(2):121, 2010. doi: 10.1680/geot.8.p.052.

P. Paniagua, E. Andò, M. Silva, A. Emdal, S. Nordal, and G. Viggiani. Soil deformation around a penetrating cone in silt. *Géotechnique Letters*, 3(4):185–191, 2013. doi: 10.1680/geolett.13.00067.

A. Papoulis. *Probability, Random Variables, and Stochastic Processes.* McGraw-Hill, 3rd ed. edition, 1991. doi: 10.2307/1266379.

I. Peinke, P. Hagenmuller, G. Chambon, and J. Roulle. Investigation of snow sintering at microstructural scale from micro-penetration tests. *Cold Reg. Sci. Technol.*, 162:43–55, 2019. ISSN 0165-232X. doi: https://doi.org/10.1016/j.coldregions.2019.03.018.

C. Pielmeier and M. Schneebeli. Stratigraphy and changes in hardness of snow measured by hand, ramsonde and snow micro penetrometer: a comparison with planar sections. *Cold Reg. Sci. Technol.*, 37:939–405, 2003. doi: 10.1016/s0165-232x(03)00079-x.

C. Pielmeier and J. Schweizer. Snowpack stability information derived from the SnowMicroPen signal. *Cold Reg. Sci. Technol.*, 47:102–107, 2007. doi: 10.1016/j.coldregions.2006.08.013.

E. A. Podolskiy, M. Barbero, F. Barpi, G. Chambon, M. Borri-Brunetto, O. Pallara, B. Frigo, B. Chiaia, and M. N. 1. Healing of snow surface-to-surface contacts by isothermal sintering. *The Cryosphere*, 8:1651–1659, 2014. doi: 10.5194/tcd-8-2465-2014.

M. Proksch, H. Löwe, and M. Schneebeli. Density, specific surface area, and correlation length of snow measured by high-resolution penetrometry. *Journal of Geophysical Research: Earth Surface*, 120:346–362, 2015. doi: 10.1002/2014jf003266.

H. R. Pruppacher. A new look at homogeneous ice nucleation in supercooled water drops. *J. Atmos. Sci.*, 52(11):1924–1933, 1995. doi: 10.1175/1520-0469(1995)052<1924:ANLAHI>2.0.CO;2.

U. Ramamurty and M. Kumaran. Mechanical property extraction through conical indentation of a closed-cell aluminum foam. *Acta Mater.*, 52:181–189, 2004. doi: 10.1016/j.actamat.2003.09.004.

R. O. Ramseier and G. W. Sander. Sintering of snow as a function of temperature. In *Symposium at Davos 1965 - Scientific Aspects of Snow and Ice Avalanches, 5-10 April 1965*, number 69, pages 119–127. Int. Assoc. of Sci. Hydrol., Geneva, Switzerland, Publ.„ 1966.

I. Reiweger, J. Schweizer, J. Dual, and H. J. Herrmann. Modelling snow failure with a fibre bundle model. *J. Glaciol.*, 55(194):997–1002, 2009. doi: 10.3189/002214309790794869.

I. Reiweger, J. Gaume, and J. Schweizer. A new mixed-mode failure criterion for weak snowpack layers. *Geophys. Res. Lett.*, 42(5):1427–1432, 2015. doi: 10.1002/2014gl062780.

B. Reuter, J. Schweizer, and A. van Herwijnen. A process-based approach to estimate point snow instability. *The Cryosphere*, 9(3):837– 847, 2015. doi: 10.5194/tc-9-837-2015.

B. Reuter, M. Proksch, H. Löwe, A. van Herwijnen, and J. Schweizer. Comparing measurements of snow mechanical properties relevant for slab avalanche release. *J. Glaciol.*, 65(249):55–67, 2019. doi: 10.1017/jog.2018.93.

P. Robertson. Soil classification using the cone penetration test. *Canadian Geotechnical Journal - CAN GEOTECH J*, 27:151–158, 02 1990. doi: 10.1139/t90-014.

P. Robertson. Interpretation of cone penetration tests - a unified approach. *Canadian Geotechnical Journal*, 46(11):1337–1355, 2009. doi: 10.1139/t09-065.

S. R. d. Roscoat, A. King, A. Philip, P. Reischig, W. Ludwig, F. Flin, and J. Meyssonnier. Analysis of snow microstructure by means of x-ray diffraction contrast tomography. *Adv. Eng. Mater.*, 13(3):128–135, 2011. doi: 10.1002/adem.201000221.

S. Ruiz, I. Straub, S. J. Schymanski, and D. Or. Experimental evaluation of earthworm and plant root soil penetration-cavity expansion models using cone penetrometer analogs. *Vadose Zone Journal*, 15(3), 2016. doi: 10.2136/vzj2015.09.0126.

S. Ruiz, A. Capelli, A. van Herwijnen, M. Schneebeli, and D. Or. Continuum cavity expansion and discrete micromechanical models for inferring macroscopic snow mechanical properties from cone penetration data. *Geophys. Res. Lett.*, 44, 2017. doi: 10.1002/2017gl074063.

P. Satyawali and M. Schneebeli. Spatial scales of snow texture as indicator for snow class. *Ann. Glaciol*, 51(54):55–63, 2010. doi: 10.3189/172756410791386544.

P. Satyawali, M. Schneebeli, C. Pielmeier, T. Stucki, and A. Singh. Preliminary characterization of alpine snow using SnowMicroPen. *Cold Reg. Sci. Technol.*, 55: 311–320, 2009. doi: 10.1016/j.coldregions.2008.09.003.

S. Schleef and H. Löwe. X-ray microtomography analysis of isothermal densification of new snow under external mechanical stress. *J. Glaciol.*, 59(214):233–243, 2013. doi: 10.3189/2013jog12j076.

J. Schmertmann. Guidelines for cone penetration test: Performance and design,. *Federal Highway Administration, Washington, D.C.*, Report FHWA-TS-78-209: 146 pp, 1978.

M. Schneebeli and J. Johnson. A constant-speed penetrometer for high-resolution snow stratigraphy. *Ann. Glaciol*, 26:107–111, 1998. doi: 10.3189/1998aog26-1-107-111.

M. Schneebeli and S. A. Sokratov. Tomography of temperature gradient metamorphism of snow and associated changes in heat conductivity. *Hydrol. Processes*, 18 (18):3655–3665, 2004. doi: 10.1002/hyp.5800.

M. Schneebeli, C. Pielmeier, and J. Johnson. Measuring snow microstructure and hardness using a high resolution penetrometer. *Cold Reg. Sci. Technol.*, 30: 101–114, 1999. doi: 10.1016/s0165-232x(99)00030-0.

J. Schweizer and T. Wiesinger. Snow profile interpretation for stability evaluation. *Cold Reg. Sci. Technol.*, 33(2):179 – 188, 2001. ISSN 0165-232X. doi: https://doi.org/10.1016/S0165-232X(01)00036-2. ISSW 2000:International Snow Science Workshop.

J. Schweizer, J. B. Jamieson, and M. Schneebeli. Snow avalanche formation. *Rev. Geophys.*, 41(4):1016, 2003. doi: 10.1029/2002rg000123.

J. Schweizer, B. Reuter, A. van Herwijnen, B. Richter, and J. Gaume. Temporal evolution of crack propagation propensity in snow in relation to slab and weak layer properties. *The Cryosphere*, 10(6):2637–2653, 2016. doi: 10.5194/tc-10-2637-2016.

M. Silva, J. Doreau-Malioche, and G. Combe. Champs cinématiques dans un sable lors de l'enfoncement d'un pieu par tomographie RX: comparaison des corrélations numérique continue et discrète. In *CFM 2015, 22ème Congrès Français de Mécanique*, 2015.

D. Szabo and M. Schneebeli. Subsecound sintering of ice. *Appl. Phys. Lett.*, 90, 2007. doi: 10.1063/1.2721391.

A.-S. Taillandier, F. Domine, W. R. Simpson, M. Sturm, and T. A. Douglas. Rate of decrease of the specific surface area of dry snow: Isothermal and temperature gradient conditions. *Journal of Geophysical Research: Earth Surface*, 112(F3), 2007. doi: 10.1029/2006jf000514.

Y. Takeuchi, Y. Nohguchi, K. Kawashima, and K. Izumi. Measurement of snow-hardness distribution. *Ann. Glaciol.*, 26:27–30, 1998. doi: 10.3189/1998AoG26-1-27-30.

X. Wang and I. Baker. Observation of the microstructural evolution of snow under uniaxial compression using X-ray computed microtomography. *Journal of Geophysical Research: Atmospheres*, 118(22):12,371–12,382, 2013. doi: 10.1002/2013JD020352. URL `https://agupubs.onlinelibrary.wiley.com/doi/abs/10.1002/2013JD020352`.

Y. Wang, K. Huang, and Z. Cao. Probabilistic identification of underground soil stratification using cone penetration tests. *Can. Geotech. J.*, 50:766–776, 2013. doi: 10.1139/cgj-2013-0004.

W. P. Wergin, A. Rango, E. F. Erbe, C. A. Murphy, et al. Low temperature sem of precipitated and metamorphosed snow crystals collected and transported from remote sites. *J. Microsc. Soc. Amer*, 2:99–112, 1996. doi: 10.1017/s1431927696210992.

D. J. White and M. D. Bolton. Displacement and strain paths during plane-strain model pile installation in sand. *Géotechnique*, 54(6):375–397, 2004. doi: 10.1680/geot.2004.54.6.375.

G. Whiteley and A. R. Dexter. The dependence of soil penetrometer pressure on penetrometer size. *J. agric. Engng Res.*, 26:467–476, 1981. doi: 10.1016/0021-8634(81)90080-9.

Z. Yaniv, B. C. Lowekamp, H. J. Johnson, and R. Beare. Simpleitk image-analysis notebooks: a collaborative environment for education and reproducible research. *J. Digit. Imaging*, 31(3):290–303, Jun 2018. ISSN 1618-727X. doi: 10.1007/s10278-017-0037-8.

Z. Yosida, H. Oura, D. Kuroiwa, T. Huzioka, K. Kojima, S. Aoki, and S. Kinosita. Physical studies on deposited snow: I. thermal properties. Technical Report 7, Institute of Low Temperature Science, Hokkaido University, Sapporo, Japan, 1955.

H. S. Yu and J. Carter. Rigorous similarity solutions for cavity expansion in cohesive-frictional soils. *Int. J. Geomech.*, 2, 04 2002. doi: 10.1061/(ASCE)1532-3641(2002)2:2(233).

H. S. Yu and J. K. Mitchell. Analysis of cone resistance: Review of methods. *J. Geotech. Geoenviron. Eng.*, 124(2):140–149, 1998. doi: 10.1061/(asce)1090-0241(1998)124:2(140).